Title
ELECTRONIC RAMAN SCATTERING IN RARE EARTH PHOSPHATE CRYSTALS

Author
Becker, P.C.

Publication Date
1986-11-01

Lawrence Berkeley Laboratory
UNIVERSITY OF CALIFORNIA

Materials & Molecular Research Division

ELECTRONIC RAMAN SCATTERING IN RARE EARTH PHOSPHATE CRYSTALS

P.C. Becker
(Ph.D. Thesis)

November 1986

Prepared for the U.S. Department of Energy under Contract DE-AC03-76SF00098

DISCLAIMER

Electronic Raman Scattering in Rare Earth Phosphate Crystals

Philippe Claude Becker

Ph.D. Thesis

Lawrence Berkeley Laboratory
University of California
Berkeley, California 94720

November 1986

This work was supported by the Director, Office of Energy Research, Office of Basic Energy Sciences, Chemical Sciences Division of the U.S. Department of Energy under Contract Number DE-AC03-76SF00098.

I would like to thank all who were involved in my graduate career. Among those who deserve special mention, first and foremost is Sumner Davis. Without his guidance, encouragement, and sense of humor, this thesis could never have been completed.

I am also very grateful to all the members of the "rare earth community" with whom I had an opportunity to interact and learn from. I would like to thank in particular Brian Judd and Richard Leavitt for a fruitful visit and collaboration on the role of g electrons, and for introducing me to a rigour of thought which hopefully someday I will attain. Many thanks to Roger Elliott, for his kindness and willingness to hold with me enlightening discussions which laid the conceptual ground work for chapter 8. Thank you to Norman Edelstein for giving me the opportunity of pursuing the research interests that excited me (lanthanides, not actinides) and for innumerable valuable suggestions during the course of this work.

And, of course, many thanks to Arnold Koningstein, who was the original inspiration for this work and who supported it enthusiastically every step of the way.

I am very grateful to those with whom I had the occasion of discussing some of the problems raised in this thesis, especially Rufus Cone; Francois Auzel, Gerhard Schaack, Allan Zalkin, Jerry Bucher, George Shalimoff, and John Conway.

I also wish to thank my fellow graduate students David Piehler, Daisik Kim, Ruben Pecyner, Glen Stark, Ray Winkel, Mark Abrams, Peter Davis, Maralene Downs, Chuck Collins, and Joe Weiner, for their assistance and penetrating questions during the progress of this work.

Heartfelt thanks to my closest collaborators, Glen Williams, Rick Russo (Capo), and Isabelle Poirot, without whom this work could never have been completed.

Finally, I wish to thank my parents and sister for their encouragement and support.

Table of Contents

List of Figures

Introduction

The work presented in this thesis is the result of investigations of electronic Raman scattering by trivalent rare earth ions, in the form of either diluted or concentrated tetragonal rare earth phosphate crystals. Electronic Raman scattering allows the observation and measurement of the frequencies and linewidths of low lying crystal field states that are not immediately accesible by other means. A number of interesting effects are explored that are dependent on both the particular rare earth crystal used and the excitation energy of the incident laser radiation, which is provided by an argon-ion laser. The purposes of the experiments are twofold; first, to use electronic Raman scattering to study the interactions between the lanthanide ion and its host lattice; second, to study the mechanisms of the interaction between the lanthanide ion and the radiation field. The intensities of the transitions provide insights into these problems.

Rare earth ions have rather unique luminescent properties. This comes from the fact that their visible radiative transitions occur within their unfilled $(4f)^N$ electronic shell. The optical transitions thus have narrow lineshapes characteristic much more of atoms or ions in the gas phase than metals or semiconductors. This leads to a number of interesting technological applications for rare earth crystals, in particular lasers. The goal here is to explore the basic linear and nonlinear optical properties of these systems and gain a better understanding of the mechanisms that govern these properties and how these depend on the particular ion or crystal host.

The starting point for these studies is provided by the electronic energy level structure of the lanthanide ions. It is as necessary as the map is to the geographer. The energy levels of the ions are basically atomic multiplets split by the electrostatic field of the lattice ions which surround the lanthanide ion. Theses split levels are known as crystal field levels. They are obtained from absorption and fluorescence studies (one-photon studies) and also two-photon studies such as electronic Raman scattering and two photon absorption. The electronic energy level structure is systematized by means of a crystal field fit and described by a semi-empirical Hamiltonian. The crystal field fit predicts fairly accurately the positions of

energy levels that have not been observed experimentally and are in the energy range of the fitted experimentally observed levels. This subject is reviewed in Chapter 1. The electronic energy level structures for the ions of interest here have been summarized in Appendix A, along with information from the crystal field fit. Due to practical considerations, this information is given only over selected energy ranges.

This thesis consists of three separate but interdependent efforts to understand electronic Raman scattering in rare earth doped phosphate crystals and its implications for the interaction between the ion and the lattice on the one hand and the ion and the radiation field on the other, and how these two are linked. Chapters 2 and 3 serve as a general introduction and background review of Raman scattering, and contain detailed information pertaining to electronic Raman scattering in rare earth ions. The experimental technique is summarized in Chapter 2. Chapter 3 collects in one place various elements necessary to the interpretation and analysis of the spectra, namely the generic characteristics of the experimental Raman spectra, the differentiation of the electronic and phonon Raman transitions, and the theory of electronic Raman transitions within the framework of the Judd-Ofelt model of lanthanide ion radiative transitions. The Judd-Ofelt theory is an attempt to explain the intensities of radiative transitions in lanthanide ions and has been fairly successful in explaining one-photon transition intensities (absorption, fluorescence) and lifetimes, but has only recently been tested for two-photon transitions.

The first effort of this thesis is directed towards observing and measuring the electronic Raman transitions of the ions Tm^{3+}, Er^{3+}, and Ho^{3+}, in both pure and diluted tetragonal rare earth phosphate crystals. The spectra for Ho^{3+} are the first reported observations of electronic Raman scattering for this ion. The measurement of the experimental electronic Raman transition intensities for Tm^{3+}, Er^{3+}, and Ho^{3+} is an important test of the Judd-Ofelt theory applied to two-photon transitions. Chapter 4 describes the experimental Raman spectra obtained for Tm^{3+}, Er^{3+}, and Ho^{3+}. Chapter 5 compares the experimental and calculated relative electronic Raman intensities for these three ions, for transitions between individual crystal field states, and discusses the implications for the Judd-Ofelt theory. It is shown that electronic Raman scattering can help to pick out the relevant intermediate states that serve in mediating the Raman transition; and to test the accuracy of the wavefunctions used for the initial and final states. The character of the intermediate states can be picked out in particular by measuring the asymmetry of the electronic Raman

transitions under interchange of the polarizations of the incident and scattered photons. This asymmetry is a rather unique feature of electronic Raman scattering. A surprising result discussed in Chapter 5 is that wavefunctions with g orbital character, which in the free ion are so high in energy as to be of negligible importance as intermediate states in two photon transitions, appear to contribute significantly for the ions in the crystal. This is indicated by all three ions Tm^{3+}, Er^{3+}, and Ho^{3+}, to varying degrees. Even taking into account the presence of g orbitals, several discrepancies remain between the calculated and observed relative electronic Raman transition intensities. A main conclusion of this work is that the atomic viewpoint of a lanthanide ion in a crystal has serious limitations. Even though the crystal field provided by the solid state environment is a small perturbation on the energy level structure, it appears to influence the optical properties of the ion to a great degree.

Chapters 6 and 7 describe the second effort, which is directed towards the studies of the electronic Raman transitions of Er^{3+} under *resonant* excitation. This experiment is possible due to the near coincidence in energy between the 488.0 nm line of the argon-ion laser and the intra-$4f^N$ transitions $^4I_{15/2} \longrightarrow {}^4F_{7/2}$ of Er^{3+}. The resonance enhancement factors of the electronic Raman transitions are observed to be in the range 10 to a 100. A number of mixed crystals $Er_xLu_{1-x}PO_4$ with x ranging from 0.01 to 1 were studied. The variation of the resonant intensities are also studied as a function of temperature, with the main effect appearing to be the self-absorption by the crystal of the scattered Raman radiation.

The resonance enhancement depends on both the strength of the "forbidden" electric dipole matrix elements of the $^4I_{15/2} \longrightarrow {}^4F_{7/2}$ crystal field transitions (assumed to be independent of the erbium concentration) *and* the precise position in energy of these transitions relative to the 488.0 nm line. Since the actual mix of erbium and lutetium delicately shifts the crystal field levels, the mixed crystals allow a quantitative study of the relative intensities of the resonant electronic Raman transitions. The study of the enhancement of electronic Raman scattering is a useful guide to enhancing higher order optical processes, such as four wave mixing, in lanthanide ion doped crystals.

Quantum mechanical interference is observed between the resonant and nonresonant pathways that contribute to the amplitude of the transitions. It is shown that a simple calculation can be made of the electronic Raman transitions under resonant excitation that agrees well with the experimental data and predicts how the relative electronic Raman

intensities would vary if the excitation were tuned across the resonant transitions. These calculations can be found in Chapter 7. These experiments also open the way to better understanding the problem of differentiating between resonance Raman scattering and fluorescence, in particular from the time resolved point of view. It is shown how an estimate of the dephasing time T_2 can be obtained by comparing the Raman intensities in the mixed crystals without resorting to time-resolved measurements, although these are an essential complement to these studies. T_2 is calculated to be at least on the order of 0.1 nsec.

The third and last part of the thesis, chapter 8, presents and discusses the experimental Raman spectra of the pure crystal $YbPO_4$ and the mixed crystals $Yb_xLu_{1-x}PO_4$ for $x = 0.25, 0.50, 0.75$. For these crystals the electronic and vibrational Raman transitions can no longer be considered to be independent.

In the semiclassical picture, the Raman transitions come from the radiation emitted by the harmonically oscillating electronic and vibrational polarizations of the medium which are driven by the incident radiation field. These polarizations can couple via a resonance type interaction. Thus if a phonon and an electronic Raman transition are almost degenerate in energy they will repulse each other (the anticrossing effect) and the transitions *actually observed* will correspond to hybrid polarizations or excitations of the material that are linear combinations of electronic and vibrational polarizations or excitations, and which exhibit a split mode spectrum with a lifting of the near energy degeneracy.

In the ytterbium phosphate crystals, this phenomenon occurs very markedly in the 300 cm^{-1} wavenumber region, where two electronic and one phonon transition coexist in the E_g symmetry spectra (the symmetries of the excitations need to be identical for the coupling to be allowed). At 4.2 K the coupled mode spectrum is spread over roughly 90 cm^{-1}, which indicates extremely strong coupling strengths. The spectra are dependent on the temperature and the ytterbium concentration. The temperature shift of the spectra is interpreted by invoking the thermal depopulation of the ground state and the broadening of the electronic components of the transitions. While the $YbPO_4$ spectra are relatively simple and can be described semi-quantitatively, those of the mixed crystals are more complex and are treated only qualitatively.

The first approach used is to treat the system using a simple two by two or three by three Hamiltonian with off-diagonal elements that constitute phenomenological coupling parameters. This approach gives a fairly accurate account of the line positions and their

variation as a function of temperature. The coupling strengths are empirically determined parameters. The second and subsequent approach which seeks to also explain the asymmetric coupled mode lineshapes involves the Greens function techniques and assumes that the transitions are coupled harmonic oscillators with damping constants that determine the linewidths. The parameters of the model are determined by making a least squares fit of the calculated to the observed spectrum as a function of frequency. This works fairly well in the temperature range 4.2 to 160 K using a three level coupled system consisting of two electronic and one vibrational excitation, but cannot be easily extended to the higher temperature range where the spectra are extremely broad and suggest rather a two level coupled system.

To summarize, the organization of the thesis is as follows:

1. A core unit which reviews the optical properties of lanthanide ions (Chapter 1) and discusses the general properties and results of electronic and vibrational Raman scattering in lanthanide phosphate crystals (Chapters 2 and 3).

2. A description of the experimental electronic Raman spectra of Tm^{3+}, Er^{3+}, and Ho^{3+} in pure and diluted phosphate hosts (Chapter 4), and a theoretical chapter that analyzes and interprets the results with respect to the intensities of the transitions (Chapter 5).

3. A description and discussion of the experimental resonant electronic Raman spectra of Er^{3+} in pure and diluted erbium phosphate crystals (Chapter 6), and a calculation of the relative intensities of the transitions that highlights quantum mechanical interference between the nonresonant and resonant intensity channels (Chapter 7).

4. A description and analysis of the coupled mode spectra of ytterbium phosphate crystals in the 300 cm^{-1} region in E_g symmetry (Chapter 8).

Chapter 1

Fundamental Properties of Trivalent Lanthanides

This chapter serves as a review of the atomic properties and optical spectra of trivalent lanthanide (rare earth) ions. The unique characteristics of the 4f orbitals of lanthanide ions are introduced first, as they are crucial to understanding the optical properties of both the free ions and those doped into crystals. The semi-empirical Hamiltonian and crystal field model, important in systematizing the electronic energy level structure of the ions, are discussed. Finally, a description is given of the various one-photon and two-photon processes in the visible spectrum of trivalent lanthanide ions and their application in spectroscopic investigations.

1.1 Atomic Theory of Trivalent Lanthanides in Crystalline Hosts

1.1.1 Introduction - The discovery of 4f orbitals

The periodic table in its conventional form sets aside the rare earth series, separating it from the rest of the elements. This is necessary because of the difference between the chemical properties of the rare earths and those of the atoms that precede it in the periodic table. This difference originates in their electronic configuration, which is characterized by a valence shell consisting of f electrons. To date, two f electron series have been identified and studied; the lanthanides, elements 57 through 71, and the actinides, elements 89 through 103. The names employed are somewhat of a misnomer, since the rare earths are neither

rare nor hidden (the Greek *lanthanos* means hidden). Lanthanides, in their trivalent state, form the object of this study.

The beginning of the study of the rare earths dates back to the work of J. Becquerel in the early 1900's [1,2,3]. He observed sharp absorption lines in the visible region of the spectrum of rare earth salts cooled to below 100K, and found that these lines were split by a magnetic field. Quantum mechanics is needed to explain the spectral structure of the absorption and emission patterns, since these are atomic in nature and resemble those of atoms in the gas phase. It was later realized that these sharp lines came from "forbidden electric-dipole" transitions within the 4f shell of the electronic configuration of the rare earth atom.

The theoretical underpinning of the atomic theory of the 4f group was provided by Maria Mayer in 1941 [4]. Even though the 4f shell is being filled with electrons as the atomic charge Z runs from Z=57 to Z=71, it is an inner orbital in the sense that the 4f radial eigenfunction is localized within the full $5s^2 5p^6$ shells. The contraction of the 4f shell occurs abruptly at Z=57. Mayer explained this by considering the effective radial potential in the Thomas-Fermi model:

$$V(r) = -\frac{e^2}{r}\left[1 + (\mathrm{Z}-1)\varphi\left(\frac{r}{\mu}\right)\right] + \frac{h^2}{8\pi^2 m}\cdot\frac{l(l+1)}{r^2} \qquad (1.1)$$

which is the Coulomb potential energy plus the centrifugal potential energy, $\varphi\left(\frac{r}{\mu}\right)$ being the Thomas-Fermi function. For f electrons l is equal to 3. The radial eigenfunction is determined by the radial part of the Schrödinger equation with $V(r)$ as the effective potential energy. The behavior of $V(r)$ as a function of Z is very enlightening. For low values of Z there is only one minimum of $V(r)$, situated at roughly 6Å. At higher values of Z there is also a second minimum of $V(r)$ at a small value of r. When this inner potential well becomes deep and large enough, the 4f eigenfunction collapses to an inner orbital with a tight binding energy. Mayer's model predicts that this will occur at Z=60, in practice this occurs for lanthanum, element 57. The scenario is quite similar for the 5f electrons of the actinides and the nd (n=3,4,5) electrons of the transition elements. Modern studies, which involve self-consistent Hartree-Fock calculations performed by computer, give more accurate predictions of the wavefunctions and the one-electron binding energies [5,6]. In addition, as one progresses along the rare earth series the average radius of the f orbitals slowly decreases. This is the so called lanthanide contraction, which is examplified by a

10% decrease in ionic radius between Ce^{3+} and Lu^{3+} [7, p. 2].

The electronic configuration of neutral lanthanide atoms is of the form $(Xe)4f^{N'}6s^2$ or $(Xe)4f^{N'-1}5d6s^2$, where (Xe) represents a xenon core. The 4f electrons have less binding energy than the electrons of the $5s^25p^6$ shell of (Xe), however their average radius of 0.7 Bohr radius is smaller than that of the $5s^25p^6$ electrons. The ionization of the lanthanides to their trivalent state involves first the removal of the two loosely bound 6s electrons, and then that of either a 4f or a 5d electron. The trivalent lanthanides, which is the most common oxidation state of these elements, thus have the electronic configuration $(Xe)4f^N$. The energy range of the ground configurations of neodymium ions and their ionization potentials are displayed in Figure 1.1, which is taken from Cowan [5, p. 602]. Even though it is an f electron which is added last to the rare earth atom as its electronic shells are built up following the *aufbau* principle, the first stage of ionization involves the removal of a 6s electron and not that of the f electron that was just added. This is because during the ionization the nuclear charge does not change and as a result the minimum energy state (which incorporates the effect of the interactions between the electrons) is that for which a 6s electron is removed. The fact that the f electrons extend so little into their environment and are shielded by the $5s^25p^6$ electrons, is paramount to explaining the atomic-like properties of lanthanides doped into solids. Figure 1.2 shows the radial distribution functions of the 4f, 5s, 5p, 5d, and 5g orbitals for the Pr^{3+} free ion as obtained from Hartree-Fock calculations [8]. The radial distribution function is defined as the square of the radial wavefunction times the squared radius. The mean radial position of a 4f electron is seen to be closer to the nucleus than that of a 5s or 5p electron. In contrast, the 5d and 5g orbitals, which belong to the excited configurations $4f^{N-1}5d$ and $4f^{N-1}5g$, are spread out over a broad range relatively far from the nucleus. The free ion wavefunctions will expand slightly when the ion is placed in a crystal. This is known as the nephelauxetic effect [9].

Figures 1.3 and 1.4 show the extent of the $4f^N$ configuration and the onset (or extent when available) of the three lowest excited configurations, $4f^{N-1}5d$, $4f^{N-1}6s$, and $4f^{N-1}6p$, for the various trivalent lanthanide free ions. Figures 1.3 and 1.4 are drawn from several different sources [10,11,12,13,14]. It should be noted that when trivalent lanthanide ions are placed into solids and subjected to the crystal field of the lattice ions surrounding it, the $4f^{N-1}5d$ configuration drops in energy by about 10,000 cm^{-1} relative to the ground $4f^N$ configuration, as compared to its free ion value. The ionization energies of the trivalent rare

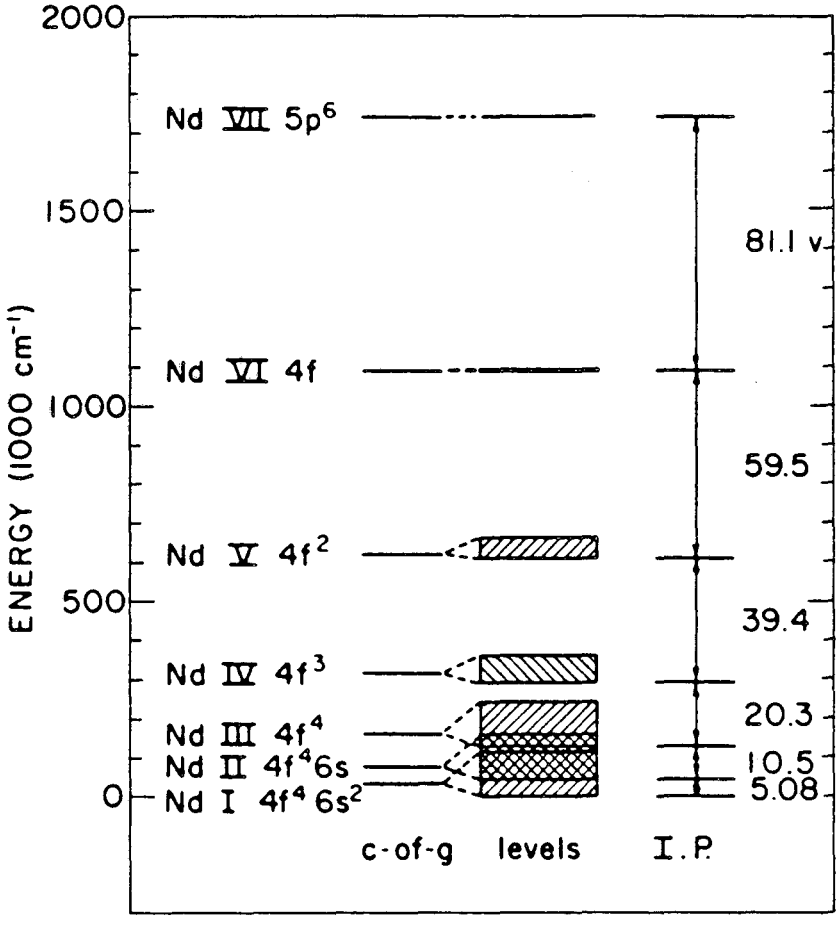

Figure 1.1: Computed energy range of the levels of the ground configurations of neodymium ions and their ionization potentials (in volts), from Cowan [5, p.602]

earth free ions range from 296,000 cm^{-1} for Ce^{3+} to 365,000 cm^{-1} for Lu^{3+} [13].

The environment provided by crystalline hosts destroys the spherically symmetric environment that rare earth atoms enjoy in the vapor phase. Thus the degeneracy of the atomic states will be lifted to some degree. The crystal lattice, or more appropriately the crystal field produced by the ions at the lattice points, provides a certain symmetry at the sites occupied by the lanthanide ion. This site symmetry can be classified by one of the 32 crystal point groups. This was recognized by Bethe, who in 1929 showed how the crystal-field splitting of the free ion levels could be characterized group theoretically [15]. This paved the way for a fuller understanding of the multitude of absorption lines that appear in the visible spectra of lanthanide doped crystals. These transitions occur between the crystal field states of the unfilled 4f shell and are as a consequence not allowed in the electric dipole approximation, since the parity must change in a dipole transition (Laporte rule). Nevertheless, these transitions are "forbidden electric dipole" in nature, with small oscillator strengths. Their presence was explained in 1937 by Van Vleck, who referred to this problem as "The Puzzle of Rare Earth Spectra in Solids" [16]. The principal mechanism is the admixture into the $4f^N$ configuration of a small amount of excited opposite parity configurations.

The necessary conceptual foundation for the study of the visible spectra of rare earth ions was thus established by 1941 and qualitatively, the spectra were reasonably well understood, if one took into acount the fact that both the atomic physics of the 4f shell and the group theoretical symmetry of the host crystal were needed to explain the observed pattern of visible absorption and emission lines. Quantitative studies were made possible by the atomic and crystal field models [7,9], which use the mathematical techniques developed by G. Racah in the 1940's [17,18,19]. The state of the spectroscopic investigations or rare earth ions in crystals was summarized up to 1968 by Dieke [20]. Hüfner's work [7] is a briefer but more recent exposition.

1.1.2 Semi-Empirical Atomic and Crystal Field Hamiltonian

The configurations of the atomic electrons of the lanthanide ions are specified by a set of one-electron orbitals. Since the closed shells are assumed to be inert with respect to optical excitations, they will not be referred to and only the ground and excited configurations of the 4f electrons will be used to specify the states. The Hamiltonian operator H that determines

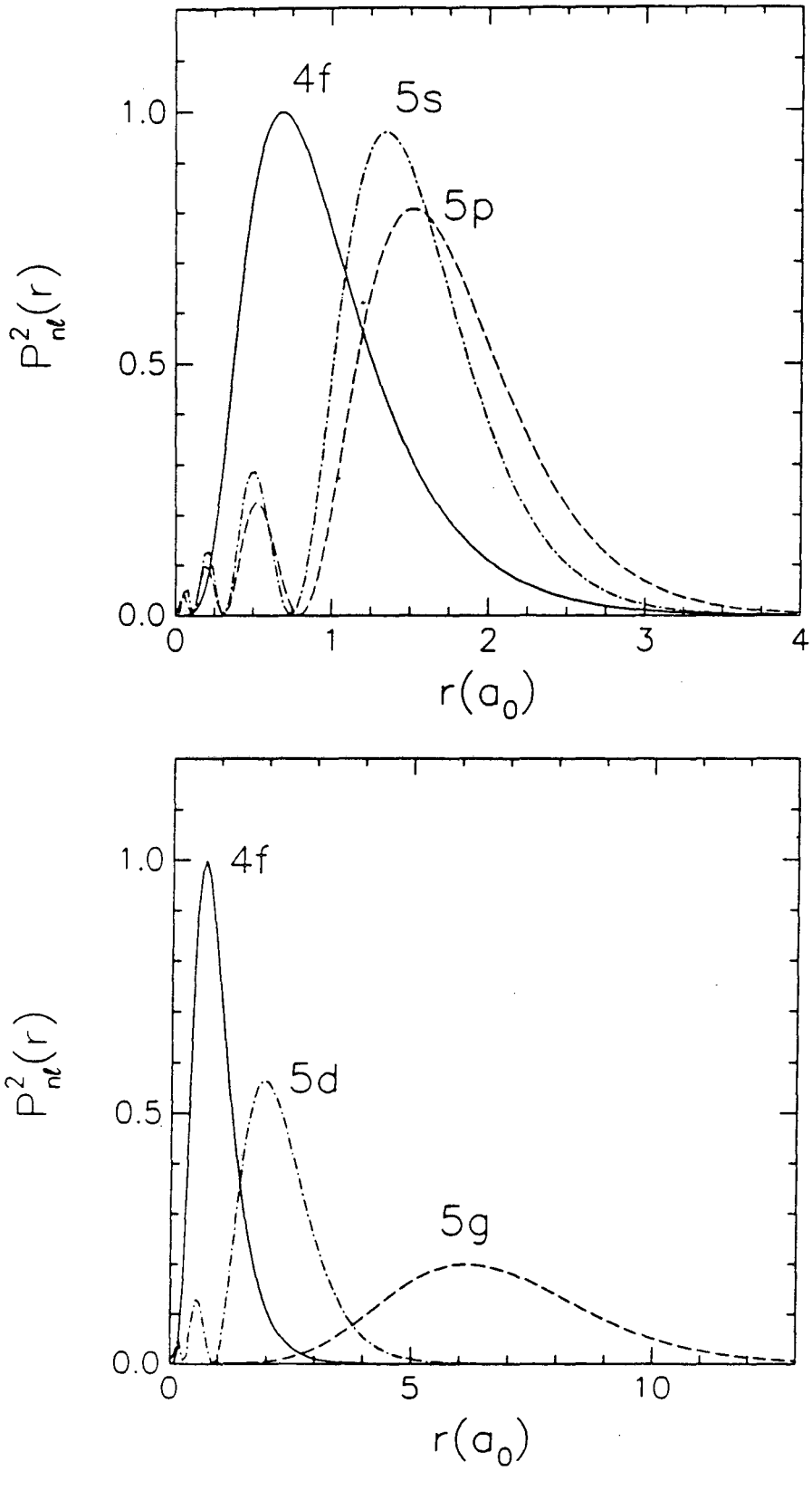

Figure 1.2: Radial distribution functions of the 4f, 5s, 5p, 5d, and 5g orbitals for the Pr^{3+} free ion, from Hartree-Fock calculations [8]. Top: 4f, 5s, and 5p orbitals of the ground configuration $4f^2 5s^2 5p^6$. Bottom: 4f, 5d, and 5g orbitals of the configurations $4f^2$, $4f5d$, and $4f5g$, respectively.

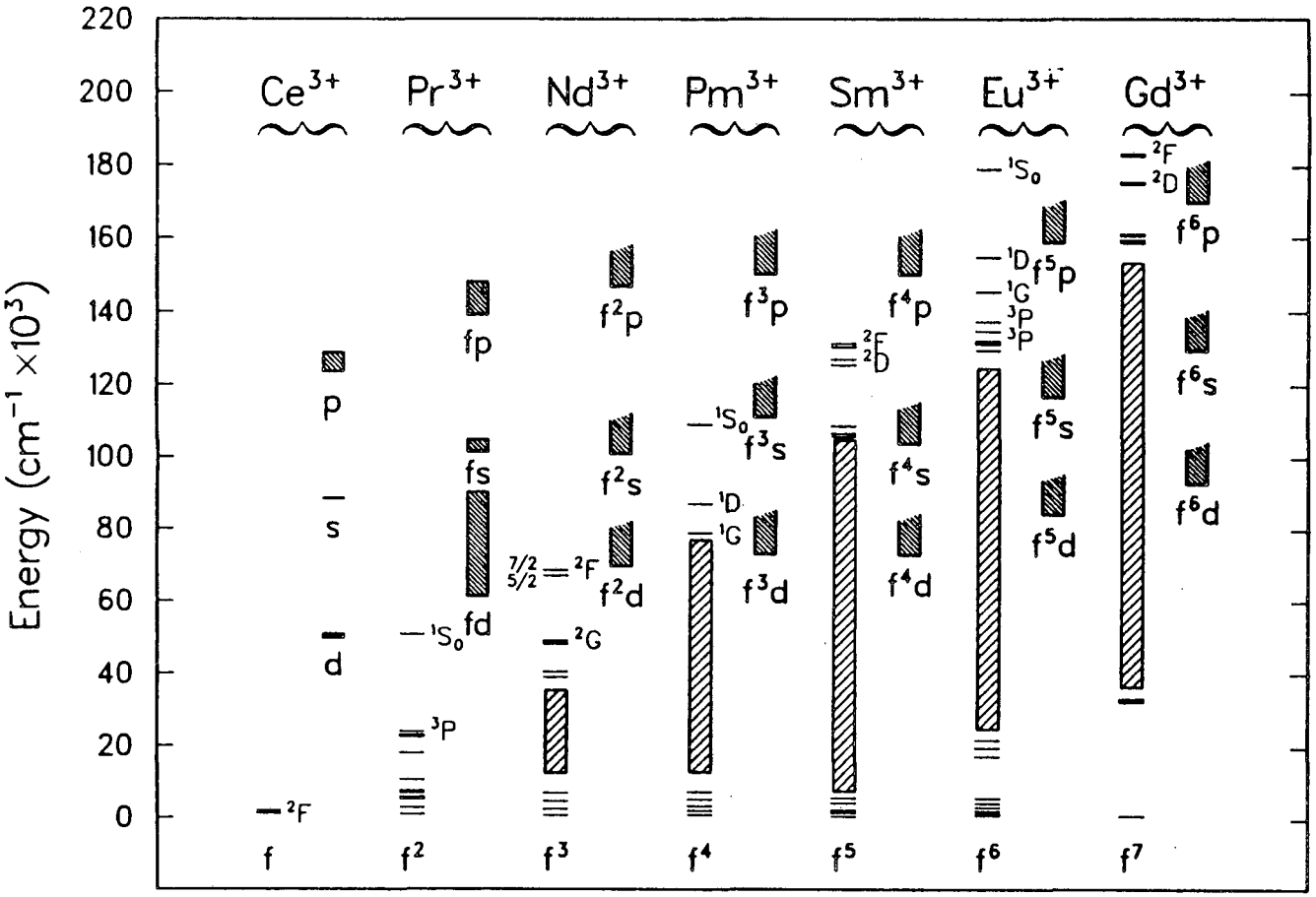

Figure 1.3: Plot of the low-lying configurations of the trivalent lanthanide free ions, Ce^{3+} through Gd^{3+}. For the $4f^N$ configuration, the shaded boxes indicate areas where the energy levels are too densely spaced to be drawn individually. For the $4f^{N-1}5d$, $4f^{N-1}6s$, and $4f^{N-1}6p$ excited configurations, the extent of the configuration is shown when available (closed boxes), otherwise only the onset of the configuration is indicated.

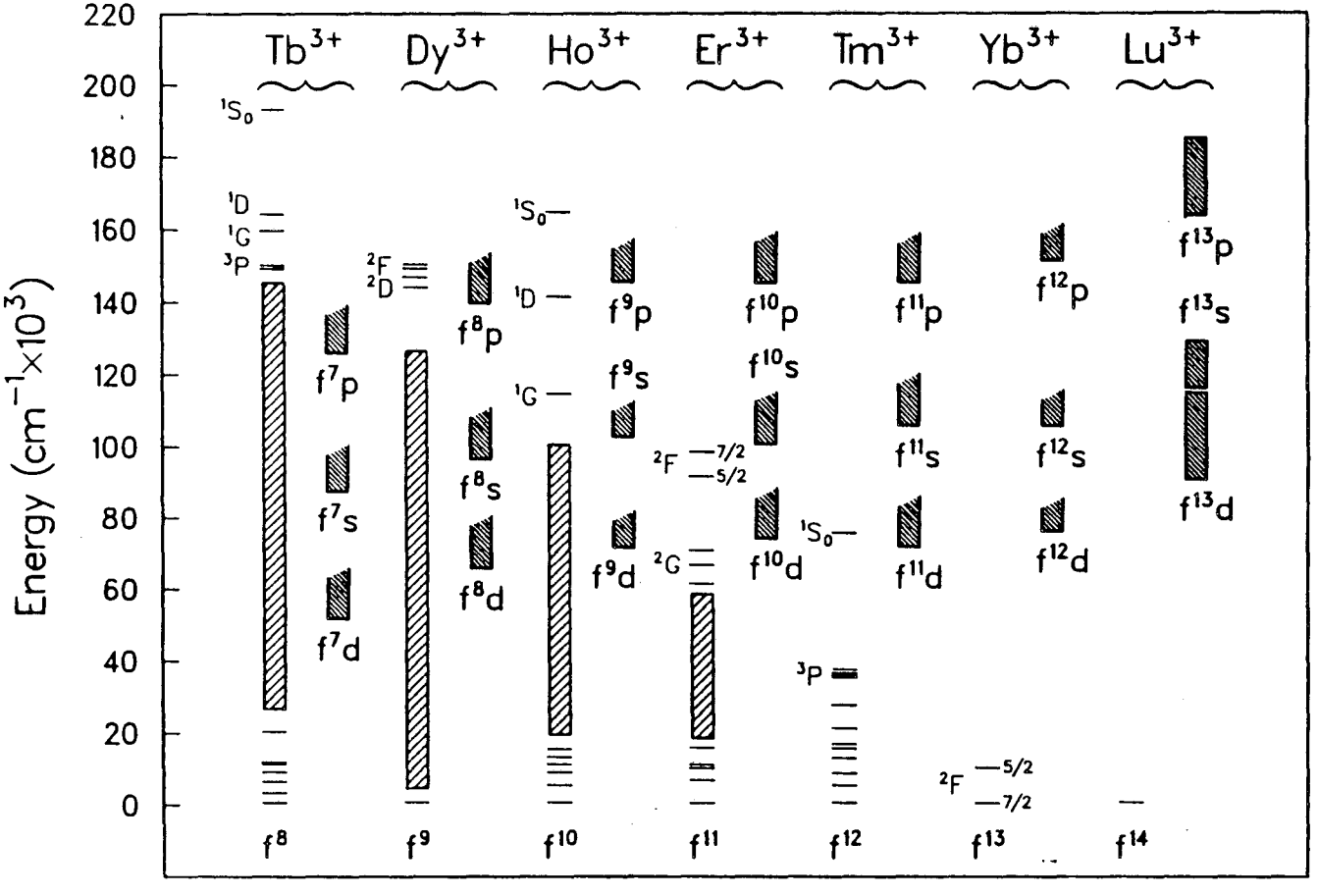

Figure 1.4: Plot of the low-lying configurations of the trivalent lanthanide free ions, Tb^{3+} through Lu^{3+}. For the $4f^N$ configuration, the shaded boxes indicate areas where the energy levels are too densely spaced to be drawn individually. For the $4f^{N-1}5d$, $4f^{N-1}6s$, and $4f^{N-1}6p$ excited configurations, the extent of the configuration is shown when available (closed boxes), otherwise only the onset of the configuration is indicated.

the wavefunctions of the 4f electrons contains terms that describe the atomic interactions of the free ion (which might be modified by the presence of the surrounding ligands), and terms that describe the interaction of the electrons with the crystal field produced by the surrounding charges. For such high atomic number systems as the rare earths, it is extremely unwieldy to calculate H and the 4f energy levels from first principles. Rather, H is written in a parameterized form and the parameters are then found by adjusting them to obtain the best fit of calculated to experimental energy levels. The Hamiltonian operator for the 4f electrons is written as follows [7,9]:

$$H = H_{atomic} + H_{cf} \tag{1.2}$$

where

$$H_{atomic} = -\frac{\hbar^2}{2m}\sum_{i=1}^{N}\nabla_i^2 - \sum_{i=1}^{N}\frac{Z^*e^2}{r_i} + \sum_{i<j}^{N}\frac{e^2}{r_{ij}} + \sum_{i=1}^{N}\varsigma(r_i)\vec{s}_i.\vec{l}_i + \text{smaller terms} \tag{1.3}$$

and

$$H_{cf} = \sum_{k,q,i} B_q^k C_q^{(k)}(i) \tag{1.4}$$

H_{atomic} is the free ion Hamiltonian in the central field approximation. N is the number of 4f electrons, Z^*e is the effective nuclear charge (which takes into account the closed shells that lie between the nucleus and the 4f electrons), and $\varsigma(r_i)$ the spin-orbit coupling function. The first two terms of H_{atomic}, which represent the kinetic energy and the Coulomb interaction of the nucleus with the 4f electrons, are spherically symmetric and do not lift the degeneracy of the $4f^N$ configuration. However the third and fourth terms, which represent the mutual Coulomb repulsion and spin-orbit interactions of the 4f electrons, are responsible for the spread of the $4f^N$ free ion levels over tens of thousands of wavenumbers. H_{cf} is the crystal field Hamiltonian where the summation over i is over all the 4f electrons of the ion. The B_q^k are constants, and the $C_q^{(k)}$ are proportional to the spherical harmonics:

$$C_q^{(k)}(\theta,\phi) = \left(\frac{4\pi}{2k+1}\right)^{\frac{1}{2}} Y_{kq}(\theta,\phi) \tag{1.5}$$

There are several schemes for describing the states of a many-electron system. For rare earth ions, it is customary to use Russell-Saunders, or SL, coupled states. To write Russell-Saunders states, one first couples the orbital angular momenta $\vec{l}_i$ to form a resultant total orbital angular monentum $\vec{L}$, and similarly for the spins $\vec{s}_i$ to form a total spin $\vec{S}$.

$\vec{L}$ and $\vec{S}$ are then coupled to form $\vec{J}$, the total angular momentum. Thus a state of the $4f^N$ configuration will be described by the ket $|4f^N \alpha S L J J_Z\rangle$, where α refers to the other quantum numbers needed to label the state. These kets form a complete set. One calculates the matrix elements of H between these states and diagonalizes H to obtain the eigenvalues and eigenvectors.

When the mutual electrostatic repulsion of the electrons is much stronger than the spin-orbit coupling, the eigenfunctions are nearly pure SL coupled states. The electrostatic interaction splits the configuration into terms ^{2S+1}L, and the spin-orbit interaction lifts the degeneracy with respect to J and splits the terms into levels $^{2S+1}L_J$. In the case of lanthanide ions, it is not quite correct to consider the electrostatic and spin-orbit interactions as successively smaller perturbations. The actual eigenstates of the system are linear combinations of $^{2S+1}L_J$ states, since these form a complete set of functions for functions of the angular variable. The only caveat to this statement is that for some configurations the seniority quantum number or a group theoretical label are needed in addition to the Russell-Saunders label to uniquely specify a state. In general, when one refers to a $^{2S+1}L_J$ level of a lanthanide ion, it constitutes the leading term in the expansion of the state in Russell-Saunders coupled states.

Similarly, it is not a good approximation to use a spin-orbit interaction of the form $\lambda \vec{L} \cdot \vec{S}$, since this operator has no off-diagonal elements in L and S, whereas $\sum_i \vec{l}_i \cdot \vec{s}_i$ does. For rare earth ions there is substantial SL mixing, an effect which grows stronger as the atomic number increases. This is due to the fact that the spin-orbit interaction increases faster than the mutual electrostatic repulsion between the 4f electrons, as one moves up the lanthanide series [5, p. 238].

There still remains a degeneracy with respect to J_Z, since spherical symmetry has not been broken by H_{atomic}. The crystal field removes that symmetry by the non-spherically symmetric distribution of charge surrounding the free ion. For 4f electrons, the crystal field Hamiltonian is a small perturbation compared to the electrostatic and spin-orbit interactions, since it is roughly a 100 times smaller in magnitude. In contrast, the crystal field splittings of the excited configurations are quite large, on the order of 20,000 cm^{-1}, since the excited orbitals (e.g. 5d or 5g) are not shielded as the 4f orbitals are.

Figure 1.5, a chart originally drawn by Dieke [21], is the energy level diagram of the low-lying f^N states of the trivalent lanthanide ions doped into $LaCl_3$, the multiplets being

labeled by the leading $^{2S+1}L_J$ component. The widths of the multiplets show the extent of the crystal field splitting. Since the crystal field of the host lattice is usually such a small perturbation, the Dieke chart is an accurate representation of the f^N electronic energy level structure for trivalent rare earth ions doped into most ionic insulating crystals.

A number of other terms are added into the Hamiltonian in an attempt to correct the simplistic assumptions that underlie it and model some of the more complex effects that can occur in many-electron systems. In its full glory, the Hamiltonian used in fitting the energy levels of the rare earth ions doped into phosphate hosts is written [22]:

$$\begin{aligned} H &= \sum_{k=0,2,4,6} F^k(\mathrm{nf},\mathrm{nf}) f_k + \zeta_{4f} a_{so} + \alpha L(L+1) + \beta G(\mathrm{G}_2) + \gamma G(\mathrm{R}_7) \\ &\quad + \sum_{k=2}^{8} T^k t_k + \sum_{k=0,2,4} M^k m_k + \sum_{k=2,4,6} P^k P_k + \sum_{k,q,i} B_q^k C_q^{(k)}(i) \end{aligned} \tag{1.6}$$

We briefly discuss the origin of these various terms.

- The expression for the electrostatic interaction of two 4f electrons i and j can be calculated from the identity

$$\frac{e^2}{r_{ij}} = \sum_{k=0}^{\infty} \frac{r_<^k}{r_>^{k+1}} \mathbf{C}^{(k)}(i) \cdot \mathbf{C}^{(k)}(j) \tag{1.7}$$

  where $r_<$ and $r_>$ are respectively the lesser and greater of r_i and r_j. For a configuration of N equivalent 4f electrons the matrix element of the Coulomb interaction separates into two parts [7,9]. The first factor is a radial integral involving $r_<$ and $r_>$ and the 4f radial eigenfunctions. This is the term $F^k(\mathrm{nf},\mathrm{nf})$ which can be calculated *ab initio* if the eigenfunctions are known, but is usually treated as a parameter. The second factor is the matrix element of a product of spherical harmonics, taken between SL states. It can be calculated using standard tensor operator techniques. These angular matrix elements have been tabulated for the various f^N configurations [23].

- The spin-orbit matrix elements can also be calculated using tensor operator methods [9,19]. The spin-orbit operator is found to be proportional to $\mathbf{V}^{(11)}$, the unit tensor of rank one in both spin and orbital angular momentum space. The matrix elements of $\mathbf{V}^{(11)}$ are also well known [23]. The part of the matrix element that depends on the radial variable is incorporated into the spin-orbit coupling constant ζ_{4f} defined by

$$\zeta_{4f} = \int R_{4f}^2(r) \zeta(r) dr. \tag{1.8}$$

  As with the F^k, it is treated as a parameter.

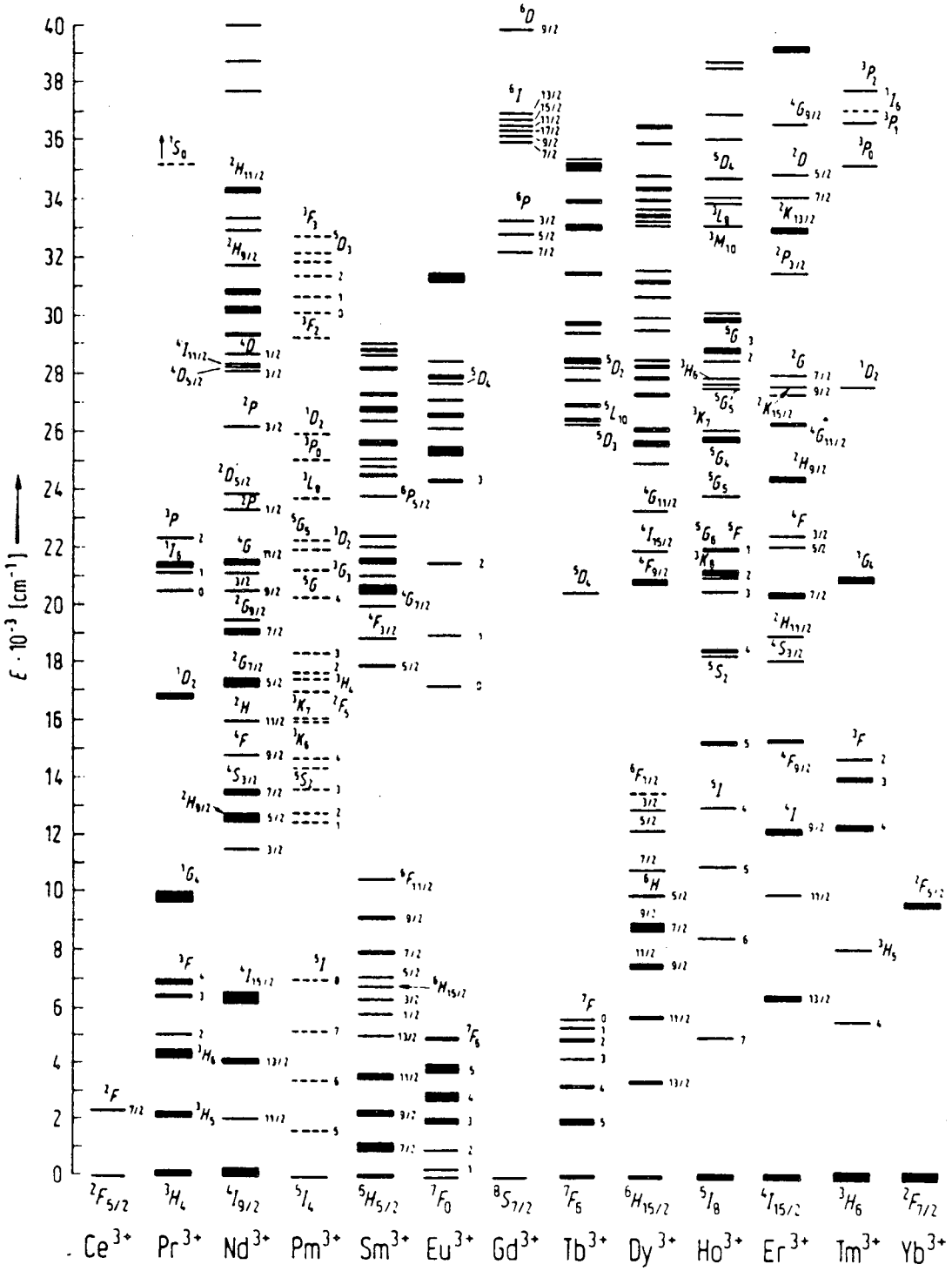

Figure 1.5: Energy level diagram of the low-lying $4f^N$ states of trivalent lanthanide ions doped into $LaCl_3$.

- $\alpha L(L+1) + \beta G(\mathrm{G}_2) + \gamma G(\mathrm{R}_7)$ models the correction to the electrostatic interaction due to two body Coulombic interactions between the ground $4f^N$ configuration and excited configurations [9,24,25]. It is derived using the assumption that the higher lying configurations are distant in energy, so that one can apply the closure theorem in angular space to the states of the excited configurations when calculating the second order correction to the electrostatic interaction between 4f electrons. $L(L+1)$, $G(\mathrm{G}_2)$, and $G(\mathrm{R}_7)$ are the eigenvalues of Casimir's operators for the groups SO(3), G_2 and R_7, respectively. The irreducible representations of the groups SO(3), G_2, and R_7, are used to classify the states of the $4f^N$ configuration [26, section 12]. $G(\mathrm{G}_2)$ and $G(\mathrm{R}_7)$ can be can be found in Wybourne [9].

- The T^k, introduced by Judd, are needed to describe the correction to the electrostatic interaction by three body configuration interactions [27]. They come into play when the number of 4f electrons is larger or equal to 3. The appearance of the two-body and three-body configuration interaction corrections can be made more transparent by using the second-quantized form of the electrostatic operator [26, sections 15,16,17].

- The remaining interactions are of a magnetic type [28] and do not have a large effect on the energy levels. They are relativistic in origin. The M^k $(k = 0, 2, 4)$ are the Marvin integrals and take into account the spin-spin and spin-other orbit interactions within the $4f^N$ configuration. The correction to the spin-orbit interaction by the electrostatic interaction of the $4f^N$ ground configuration with higher excited configurations are taken into account by the P^k $(k = 2, 4, 6)$.

- The form in which the crystal-field Hamiltonian has been written is merely a statement that the spherical harmonics are a complete set of functions insofar as the angular variables are involved. The summation over i is over all the 4f electrons of the ion. The method for calculating the matrix elements of is given by Whybourne [9, Chapter 6]. Only a few of the B_q^k are non-zero. For f electrons the Wigner-Eckart theorem imposes $k \leq 6$. The point group symmetry at the site where the rare earth ion is located further restricts the number of non-zero B_q^k [7,9].

  A modern review of the various atomic effects associated with complex spectra is given by Judd [26].

1.1.3 Energy Level Fitting and Validity of the Semi-Empirical Hamiltonian

The semi-empirical Hamiltonian that was introduced in the previous section contains a large number of effective operators. These operators were added in a piecemeal fashion as the art of fitting complex spectra advanced throughout the 1960's. The reason that this parameter based method has remained so prevalent is heuristic in nature, in the sense that with a relatively small number of parameters one can reasonably accurately reproduce observed spectra. In practice, one performs a least-squares fit of the calculated energy levels to the observed energy levels, or more appropriately to the observed transitions. The accuracy of the fit is characterized by the reduced root-mean-square energy deviation, defined as

$$\sigma = \left(\sum_i \frac{\Delta_i^2}{m-n} \right)^{\frac{1}{2}} \tag{1.9}$$

where the Δ_i are the differences between the observed and calculated energy levels, m being the number of levels and n the number of free parameters. The prototypical example of the use of this type of Hamiltonian in systematizing the $4f^N$ spectra of the trivalent lanthanides is the work of Carnall, Crosswhite, and Crosswhite, using the host crystals LaF_3 and $LaCL_3$ [29].

Typically, 50 to 150 energy levels up to 50,000 cm^{-1} are assigned and can be fit with 10 to 20 parameters, yielding rms energy deviations in the range 10 to 30 cm^{-1}. This is quite good if one considers that the $4f^N$ configuration can go up to 200,000 cm^{-1} in energy so that σ is on the order of 0.1-0.01% of the spread in energy of the configuration. However, experimentally these energies can be found to within 0.1 cm^{-1} accuracy, so that there is still quite a lot of room for the theory to improve. A more modern approach would be to use the orthogonalized operators of Judd [30,31,32,33].

The present work uses the energy level fits of the ions Yb^{3+}, Tm^{3+}, Er^{3+}, and Ho^{3+}, doped in $LuPO_4$ and YPO_4 [34,35]. The energy levels, wavefunctions, and atomic and crystal field parameters determined by these fits are listed and discussed in Appendix A.

1.2 One-Photon Spectroscopy of Trivalent Lanthanides in Crystalline Hosts

1.2.1 The Character of $4f^N \rightarrow 4f^N$ Optical Transitions

Several mechanisms come into play to give the forbidden electric dipole transitions small but significant amplitudes [5]. A brief description is given of these mechanisms. Peacock has given a review which covers through 1975 [36].

- In cases where the site symmetry is not a center of inversion, the crystal field Hamiltonian can contain odd-parity terms. These terms introduce into the 4f wavefunctions small components of opposite parity higher energy configurations, such as $4f^{N-1}5d$. The intensity of a particular transition is then determined by the amount of opposite parity configurations which have been mixed into the initial and final states.

- Crystal vibrations of odd-symmetry can also admix odd-parity $4f^{N-1}nl$ configurations into the $4f^N$ manifold. For a centro-symmetric crystal, this is the only source of "forbidden electric dipole" transitions.

- Magnetic dipole transitions are allowed since no change in parity is needed for this process. The intensities of magnetic dipole transitions are usually weaker then the "forbidden electric dipole" transitions (for non centro symmetric crystals). There are fewer magnetic dipole transitions since they must satisfy the selection rules
  $\Delta J = 0, \pm 1$, $\Delta L = 0$, $\Delta S = 0$, $J = 0 \rightarrow J = 0$ transitions forbidden.

  Most of the intensity calculations have centered only on the rare-earth ion, using its wavefunctions in the free-ion sense. More recent work has taken into consideration the surrounding ligands as active participants in the interaction between the radiation field and the solid [37,38,39]. In this picture the f electrons of the rare-earth ion are considered to polarize the charge clouds of the surrounding ions, which then interact with the radiation field via a non-zero total dipole moment (if the rare earth ion is not situated at a center of inversion). These effects are usually called ligand polarization effects.

1.2.2 Intensities of one-photon transitions and the Judd-Ofelt Theory

The bulk of experimental evidence supports Van Vleck's conjecture, namely that the mechanism responsible for the sharp line optical absorption and emission transitions in rare-earth compounds is "forbidden electric dipole" in nature. The oscillator strengths of these transitions, being on the order of 10^{-6}, are too weak to be allowed 4f $\rightarrow$ 5d transitions. Electric quadrupole transitions are predicted to be even weaker and have not yet been observed. Magnetic dipole transitions are observed only under very favourable circumstances due to the selection rules. Thus the major part of the 4f $\rightarrow$ 4f one-photon lanthanide intensities have their origin in static or dynamic admixtures of opposite parity configurations. The static admixture is caused by odd terms in the crystal field potential (for a non centrosymmetric rare-earth site), and the dynamic part by odd parity vibrations. An order of magnitude estimate for the amount of admixture of the opposite parity configurations can be obtained from perturbation theory by the ratio:

$$\frac{B_q^k(k_{odd})}{E(4f^{N-1}nl) - E(4f^N)} \tag{1.10}$$

where B_q^k is on the order of a few hundred cm^{-1} and the configuration energy difference $E(4f^{N-1}nl) - E(4f^N)$ is on the order of 100,000 cm^{-1} for the next highest configuration, $4f^{N-1}5d$. As a consequence, we expect that the $4f^{N-1}5d$ configuration will contribute only 0.1% to the composition of the ground configuration. For energy level calculations, this effect can be neglected and the ground configuration assumed to be pure $4f^N$. Insofar as intensity calculations are concerned, this tiny admixture becomes extremely important. An order of magnitude estimate of the oscillator strength of the 4f $\rightarrow$ 4f transitions is obtained by squaring equation (1.10), which yields the value 10^{-6}.

The theory of the intensities of rare-earth one-photon $4f^N$ transitions was cast into a mathematical framework by Judd and Ofelt, and has become known as the Judd-Ofelt theory [40,41]. The wavefunction for a particular state is written using first order perturbation theory:

$$|i\rangle = \sum_{SLJJ_Z} \left(|4f^N \alpha SLJJ_Z\rangle + \sum_{\psi'} \frac{|\psi'\rangle\langle\psi'|V_{odd}|4f^N \alpha SLJJ_Z\rangle}{E(\psi') - E(4f^N \alpha SLJJ_Z)} \right) \tag{1.11}$$

where V_{odd} represents the odd parity part of the crystal field and $|\psi'\rangle$ represents the possible intermediate states of the system. The matrix element of the electric dipole operator $\vec{D}$ between the states $|i\rangle$ and $|f\rangle$ of the $4f^N$ configuration will thus involve a sum over

intermediate states of the form

$$\sum_{\psi'} \frac{\langle f|\vec{D}|\psi'\rangle\langle\psi'|V_{odd}|i\rangle}{E(\psi') - E(4f^N \alpha S L J J_Z)} \tag{1.12}$$

where the states $|i\rangle$ and $|f\rangle$ are written in zeroth order. Barring some drastic simplification, this infinite sum is mathematically intractable. The idea, originally due to Griffith [42], is to approximate the energy denominator by an average denominator, which then allows use of the closure relation $\sum_{\psi'} |\psi'\rangle\langle\psi'| = 1$ to dispense with the sum over intermediate states. The details of the calculation, which makes extensive use of tensor operator techniques, can be found in Judd [40]. The excited configurations which enter equation (1.12) as intermediate states are $4f^{N-1}nd$, $4f^{N-1}ng$, $4f^{N+1}nd^{-1}$, and the continuum d and g configurations. Several points can be made about the derivation and its underlying assumptions [36]:

- The closure is performed over each individual excited configuration. As such it is not a full quantum mechanical closure over a complete set of eigenfunctions of the Schrödinger equation. Rather, it is a closure over the angular variables only. The assumption here is that the spread in energy of the excited configuration is small compared to the average difference in energy between that configuration and the ground $4f^N$ configuration. This is not a very good approximation for rare-earth ions for which the $4f^{N-1}5d$ configuration does not lie very much higher in energy than the $4f^N$ ground configuration.

- The Judd-Ofelt theory involves three parameters, usually labeled $\Omega_2, \Omega_4, \Omega_6$. They parameterize the oscillator strengths for the absorption and fluorescence transitions between various multiplets of the $4f^N$ configuration. The Ω_k are usually calculated to provide the best fit to the experimental data. The scheme has met with good success, considering the approximations involved. Except for the case of the hypersensitive transitions [43,44,36], it is a good phenomenological model.

1.3 Two-Photon Spectroscopy of Trivalent Lanthanides in Crystalline Hosts

1.3.1 Two-Photon Spectroscopy as a Complement to One-Photon Spectroscopy

Electric dipole transitions are allowed only if there is a change in parity between the initial and final states, since the electric dipole operator is of odd parity. This is the cause of the weakness of the intra-$4f^N$ absorption and fluorescence lines, which are allowed only by the small admixture of higher energy opposite parity configurations. For two-photon transitions, such as two-photon absorption and electronic Raman scattering, the situation is different. In this case, the parity selection rule is that the parities of the initial and final states must be equal, since now two electric dipole operators intervene between the initial and final states. Hence two-photon transitions between the $4f^N$ states are allowed by the parity selection rule and should be observable.

The quantum mechanical amplitudes for two-photon transitions are calculated by standard second-order perturbation theory. The derivation follows the same lines as the one-photon Judd-Ofelt calculation [45]. The intermediate states involved are again $4f^{N-1}nd$, $4f^{N-1}ng$, and $4f^{N+1}nd^{-1}$, since the electric dipole operator is a tensor of rank one in orbital angular momentum space. The difference lies in the fact that for two-photon transitions the second matrix element is that of an electric dipole operator, while for the one-photon case it is the matrix element of the odd-parity crystal field. In oscillator strength units, the two-photon transition probability is on the order of $\left(\frac{1\times 1}{\Delta E}\right) = \left(\frac{1}{10^5}\right)^2 = 10^{-10}$. This is 10^4 times smaller than the one-photon transition probabilities. However, with the high intensities provided by laser sources, the two-photon process is readily observable [46,47,48,49,50,51,52,53,54].

Two-photon spectroscopy can be seen to complement one-photon spectroscopy in a very convenient manner:

- The group-theoretical selection rules are different for two-photon transitions as opposed to one-photon transitions. Additional levels can thus be observed and identified.
- In the case of two-photon absorption, the ultraviolet region of the optical spectrum can be studied, since sufficiently intense radiation of frequency ω will explore the

absorption region at 2ω. As an example, one of the notable achievements of the two-photon absorption experiments has been the observation of the $4f^2$ state $^1S_0$ of Pr^{3+} doped in $LaCl_3$, which is 47,000 cm^{-1} above the ground state and embedded within the $4f^{N-1}5d$ configuration [55]. In some cases, two-photon transitions between the $4f^N$ configuration and the $4f^{N-1}5d$ configuration can also be observed although they are electric dipole forbidden [56].

- Electronic Raman spectroscopy explores the infrared region of the optical spectra of the trivalent lanthanides. This again allows for the observation of transitions not easily acessible by one-photon spectroscopic methods [54,57].

- The intensities of two-photon processes can be studied in the same fashion as the intensities of the one-photon transitions so as to elucidate the mechanism of the interaction between the radiation field and the lanthanide ion in its crystalline environment. The Judd-Ofelt closure technique is again the starting point for a theoretical interpretation of the experimental intensities. It is however subjected to a more stringent test than in the one-photon case due to the relative paucity of adjustable parameters [49,58].

- Two-photon spectroscopy offers to the experimentalist the added dimension of intermediate resonances, whereby one of the two photons is very close in energy to one of the states of the ion. This can dramatically alter and amplify the spectrum that was obtained in a non-resonant configuration, and provide additional information on the energy level structure and the two-photon inelastic light scattering process [59].

1.3.2 Two-Photon Absorption and the Judd-Ofelt Theory Revisited

The first experimental demonstration of two-photon absorption in a physical system was performed in 1961, with the rare-earth ion Eu^{2+} doped in CaF_2 [60]. However, the technique attracted the attention of very few rare-earth spectroscopists. Starting in 1981, the work of Downer and Bloembergen on two-photon $4f^7 \rightarrow 4f^7$ transitions, and their discovery of new mechanisms of interaction between the radiation and the rare-earth ion, revitalized the field [49,50,61,62,63,64]. The Judd-Ofelt closure technique can be easily applied to the two-photon process, as recognized by Axe in 1964 [45], and yields quantitative predictions regarding the two-photon transition probabilities.

For the Judd-Ofelt two-photon transition intensities, there are only two adjustable parameters, α_1' and α_2' in Axe's nomenclature. In the case of two-photon absorption where both photons come from the same input beam, the parameter α_1' does not appear and the intensities are all proportional to α_2'. As a consequence, the *relative* intensities of the transitions between the crystal-field components of various multiplets are uniquely determined with no parameter available to fit the theoretical predictions to the experimental intensities. This is a very stringent test of the assumptions that underlie the Judd-Ofelt theory [49].

The angular momentum selection rules for two-photon absorption are well known to be $\Delta J \leq 2$, $\Delta L \leq 2$, $\Delta S = 0$. These selection rules were found to be strongly violated in Downer's experiments on Gd^{3+} in LaF_3 [62], in which he observed "forbidden" transitions characterized by $\Delta S = 1$, and ΔL and ΔJ ranging in value up to 6. These discrepancies were subsequently explained by the inclusion of third and fourth order terms in the perturbation expansion for the radiative process, involving spin-orbit and crystal field interactions in the higher $4f^{N-1}nd$ and $4f^{N-1}ng$ configurations [63]. This idea is originally due to Judd and Pooler [65]. We consider for example the form of the third-order term

$$\sum_{r,s} \frac{\langle f|\vec{E}\cdot\vec{D}|r\rangle\langle r|V|s\rangle\langle s|\vec{E}\cdot\vec{D}|i\rangle}{(\hbar\omega_{ri}-\hbar\omega)(\hbar\omega_{si}-\hbar\omega)} \tag{1.13}$$

where V is a perturbing potential which in the work of Downer is taken to be H_{so} (the spin-orbit interaction) or H_{cf}, and $\vec{D}$ is the electric dipole operator. The states r and s are assumed to belong to the lowest excited configuration, $4f^{N-1}5d$. An extra energy denominator, on the order of 10^5 cm^{-1}, is present. However the extra matrix element, $\langle r|V|s\rangle$, which represents interactions within the excited configuration, can be quite large. In the case where $V = H_{cf}$ this matrix element is on the order of 10^4 cm^{-1} as the excited d orbital is not shielded and sees the full effect of the crystal field. If the second-order term is forbidden by a selection rule, then the third order term provides the amplitude responsible for the transition. Since H_{so} and H_{cf} carry spin and orbital angular momentum, it is easy to see that the inclusion of the third order terms extends the angular momentum selection rules to $\Delta S \leq 1$ and $\Delta L, \Delta J \leq 6$. A full treatment of these effects can be found in Downer's doctoral thesis [64].

1.3.3 Electronic Raman Spectroscopy

The experimental observation of electronic Raman scattering preceded by many years that of two-photon absorption. Rasetti, in 1932, observed the $^2\Pi_{1/2} \rightarrow {}^2\Pi_{3/2}$ electronic Raman transition in the NO molecule [66]. The weakness of the lines made the technique experimentally difficult, and not much use was made of it. In 1963 Elliott and Loudon predicted that impurity ions, transition metal or lanthanide, would be suitable candidates for electronic Raman scattering [67]. This was followed shortly after by Hougen and Singh's observation of electronic Raman transitions in Pr^{3+} in a $PrCl_3$ crystal, using a mercury lamp as the source of excitation [68]. The advent of the laser, and the high monochromatic intensities it offered, gave a major impetus to the field. The bulk of the laser Raman spectroscopic studies of the lanthanide ions can be attributed to Koningstein, beginning in 1966 [51,52,53,54,69]. Some work was also done by Wadsack *et al* [70]. Transition metal ions have also been studied in this fashion [71,72,73,74]. The field is reviewed to 1982 by Clark and Dines [57].

The advantage of electronic Raman spectroscopy lies in its ability to identify and characterize the low-lying energy states of the lanthanide ions. Since the initial and final states correspond to irreducible representations of the site symmetry group, the electronic Raman process has well defined selection rules relative to the polarizations of the incident and scattered photons. A measurement of the intensities of the transitions in various polarization combinations allowed by the scattering geometry thus gives important clues as to the levels involved and their interaction with the radiation field. The transition amplitudes are characterized by the Raman scattering tensor $\alpha_{\rho\sigma}$, where ρ and σ are cartesian coordinates and are, respectively, the polarizations of the scattered and incident photons [75].

One of the central features of electronic Raman scattering is the appearance of asymmetric transitions for which $\alpha_{\rho\sigma} \neq \alpha_{\sigma\rho}$ [76,77]. The nonresonant vibrational Raman spectrum is well known to be symmetric, so that for phonon peaks $\alpha_{\rho\sigma} = \alpha_{\sigma\rho}$. For electronic Raman peaks there is, however, a significant change in intensity when the polarizations of the incident and scattered photons are interchanged. This is one of the most intriguing features of electronic Raman scattering. A measurement of the amount of asymmetry of the intensities gives important clues as to what virtual intermediate states are involved in the second order process. A theoretical discussion of antisymmetric light scattering has been given by Barron and Svendsen [78]. Chapters 4 and 5 of this thesis describe the observation of asymmetric

electronic Raman scattering in rare earth phosphate crystals and analyze its importance in determining light scattering mechanisms in rare earth ions.

References

[1] J. Becquerel, C.R. Acad. Sci. **142**, 775 (1906).

[2] J. Becquerel, Le Radium **4**, 328 (1907).

[3] J. Becquerel and H. Kammerlingh Onnes, Proc. Acad. Amsterdam **10**, 592 (1908).

[4] M. Mayer, Phys. Rev. **60**, 184 (1941).

[5] R.D. Cowan, *The Theory of Atomic Structure and Spectra* (University of California Press, Berkeley, 1981).

[6] D.C. Griffin, K.L. Andrew, and R.D. Cowan, Phys. Rev. **177**, 62 (1969).

[7] S. Hüfner, *Optical Spectra of Rare Earth Compounds* (Academic Press, New York, 1978).

[8] N. Edelstein, Lawrence Berkeley Laboratory, unpublished results. The curves were generated from relativistic Hartree-Fock wavefunction calculations performed on a Cray XMP computer with R.D. Cowan's code RCN32.

[9] B.G. Wybourne, *Spectroscopic Properties of Rare Earths* (Interscience Publishers, New York, 1965).

[10] W.T. Carnall and H.M. Crosswhite, *Optical Spectra and Electronic Structure of Actinide Ions in Compounds and Solution* (Argonne National Laboratory Report ANL-84-90, 1985).

[11] J.G. Conway, *Proc. Int. Symp. on Rare Earths Spectroscopy, Wroclaw, Poland, 1984*, eds. B. Jezówska-Trzebiatowska, J. Legendziewicz, and W. Stręk (World Scientific Publishing Co., Philadelphia, 1985), p. 3.

[12] L. Brewer, *Systematics and the Properties of the Lanthanides*, ed. S.P. Sinha (D. Reidel Publishing Company, Boston, 1983), p. 17.

[13] W.C. Marten, R. Zalubas, and L. Hagen, *Atomic Energy Levels-The Rare Earth Elements* (NSRDS-NBS60, U.S. Government Printing Office, Washington, D.C.,1978).

[14] L. Brewer, J. Opt. Soc. Am. **61**, 1666 (1971).

[15] H. Bethe, Ann. Physik **3**, 133 (1929).

[16] J.H. Van Vleck, J. Phys. Chem. **41**, 67 (1937).

[17] G. Racah, Phys. Rev. **62**, 438 (1942).

[18] G. Racah, Phys. Rev. **76**, 1352 (1949).

[19] B.R. Judd, *Operator Techniques in Atomic Spectroscopy* (McGraw Hill Book Company, New York, 1963).

[20] G.H. Dieke, *Spectra and Energy Levels of Rare Earth Ions in Crystals*, eds. H.M. Crosswhite and H. Crosswhite (Interscience, New York, 1968).

[21] G.H. Dieke and H.M. Crosswhite, Appl. Opt. **2**, 675 (1963).

[22] W.T. Carnall, H. Crosswhite, H.M. Crosswhite, J.P. Hessler, N. Edelstein, J.G. Conway, and G.V. Shalimoff, J. Chem. Phys. **72**, 5089 (1980).

[23] C.W. Nielson and G.F. Koster, *Spectroscopic Coefficients for the p^n, d^n, and f^n Configurations* (The M.I.T. Press, Cambridge, Massachussetts, 1963).

[24] K. Rajnak and B.G. Wybourne, Phys. Rev. **132**, 280 (1963).

[25] R.E. Trees, J. Opt. Soc. Am. **54**, 651 (1964).

[26] B.R. Judd, Rep Prog. Phys. **48**, 907 (1985).

[27] B.R. Judd, Phys. Rev. **141**, 4 (1966).

[28] B.R. Judd, H.M. Crosswhite, and H. Crosswhite, Phys. Rev. **169**, 130 (1968).

[29] W.T. Carnall, H. Crosswhite, and H.M. Crosswhite, *Energy Level Structure and Transition Probabilities of Trivalent Lanthanides in LaF_3* (Argonne National Laboratory Report, 1977).

[30] B.R. Judd, J.E. Hansen, and A. Raassen, J. Phys. B **15**, 1457 (1982).

[31] B.R. Judd and H. Crosswhite, J. Opt. Soc. Am. B1, 255 (1984).

[32] B.R. Judd and M. Suskin, J. Opt. Soc. Am. B1, 261 (1984).

[33] B.R. Judd, *Operator Averages and Orthogonalities. Lecture Notes in Physics.* vol. 201 (Springer-Verlag, Berlin, 1984), p.340.

[34] T. Hayhurst, G. Shalimoff, N. Edelstein, L.A. Boatner, and M.M. Abraham, J. Chem. Phys. **74**, 5449 (1981).

[35] P.C. Becker, T. Hayhurst, G. Shalimoff, J.G. Conway, N. Edelstein, L.A. Boatner, and M.M. Abraham, J. Chem. Phys. **81**, 2872 (1984).

[36] R.D. Peacock, Structure and Bonding **22**, 83 (1975).

[37] B.R. Judd, J. Chem. Phys. **70**, 4830 (1979).

[38] M.F. Reid and F.S. Richardson, J. Chem. Phys. **79**, 5735 (1983).

[39] M.F. Reid and F.S. Richardson, J. Chem. Phys. **79**, 5743 (1983).

[40] B.R. Judd, Phys. Rev. **127**, 750 (1962).

[41] G.S. Ofelt, J. Chem. Phys. **37**, 511 (1962).

[42] J.S. Griffith, Mol. Phys. **3**, 477 (1960).

[43] C.K. Jørgensen and B.R. Judd, Mol. Phys. **8**, 281 (1964).

[44] S.F. Mason, R.D. Peacock, and B. Stewart, Mol. Phys. **30**, 1829 (1975).

[45] J.D. Axe, Phys. Rev. **136A**, 42 (1964).

[46] U. Fritzler and G. Schaack, J. Phys. C **9**, L23 (1976).

[47] U. Fritzler, Z. Physik B **27**, 289 (1977).

[48] A.G. Makhanek and G.A. Skripko, Phys. stat. sol. (a) **53**, 243 (1979).

[49] M. Dagenais, M. Downer, R. Neumann, and N. Bloembergen, Phys. Rev. Lett. **46**, 561 (1981).

[50] C.D. Cordero-Montalvo and N. Bloembergen, Phys. Rev. B **30**, 438 (1984).

[51] J.A. Koningstein, J. Opt. Soc. Am. **56**, 1405 (1966).

[52] J.A. Koningstein, J. Chem. Phys. **46**, 2811 (1967).

[53] J.A. Koningstein, Can. J. of Chem. **49**, 2336 (1971).

[54] J.A. Koningstein and O.S. Mortensen, *The Raman Effect, Vol. 2*, ed. A. Anderson, (Dekker, New York, 1973), p. 519.

[55] R.S. Rana, C.D. Cordero-Montalvo, and N. Bloembergen, J. Chem. Phys. **81**, 2951 (1984).

[56] S.K. Gayen and D.S. Hamilton, Phys. Rev. B **28**, 3706 (1983).

[57] R.J.H. Clark and T.J. Dines, in *Advances in Infrared and Raman Spectroscopy*, Vol. 9, eds. R.J.H. Clark and R.E. Hester (Heyden, London, 1982), p. 282.

[58] P.C. Becker, N. Edelstein, G.M. Williams, J.J. Bucher, R.E. Russo, J.A. Koningstein, L.A. Boatner, and M.M. Abraham, Phys. Rev. B **31**, 8102 (1985).

[59] P.C. Becker, G.M. Williams, R.E. Russo, N. Edelstein, J.A. Koningstein, L.A. Boatner, and M.M. Abraham, Opt. Lett. **11**, 282 (1986).

[60] W. Kaiser and C.G.B. Garrett, Phys. Rev. Lett. **7**, 229 (1961).

[61] M.C. Downer, A. Bivas, and N. Bloembergen, Opt. Comm. **41**, 335 (1982).

[62] M.C. Downer and A. Bivas, Phys. Rev. B **28**, 3677 (1983).

[63] M.C. Downer, C.D. Cordero-Montalvo, and H. Crosswhite, Phys. Rev. B **28**, 4931 (1983).

[64] M.C. Downer, Ph.D thesis, Harvard University, Cambridge, 1983 (unpublished).

[65] B. R. Judd and D.R. Pooler, J. Phys. C **15**, 591 (1982).

[66] F. Rasetti, Z. Phys. **66**, 646 (1930).

[67] R.J. Elliott and R. Loudon, Phys. Lett. **3**, 189 (1963).

[68] J.T. Hougen and S. Singh, Phys. Rev. Lett. **10**, 406 (1963).

[69] D. Nicollin and J.A. Koningstein, Chem. Phys. **49**, 377 (1980).

[70] R.L. Wadsack, J.L. Lewis, B.E. Argyle, and R.K. Chang, Phys. Rev. **3**, 4342 (1971).

[71] J.H. Christie and D.J. Lockwood, Chem. Phys. Lett. **8**, 120 (1971).

[72] J.T. Hoff, P. Grünberg, and J.A. Koningstein, Appl. Phys. Lett. **20**, 358 (1972).

[73] G.D. Jones and M.H. Kuok, J. Phys. C **12**, 715 (1979).

[74] D.J. Lockwood, in *Light Scattering in Solids III*, eds. M. Cardona and G. Güntherodt (Springer-Verlag, Berlin, 1982), p. 59.

[75] J.A. Koningstein, *Introduction to the Theory of the Raman Effect* (D. Reidel Publishing Co., Dordrecht-Holland, 1972).

[76] J.A. Koningstein and O.S. Mortensen, Nature **217**, 445 (1968).

[77] O.S. Mortensen and J.A. Koningstein, J. Chem. Phys. **48**, 3971 (1968).

[78] L.D. Barron and E.N. Svendsen, in *Advances in Infrared and Raman Spectroscopy*, Vol. 8, eds. R.J.H. Clark and R.E. Hester (Heyden, London, 1981), p. 322.

Chapter 2

Experimental Aspects

2.1 Experimental Setup for CW Raman Spectroscopy

The experimental arrangement for the Raman work described in this thesis is shown in Figure 2.1. The excitation is provided by a cw argon-ion laser. The scattered light is collected at an angle of 90° with respect to the input beam direction and dispersed by a spectrometer. The signal level is measured by a photomultiplier tube employed in the photon counting mode, and recorded on a strip chart recorder. The spectra can be digitized for eventual computer analysis.

2.1.1 Laser

The laser used in the Raman scattering experiments is a Coherent model CR-8 argon-ion laser. Its spectral output consists of a number of discretely spaced laser lines, which are selected by a prism located within the laser cavity. The laser lines used were in the blue and green regions of the spectrum. There are other laser lines in other regions of the spectrum, however, which for the CR-8 laser are too weak in intensity to be of any use. Half of the power output of the laser is concentrated in the two lines at 514.5 nm (19429.8 cm^{-1}) and 488.0 nm (20486.7 cm^{-1}) which were used for the majority of the results reported in this study. Other lines were also used to verify that the non-resonant electronic Raman intensities did not depend on the excitation wavelength, and to excite fluorescent transitions in some of the samples investigated. The wavelengths and wavenumbers of the argon-ion laser lines in the blue and green region regions of the spectrum are given in Table 2.1. The wavenumbers of the laser lines are given in both air and vacuum, the wavelengths in air only. The electronic energy levels of the lanthanide ions are usually listed in vacuum

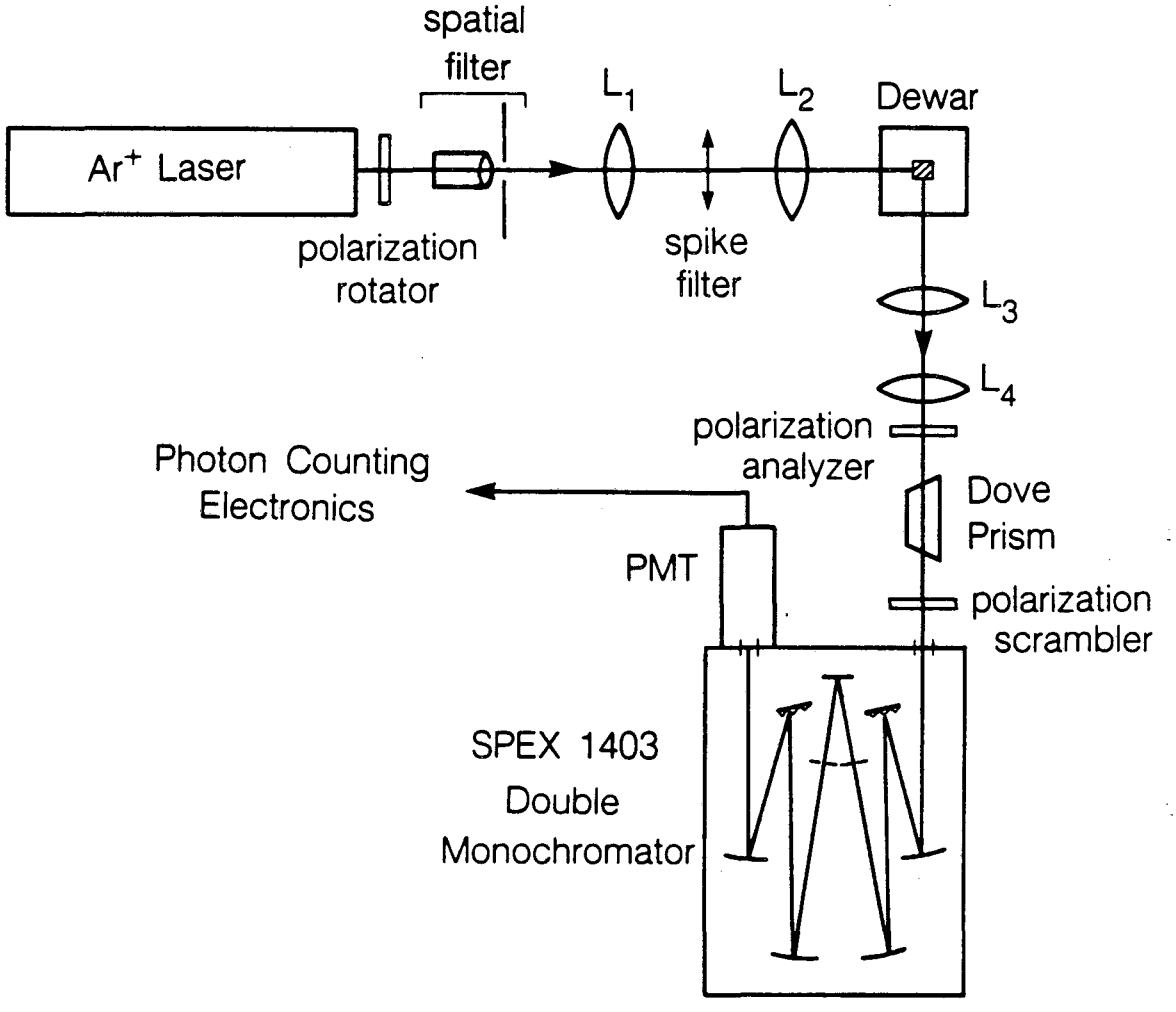

Figure 2.1: Experimental arrangement for CW Raman spectroscopy

wavenumbers. The excitation power at the samples was usually in the range 20 to 50 mW.

Table 2.1: Wavelengths and wavenumbers of argon-ion laser lines.

Wavelength (nm)	Wavenumber (cm^{-1})	
	Air	Vacuum
514.53	19,435.1	19,429.7
501.71	19,931.6	19,926.0
496.51	20,140.6	20,135.0
487.99	20,492.4	20,486.7
476.49	20,986.9	20,981.0
472.69	21,155.6	21,149.7
465.79	21,468.7	21,462.7
457.94	21,837.1	21,831.0

A spectral analysis of the light emitted by the argon-ion laser operating in the single line regime reveals that besides the strong laser line there are a number of weak auxiliary peaks which correspond to radiative transitions of the argon ions. These so-called plasma lines appear as extraneous peaks in the Raman spectra since the light collection system employed detects very weak signals. For the excitation lines at 514.5 and 488.0 nm spike filters are placed immediately after the collimating lens (see Fig. 2.1). These are narrow band Fabry-Perot filters which remove the unwanted plasma lines in a spectral region of $\pm$ 2,000 cm^{-1} about the laser line. Beyond that region, or for other excitation lines where no spike filter is used, the plasma lines are simply catalogued by analyzing the spectrum of the laser light scattered by stainless steel or copper, since these materials do not exhibit any sharp Raman or fluorescent transitions in the visible region.

The linewidth of an argon-ion laser line is given by the Doppler width of the argon ion levels, which is approximately 3500 MHz, or 0.1 cm^{-1}. An etalon can be placed in the laser cavity which will produce a single-mode output and thus reduce the linewidth. This was not necessary for this work since 0.1 cm^{-1} is already much smaller than the inhomogeneous linewidths of the rare-earth ion electronic energy levels.

2.1.2 Cryostat and Sample Mount

The observation of electronic Raman transitions necessitates the cooling of the crystal sample to liquid helium and liquid nitrogen temperatures. This is accomplished by mounting the sample at the tip of a Janis Research "Supertran" cold-finger dewar. The advantage of this dewar is that the sample is surrounded by vacuum, so that there is none of the scattered light that would arise if the sample were immersed directly in liquid helium. The disadvantage is that the sample temperature is not very accurately known or controlled, since the sample temperature depends on the thermal conductivity of the sample and that of the agent which binds it to the copper tip of the dewar.

The sample mount is made out of oxygen-free copper and fixed with screws onto the bottom of the cold finger. The crystal is glued onto the bottom of the mount with silver epoxy. In most cases the long axis of the crystal, which is the crystallographic Z axis, is mounted vertically. The length of the mount is determined by the fact that the crystal needs to be centered with respect to the dewar windows through which the incident and scattered light passes.

An estimate of the temperature of the sample can be made by comparing the intensities of the Stokes and anti-Stokes peaks of a specific nonresonant Raman transition, since their ratio is directly proportional to the Boltzmann factor (and a possible asymmetry factor for certain electronic Raman transitions as discussed in Chapter 5). This temperature can then be compared to the value given by the Si diode temperature sensor which is mounted on the copper tip of the cold finger. For nonresonant scattering this ratio shows that the sample temperature is accurately given by the Si diode temperature sensor down to about 15 K. Below that temperature the anti-Stokes intensities are too weak to allow an accurate measurement of the temperature. We estimate, however, that when the sensor readout is at 4.2 K the sample temperature is in the range 5-12 K. In the resonance experiments, where there is absorption by the sample, laser heating can occur and the temperature is probably higher than in the nonresonance case. The temperature uncertainty is $\pm$ 2 K, except between 5 and 12 K where the temperature sensor might not be giving an accurate readout of the temperature at the sample. Variable temperature operation between 4.2 K and 300 K is achieved by supplying current to a nichrome wire wound around the copper block of the cold finger tip. This feature was used quite extensively.

2.1.3 Focusing and Collection Optics

The primary purpose of the optics is to produce and collect the largest amount of Raman scattered light relative to the Rayleigh scattered light and specularly reflected stray light. In this way a high signal to noise ratio is achieved. The focusing optics consist of the spatial filter, the collimating lens L_1, an optional spike filter to reject plasma lines, and the focusing lens L_2. The spatial filter is a Newport Research Corporation model 900, with a 0.5 cm focal length microscope objective and a 25μ pinhole. The purpose of the spatial filter is two-fold: first, to clean up the intensity profile of the laser beam and reduce scattered light from the crystal; second, to expand the laser beam to a larger diameter which then allows a tighter focus on the sample. Collimating lens L_1 is an achromatic doublet lens with a focal length of 14.5 cm. The beam diameter at L_1 is 2.0 cm. After passing through the optional spike filter the beam is then stepped up horizontally by two right-angle prisms. Lens L_2 is identical to L_1 and has a focal length of 14.5 cm.

The collection lens L_3 is a Canon FD camera lens with focal length 50 mm and an f-number of 1.2. The sample is at the focal point of L_3 which is chosen to collect the largest amount of scattered light. The beam is then focused on to the entrance slits by lens L_4. L_4 is an achromatic doublet with a focal length of 330 mm. L_4 is chosen so as to achieve maximum illumination of the spectrometer grating. The spectrometer has an entrance f-number of 7.8, so that lens L_4 is ideally suited to image the light collected by lens L_3 over the entire spectrometer grating. The scattered light has an aperture of 40 mm at L_4, so that L_4 has an effective f-number of $330/40 = 8.2$ which matches well the entrance f-number of the spectrometer. The Dove prism placed after L_4 effects a 90° rotation of the scattered light so that it is now parallel to the entrance slits. This is necessary because the trace of the incident beam in the crystal is a horizontal line and the entrance slits of the spectrometer are vertical. It was found that use of the Dove prism increased the signal by at least a factor of 5.

The choice of the collection optics is dictated by the need to collect the largest amount of scattered light and to image it into the spectrometer so as to completely fill the diffraction grating. The focusing optics can be chosen to maximize the amount of Raman scattered light, given the magnification of the collection optics (which is 6.6 in our case) and the dimensions of the entrance slit of the spectrometer. The relevant parameters of the excitation beam are its diameter, D, and the focal length f of the focusing lens L_2. Since the beam

is expanded to fill the spike filter and minimize optical damage to it, we have D=21 mm. Schwiesow's calculations [1] then tell us that the optimum f (for the case of narrow slits) is then given by the expression:

$$(f/D)_{opt} = \left(\frac{\nu h}{14M}\right)^{\frac{1}{2}} \simeq 21 \tag{2.1}$$

where M is the magnification of the collection optics. Empirically, we find that (f/D)$\simeq$7 gives us the best signal level. The reason for the discrepancy is that the focused beam does not have the expected Gaussian beam profile, and the focused spot size is significantly larger than the predicted diffraction limited value. According to Yariv [2, chapter 6], the beam waist of the focused spot is given by:

$$\omega_0 \simeq \frac{\lambda}{\pi}\left(\frac{f}{D}\right) \simeq 1.2\,\mu \tag{2.2}$$

and the confocal beam parameter of the focused beam is:

$$b = \frac{2\pi}{\lambda}\omega_0^2 \simeq 17.6\,\mu \tag{2.3}$$

The beam diameter is given by $2\omega_0$. Experimentally, the beam spot size and confocal parameter is found to be much larger. Figure 2.2 shows the results obtained when scanning a 10 μ slit across the beam in the focal point region. We find that:

$$(\omega_0)_{exp} \simeq 58\,\mu$$

and

$$(b)_{exp} \simeq 2000\,\mu$$

where $(b)_{exp}$ is defined as twice the distance over which the beam diameter increases by $\sqrt{2}$.

It is obvious that $(b)_{exp}$ and $(\omega_0)_{exp}$ are not related by the Gaussian beam expression (2.3). The fact that the experimental beam waist and confocal parameter are so much larger than the expected value is most probably due to the finite divergence of the incident beam at L_2. Since our focused beam does not behave according to Schwiesow's assumptions it is understandable that his prescription for maximizing the amount of Raman scattered light does not work very well in our case. With a magnification factor of 6.6 the image on the entrance slit of the scattering volume is significantly larger than 200 μ in width, so that some signal is being lost. The signal level is, however, high enough to enable the observation of most of the transitions of interest to this study.

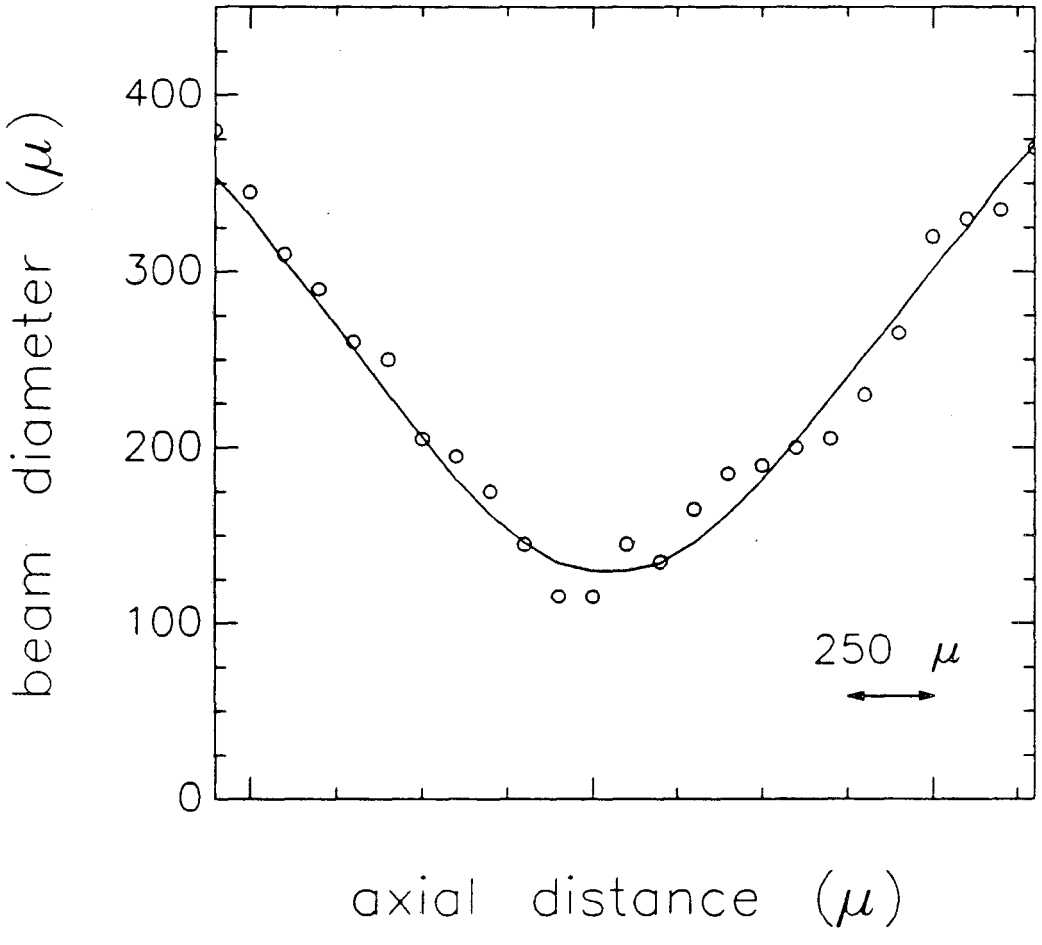

Figure 2.2: Argon ion laser beam diameter in the focal region of lens L_2 as measured with a 10μ slit scanned across the beam profile. The smooth curve represents the best fit of a Gaussian to the experimental points.

2.1.4 Spectrometer and Photon Counting System

The spectrometer used to analyze the radiation scattered by the crystal is a SPEX Industries model 1403 double monochromator. It has a focal length of 0.85 m and an f-number of 7.8. The two gratings are in a modified Czerny-Turner mount. The primary purpose of the spectrometer is to produce a high signal to noise ratio, as the electronic Raman intensities are in general quite weak and can be easily swamped by too high a background of scattered laser light. For this reason a double monochromator is used since it has a very high stray light rejection ratio. Very finely ruled holographic gratings with 1800 grooves/mm are used. These gratings produce less ghosts and scattered light than diamond ruled gratings. Their spectral range runs from roughly 300 to 1000 nm. The grating spectral response also depends on the polarization of the incident light. However, a polarization scrambler is placed at the entrance slits which eliminates the need to correct for the different polarization efficiencies. The polarization scrambler, or depolarizer, consists of a 2° crystal quartz wedge with a second compensating fused silica wedge.

Standard entrance and exit slit widths for the work reported in this thesis are 200 μ (the intermediate slits are also at 200 μ). This corresponds to a spectral bandpass of roughly 2.5 cm^{-1} in the blue and green regions of the spectrum. This is sufficient for most of the Raman studies reported in this work. When better resolution is required the slits are closed down to 80-100 μ. The calibration of the spectrometer is performed using the lines of the mercury lamp, and is maintained to within $\pm$ 0.5 cm^{-1}. Variations in the ambient temperature of the laboratory can result in slight shifts of the wavenumber calibration of the spectrometer during day to day operation.

The light dispersed by the double monochromator is collected by an RCA C31034 photomultiplier tube. This tube has both a very high gain (10^6) and a very low dark count (10-20 counts per second when cooled). It is thus quite suitable for low light level photon counting experiments such as Raman scattering. The voltage across the tube is 1500V. The tube is placed in a Products for Research TE-104RF refrigerated chamber which cools the photomultiplier down to about -25°C. It also shields against electromagnetic interference which would otherwise produce spurious counts. This tube operates in the spectral range of roughly 220 to 880 nm.

The photomultiplier tube is operated in the photon counting mode with the SPEX DPC2 digital photometer system. It consists of an external preamp-discriminator which

converts the current pulses from the PMT into digital pulses which are then counted by the DPC2. The spectrometer is driven by a SPEX Compudrive. Typical scan times are in the range 0.05 to 0.5 cm^{-1} and the corresponding integration times are 5 to 0.5 seconds. The slower scan rates are needed to achieve a high signal to noise ratio for the weaker signals. The spectra are directly recorded on a strip chart recorder. In some cases the spectra were digitized with a digitization pad for computer processing with a DEC VAX computer.

2.1.5 Efficiency of the Light Collection System:

It is useful to estimate the efficiency of the collection optics so as to be able to get an idea of the absolute amount of radiation scattered by the crystal. None of the elements of the collection system transmit 100% of the light incident upon them. In this section we catalogue the efficiency of these various elements for the wavelengths 514.5 nm and 488.0 nm. The efficiency is defined as the ratio of transmitted light to incident light, and is given in percent.

- Photomultiplier tube: The RCA C31034 photomultiplier has a quantum efficiency in the blue-green region of the spectrum of approximately 15% [3].

- Double monochromator: The mirrors are assumed to be perfectly reflecting. Each grating has an efficiency of 65% at 514.5 nm and 55% at 488.0 nm. For two gratings the resulting total efficiency is 42% at 514.5 nm and 30% at 488.0 nm.

- Collection optics: We assume that each glass surface has a 95% transmission factor. Overall we thus have an efficiency of 65%. In addition the sheet polarizer used to analyze the polarization of the scattered light has an efficiency of only about 30% in the blue and green regions of the spectrum.

- Solid-angle of the collection lens: The camera lens used to gather the light scattered from the crystal has a diameter of 40 mm and is 50 mm away from the sample. It thus collects over a solid-angle of 0.5 steradians.

  The angular dependence of the Raman scattering intensity is proportional to $sin^2\theta\, d\Omega$, where θ is the angle between the direction of observation and the axis of the induced dipole moment of the radiating system, and $d\Omega$ the solid angle into which the light is scattered [4,5]. For the 90° scattering geometry employed in this work $\theta = 90°$ and

the scattering is maximized. Integrating the intensity per solid angle over the full 4π solid angle, it can be seen that the relative Raman intensity scattered into a small solid angle $\Delta\Omega$ at $\theta = 90°$ is $\frac{3}{8\pi}\Delta\Omega$. For our collection lens the amount of scattered light collected is thus 6% of the total amount radiated. Taking into account all the elements of our light collection system, the overall efficiency at 514.5 nm is:

$$\frac{\text{number of collected photons}}{\text{total number of radiated photons}} = .15 \times .42 \times .65 \times .30 \times .06 = 7.4\,10^{-4}$$

2.2 Absorption Measurements

The absorption spectra of the rare earth phosphates were obtained using several different techniques. High resolution photographic observations were made on a 3.4 m Ebert spectrograph with a reciprocal dispersion of about 5.2 Å in the first order. Linear polarization of the spectra was obtained in the directions perpendicular and parallel to the crystal axis, which allows the classification of the irreducible representations of the levels. The observations were made with sample temperatures of ~4.2 and 77 K. The higher temperature spectra allowed the observation of some of the ground multiplet excited crystal field energy levels. The measurements were also done with a magnetic field of 26 kG applied to the sample to determine the g values of the states. Lower resolution spectra were obtained with a Cary model 17 spectrophotometer. Details of these measurements can be found in Hayhurst *et al* [6] and Becker *et al* [7].

The calculation of the relative resonant Raman intensities in the case of the erbium phosphate crystals necessitated the measurement of the absolute oscillator strengths of the $^4I_{15/2} \rightarrow {}^4F_{7/2}$ transitions. This was performed using tunable pulsed laser absorption by Williams [8].

2.3 Crystal Samples

The rare earth phosphates $(RE)PO_4$ are ionic insulating crystals which crystallize in two different forms. The rare earth phosphates with rare earths belonging to the first half of the lanthanide series, $LaPO_4$ to $GdPO_4$, have the monazite monoclinic structure. The second half of the series, $TbPO_4$ to $LuPO_4$, and also YPO_4 (xenotime) and $ScPO_4$, have the tetragonal zircon structure. In this work we have utilized only the tetragonal crystals,

in particular $HoPO_4$, $ErPO_4$, $TmPO_4$, $YbPO_4$, and Ho, Er, Tm, and Yb doped in varying amounts into $LuPO_4$ and YPO_4.

The zircon structure is a tetragonal arrangement consisting of alternating PO_4 tetrahedra and rare earth atoms [9, p. 334-335]. A unit cell contains four formula units, however, a primitive cell can be found which contains only two formula units since the lattice is body-centered cubic. The lattice space group is D_{4h}^{19}, and the point symmetry group at the rare earth ion site is D_{2d}. This has been verified directly by x-ray diffraction structural determinations [11,12]. All the rare earth ion sites are equivalent, as the two ions in the primitive cell are related by a center of inversion situated midway between the two ions. The immediate environment of the lanthanide ion is determined by eight O^{2-} ions, arranged in two distinct tetrahedra centered about the rare earth ion. The oxygen ions are roughly 2.3Å from the rare earth ion. There are four other rare earth ions equidistant from each rare earth ion, at a distance of about 3.7Å. The cell dimensions are 6.8Å x 6.8Å x 6.0Å (for $LuPO_4$). Details of the crystallographic structure can be found in Linares *et al* [13], and a picture of the crystal structure can be found in Elliott *et al* [14].

It is interesting to note that mixed crystals containing different lanthanides, such as $Yb_xLu_{1-x}PO_4$, have exactly the same spatial structure as the pure lanthanide phosphates [15]. This means that these crystals can be tailored to control the optical properties of the ions, as was done for erbium phosphates (see chapter 5) and for ytterbium phosphates (see chapter 6).

The crystals were grown at Oak Ridge National Laboratory by L.A. Boatner and M.M. Abraham [16]. The original impetus for this effort was the search for a suitable host for storage of nuclear wastes [17]. The crystals were grown using a flux technique initially described by Feigelson [18] and described in more detail by Rappaz *et al* [10] and Milligan *et al* [11].

The samples used in the Raman scattering experiments were in the form of platelets with typical dimensions 15 mm × 4 mm × 1 mm. Figure 2.3 shows the appearance of these crystals and the definitions of the crystallographic X, Y, and Z axes. Also shown are the x, y, and z symmetry axes of the lanthanide ion's D_{2d} site symmetry group. The faces perpendicular to the X and Y axes were quite smooth and did not need polishing. The edges perpendicular to the Z axis were jagged, but no effort was made to polish these edges as the crystals were quite brittle and spectra of sufficiently high quality could be obtained

with the crystal in its "raw" state.

2.4 Accuracy of the Polarization Measurements

The determination of the electronic Raman intensities in the various polarization combinations allowed by the experimental geometry forms an important part of this work. A particular problem that arises in these measurements is the leakage of intensity from one polarization into another. This can potentially vitiate the experimental data. It has been noted previously by Porto and co-workers [19,20] that such leakage can be explained for birefringent crystals as arising from the finite solid angle subtended by the collection lens. The explanation is that since the ordinary and extraordinary rays propagate at different velocities within the crystal, a particular ray can pick up a polarization component it did not have to start out with, due to changes in interference between the ordinary and extraordinary rays as they propagate in the crystal. The rare earth phosphate crystals are in fact birefringent. The crystal YPO_4 is known to be positive uniaxial, with the indices of refraction $n_0 = 1.721$ and $n_e = 1.816$ at $\lambda = 5893$ Å [21]. We expect the indices of refraction for the other rare earth phosphate crystals to be quite similar.

The extent of the polarization leakage can be readily determined by that exhibited by the phonons, which have well defined selection rules with respect to the polarization of the incident and scattered photons. Section 3.1 describes in more detail the definition of the polarization scattering tensors and their group theoretical form.

It became immediately apparent that the major leakage problem exists primarily between the XX, YY and XY, YX polarization combinations (between the B_{1g} and B_{2g} symmetries in group theory language). This was also the observation of Elliott *et al* [14] for several rare earth phosphate and vanadate crystals. They attributed the phenomenon to static strains within the crystals. The study of numerous rare earth phosphate crystals for the purpose of the investigations reported here lead to the conclusion that the polarization leakage depends for the most part on the crystal alignment, the particular area of the crystal irradiated by the laser beam, the sample used, and in some cases the excitation wavelength. The birefringence effects mentioned by Porto do not seem to play a large role. The measurements reported here were all done with the incident light propagating along X and the scattered light along Y. For this geometry the birefringence effects would cause

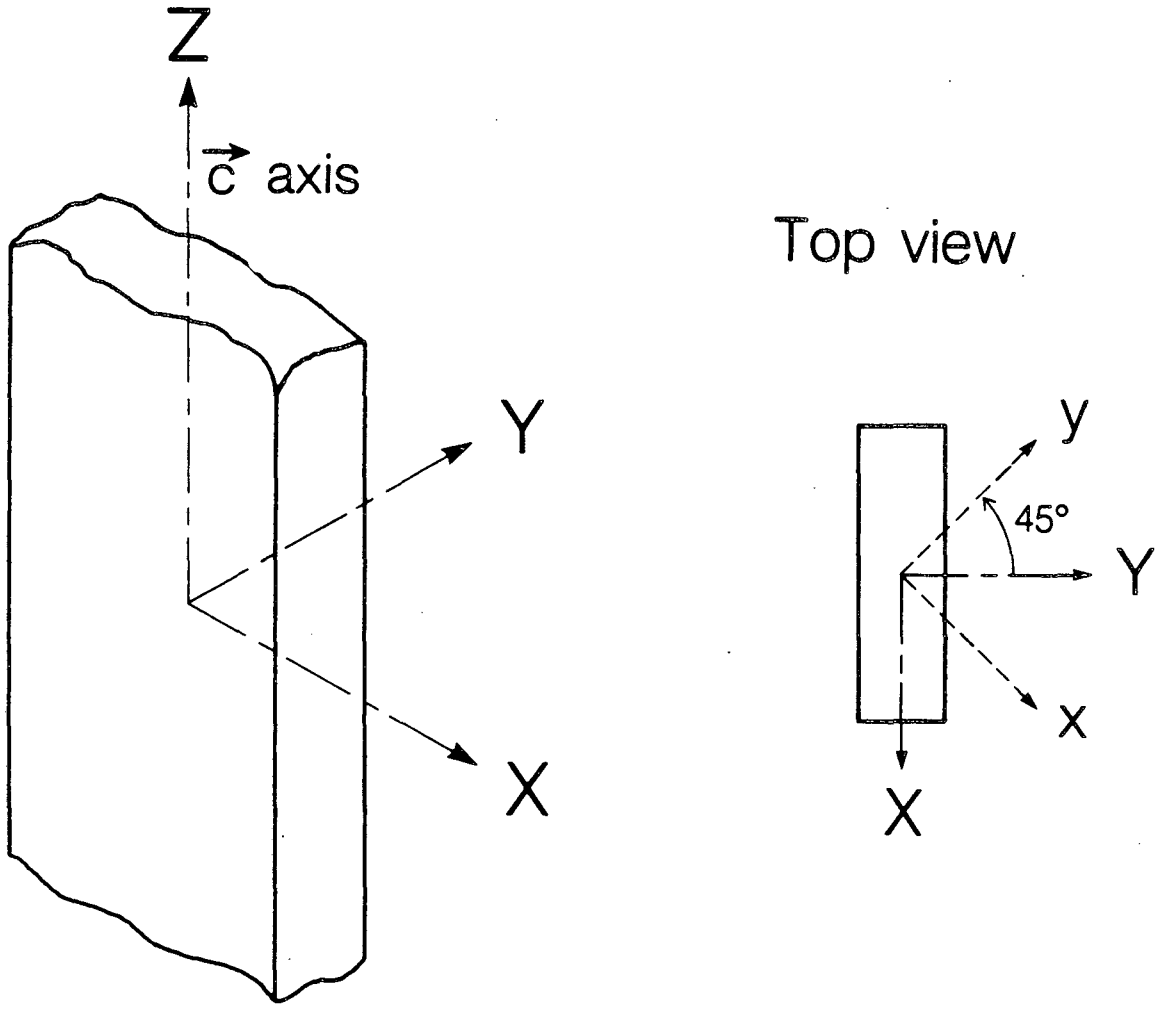

Figure 2.3: Appearance of the rare earth phosphate crystals and definition of the crystallographic X, Y, and Z axes and the local x, y, and z symmetry axes.

leakage between XZ and ZZ. However, in practice this leakage is negligible. Much more leakage is observed when the incident beam is along Z, due to the crystal imperfections at the ends.

Intensity measurements were retained only for those spectra which showed polarization leakage of at most 10% between the B_{1g} and B_{2g} symmetries, and at most 5% for all the other symmetries, based on the phonons. Since measurement of the electronic asymmetry with respect to interchange of the polarization of the incident and scattered photons is one of the more important goals of this work, special care was taken to ensure that the phonon spectrum was symmetric for the scans used for intensity determinations.

References

[1] R.L. Schwiesow, J. Opt. Soc. Am. **59**, 1285 (1969).

[2] A. Yariv, *Quantum Electronics* (John Wiley and Sons, New York, second edition, 1975).

[3] RCA photomultiplier tube catalog PIT-700C (RCA, Solid State Division, Electro optics and devices, Lancaster, PA, 1976).

[4] J.A. Koningstein, *Introduction to the Theory of the Raman Effect* (D. Reidel Publishing Co., Dordrecht-Holland, 1972).

[5] G. Placzek, *Handbuch der Radiologie*, ed. E. Marx (Leipzig, Akademische Verlagsgesellschaft), vol. VI, p.209 (1934), also available in english as UCRL Trans. No. 526 (L).

[6] T. Hayhurst, G. Shalimoff, N. Edelstein, L.A. Boatner, and M.M. Abraham, J. Chem. Phys. **74**, 5449 (1981).

[7] P.C. Becker, T. Hayhurst, G. Shalimoff, J.G. Conway, N. Edelstein, L.A. Boatner, and M.M. Abraham, J. Chem. Phys. **81**, 2872 (1984).

[8] G.M. Williams, Lawrence Berkeley Laboratory, unpublished data.

[9] J.V. Smith, *Geometrical and Structural Crystallography* (John Wiley and Sons, New York, 1982).

[10] M. Rappaz, L.A. Boatner, and M.M. Abraham, J. Chem. Phys. **73**, 1095 (1980).

[11] W.O. Milligan, D.F. Mullica, G.W. Beall, and L.A. Boatner, Inorg. Chim. Act. **70**, 133 (1983).

[12] W.O. Milligan, D.F. Mullica, G.W. Beall, and L.A. Boatner, Acta Cryst. C**39**, 23 (1983).

[13] C. Linares, A. Louat, and M. Blanchard, Structure and Bonding **33**, 179 (1977).

[14] R.J. Elliott, R.T. Harley, W. Hayes, and S.R.P. Smith, Proc. R. Soc. Lond. **A. 328**, 217 (1972).

[15] D.F. Mullica, D.A. Grossie, and L.A. Boatner, submitted to Inorg. Chim. Acta - f block Elements.

[16] L.A. Boatner and M.M. Abraham, Solid State Division, Oak Ridge National Laboratory, Oak Ridge, Tennessee 37830.

[17] M. Petek, M.M. Abraham, and L.A. Boatner, *Scientific Basis for Nuclear Waste Management*, ed. S.V. Topp (Elsevier-North Holland, New York, 1982), vol. 4, p.181.

[18] R.S. Feigelson, J. Am. Ceram. Soc. **47**, 257 (1964).

[19] S.P.S. Porto, J.A. Giordmaine, and T.C. Damen, Phys. Rev. **147**, 608 (1966).

[20] A. Chaves and S.P.S. Porto, Sol. St. Comm. **10**, 1075 (1972).

[21] *CRC Handbook of Chemistry and Physics* (CRC Press, West Palm Beach, Florida, 1979), 59^{th} ed., p. B-225.

Chapter 3

Basics of Raman Scattering in Rare Earth Phosphates

This chapter is a collection of fundamental results necessary to the interpretation and analysis of the Raman spectra obtained. The group theoretical form of the Raman scattering tensors for both phonon and electronic Raman scattering is given. The experimental phonon spectrum is discussed for the tetragonal rare earth phosphate crystals. Finally, the amplitude of electronic Raman transitions is computed within the Judd-Ofelt framework, using the techniques of second quantization applied to the calculation of atomic matrix elements.

3.1 Crystal Scattering Tensors

The polarization characteristics of the vibrational or electronic Raman transitions permit the identification of the symmetries of the levels that participate in the process. This section describes the various scattering tensors for the rare earth phosphate crystals.

3.1.1 Definition of the Scattering Tensor

The Raman scattering process can be described by a scattering tensor, denoted as $\alpha_{\rho\sigma}$, where ρ and σ are either Cartesian or spherical coordinates [1]. $\alpha_{\rho\sigma}$ represents the amplitude of a scattering process in which an incident light wave of polarization σ is inelastically scattered into a light wave of polarization ρ. In this work Cartesian coordinates are used, so that ρ,σ = X,Y,Z, where X,Y, and Z are defined by the crystallographic axes of the crystals as shown in figure 2.3. The intensity of the Raman process is proportional to $|\alpha_{\rho\sigma}|^2$, the

absolute square of the Raman amplitude. $\alpha_{\rho\sigma}$ can be conveniently written in the form of a three by three matrix:

$$\alpha_{\rho\sigma} = \begin{pmatrix} \alpha_{XX} & \alpha_{XY} & \alpha_{XZ} \\ \alpha_{YX} & \alpha_{YY} & \alpha_{YZ} \\ \alpha_{ZX} & \alpha_{ZY} & \alpha_{ZZ} \end{pmatrix} \tag{3.1}$$

The matrix with elements $|\alpha_{\rho\sigma}|^2$ will be called the scattering matrix.

A particular scattering geometry is uniquely described by listing the polarizations and directions of propagation of the incident and scattered photons. The notation used in this thesis has the form:

$$\mathrm{K}_s\ (\mathrm{E}_s\ \mathrm{E}_i)\ \mathrm{K}_i$$

with

K_s: direction of propagation of the scattered photon

E_s: polarization of the scattered photon

E_i: polarization of the incident photon

K_i: direction of propagation of the incident photon

where the frame of reference used is defined by the crystallographic axes X, Y, and Z. For example, Y(XZ)X represents a Raman process with Z polarized incident photons traveling along X, and X polarized scattered photons traveling along Y. This is the reverse of the notation used by Porto *et al* [2]. The notation above places the incident photon on the right and the scattered photon on the left so as to mimic the expression for the quantum mechanical amplitude of the process as calculated in section 3.3:

final state $\leftarrow$ scattered photon $\leftarrow$ intermediate state $\leftarrow$ incident photon $\leftarrow$ initial state

since the the initial state is a ket and the final state a bra.

The symmetry of the crystal lattice determines the selection rules for the vibrational and electronic Raman scattering processes. The vibrational and electronic energy levels are labeled by the irreducible representations of the symmetry groups which describe their invariance properties. As a result of the group theoretical selection rules, some of the elements of the scattering tensor $\alpha_{\rho\sigma}$ will be zero. This is described for Raman scattering by both phonons and electronic states.

3.1.2 Phonon Scattering Tensors

The phonons are classified by the irreducible representations of the group D_{4h}, which is the symmetry group of the unit cell, also known as the factor group [3]. Since there are two $(RE)PO_4$ molecules per primitive cell there are $3 \times 2 \times 6 = 36$ modes of vibration with $\vec{k} = 0$ of which 33 are optical modes. Using the irreducible representations of D_{4h}, these can be written $2A_{1g} + A_{2g} + 4B_{1g} + B_{2g} + 5E_g + A_{1u} + 3A_{2u} + B_{1u} + 2B_{2u} + 4E_u$. Modes subscripted g (*gerade*) are of even parity while those subscripted u (*ungerade*) are of odd parity. There are a total of twelve Raman active frequencies: $2A_{1g} + 4B_{1g} + B_{2g} + 5E_g$. The E_g modes are doubly degenerate, all the other modes being singly degenerate. The A_{2g} symmetry mode is not Raman active as the tensor which transforms as A_{2g} is antisymmetric and only symmetric tensors are allowed for nonresonant Raman scattering by phonons. The vibrational spectrum of the zircon structure has been treated in great detail by Miller *et al* [4] and Dawson *et al* [5]. The polarization dependence of these Raman modes is contained in their respective Raman tensors listed below in Table 3.1 (from Loudon [6]). The axes used are the X,Y,Z crystallographic axes.

Table 3.1: Phonon Raman scattering tensors for the zircon structure (D_{4h}).

$$A_{1g}\begin{pmatrix} a & 0 & 0 \\ 0 & a & 0 \\ 0 & 0 & b \end{pmatrix} \quad B_{1g}\begin{pmatrix} c & 0 & 0 \\ 0 & -c & 0 \\ 0 & 0 & 0 \end{pmatrix} \quad B_{2g}\begin{pmatrix} 0 & d & 0 \\ d & 0 & 0 \\ 0 & 0 & 0 \end{pmatrix}$$

$$E_g\begin{pmatrix} 0 & 0 & e \\ 0 & 0 & 0 \\ e & 0 & 0 \end{pmatrix} \quad \text{and} \quad \begin{pmatrix} 0 & 0 & 0 \\ 0 & 0 & f \\ 0 & f & 0 \end{pmatrix}$$

3.1.3 Electronic Scattering Tensors

The general form of the tensors $\alpha_{\rho\sigma}$ for Raman scattering from electronic levels can be obtained from group theoretical considerations, as was done for the phonons. The electronic levels are classified by the irreducible representations of the point group D_{2d}, which is the site symmetry group of the lanthanide ion in the zircon structure $(RE)PO_4$ crystal lattice. There

is, however, an added subtlety in the electronic case in that two of the ion's symmetry axes are rotated by 45° relative to the crystallographic axes. In what follows, the local symmetry axes of the lanthanide ion will be denoted using lower case letters, to distinguish them from the crystallographic axes. We assume for the time being that the elctronic Raman effect is a process involving only a single ion.

The x and y axes, which are the two-fold C_2 axes of D_{2d}, are rotated in the X-Y crystallographic plane by 45° relative to the X and Y axes (see figure 2.3). The z axis is parallel to the Z axis. Since the symmetry properties of light scattering processes involving the rare earth ion are derived in the local D_{2d} symmetry (the x,y,z frame), a transformation is necessary to express the results in the crystallographic X,Y,Z frame. The crystallographic axes are used to label the experimental data as they are the major macroscopic axes of the crystal. In particular, certain scattering tensors will look different when viewed in the x,y,z frame as opposed to the X,Y,Z frame. A Raman scattering tensor $\alpha_{\lambda\mu}$ that is calculated in the rotated x,y,z frame is related to the tensor $\alpha_{\rho\sigma}$ expressed in the X,Y,Z frame by the equation:

$$\alpha_{\rho\sigma} = R\,\alpha_{\lambda\mu}\,R^t \tag{3.2}$$

R being the matrix of a 45° rotation about the Z axis, R^t its transpose, ρ,σ = X,Y,Z, and λ,μ = x,y,z [1]. We have

$$R = \begin{pmatrix} \cos(45°) & \sin(45°) & 0 \\ -\sin(45°) & \cos(45°) & 0 \\ 0 & 0 & 1 \end{pmatrix} \tag{3.3}$$

In this work the scattering tensors are first calculated in the local x,y,z frame and then rotated into the X,Y,Z frame.

The electronic scattering tensors $\alpha_{\lambda\mu}$ can be either symmetric or antisymmetric, in contrast to the phonons, which contain only symmetric tensors (for nonresonant Raman processes). The form of these tensors for the various irreducible representations of D_{2d} is given below in Table 3.2, in both the x,y,z and X,Y,Z axes. The notation used for the irreducible representations is that of Koster and Dimmock [7]. The most visible effect of this rotation is that some tensors having diagonal elements may be transformed into tensors having diagonal elements equal to zero, and vice-versa. This occurs in particular for the symmetries Γ_3 and Γ_4, which are essentially interchanged. Neglect of this effect can lead to

Table 3.2: Electronic Raman scattering tensors for D_{2d}.

	axes x, y, z		axes X, Y, Z	
Γ_1	$\begin{pmatrix} a & 0 & 0 \\ 0 & a & 0 \\ 0 & 0 & b \end{pmatrix}$	$\longmapsto$	$\begin{pmatrix} a & 0 & 0 \\ 0 & a & 0 \\ 0 & 0 & b \end{pmatrix}$	
Γ_2	$\begin{pmatrix} 0 & c & 0 \\ -c & 0 & 0 \\ 0 & 0 & 0 \end{pmatrix}$	$\longmapsto$	$\begin{pmatrix} 0 & c & 0 \\ -c & 0 & 0 \\ 0 & 0 & 0 \end{pmatrix}$	
Γ_3	$\begin{pmatrix} d & 0 & 0 \\ 0 & -d & 0 \\ 0 & 0 & 0 \end{pmatrix}$	$\longmapsto$	$\begin{pmatrix} 0 & d & 0 \\ d & 0 & 0 \\ 0 & 0 & 0 \end{pmatrix}$	
Γ_4	$\begin{pmatrix} 0 & e & 0 \\ e & 0 & 0 \\ 0 & 0 & 0 \end{pmatrix}$	$\longmapsto$	$\begin{pmatrix} -e & 0 & 0 \\ 0 & e & 0 \\ 0 & 0 & 0 \end{pmatrix}$	
Γ_5 (symmetric)	$\left\{ \begin{pmatrix} 0 & 0 & f \\ 0 & 0 & 0 \\ f & 0 & 0 \end{pmatrix} \begin{pmatrix} 0 & 0 & 0 \\ 0 & 0 & g \\ 0 & g & 0 \end{pmatrix} \right.$	$\longmapsto$	$\begin{pmatrix} 0 & 0 & f' \\ 0 & 0 & f' \\ f' & f' & 0 \end{pmatrix} \begin{pmatrix} 0 & 0 & -g' \\ 0 & 0 & g' \\ -g' & g' & 0 \end{pmatrix}$	$\begin{cases} f' = f/\sqrt{2} \\ g' = g/\sqrt{2} \end{cases}$
Γ_5 (antisymmetric)	$\left\{ \begin{pmatrix} 0 & 0 & h \\ 0 & 0 & 0 \\ -h & 0 & 0 \end{pmatrix} \begin{pmatrix} 0 & 0 & 0 \\ 0 & 0 & i \\ 0 & -i & 0 \end{pmatrix} \right.$	$\longmapsto$	$\begin{pmatrix} 0 & 0 & h' \\ 0 & 0 & h' \\ -h' & -h' & 0 \end{pmatrix} \begin{pmatrix} 0 & 0 & -i' \\ 0 & 0 & i' \\ i' & -i' & 0 \end{pmatrix}$	$\begin{cases} h' = h/\sqrt{2} \\ i' = i/\sqrt{2} \end{cases}$

an erroneous identification of the symmetry of a transition. Also, it should be pointed out that since the x and y axes are equivalent (the crystal in uniaxial) one must have

$$\mathrm{g} = e^{i\phi}\,\mathrm{f} \qquad \text{and} \qquad \mathrm{i} = e^{i\phi}\,\mathrm{h}$$

since their absolute squares represent physically observable intensities which by symmetry are required to be equal.

Consider an initial state labeled by the irreducible representation Γ_i and a final state labeled Γ_f. To obtain the symmetry of the Raman tensor $\alpha_{\rho\sigma}$ one simply requires that the direct product $\Gamma_i \otimes \Gamma(\alpha_{\rho\sigma}) \otimes \Gamma_f$ contain the identity representation. This means that the allowed tensors are given by the decomposition of $\Gamma_i \otimes \Gamma_f$ into irreducible representations .

Of particular interest are the scattering tensors of symmetry Γ_5. Since the Γ_5 irreducible representation is two dimensional it actually represents the transformation properties of a pair of tensors. The two tensors of this pair can be written Γ_{5X} and Γ_{5Y} for obvious reasons. Now, in obtaining the scattering ***intensity*** for a particular transition, it is necessary to first square the scattering ***amplitudes*** for each allowed symmetry, and then to add them. Tensors of different symmetry correspond to different initial and/or final states which is why quantum mechanics requires that the tensors be squared before they are added. A transition of some particular energy can have intensity contributions from more than one symmetry channel only if there are any degeneracies in either the initial or final state. The scattering matrix thus corresponds to an incoherent sum of the squares of the various symmetry scattering tensors. As shown in Table 3.2, Γ_5 represents both a symmetric and an antisymmetric tensor. For a transition that is Γ_5 allowed, the symmetric and antisymmetric tensors are added coherently, since it is impossible to distinguish experimentally between the symmetric amplitude channel and the antisymmetric one. This is done for both Γ_{5X} and Γ_{5Y}. The final scattering matrix for a Γ_5 transition, irrespective of any rotation about the Z axis will thus have the form:

$$\begin{pmatrix} 0 & 0 & |f+h|^2 \\ 0 & 0 & |f+h|^2 \\ |f-h|^2 & |f-h|^2 & 0 \end{pmatrix} \tag{3.4}$$

It is immediately apparent that such a transition is asymmetric. Reversing the polarizations of the incident and scattered photons results in a different scattered intensity. This is in stark contrast to phonon Raman scattering which is always symmetric (under nonresonant

excitation). The amount of asymmetry can be measured by the ratio:

$$\frac{I_{xz}}{I_{zx}} = \frac{I_{yz}}{I_{zy}} = \frac{|f+h|^2}{|f-h|^2} \tag{3.5}$$

the value of which depends on the relative strengths of the symmetric and antisymmetric contributions. The observation of strongly asymmetric electronic Raman scattering processes is one of the main results of this work. As discussed in chapter 5, the measurement of the asymmetry ratio is a sensitive test of the theory used to predict the electronic Raman scattering intensities.

3.2 Experimental Phonon Spectrum

The phonon spectra of the tetragonal rare earth phosphate crystals do not vary much as the constituent lanthanide ion is changed. This is due to the fact that the ionic radii and atomic masses of the various trivalent lanthanides are quite similar, so that the crystals have almost identical distances and restoring forces. As a result, the phonon frequencies and intensities do not vary much from one tetragonal rare earth phosphate to another. The exception is YPO_4, which has markedly different phonon frequencies than the other crystals in the 100-200 cm^{-1} region. This is not too surprising as Y has a substantially different atomic weight compared to the lanthanide series elements, and is not a "true" rare earth. This section describes the experimental phonon spectrum and catalogues the phonon frequencies for the different crystals studied. This knowledge is of vital importance, as the phonon spectrum is the backdrop against which the electronic peaks arise at low temperature.

3.2.1 Phonon Spectrum of $LuPO_4$

The group theoretical classification of the optical phonons of $LuPO_4$ was introduced in section 3.1.2. There are a total of twelve Raman active phonons, which can be labeled by the irreducible representations of D_{4h}. Polarized Raman scans allow the identification of the symmetry of each phonon observed, via the scattering tensors shown in Table 3.1.

Figure 3.1 gives a general view of the optical phonon spectrum of $LuPO_4$, at the temperatures 295, 77, and approximately 4.2 K. It is typical of the phonon Raman spectra of any of the rare earth phosphates. The phonons are in the 0-1100 cm^{-1} region. Figure

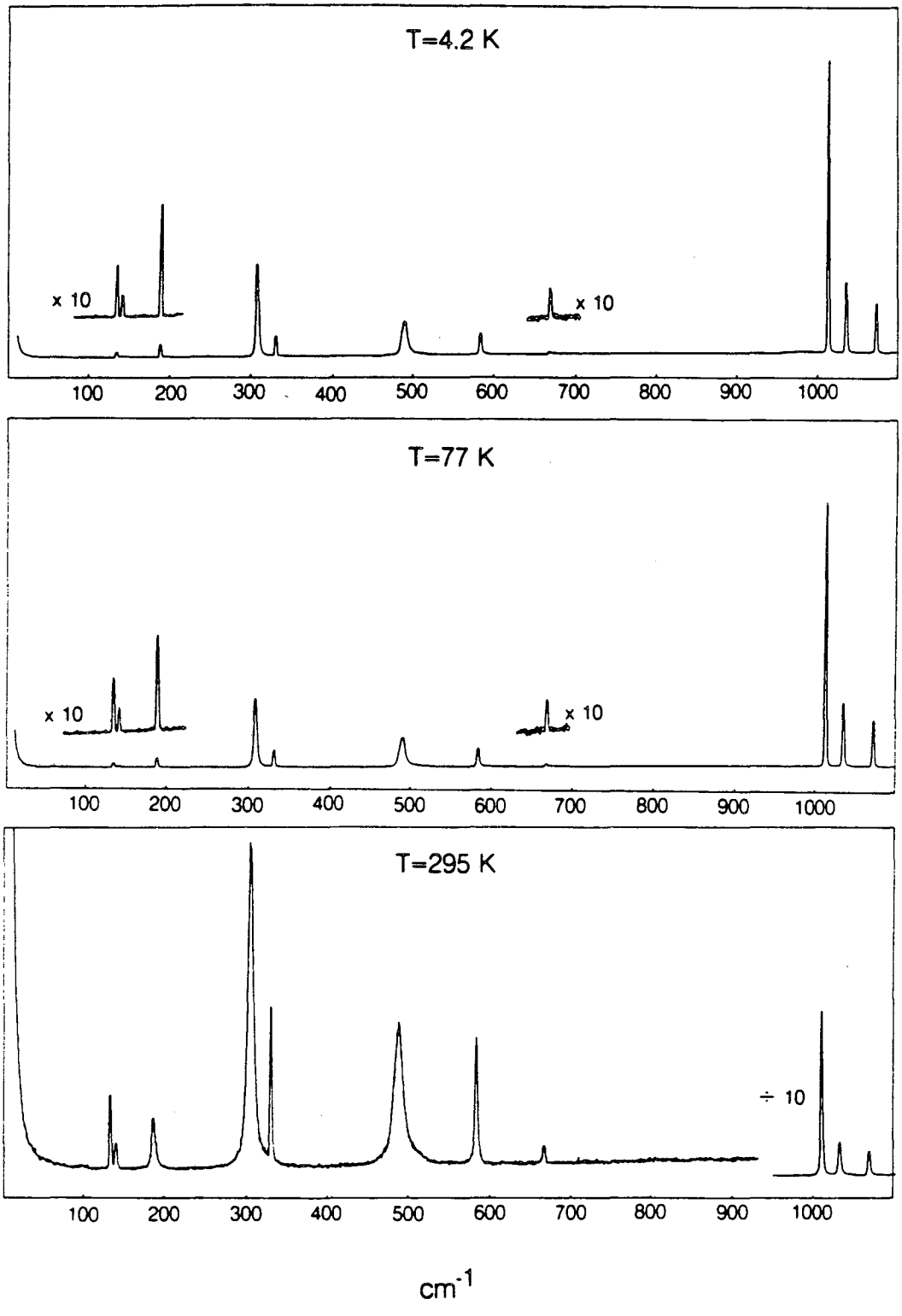

Figure 3.1: Unpolarized phonon Raman spectra of $LuPO_4$ at the temperatures 295, 77, and 4.2 K. The full scale is 50,000 counts per second for the T = 4.2 K and T = 77 K scans, and 5,000 counts per second for the T = 295 K scan.

3.1 was obtained with the incident beam polarized 50% along Z and 50% along Y and with no polarization analyzer at the entrance slits of the spectrometer. All the slits were opened to 200 μ, and the excitation was at 514.5 nm. The incident power was 25 mW. The strongest phonons are those in the 1000 cm^{-1} region. These phonons correspond to stretching modes of the $(PO_4)^{3-}$ group. Polarized scans with the polarization combinations (XY), (XZ), (ZY), and (ZZ) of the scattered and incident photons, are shown in Figure 3.2 at approximately 4.2 K (see section 3.1.1 for the definition of the polarization labels). The experimental conditions for Figure 3.2 are the same as for Figure 3.1. The symmetry characteristics of the various phonons is quite clear in Figure 3.2. Polarization leakage can be observed in these spectra. The B_{1g} modes which are allowed only in (XX) and (YY) are seen in the (XY) spectrum. This is the most prevalent leakage problem, as mentioned earlier. The strong phonon A_{1g}^2 also leaks through to the other polarizations. The amount of leakage is at most 10% for the spectra of figure 3.2.

The optical phonons of $LuPO_4$ can also be classified fairly accurately according to whether they originate from vibrations of the phosphate tetrahedron (so called *internal* modes), or from the relative motion of the lanthanide ions and the phosphates (so called *external* modes). The external modes are lower in frequency than the internal modes as the groups of atoms involved are heavier and further apart. The internal modes come from the four vibrational modes of the PO_4 molecule, which have the frequencies 420, 567, 938, and 1017 cm^{-1} [8]. Their degeneracy is lifted first by the nonisotropic environment that the $(PO_4)^{3-}$ molecules encounter when placed in the crystal lattice, and which has the symmetry D_{2d}. The interaction between the two phosphate groups in the primitive cell further splits the phonons into g (symmetric) and u (antisymmetric) modes. The progressive lifting of the degeneracies involved is discussed in more detail by Miller *et al* [4], Dawson *et al* [5], and Lazarev *et al* [9]. Miller *et al* [4] and Dawson *et al* [5] also show pictures of the motions of the atoms for each of the vibrational modes.

3.2.2 Frequencies of the Raman Active Phonons

Table 3.3 lists the frequencies of the Raman active phonons of $LuPO_4$, $YbPO_4$, $TmPO_4$, $ErPO_4$, $HoPO_4$, and YPO_4, at the temperatures 295, 77, and approximately 4.2 K.

The phonons are labeled by the irreducible representations of D_{4h}. The first five phonons are external modes of vibration, while the last seven are internal modes [10]. The super-

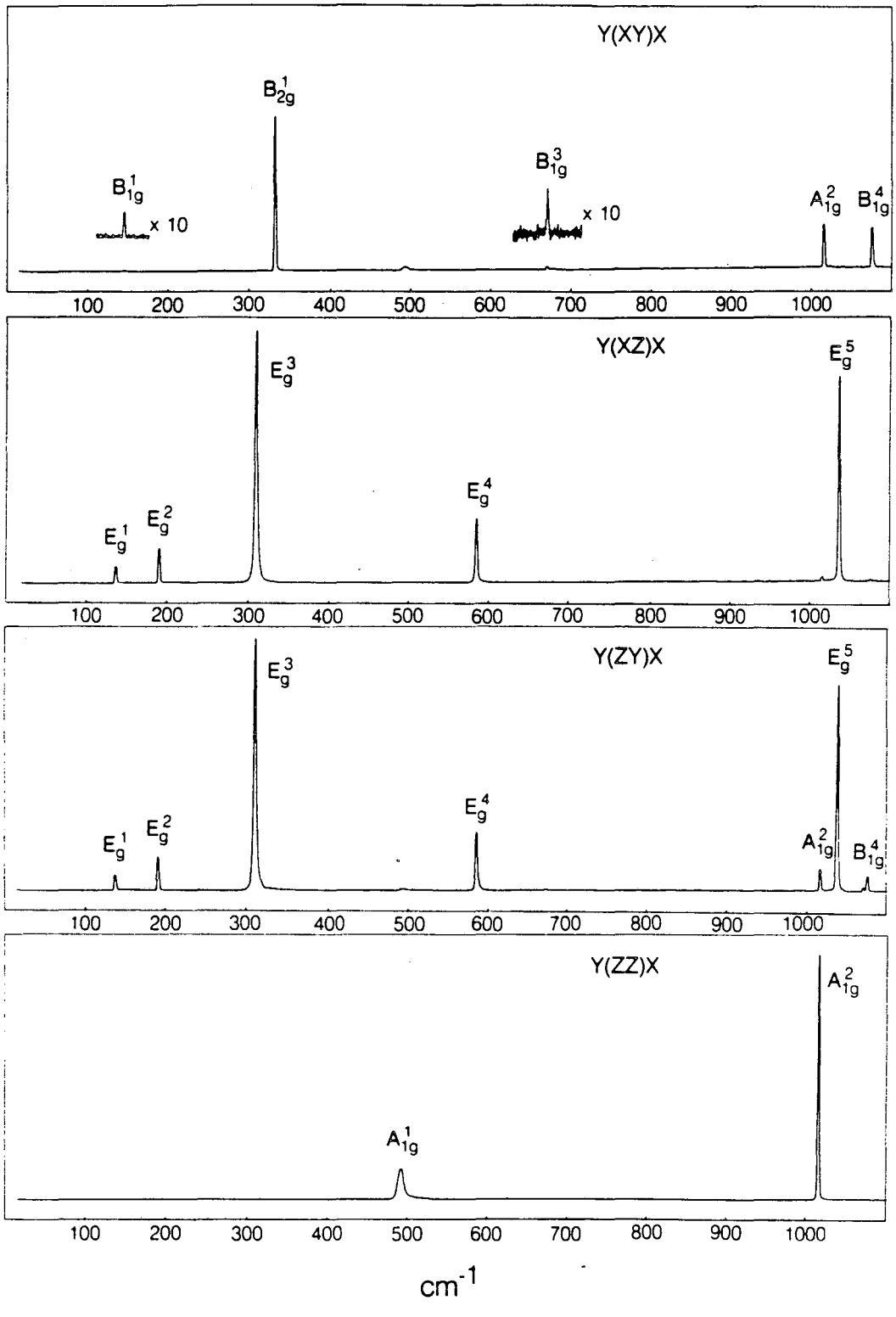

Figure 3.2: Polarized phonon Raman spectra of $LuPO_4$ at approximately 4.2 K. The full scale is 50,000 counts per second for the Y(ZZ)X scan and 10,000 counts per second for all the other scans.

Table 3.3: Frequencies (cm^{-1}) and symmetries of the Raman active phonons of $LuPO_4$, $YbPO_4$, $TmPO_4$, $ErPO_4$, $HoPO_4$, and YPO_4, at 295, 77, and approximately 4.2 K.

	E_g^1	B_{1g}^1	E_g^2	B_{1g}^2	E_g^3	B_{2g}^1	A_{1g}^1	E_g^4	B_{1g}^3	A_{1g}^2	E_g^5	B_{1g}^4
						$LuPO_4$						
295 K	133	139	186	a	305	329	488	582	666	1011	1032	1069
77 K	133	138	186	a	305	330	488	583	665	1012	1033	1070
4.2 K	133	140	187	a	307	329	490	583	666	1013	1034	1072
						$YbPO_4$						
295 K	133	139	186	a	b	330	490	583	664	1010	1030	1068
77 K	134	145	186	a	b	330	492	583	665	1011	1033	1072
4.2 K	134	149	187	a	b	330	492	584	666	1011	1033	1072
						$TmPO_4$						
295 K	133	139	186	a	304	331	488	581	662	1006	1025	1064
7B K	133	139	188	a	310	331	491	582	664	1009	1031	1070
4.2 K	134	137	188	a	309	330	490	580	662	1009	1031	1071
						$ErPO_4$						
295 K	132	a	185	a	299	330	486	578	658	1003	1023	1060
77 K	132	140	185	a	302	330	488	580	659	1004	1026	1063
4.2 K	133	140	186	a	303	329	487	579	659	1004	1026	1064
						$HoPO_4$						
295 K	131	140	184	a	297	332	486	578	656	1000	1022	1057
77 K	131	142	181	a	301	331	487	578	658	1003	1025	1062
4.2 K	130	141	180	a	302	330	488	578	657	1003	1025	1062
						YPO_4						
295 K	157	185	210	a	299	331	484	581	660	1002	1027	1059
77 K	157	186	211	a	303	332	485	582	661	1003	1028	1062
4.2 K	157	187	211	a	303	332	485	582	662	1004	1029	1062

a: not observed.

b: in $YbPO_4$, E_g^3 couples to electronic transitions (see chapter 8).

scripts distinguish different phonons with the same irreducible representation label. The frequencies have been averaged from several scans and have an accuracy of ± 1 cm^{-1}. The room temperature values are fairly close to those reported by Begun *et al* [8], although a careful comparison between the two sets of numbers reveals that in some cases there are discrepancies on the order of ± 3 cm^{-1}. It should be noted, however, that some of Begun *et al's* symmetry assignments are in error, which is not surprising as their samples were in the form of powders. The symmetry assignments presented here agree with those of Elliott *et al* for $DyPO_4$ [10].

The Raman spectrum of $TmPO_4$ has been reported by Guha [11]. The phonon frequencies presented here agree with Guha's in the low wavenumber region. However, they increasingly disagree with his values from 300 cm^{-1} up to 1100 cm^{-1}, as his data seems to be tainted by some kind of systematic error.

The B_{1g}^2 phonon is too weak to be observed. In YVO_4, where the phonon frequencies are substantially lower than in the rare earth phosphates, this phonon is reported to be at 265 cm^{-1} [10].

The phonon spectrum of $LuPO_4$ and $YbPO_4$ was taken with the green argon-ion laser line at 514.5 nm at the temperatures 4.2, 77, and 295 K, and also with the blue line at 488.0 nm at 4.2 K. The Raman spectrum of $YbPO_4$ is extremely peculiar in that strong electron-phonon coupling effects seem to be manifesting themselves. This situation is discussed more fully in chapter 6. At room temperature the $ErPO_4$ phonon spectrum was observed only with the 457.9 nm line, as strong fluorescence is observed from the sample with excitation at 514.5 and 488.0 nm. At 77 K only the 457.9 nm line was again used. At 4.2 K, the lines at 457.9, 488.0, and 514.5 nm were all used. The phonon spectrum of $HoPO_4$ was measured with the 514.5 nm line at 295 and 77 K, and with both the 514.5 and 488.0 nm lines at 4.2 K. For YPO_4, all the phonon measurements were made with the green line at 514.5 nm.

It is found that the relative intensities of the external modes varies quite a bit from sample to sample and also depends on the choice of the sampling volume within the crystal. This does not occur for the internal modes, which suggests the presence of strains within the crystals that affect more the external modes. In the worst cases, it was sometimes observed that the external E_g modes were sometimes not symmetric with respect to interchange of the polarizations of the incident and scattered photons. However, for all the samples a strain free region of the crystal could usually be found for which the E_g phonons were "well

behaved". This was necessary to ensure an accurate measurement of the asymmetry of certain electronic Raman transitions.

3.3 Judd-Ofelt Theory of Two-Photon Processes in Trivalent Lanthanides

3.3.1 Second Quantization and Atomic Theory

The methods of second quantization can be exceedingly useful for the calculation of atomic matrix elements. In particular, second quantization provides a very powerful and elegant means for computing matrix elements that make use of the closure relation in angular momentum space as an intermediate step of the calculation. The application of the methods of second quantization to atomic calculations has been largely the work of Judd [12,13].

The technique has been found to be of particular interest in the calculation of two-photon matrix elements for trivalent lanthanides. Judd used second quantization to calculate the third-order two-photon matrix elements involving spin-orbit interactions in the intermediate states [14]. Similarly, Downer [15,16,17] calculated third-order and fourth-order matrix elements involving both spin-orbit and crystal field interactions in the intermediate states. Second quantization is thus the method of choice for the calculation of the various transition amplitudes that are of interest in this work. Some of the basic properties of the method are summarized here to aid in the understanding of the calculations that follow. The reader is urged to consult the works of Judd for more detail and rigour.

The principal actors of the second quantization method are the creation and annihilation operators $a_k^\dagger$ and $a_{k'}$ which create and destroy fermions specified by the quantum numbers $k \equiv (nlm_s m_l)$ and $k' \equiv (n'l'm_s'm_l')$. They obey the anticommutation rules:

$$\{a_k^\dagger, a_{k'}^\dagger\} = \{a_k, a_{k'}\} = 0 \qquad \text{and} \qquad \{a_k^\dagger, a_{k'}\} = \delta_{kk'} \tag{3.6}$$

For a specific shell (nl) of fermions of spin s the various $a_k^\dagger$ form the components of a double tensor $\mathbf{a}^\dagger$ of rank s in spin space and l in orbital angular momentum space. The situation is similar for the tensor $\mathbf{a}$. In the case of the trivalent lanthanides, these tensors will be $\mathbf{f}$ and $\mathbf{f}^\dagger$ which annihilate and create the 14 states of an f electron, $\mathbf{d}$ and $\mathbf{d}^\dagger$ which annihilate and create the ten states of a d electron, and $\mathbf{g}$ and $\mathbf{g}^\dagger$ which perform the same functions

for the eighteen states of a g electron. The annilation and creation tensors can be coupled in the same fashion as other tensor operators. In so doing, they can be made to represent certain well known physical tensors, although the connection is not always transparent. For example, $(\mathrm{a}^\dagger\mathrm{a})^{(10)}$ is proportional to $\vec{S}$ and $(\mathrm{a}^\dagger\mathrm{a})^{(01)}$ is proportional to $\vec{L}$. Note that in the notation $(\mathrm{a}^\dagger\mathrm{a})^{(pt)}$, p is the rank of the coupled double tensor in spin space, and t its rank in orbital angular momentum space.

3.3.2 Tensor Operator Recoupling Techniques

The calculations that follow make extensive use of tensor operator recoupling. This is done with the intent of isolating certain groups of tensors, in particular conbinations of creation and annihilation operators, which are found to be proportional to some well known unit tensors. These recoupling relations are summarized here to help in the understanding of section 3.4.3. The techniques of operator recoupling are discussed in Judd [18] and Edmonds [19]. The coupling of two tensors $\mathbf{T}^{(j_1)}$ and $\mathbf{U}^{(j_2)}$ to form a resulting tensor $\mathbf{X}^{(j)}$ is done with the Clebsch-Gordan coefficients:

$$X^{(j)}_m = \sum_{m_1,m_2} (j_1 m_1 j_2 m_2 | j_1 j_2 j m)\, T^{(j_1)}_{m_1} U^{(j_2)}_{m_2} \tag{3.7}$$

and the Clebsch-Gordan coefficients can be written in terms of the 3-J symbols:

$$(j_1 m_1 j_2 m_2 | j_1 j_2 j m) = (-1)^{j_1 - j_2 + m}(2j+1)^{\frac{1}{2}} \begin{pmatrix} j_1 & j_2 & j \\ m_1 & m_2 & -m \end{pmatrix} \tag{3.8}$$

The coupling of three tensor operators, or equivalently of three angular momenta j_1, j_2, j_3, to form a resultant angular momentum j, takes place in two stages. One can first couple j_1 and j_2 to form j_{12}, which is then coupled with j_3 to form j. This would be written as

$$|j_1 j_2 (j_{12}), j_3, jm\rangle = \left(\left(\mathbf{T}^{(j_1)} \mathbf{U}^{(j_2)} \right)^{(j_{12})} \mathbf{V}^{(j_3)} \right)^{(j)}_m \tag{3.9}$$

The other way is to first couple j_2 and j_3 into j_{23}, which is then coupled with j_1 to form j. This would be denoted as

$$|j_1, j_2 j_3 (j_{23}), jm\rangle = \left(\mathbf{T}^{(j_1)} \left(\mathbf{U}^{(j_2)} \mathbf{V}^{(j_3)} \right)^{(j_{23})} \right)^{(j)}_m \tag{3.10}$$

The connection between the two coupling schemes is given by the relation:

$$|j_1, j_2 j_3 (j_{23}), jm\rangle = \sum_{j_{12}} ((j_1 j_2) j_{12}, j_3, jm | j_1, (j_2 j_3) j_{23}, jm)\, |j_1 j_2 (j_{12}), j_3, jm\rangle \tag{3.11}$$

The recoupling coefficient for the coupling of three angular momenta can be written with the help of the 6-J symbol:

$$((j_1 j_2) j_{12}, j_3, j | j_1, (j_2 j_3) j_{23}, j) = (-1)^{j_1+j_2+j_3+j} [(2j_{12}+1)(2j_{23}+1)]^{\frac{1}{2}} \begin{Bmatrix} j_1 & j_2 & j_{12} \\ j_3 & j & j_{23} \end{Bmatrix} \quad (3.12)$$

Similarly, there are two schemes for the coupling of four angular momenta, and the recoupling coefficient is usually written in terms of a 9-J symbol:

$$((j_1 j_2) j_{12}, (j_3 j_4) j_{34}, j | (j_1 j_3) j_{13}, (j_2 j_4) j_{24}, j) = [(2j_{12}+1)(2j_{34}+1)(2j_{13}+1)(2j_{24}+1)]^{\frac{1}{2}} \begin{Bmatrix} j_1 & j_2 & j_{12} \\ j_3 & j_4 & j_{34} \\ j_{13} & j_{24} & j \end{Bmatrix} \quad (3.13)$$

A 9-J symbol can be reduced to a 6-J symbol if one of its elements is equal to zero [19, p. 105].

Finally, the dot product of two tensors can be written as a coupled tensor of zeroth rank:

$$\mathbf{T}^{(k)} \cdot \mathbf{U}^{(k)} = \sum_q (-1)^q T_q^{(k)} U_{-q}^{(k)} = (-1)^k (2k+1)^{\frac{1}{2}} \left(\mathbf{T}^{(k)} \mathbf{U}^{(k)} \right)^{(0)} \quad (3.14)$$

3.3.3 The Kramers-Heisenberg Dispersion Formula

In its most general form, the radiative transition rate between an initial state $|i\rangle$ and a final state $|f\rangle$ of a material system interacting with a radiation field is written:

$$\frac{1}{\tau} = \frac{2\pi}{\hbar^2} \left| \langle f|\mathcal{H}_I|i\rangle - \frac{1}{\hbar} \sum_j \frac{\langle f|\mathcal{H}_I|j\rangle\langle j|\mathcal{H}_I|i\rangle}{\omega_j - \omega_i} + \ldots \right|^2 \quad (3.15)$$

where $\mathcal{H}_I$ is the material-radiation interaction Hamiltonian [20]. This equation is the result of time-dependent perturbation theory, and is displayed up to second order. The interaction Hamiltonian can be approximated, for radiation in the visible impinging upon an atomic system, as the sum of several terms:

$$\mathcal{H}_I = \mathcal{H}_{ED} + \mathcal{H}_{EQ} + \mathcal{H}_{MD} + \mathcal{H}_{NL} \quad (3.16)$$

where the main contribution is from the electric-dipole Hamiltonian:

$$\mathcal{H}_{ED} = e \sum_i \vec{r}_i \cdot \vec{E}(0) = e\vec{D} \cdot \vec{E}(0) \quad (3.17)$$

The sum is over the i electrons of the atom, and the electric field is evaluated at the center of the atom. The rationale for these approximations is that radiation in the visible has a wavelength of roughly 5000 Å, whereas an atom has a typical dimension of 1 Å, so that spatially the electromagnetic field is essentially constant over the extent of the atom. In this approximation, the electric-quadrupole and magnetic-dipole Hamiltonians are smaller in magnitude than the electric-dipole Hamiltonian by a factor of $\alpha = \frac{1}{137}$. The electric-quadrupole Hamiltonian is:

$$\mathcal{H}_{EQ} = \frac{1}{2} e \sum_i \left(\vec{r}_i \cdot \vec{\nabla}\right)\left(\vec{r}_i \cdot \vec{E}(0)\right) = -\vec{\nabla} \cdot \vec{Q} \cdot \vec{E}(0) \tag{3.18}$$

where $\vec{Q}$ is the electric quadrupole moment of the atom. The magnetic-dipole Hamiltonian is:

$$\mathcal{H}_{MD} = \frac{e}{2m} \vec{J} \cdot \vec{B}(0) \tag{3.19}$$

where $\vec{J} = \sum_i \vec{j}_i = \sum_i (\vec{l}_i + 2\vec{s}_i)$. is the total angular momentum of the atom and the magnetic field $\vec{B}$ is evaluated at the center of the atom. $\mathcal{H}_{NL}$ depends on the square of the magnetic field:

$$\mathcal{H}_{NL} = \frac{e^2}{8m} \sum_i \left(\vec{r}_i \times \vec{B}(0)\right)^2 \tag{3.20}$$

and is usually of negligible magnitude.

In the case of a two-photon process such as the inelastic scattering of monochromatic radiation of frequency ω, equation (3.15) can be used to derive the following differential scattering cross section:

$$\frac{d\sigma}{d\Omega} = \frac{e^4 \omega (\omega - \omega_f)^3}{16\pi\epsilon_0^2 \hbar^2 c^4} \left| -\sum_j \left[\frac{\langle f|\hat{e}_s \cdot \vec{D}|j\rangle\langle j|\hat{e} \cdot \vec{D}|i\rangle}{\hbar\omega_j - \hbar\omega} + \frac{\langle f|\hat{e} \cdot \vec{D}|j\rangle\langle j|\hat{e}_s \cdot \vec{D}|i\rangle}{\hbar\omega_j + \hbar\omega_s} \right] \right|^2 \tag{3.21}$$

where ω and $\hat{e}$ are the frequency and unit polarization vector of the incident photon, ω_s and $\hat{e}_s$ are the corresponding quantities for the scattered photon, and $\hbar\omega_j$ is the energy of the intermediate state. This expression is known as the Kramers-Heisenberg dispersion formula. It is derived assuming that only $\mathcal{H}_{ED}$ contributes significantly to the scattering via a second-order perturbational mechanism. The calculation is described by Loudon [20]. It is a fully quantum mechanical calculation in that the electromagnetic field is written in second quantized form. The semi-classical calculation for spontaneous Raman scattering is described by Koningstein [1] and Placzek [21]. In the semi-classical picture the incident radiation field induces oscillating dipole moments in the material system which are then

assumed to radiate like classical dipoles. Raman cross sections calculated by this method have a factor of $(\omega - \omega_f)^4$ for the total radiated power instead of the $\omega(\omega - \omega_f)^3$ factor of equation (3.21).

The two terms in equation (3.20) correspond to the two possible time orderings of the virtual absorption and emission processes. Inelastic Raman scattering can occur for both $\omega_s \leq \omega$ (Stokes radiation) and for $\omega_s \geq \omega$ (anti-Stokes radiation). Anti-Stokes radiation can originate only from a higher excited state of the material system, which means that the excited state needs to be populated, thermally or otherwise. The Kramers-Heisenberg formula can be applied to two-photon absorption by simply replacing ω_s with $-\omega_s$. The scattering tensor, which represents the amplitude of the scattering of an incident photon of polarization σ and energy $\hbar\omega$ into a photon of polarization ρ and energy $\hbar\omega_s$, the atomic system making a transition from state $|i\rangle$ to state $|f\rangle$, can thus be written:

$$(\alpha_{\rho\sigma})_{fi} = -\sum_j \left[\frac{\langle f|D_\rho|j\rangle\langle j|D_\sigma|i\rangle}{\hbar\omega_j - \hbar\omega} + \frac{\langle f|D_\sigma|j\rangle\langle j|D_\rho|i\rangle}{\hbar\omega_j + \hbar\omega_s} \right] \tag{3.22}$$

Quite often this equation is quoted in the literature without the minus sign that precedes it. This can lead to serious errors if interference with other amplitude channels are being considered. Equation (3.21) forms the starting point of our theoretical investigations.

3.3.4 Second Quantization Derivation of the Electronic Raman Tensor - Contributions of the d and g Orbitals

To evaluate expression (3.22) for the scattering tensor, the Judd-Ofelt closure technique will be used, since otherwise the infinite sum would be quite intractable. The intermediate states that contribute the most in the sum of equation (3.22) are usually assumed to be states of the excited $4f^{N-1}5d$ configuration. This assumption will be tested by our experimental results. The $4f^N$ configuration is dropped from the sum since, except in the near resonance case, the forbidden electric-dipole $4f^N$ - $4f^N$ oscillator strengths are too small to contribute any appreciable amplitude. In contrast, $4f^N$ - $4f^{N-1}n'd$ and $4f^N$ - $4f^{N-1}n'g$ matrix elements are electric-dipole allowed, with oscillator strengths on the order of 1 to 0.1. The opposite parity configuration with the lowest energy denominator is $4f^{N-1}5d$, which is why it is usually assumed to give the main contribution to 4f - 4f second order processes involving infinite sums over virtual intermediate states (in the electric dipole approximation). For the other opposite parity configurations, the energy denominator is significantly higher

than that for $4f^{N-1}5d$, which is why their role is usually neglected. Note that because of the electric-dipole selection rules, the only intermediate configurations that can *a priori* be pathways for the Raman amplitude are $4f^{N-1}n'd$, $4f^{N-1}n'g$, and $4f^{N+1}n'd^9$, this last configuration involving the excitation of a core d electron (n'=3,4) into the 4f shell.

The calculation of the electronic Raman amplitude follows the steps of Judd and Pooler [14] and Downer [17]. There are some slight differences since the above author's treatment is directed towards two-photon absorption with one input beam. Also, for more generality, we calculate the amplitude with intermediate states that belong to either the configuration $4f^{N-1}n'd$ or the configuration $4f^{N-1}n'g$.

In an electric dipole transition between the shell (nl) and the shell $(n'l')$, the electric dipole operator can be derived to have the following second quantized form [22]:

$$\begin{aligned}\vec{D} = \sum_i \vec{r}_i \;\; &= \;\; (-1)^l (2)^{\frac{1}{2}} \left[\frac{(2l+1)(2l'+1)}{3}\right]^{\frac{1}{2}} \begin{pmatrix} l & 1 & l' \\ 0 & 0 & 0 \end{pmatrix} \\ &\quad \times \langle nl|r|n'l'\rangle \left[(\mathbf{a}^\dagger \mathbf{b})^{(01)} - (\mathbf{b}^\dagger \mathbf{a})^{(01)}\right] \end{aligned} \tag{3.23}$$

where i denotes the electrons that participate in the transition, $\mathbf{a}^\dagger$ and $\mathbf{a}$ are the creation and annihilation operators for the (nl) shell, and $\mathbf{b}^\dagger$ and $\mathbf{b}$ those for the $(n'l')$ shell. This result can be derived using the rules prescribed by Judd for finding the second quantized form of an atomic one-particle operator [18]. Since our initial state belongs to the (4f) shell, $\mathbf{a}^\dagger, \mathbf{a} = \mathbf{f}^\dagger, \mathbf{f}$ and $l = 3$:

$$\vec{D} = -(2)^{\frac{1}{2}} \left[\frac{7(2l'+1)}{3}\right]^{\frac{1}{2}} \begin{pmatrix} 3 & 1 & l' \\ 0 & 0 & 0 \end{pmatrix} \langle 4f|r|n'l'\rangle \left[(\mathbf{f}^\dagger \mathbf{b})^{(01)} - (\mathbf{b}^\dagger \mathbf{f})^{(01)}\right] \tag{3.24}$$

For d electrons we have $l' = 2$ and the electric dipole operator is:

$$\vec{D} = (2)^{\frac{1}{2}} \left[(\mathbf{f}^\dagger \mathbf{d})^{(01)} - (\mathbf{d}^\dagger \mathbf{f})^{(01)}\right] \langle 4f|r|n'\mathrm{d}\rangle \tag{3.25}$$

and for g electrons it is:

$$\vec{D} = -\frac{(2)^{\frac{3}{2}}}{(3)^{\frac{1}{2}}} \left[(\mathbf{f}^\dagger \mathbf{g})^{(01)} - (\mathbf{g}^\dagger \mathbf{f})^{(01)}\right] \langle 4f|r|n'\mathrm{g}\rangle \tag{3.26}$$

Dropping the radial integral and numerical factors, the first term on the right hand side of equation (3.22) is:

$$\sum_{4f^{N-1}n'l'} \frac{\langle f|\hat{\mathbf{e}}_s^{(01)} \cdot (\mathbf{f}^\dagger \mathbf{b})^{(01)}|j\rangle \langle j|\hat{\mathbf{e}}^{(01)} \cdot (\mathbf{b}^\dagger \mathbf{f})^{(01)}|i\rangle}{\hbar\omega_j - \hbar\omega} \tag{3.27}$$

The Judd-Ofelt closure approximation is then applied:

$$\sum_j \frac{|j\rangle\langle j|}{\hbar\omega_j - \hbar\omega} \simeq \frac{1}{E_{l'\mathrm{f}} - \hbar\omega} \sum_j |j\rangle\langle j| = \frac{1}{E_{l'\mathrm{f}} - \hbar\omega} \tag{3.28}$$

where $E_{l'\mathrm{f}}$ is the average energy difference between the configurations $4\mathrm{f}^N$ and $4\mathrm{f}^{N-1}\mathrm{n}'l'$. Expression (3.27) becomes:

$$\frac{1}{E_{l'\mathrm{f}} - \hbar\omega} \langle f|\mathbf{e}_s^{(01)} \cdot (\mathbf{f}^\dagger\mathbf{b})^{(01)}\mathbf{e}^{(01)} \cdot (\mathbf{b}^\dagger\mathbf{f})^{(01)}|i\rangle \tag{3.29}$$

The goal here is to pass $\mathbf{b}$ to the right so as to make use of the relation $\mathbf{b}|i\rangle = 0$, since the initial state $|i\rangle$ contains no $(\mathrm{n}'l')$ electrons. When $\mathbf{b}$ crosses $\mathbf{b}^\dagger$, use can be made of the anticommutation relations (3.6). Also, note that the ranks of the tensors $\mathbf{f}$, $\mathbf{f}^\dagger$ and $\mathbf{b}$, $\mathbf{b}^\dagger$ are, respectively, $\left(\frac{1}{2}3\right)$ and $\left(\frac{1}{2}l'\right)$. The scalar products of equation (3.29) are written as tensors of zeroth rank:

$$\mathbf{e}_s^{(01)} \cdot (\mathbf{f}^\dagger\mathbf{b})^{(01)}\mathbf{e}^{(01)} \cdot (\mathbf{b}^\dagger\mathbf{f})^{(01)} = 3\left(\mathbf{e}_s^{(01)}(\mathbf{f}^\dagger\mathbf{b})^{(01)}\right)^{(00)}\left(\mathbf{e}^{(01)}(\mathbf{b}^\dagger\mathbf{f})^{(01)}\right)^{(00)} \tag{3.30}$$

This expression can be recoupled so as to isolate $\mathbf{b}$ and $\mathbf{b}^\dagger$:

$$\left(\mathbf{e}_s^{(01)}(\mathbf{f}^\dagger\mathbf{b})^{(01)}\right)^{(00)} = \sum_{r,t}(0,(\tfrac{1}{2},\tfrac{1}{2})0,0|(0\tfrac{1}{2})r,\tfrac{1}{2},0)\,(1,(3l')1,0|(13)t,l',0)\left((\mathbf{e}_s^{(01)}\mathbf{f}^\dagger)^{(rt)}\mathbf{b}\right)^{(00)} \tag{3.31}$$

Notice that the recoupling is done independently in both spin and orbital angular momentum space. Necessarily $r = \frac{1}{2}$, and since t must be coupled to l' to form 0, $t = l'$. We find that both recoupling coefficients are equal to one:

$$3\left(\mathbf{e}_s^{(01)}(\mathbf{f}^\dagger\mathbf{b})^{(01)}\right)^{(00)}\left(\mathbf{e}^{(01)}(\mathbf{b}^\dagger\mathbf{f})^{(01)}\right)^{(00)} = 3\left((\mathbf{e}_s^{(01)}\mathbf{f}^\dagger)^{(\frac{1}{2}l')}\mathbf{b}\right)^{(00)}\left((\mathbf{e}^{(01)}\mathbf{f})^{(\frac{1}{2}l')}\mathbf{b}^\dagger\right)^{(00)} \tag{3.32}$$

$\mathbf{b}$ and $\mathbf{b}^\dagger$ are now brought together:

$$3\left((\mathbf{e}_s^{(01)}\mathbf{f}^\dagger)^{(\frac{1}{2}l')}\mathbf{b}\right)^{(00)}\left((\mathbf{e}^{(01)}\mathbf{f})^{(\frac{1}{2}l')}\mathbf{b}^\dagger\right)^{(00)} = -3\sum_{r,t}((\tfrac{1}{2}\tfrac{1}{2})0,(\tfrac{1}{2}\tfrac{1}{2})0,0|(\tfrac{1}{2}\tfrac{1}{2})r,(\tfrac{1}{2}\tfrac{1}{2})r,0)((l'l')0,(l'l')0,0|(l'l')t,(l'l')t,0) \times \left((\mathbf{e}_s^{(01)}\mathbf{f}^\dagger)^{(\frac{1}{2}l')}(\mathbf{e}^{(01)}\mathbf{f})^{(\frac{1}{2}l')}\right)^{(rt)}(\mathbf{b}\mathbf{b}^\dagger)^{(rt)} \tag{3.33}$$

The sign change comes from passing $\mathbf{b}$ to the right of $\mathbf{f}$. We then make use of the commutation relation:

$$(\mathbf{b}\mathbf{b}^\dagger)^{(\kappa k)} + (-1)^{2l+2s-\kappa-k}(\mathbf{b}^\dagger\mathbf{b})^{(\kappa k)} = \delta(\kappa,0)\delta(k,0)(2s+1)^{\frac{1}{2}}(2l'+1)^{\frac{1}{2}} \tag{3.34}$$

whichs says that for $(rt) \neq (00)$, $(\mathbf{bb}^\dagger)^{(rt)}$ is proportional to $(\mathbf{b}^\dagger\mathbf{b})^{(rt)}$, at which point $\mathbf{b}|i\rangle = 0$ can be invoked so that the only term that will remain on the right hand side of equation (3.29) is that in $(\mathbf{bb}^\dagger)^{(00)}$. From (3.34) $(\mathbf{bb}^\dagger)^{(00)} = (2)^{\frac{1}{2}}(2l'+1)^{\frac{1}{2}}$ and the recoupling coefficients can be evaluated to be respectively $\frac{1}{2}$ and $(2l'+1)^{-1}$. We obtain:

$$\mathbf{e}_s^{(01)} \cdot (\mathbf{f}^\dagger\mathbf{b})^{(01)}\mathbf{e}^{(01)} \cdot (\mathbf{b}^\dagger\mathbf{f})^{(01)} = -\frac{3}{[2(2l'+1)]^{\frac{1}{2}}}\left((\mathbf{e}_s^{(01)}\mathbf{f}^\dagger)^{(\frac{1}{2}l')}(\mathbf{e}^{(01)}\mathbf{f})^{(\frac{1}{2}l')}\right)^{(00)} \tag{3.35}$$

The final recoupling brings together $\mathbf{f}$ and $\mathbf{f}^\dagger$, and the two electric field polarization vectors:

$$\begin{aligned}-\frac{3}{[2(2l'+1)]^{\frac{1}{2}}}&\left((\mathbf{e}_s^{(01)}\mathbf{f}^\dagger)^{(\frac{1}{2}l')}(\mathbf{e}^{(01)}\mathbf{f})^{(\frac{1}{2}l')}\right)^{(00)} = \\ &\times\frac{3}{[2(2l'+1)]^{\frac{1}{2}}}\sum_{r,t}((0\tfrac{1}{2})\tfrac{1}{2},(0\tfrac{1}{2})\tfrac{1}{2},0|(00)r,(\tfrac{1}{2}\tfrac{1}{2})r,0)((13)l',(13)l',0|(11)t,(33)t,0) \\ &\times\left((\mathbf{e}_s^{(01)}\mathbf{e}^{(01)})^{(rt)}(\mathbf{f}^\dagger\mathbf{f})^{(rt)}\right)^{(00)}\end{aligned} \tag{3.36}$$

Necessarily $r = 0$, so that the first recoupling coefficient is equal to 1. t can only take on the values 0,1,2, and the second recoupling coefficient is:

$$\begin{aligned}((13)l',(13)l',0|(11)t,(33)t,0) &= (2l'+1)(2t+1)\begin{Bmatrix}1 & 3 & l'\\ 1 & 3 & l'\\ t & t & 0\end{Bmatrix} \\ &= (-1)^t(2l'+1)^{\frac{1}{2}}(2t+1)^{\frac{1}{2}}\begin{Bmatrix}1 & 3 & l'\\ 3 & 1 & t\end{Bmatrix}\end{aligned} \tag{3.37}$$

One can derive for any set of creation and annihilation operators $\mathbf{a}^\dagger$ and $\mathbf{a}$ belonging to a given shell (nl), the following identity:

$$(\mathbf{a}^\dagger\mathbf{a})^{(0t)} = -\left[\left(\frac{1}{2}\right)(2t+1)\right]^{\frac{1}{2}}\mathbf{U}^{(t)} \tag{3.38}$$

where $\mathbf{U}^{(t)}$ is the unit tensor in orbital angular momentum space. The zeroth order coupled tensor is converted to a dot product and one has:

$$\langle f|\mathbf{e}_s^{(01)} \cdot (\mathbf{f}^\dagger\mathbf{b})^{(01)}\mathbf{e}^{(01)} \cdot (\mathbf{b}^\dagger\mathbf{f})^{(01)}|i\rangle = \frac{3}{2}\sum_t(2t+1)^{\frac{1}{2}}\begin{Bmatrix}1 & 3 & l'\\ 3 & 1 & t\end{Bmatrix}(\mathbf{e}_s\mathbf{e})^{(t)} \cdot \mathbf{U}^{(t)} \tag{3.39}$$

Note that $(\mathbf{e}_s\mathbf{e})^{(0t)} = (\mathbf{e}_s\mathbf{e})^{(t)}$ only because the electric field vectors do not act in wavefunction space. Interchanging $\mathbf{e}_s$ and $\mathbf{e}$ in the above derivation leads quite readily to the matrix element in the second term on the right hand side of equation (3.22):

$$\langle f|\mathbf{e}_s^{(01)} \cdot (\mathbf{f}^\dagger\mathbf{b})^{(01)}\mathbf{e}^{(01)} \cdot (\mathbf{b}^\dagger\mathbf{f})^{(01)}|i\rangle = \frac{3}{2}\sum_t(2t+1)^{\frac{1}{2}}\begin{Bmatrix}1 & 3 & l'\\ 3 & 1 & t\end{Bmatrix}(\mathbf{e}\mathbf{e}_s)^{(t)} \cdot \mathbf{U}^{(t)} \tag{3.40}$$

Using the properties of the Clebsch-Gordan coefficients, we can write:

$$(\mathbf{e}\mathbf{e}_s)^{(t)} = (-1)^t(\mathbf{e}_s\mathbf{e})^{(t)} \tag{3.41}$$

Collecting the two terms together, and reinserting the numerical factors and radial matrix element of equation (3.23) we have the final expression for the electronic Raman amplitude:

$$\sum_{4f^{N-1}n'l'} 7(2l'+1)\begin{pmatrix} 3 & 1 & l' \\ 0 & 0 & 0 \end{pmatrix}^2 \langle 4f|r|n'l'\rangle^2$$
$$\times \textstyle\sum_t (2t+1)^{\frac{1}{2}} \begin{Bmatrix} 1 & 3 & l' \\ 3 & 1 & t \end{Bmatrix} \left[\frac{1}{E_{n'l'} - \hbar\omega} + \frac{(-1)^t}{E_{n'l'} + \hbar\omega_s}\right] (\mathbf{e}\mathbf{e}_s)^{(t)} \cdot \mathbf{U}^{(t)} \tag{3.42}$$

The two-photon amplitude can be easily obtained from this expression by making the replacement $\omega_s \rightarrow -\omega_s$. In the case of two-photon absorption with a single input beam the extra factor of two should be ignored, as the Feynmann graphs which correspond to the two terms of equation (3.22) become indistinguishable.

The above calculations can be retraced using the core excitation $4f^{N+1}n'd^9$ configurations as the intermediate states. It is easy to verify that the final result is identical to that for $4f^{N-1}n'd$ as far as the angular variables are concerned. The only differences appear in the energy denominators and the radial matrix elements.

An older version of this calculation which makes use only of tensor operator techniques and does not involve second quantization techniques can be found in Axe [23]. Essentially, Axe makes use of the closure relation derived by Judd [24, eq. 9].

Returning to the case of electronic Raman scattering, we make the approximations $\omega \approx \omega_s$ and $\omega \ll E_{df}$. The term with $t = 0$ contributes only to Rayleigh scattering. This comes from the fact that $\mathbf{U}^{(0)}$ is a scalar and can only connect identical initial and final states. The term with $t = 1$ is:

$$7(3)^{\frac{1}{2}} \sum_{4f^{N-1}n'l'} (2l'+1)\langle 4f|r|n'l'\rangle^2 \begin{pmatrix} 3 & 1 & l' \\ 0 & 0 & 0 \end{pmatrix}^2 \begin{Bmatrix} 1 & 3 & l' \\ 3 & 1 & 1 \end{Bmatrix} \frac{2\hbar\omega}{E^2_{l'f}} (\mathbf{e}\mathbf{e}_s)^{(1)} \cdot \mathbf{U}^{(1)} \tag{3.43}$$

and the term with $t = 2$ is:

$$7(5)^{\frac{1}{2}} \sum_{4f^{N-1}n'l'} (2l'+1)\langle 4f|r|n'l'\rangle^2 \begin{pmatrix} 3 & 1 & l' \\ 0 & 0 & 0 \end{pmatrix}^2 \begin{Bmatrix} 1 & 3 & l' \\ 3 & 1 & 2 \end{Bmatrix} \frac{2}{E_{l'f}} (\mathbf{e}\mathbf{e}_s)^{(2)} \cdot \mathbf{U}^{(2)} \tag{3.44}$$

The important point to note is that due to relation (3.41) the term in $t = 1$ changes sign when the polarizations of the incident and scattered photons are interchanged whereas the

term in $t = 2$ does not. The $t = 1$ term is thus the *antisymmetric* contribution to the scattering tensor, and the $t = 2$ term the *symmetric* contribution. Note that the $t = 1$ term is necessarily zero if $\mathbf{e} = \mathbf{e}_s$, as is the case for two-photon absorption with a single input beam. The antisymmetric content of the scattering tensor is one of the more unique features of the electronic Raman effect. The antisymmetric term is roughly a factor of $\hbar\omega/E_{\mathrm{df}}$ smaller than the symmetric term. For the 514.5 nm line of the Ar^+ laser, and considering the configuration $4f^{N-1}5d$, this factor is about 0.2. Experimentally, this antisymmetric contribution can be readily observed.

It is interesting to compare separately the contributions of the d and g orbital configurations. For d orbitals, the term with $t = 1$ is:

$$-\frac{(2)^{\frac{3}{2}}(3)^{\frac{1}{2}}}{(7)^{\frac{1}{2}}}\frac{\hbar\omega}{E_{\mathrm{df}}^2}\langle 4\mathrm{f}|r|\mathrm{n'd}\rangle^2(\mathbf{e}\mathbf{e}_s)^{(1)}\cdot\mathbf{U}^{(1)} \tag{3.45}$$

and for g orbitals it is:

$$\frac{(2)^{\frac{3}{2}}(3)^{\frac{1}{2}}}{(7)^{\frac{1}{2}}}\frac{\hbar\omega}{E_{\mathrm{gf}}^2}\langle 4\mathrm{f}|r|\mathrm{n'g}\rangle^2(\mathbf{e}\mathbf{e}_s)^{(1)}\cdot\mathbf{U}^{(1)} \tag{3.46}$$

The d and g orbitals have contributions to the $t = 1$ term that are opposite in sign. A measurement of the amount of asymmetry thus allows the determination of the relative importance of the d and g orbitals in the summation over the intermediate states.

The term with $t = 2$ for d orbitals is:

$$\frac{3(2)^{\frac{3}{2}}}{(5)^{\frac{1}{2}}(7)^{\frac{1}{2}}}\frac{1}{E_{\mathrm{df}}}\langle 4\mathrm{f}|r|\mathrm{n'd}\rangle^2(\mathbf{e}\mathbf{e}_s)^{(2)}\cdot\mathbf{U}^{(2)} \tag{3.47}$$

and for g orbitals it is:

$$\frac{(2)^{\frac{3}{2}}(5)^{\frac{1}{2}}}{(3)(7)^{\frac{1}{2}}}\frac{1}{E_{\mathrm{gf}}}\langle 4\mathrm{f}|r|\mathrm{n'g}\rangle^2(\mathbf{e}\mathbf{e}_s)^{(2)}\cdot\mathbf{U}^{(2)} \tag{3.48}$$

Thus for the term with $t = 2$ the contributions of the d and g orbitals add constructively. A detailed study of the electronic Raman intensities, and a comparison of the calculated and observed intensities, is presented in chapter 5 for the ions Tm^{3+}, Er^{3+}, and Ho^{3+}.

3.3.5 The F_1 and F_2 Parameters

It is convenient to make use of the $F(1,\nu)$ ($\equiv F_1$) and $F(2,\nu)$ ($\equiv F_2$) parameters originally defined by Mortensen and Koningstein [25]. These parameters group together the numerical

factors, radial integrals, and energy denominators that appear in the expression for the electronic Raman amplitude. The general definition of F_t is:

$$F_t = (-1)^t \sum_{4f^{N-1}n'l'} 7(2l'+1) \begin{pmatrix} 3 & 1 & l' \\ 0 & 0 & 0 \end{pmatrix}^2 \langle 4f|r|n'l'\rangle^2$$
$$\times (2t+1)^{\frac{1}{2}} \begin{Bmatrix} 1 & 3 & l' \\ 3 & 1 & t \end{Bmatrix} \left[\frac{1}{E_{df} - \hbar\omega} + \frac{(-1)^t}{E_{df} + \hbar\omega} \right] \tag{3.49}$$

F_1 represents the antisymmetric contribution to the electronic Raman tensor:

$$F_1 = -7(3)^{\frac{1}{2}} \sum_{4f^{N-1}n'l'} (2l'+1)\langle 4f|r|n'l'\rangle^2 \begin{pmatrix} 3 & 1 & l' \\ 0 & 0 & 0 \end{pmatrix}^2 \begin{Bmatrix} 1 & 3 & l' \\ 3 & 1 & 1 \end{Bmatrix} \frac{2\hbar\omega}{E_{l'f}^2} \tag{3.50}$$

while F_2 represents the symmetric contribution to the electronic Raman tensor:

$$F_2 = 7(5)^{\frac{1}{2}} \sum_{4f^{N-1}n'l'} (2l'+1)\langle 4f|r|n'l'\rangle^2 \begin{pmatrix} 3 & 1 & l' \\ 0 & 0 & 0 \end{pmatrix}^2 \begin{Bmatrix} 1 & 3 & l' \\ 3 & 1 & 2 \end{Bmatrix} \frac{2}{E_{l'f}} \tag{3.51}$$

To compare the above expressions with those given in the references, use can be made of the equation:

$$\langle l||\mathbf{C}^{(1)}||l'\rangle = (-1)^l \left[(2l+1)(2l'+1)\right]^{\frac{1}{2}} \begin{pmatrix} l & k & l' \\ 0 & 0 & 0 \end{pmatrix} \tag{3.52}$$

The ratio F_1/F_2 is a measure of the amount of asymmetry for a transition that has both antisymmetric and symmetric contributions. The usefulness of the F_1 and F_2 parameters will become more apparent in the next section where it is shown how to calculate the electronic Raman tensor in spherical coordinates using intermediate coupling wavefunctions for the initial and final states.

3.3.6 Calculation of the Electronic Raman Tensor With Intermediate Coupling Wavefunctions

The preceding calculations have set the stage for a complete computation of the electronic Raman transition amplitudes between various initial and final states. Since the intermediate states have been dispensed with by means of the Judd-Ofelt closure technique, the only wavefunctions necessary are those of the initial and final states, which belong to the $4f^N$ configuration. These wavefunctions are available from crystal field fits performed previously and the essential results of which have been tabulated in Appendix A for the ions

of interest in this study. The crystal field fits are based upon absorption and fluorescence spectra. The wavefunctions yielded by the fit also allow the caculation of such quantities as the g-values of the states and their magnetic susceptibilities. The semi-empirical Hamiltonian used for the crystal field fit has been described in chapter 1. The complete set of wavefunctions used as the basis states are the Russell-Saunders coupled wavefunctions $|4f^N \alpha S L J J_z\rangle$, the eigenfunctions of the semi-empirical Hamiltonian being expressed as linear combinations of these wavefunctions. These are the so-called intermediate coupling wavefunctions. We write the initial state as:

$$|i\rangle = \sum_{\alpha S L J J_z} a(i; 4f^N \alpha S L J J_z) |4f^N \alpha S L J J_z\rangle \tag{3.53}$$

and similarly the final state is written:

$$|f\rangle = \sum_{\alpha' S' L' J' J'_z} a'(f; 4f^N \alpha' S' L' J' J'_z) |4f^N \alpha' S' L' J' J'_z\rangle \tag{3.54}$$

It will be advantageous at this point to express the electronic Raman tensor using spherical tensors. The electronic Raman transition amplitude given in equation (3.42) can be written using the F_1 and F_2 parameters:

$$\sum_t \sum_{4f^{N-1} n' l'} (-1)^t F_t (ee_s)^{(t)} \cdot \mathbf{U}^{(t)} \tag{3.55}$$

We can write the tensorial dot product as:

$$(ee_s)^{(t)} \cdot \mathbf{U}^{(t)} = \sum_q (-1)^q (ee_s)^{(t)}_q U^{(t)}_{-q} = \sum_q \sum_{q_1 q_2} (-1)^q (1 q_1 1 q_2 | 1 1 t q) (e)_{q_1} (e_s)_{q_2} U^{(t)}_{-q} \tag{3.56}$$

and $q_1 + q_2 = -q$. In spherical coordinates, the transition amplitude would be written:

$$\sum_{qq'} (-1)^{q+q'} \alpha_{qq'} (e)_{-q} (e_s)_{-q'} \tag{3.57}$$

We make the relacement $q_1 \rightarrow -q_1$ and $q_2 \rightarrow -q_2$ which leads to:

$$\sum_t \sum_{4f^{N-1} n' l'} (-1)^t F_t (ee_s)^{(t)} \cdot \mathbf{U}^{(t)} =$$
$$\sum_t \sum_{4f^{N-1} n' l'} \sum_q \sum_{q_1 q_2} (-1)^t F_t (-1)^{-q} (1 - q_1 1 - q_2 | 1 1 t - q) (e)_{-q_1} (e_s)_{-q_2} U^{(t)}_q \tag{3.58}$$

The Raman tensor is thus seen to be:

$$\alpha_{q_1 q_2} = \sum_t \sum_{4f^{N-1} n' l'} (-1)^t F_t (1 - q_1 1 - q_2 | 1 1 t - q) U^{(t)}_q \tag{3.59}$$

with $q_1 + q_2 = q$. $\alpha_{q_1 q_2}$ transforms as the product of two tensors of rank one. However, two tensors of rank one can be coupled to form tensors of ranks 0, 1, and 2. We thus couple the various tensors $\alpha_{q_1 q_2}$ to form the spherical tensors $\alpha_q^{(t)}$ with $t = 0, 1, 2$:

$$\alpha_q^{(t)} = \sum_{q_1 q_2} (1 q_1 1 q_2 | 1 1 t q) \alpha_{q_1 q_2} \tag{3.60}$$

So that we now have:

$$\alpha_q^{(t)} = \sum_{q_1 q_2} \sum_{t'} \sum_{4f^{N-1} n' l'} (-1)^{t'} F_{t'} (1 - q_1 1 - q_2 | 1 1 t' - q)(1 q_1 1 q_2 | 1 1 t q) U_q^{(t)} \tag{3.61}$$

and we use the properties of the 3-J symbols to write this as:

$$\begin{aligned} \alpha_q^{(t)} &= \sum_{q_1 q_2} \sum_{t'} \sum_{4f^{N-1} n' l'} (-1)^{t'} F_{t'} (-1)^{t'} (1 q_1 1 q_2 | 1 1 t' q)(1 q_1 1 q_2 | 1 1 t q) U_q^{(t)} \\ &= \sum_{t'} F_{t'} \delta(t, t') U_q^{(t)} = F_t U_q^{(t)} \end{aligned} \tag{3.62}$$

This very simple expression shows that $\alpha^{(2)}$ represents the *symmetric* contribution and $\alpha^{(1)}$ the *antisymmetric* contribution to the electronic Raman tensor. The F_t parameters carry the information regarding the excitation energy and the intermediate states involved. The matrix elements of the unit tensors can be readily evaluated. The electronic Raman amplitude for the transition between states $|i\rangle$ and $|f\rangle$ is thus given by the matrix elements of the spherical tensor operators:

$$\begin{aligned} \langle f | \alpha_q^{(t)} | i \rangle &= F_t \sum_{\alpha S L J J_z} \sum_{\alpha' S' L' J' J'_z} a(i; 4f^N \alpha S L J J_z) a'(f; 4f^N \alpha' S' L' J' J'_z) \\ &\quad \times \langle 4f^N \alpha' S' L' J' J'_z | U_q^{(t)} | 4f^N \alpha S L J J_z \rangle \end{aligned} \tag{3.63}$$

Since $\mathbf{U}^{(t)}$ carries no spin angular momentum, necessarily $S = S'$. The matrix element of the unit tensor can be calculated first with the Wigner-Eckart theorem:

$$\langle 4f^N \alpha' S L' J' J'_z | U_q^{(t)} | 4f^N \alpha S L J J_z \rangle = (-1)^{J' - J'_z} \begin{pmatrix} J' & t & J \\ -J'_z & q & J_z \end{pmatrix} \langle S L' J' || U^{(t)} || S L J \rangle \tag{3.64}$$

The reduced matrix element in equation (3.64), which we denote as $U(t)$, can be reduced further:

$$\begin{aligned} U(t) &= \langle S L' J' || U^{(t)} || S L J \rangle = \\ &\quad (-1)^{S+L+J'+T} \left[(2J' + 1)(2J + 1) \right]^{\frac{1}{2}} \begin{Bmatrix} L' & J' & S \\ J & L & t \end{Bmatrix} \langle S L' || U^{(t)} || S L \rangle \end{aligned} \tag{3.65}$$

The values of the reduced matrix elements $\langle SL'||U^{(t)}||SL\rangle$ are tabulated by Nielson and Koster [27]. In the following chapter we use the theory developed here to compare experimental and calculated electronic Raman transition intensities for the crystal field states of Tm^{3+}, Er^{3+}, and Ho^{3+} in tetragonal phosphate hosts.

3.3.7 Converting from Spherical to Cartesian Tensors

Once the spherical Raman tensors have been calculated using the method described in the previous section, it is easy to convert the results to the Cartesian frame of reference used to define the polarizations. The equations are as follows:

$$\begin{cases} \alpha_{XX} = -\frac{1}{\sqrt{3}}\alpha_0^{(0)} + \frac{1}{2}\alpha_2^{(2)} + \frac{1}{2}\alpha_{-2}^{(2)} - \frac{1}{\sqrt{6}}\alpha_0^{(2)} \\ \alpha_{YY} = -\frac{1}{\sqrt{3}}\alpha_0^{(0)} - \frac{1}{2}\alpha_2^{(2)} - \frac{1}{2}\alpha_{-2}^{(2)} - \frac{1}{\sqrt{6}}\alpha_0^{(2)} \\ \alpha_{ZZ} = -\frac{1}{\sqrt{3}}\alpha_0^{(0)} + \frac{2}{\sqrt{6}}\alpha_0^{(2)} \\ \alpha_{XY} = -i\frac{1}{\sqrt{2}}\alpha_0^{(1)} - i\frac{1}{2}\alpha_2^{(2)} + i\frac{1}{2}\alpha_{-2}^{(2)} \\ \alpha_{XZ} = -\frac{1}{2}\alpha_1^{(1)} - \frac{1}{2}\alpha_{-1}^{(1)} - \frac{1}{2}\alpha_1^{(2)} + \frac{1}{2}\alpha_{-1}^{(2)} \\ \alpha_{YZ} = i\frac{1}{2}\alpha_1^{(1)} - i\frac{1}{2}\alpha_{-1}^{(1)} + i\frac{1}{2}\alpha_1^{(2)} + i\frac{1}{2}\alpha_{-1}^{(2)} \\ \alpha_{YX} = i\frac{1}{\sqrt{2}}\alpha_0^{(1)} - i\frac{1}{2}\alpha_2^{(2)} + i\frac{1}{2}\alpha_{-2}^{(2)} \\ \alpha_{ZX} = \frac{1}{2}\alpha_1^{(1)} + \frac{1}{2}\alpha_{-1}^{(1)} - \frac{1}{2}\alpha_1^{(2)} + \frac{1}{2}\alpha_{-1}^{(2)} \\ \alpha_{ZY} = -i\frac{1}{2}\alpha_1^{(1)} + i\frac{1}{2}\alpha_{-1}^{(1)} + i\frac{1}{2}\alpha_1^{(2)} + i\frac{1}{2}\alpha_{-1}^{(2)} \end{cases} \tag{3.66}$$

References

[1] J.A. Koningstein, *Introduction to the Theory of the Raman Effect* (D. Reidel Publishing Co., Dordrecht-Holland, 1972).

[2] T.C. Damen, S.P.S. Porto, and S.B. Bell, Phys. Rev. **142**, 570 (1966).

[3] M. Cardona, in *Light Scattering in Solids II* (Springer-Verlag, Berlin, 1982), p. 19, see in particular section 2.1.10.

[4] S.A. Miller, H.H. Caspers, and H.E. Rast, Phys. Rev. **168**, 964 (1968).

[5] P. Dawson, M.M. Hargreave, and G.R. Wilkinson, J. Phys. C **4**, 240 (1971).

[6] R. Loudon, Adv. in Phys. **13**, 423 (1964).

[7] G.F. Koster, J.O. Dimmock, R.G. Wheeler, and H. Statz, *Properties of the Thirty-Two Point Groups* (M.I.T. Press, Cambridge, Massachussetts, 1963).

[8] G.M. Begun, G.W. Beall, L.A. Boatner, and W.J. Gregor, J. Raman Spec. **11**, 273 (1981).

[9] A.N. Lazarev, N.A. Mazhenov, and A.P. Mirgorodskii, Inorg. Mat. USSR, **14(11)**, 1641 (1979).

[10] R.J. Elliott, R.T. Harley, W. Hayes, and S.R.P. Smith, Proc. R. Soc. Lond. A **328**, 217 (1972).

[11] S. Guha, Phys. Rev. B **23**, 6790 (1981).

[12] B.R. Judd, ***Second Quantization and Atomic Spectroscopy - G.H. Dieke Memorial Lectures*** (The Johns Hopkins Press, Baltimore, 1967).

[13] B.R. Judd, Rep. Prog. Phys. **48**, 907 (1985).

[14] B.R. Judd and D.R. Pooler, J. Phys. C **15**, 591 (1982).

[15] M.C. Downer, A. Bivas, and N. Bloembergen, Opt. Comm. **41**, 335 (1982).

[16] M.C. Downer and A. Bivas, Phys. Rev. B **28**, 3677 (1983).

[17] M.C. Downer, Ph.D. thesis, Harvard University, Cambridge, 1983 (unpublished).

[18] B.R. Judd, *Operator Techniques in Atomic Spectroscopy* (McGraw-Hill Book Co., New York, 1963).

[19] A.R. Edmonds, *Angular Momentum in Quantum Mechanics* (Princeton University Press, Princeton, 1960).

[20] R.Loudon, *The Quantum Theory of Light* (Clarendon Press, Oxford, 1983).

[21] G. Placzek, *Handbuch der Radiologie*, ed. E. Marx (Leipzig, Akademische Verlagsgesellschaft), vol. VI, p.209 (1934), also available in english as UCRL Translation No. 526 (L).

[22] As mentioned by M.C. Downer (Phys. Rev. B **28**, 3677 (1983), footnote 40), some of the earlier expressions published in the literature for the second quantized form of $\vec{D}$ are in error.

[23] J.D. Axe, Phys. Rev. **136**, A42 (1964). Note that this reference is missing an overall minus sign in the definition of the second order tensor, equation (1).

[24] B.R. Judd, Phys. Rev. **127**, 750 (1962).

[25] J.A. Koningstein and O. Sonnich Mortensen, Phys. Rev. **168**, 75 (1968). In equation (8) of this reference, $(-1)^{K+1}$ should be replaced by $(-1)^{K}$ as the authors are missing an overall minus sign in the definition of the electronic Raman tensor.

[26] P.C. Becker, N. Edelstein, G.M. Williams, J.J. Bucher, R.E. Russo, J.A. Koningstein, L.A. Boatner, and M.M. Abraham, Phys. Rev. B **31**, 8102 (1985).

[27] C.W. Nielson and G.F. Koster, *Spectroscopic Coefficients of the p^n, d^n, and f^n Configurations* (The M.I.T. Press, Cambridge, Massachussetts, 1963).

Chapter 4

Electronic Raman Scattering in Tm^{3+}, Er^{3+}, and Ho^{3+} in Tetragonal Phosphate Crystal Hosts - Experimental Results

This chapter presents the experimental results of electronic Raman scattering in pure and dilute tetragonal rare earth phosphate crystals. The ions Tm^{3+}, Er^{3+}, and Ho^{3+} are those under study.

The crystal field fits of the diluted lanthanide ions in $LuPO_4$ and YPO_4 are a guide to the location of the energy level transitions that can be potentially observed by electronic Raman scattering. It is expected that the energy level structure of the pure phosphate crystals will be very similar to that of the diluted phosphate crystals, in which the optically active rare earth ion is replaced by Lu. The variations in the energy level values between the pure and diluted crystals appear to be at the most 15 cm^{-1}, as it is the nearest neighbor oxygen ions which contribute the bulk of the crystal field at the rare earth ion site. As a consequence, replacing Lu by Tm, Er, or Ho, does not have a very large effect on the energy levels or their wavefunctions. Replacing Lu by Y has a somewhat larger effect on the energy values, but only a very small effect on the wavefunctions.

The following chapter, chapter 5, discusses the calculation of the electronic Raman intensities and compares them to the experimental intensities determined from the spectra presented here.

4.1 Preamble: How to Identify and Recognize Electronic Raman Transitions

The high symmetry of the tetragonal rare earth phosphates and the good optical quality of most of the crystals makes it relatively easy to obtain Raman spectra that exhibit clearly recognizable electronic peaks. Several standard techniques can be used to identify these electronic Raman transitions.

- The first step is to ensure that the transitions are indeed Raman peaks, and not fluorescence or some other extraneous transition. This is done by obtaining spectra with several different excitation lines of the argon ion laser. The Raman peaks should appear with the same frequency shift relative to the excitation frequency, irrespective of the excitation. The intensities might of course vary if any resonance effects come into play. Fluorescent transitions, which are fixed at an absolute frequency, will have a Raman shift that varies in a systematic way with the excitation energy. The appearance of an anti-Stokes Raman peak that corresponds in frequency to the Stokes Raman peak is also evidence that the transition is a Raman one. Of course, higher temperatures are needed to observe the anti-Stokes peaks since these originate in the excited states, as shown in figure 4.10.

- Temperature is an important experimental variable. The vibrational Raman spectrum is present at all temperatures, whereas to observe the electronic transitions temperatures in the range 4.2 to 100 K are needed for the majority of the crystals studied. An initial room temperature scan allows the identification of the phonon peaks. When the crystal is cooled, the electronic peaks can then be identified among the "extra" peaks that arise at low temperature. In addition, the electronic Raman transitions broaden fairly rapidly as the temperature is raised from 4.2 to 100 K, whereas the phonon linewidths do not increase very much between 4.2 and 295 K. The intensities of the electronic transitions that originate in the ground state decrease with temperature as the ground state depopulates and the low-lying excited crystal field states become thermally populated, since the intensity of an electronic transition is proportional to the population of the initial state. There are not very many phonons because of the high symmetry of the crystal, which substantially lowers the probability that a phonon

peak will obscure or cover up an electronic one. A range of intensities are observed for the electronic Raman transitions, from transitions very much weaker than the lowest intensity phonons, to transitions that are as intense as the extremely strong phonons in the 1000 cm^{-1} region.

- For the tetragonal rare earth phosphate crystals studied in the present work, absorption spectra and crystal field fits are available. Thus the rough locations of the electronic transitions are known, which facilitates the search for them.

- The symmetries of the transitions are obtained by taking polarized spectra with all the polarization combinations of incident and scattered light allowed by the scattering geometry. The scattering tensor can then be contructed and compared to those in Table 3.2 to obtain its symmetry. Since the symmetry of the ground state (which is the initial state in most cases) is usually well known from the crystal field fit, the symmetry of the final state can be deduced from the scattering tensor. The crystal field fit predicts the symmetry of a state along with its energy value so that it is possible to see whether the assignment of the Raman peak agrees with the crystal field fit, when the latter is available. The symmetry properties of the phonon peaks and of the fluorescent transitions are different than those of the electronic Raman transitions.

4.2 Experimental Raman Spectra of Tm^{3+} in Tetragonal Phosphate Hosts

4.2.1 Tm^{3+} - Selection Rules

Tm^{3+} has the open shell configuration $4f^{12}$. This configuration can be decribed as consisting of two holes in the f shell and as such is formally equivalent to the f^2 system Pr^{3+}. Tm^{3+} has an even number of electrons so that the electronic states are labeled by the irreducible representations Γ_1, Γ_2, Γ_3, Γ_4, and Γ_5 of D_{2d}. The optical absorption spectrum and crystal field fit of Tm^{3+} doped at low concentrations ($\sim$ 1%) in $LuPO_4$ and YPO_4 has been described by Becker *et al* [1]. The crystal field fit and energy level structure of Tm^{3+} in $LuPO_4$ is summarized in appendix A, section A2.

The ground multiplet of Tm^{3+} is $^3H_6$. Electronic Raman transitions were observed between the crystal field states of the ground multiplet and also between the ground state and the crystal field states of the first excited multiplet $^3F_4$, situated roughly 5,700 cm^{-1} above the ground state. The decomposition of the ground multiplet into irreducible representations is given by $2\Gamma_1 + \Gamma_2 + 2\Gamma_3 + 2\Gamma_4 + 3\Gamma_5$. The $^3F_4$ multiplet splits up into the states $2\Gamma_1 + \Gamma_2 + \Gamma_3 + \Gamma_4 + 2\Gamma_5$. The ground crystal field state has the symmetry Γ_1. We can calculate the selection rules for Raman transitions from the Γ_1 ground state to the other states by taking the direct product of Γ_1 with the irreducible representation of the final state. The case of $TmPO_4$ is particularly simple as Γ_1 is the identity representation and so $\Gamma_1 \otimes \Gamma_i = \Gamma_i$. We summarize the selection rules for the Raman transitions originating in the ground state:

transition	scattering tensor symmetry
$\Gamma_1 \longleftrightarrow \Gamma_1$	Γ_1
$\Gamma_1 \longleftrightarrow \Gamma_2$	Γ_2
$\Gamma_1 \longleftrightarrow \Gamma_3$	Γ_3
$\Gamma_1 \longleftrightarrow \Gamma_4$	Γ_4
$\Gamma_1 \longleftrightarrow \Gamma_5$	Γ_5

The scattering tensors are listed in Table 3.2.

The 3-J symbol of equation (3.64) implies that J, J', and t (where t is the rank of the spherical Raman tensor discussed in section 3.3.6) must satisfy the triangle rule for angular momenta. Since $J = J'$ for transitions between the crystal field states of the ground multiplet, both $\alpha^{(1)}$ and $\alpha^{(2)}$ can contribute to the Raman amplitude of these transitions. Thus, asymmetric transitions with the ground state as the initial state can occur for Γ_5 final states belonging to the ground multiplet. For the excited multiplet $^3F_4$ we have $J' - J = 2$ so that only the Raman tensor $\alpha^{(2)}$ will contribute to the scattering intensity for transitions from the ground state to the $^3F_4$ multiplet. As a result the Raman transitions between the ground state and the $^3F_4$ excited multiplet are fully symmetric with respect to interchange of the polarizations of the incident and scattered photons. This is confirmed by the experimental spectra.

4.2.2 Tm^{3+} - Experimental Raman Spectra

The low temperature experimental Raman spectrum of $TmPO_4$ has been published previously by Guha [2] and Becker *et al* [3]. The results presented here are a more detailed exposition of the work reported in the latter reference. The polarized spectra obtained for $TmPO_4$ at ~4.2 K in the low wavenumber region 0-300 cm^{-1} are shown in Figure 4.1. Four electronic Raman transitions are observed at 30, 86, 138, and 280 cm^{-1}. The polarized spectra at ~4.2 K for transitions to the $^3F_4$ multiplet are shown in Figure 4.2. Electronic Raman transitions are observed at 5602, 5676, 5688, and 5870 cm^{-1}. In both Figures 4.1 and 4.2 the excitation was with the 514.5 nm line of the argon-ion laser, with an average power of about 30 mW at the sample. Raman spectra taken at ~4.2 K with excitation at 488.0, 476.5, and 457.9 nm for the $^3H_6$ transitions, and at 488.0 nm for the $^3F_4$ transitions, were identical to those shown in Figures 4.1 and 4.2.

The (XY) transition at 86 cm^{-1} is the strongest electronic Raman transition observed in this work. It has a scattering intensity comparable to that of the phonons in the 1000 cm^{-1} region. Note that in Figure 4.1 the scale of the Y(XY)X spectrum is ten times stronger than that for Y(XZ)X and Y(ZY)X. Three Γ_5 transitions are observed. The weakest one at 30 cm^{-1} shows some asymmetry, whereas the two transitions at 138 and 280 cm^{-1} appear to be symmetric within experimental error. The transition at 138 cm^{-1} is very close to phonon E_g^1 but is clearly resolved. Closing down the spectrometer slits separates the two peaks better and allows a more accurate measurement of the intensity and linewidth of the 138 cm^{-1} transition. The Y(ZZ)X spectra shows no peaks except for slight leakage of the E_g phonons and so is not included in Figure 4.1.

Spectra were also taken in other scattering geometries than those used for Figures 4.1 and 4.2. However, they have a much higher scattered light background and polarization leakage since for those geometries the incident and scattered light does not pass through smooth crystal faces. The relative intensities of the electronic transitions are nevertheless the same as those in Figure 4.1. The other scattering geometries in which spectra were obtained for the $^3H_6$ multiplet are X(YX)Y, X(ZX)Y, X(YZ)Y, X(ZZ)Y, Z(YZ)Y, Z(XZ)Y, Z(XX)Y, and Z(YX)Y.

The identification of the electronic transitions to the 5,500 cm^{-1} region $^3F_4$ states is complicated by the presence of plasma lines from the argon-ion laser, which are outside the operative range of the spike filter. The plasma lines seen in Figure 4.2 are labeled p. The

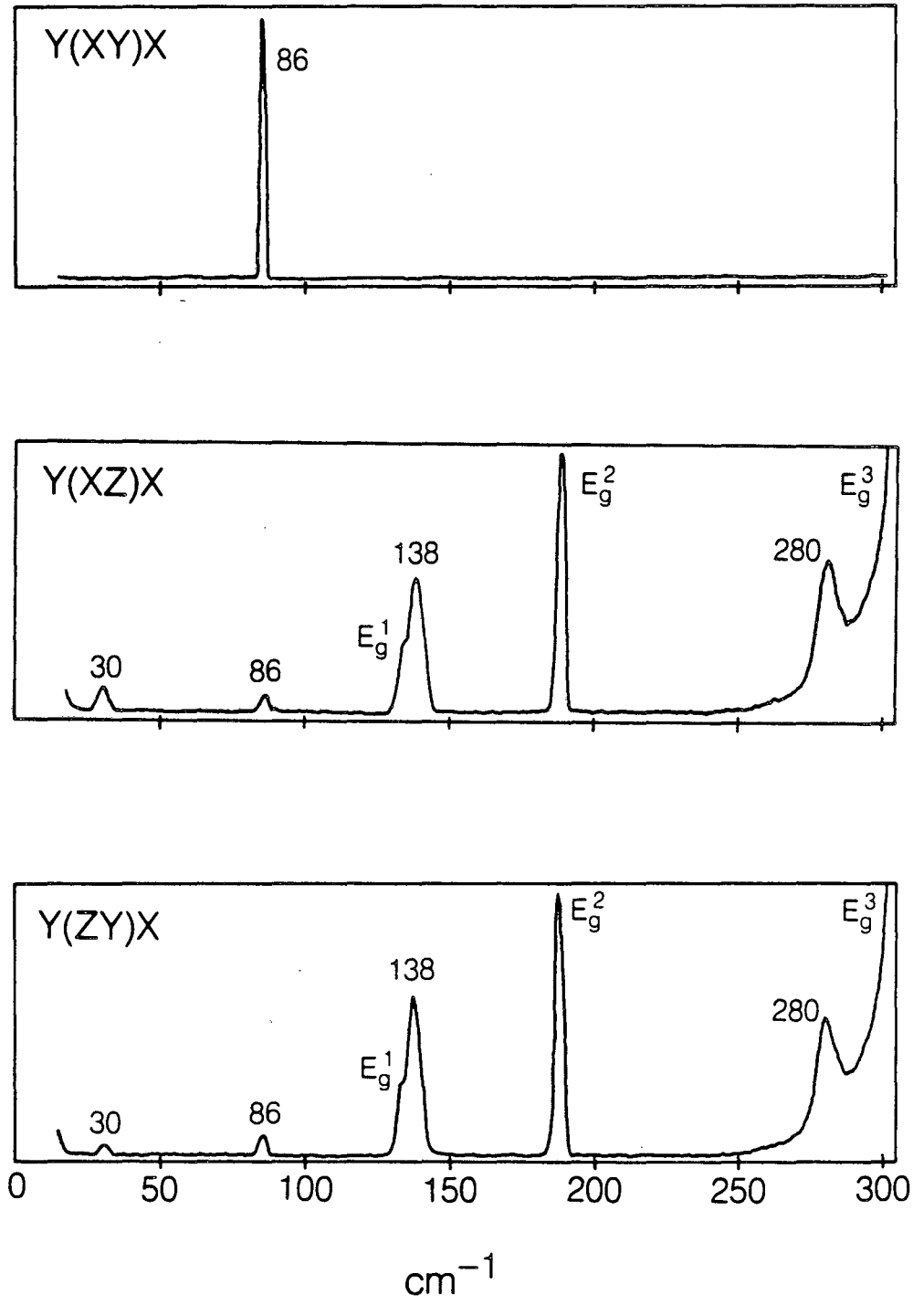

Figure 4.1: $TmPO_4$ polarized Raman spectra at ~4.2 K in the 0-300 cm^{-1} region. The full scale is 25,000 counts per second for the Y(XY)X spectrum, and 2,500 cps for the Y(XZ)X and Y(ZY)X spectra. The spectrometer bandpass is 2.5 cm^{-1}.

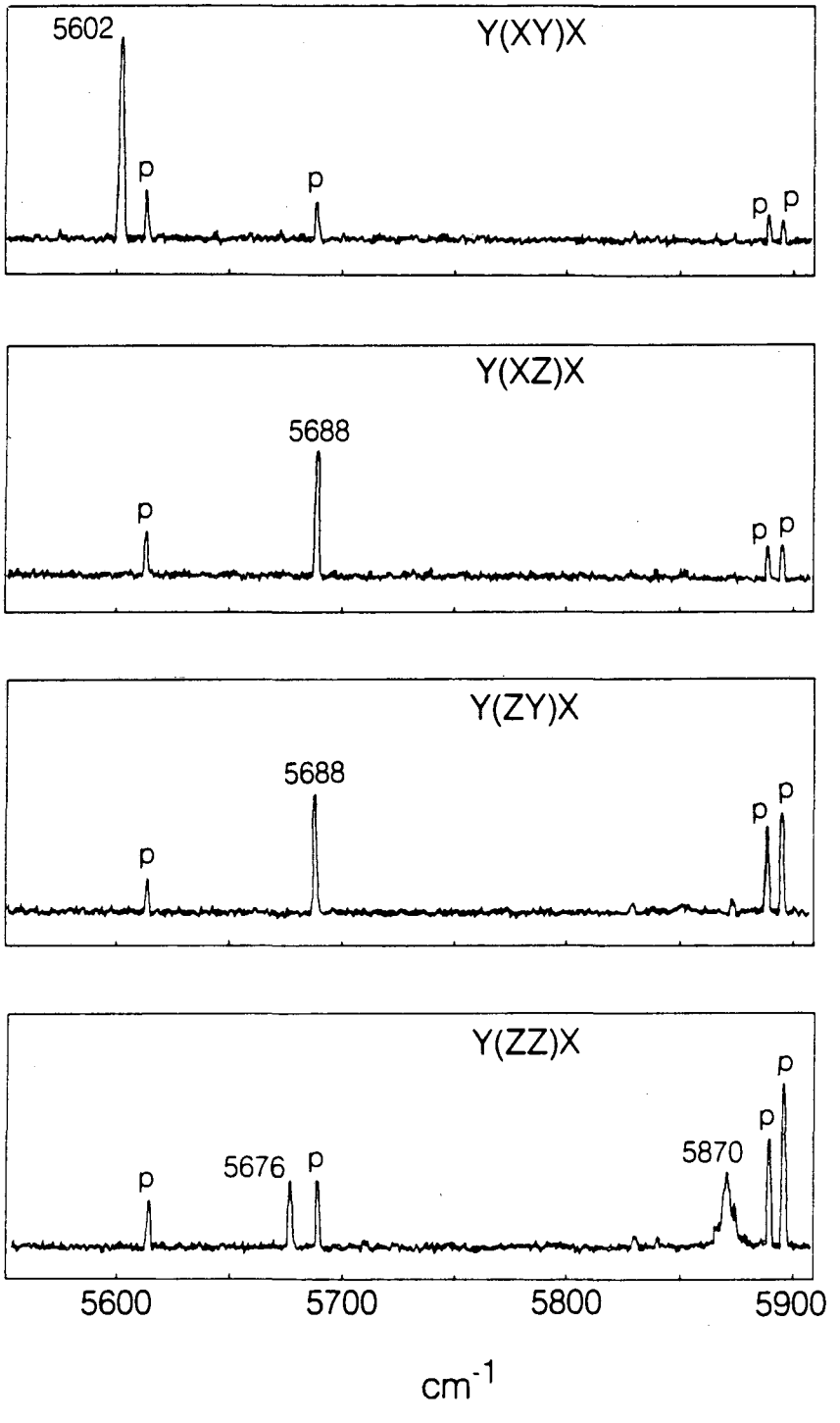

Figure 4.2: $TmPO_4$ polarized Raman spectra at ~4.2 K in the 5,550-5,900 cm^{-1} region. The full scale is 1,000 counts per second in all polarizations. The spectrometer bandpass is 2.5 cm^{-1}.

Table 4.1: Energy level values for the Tm^{3+} $^3H_6$ multiplet.

	Energy (cm^{-1})		
Symmetry	Optical Absorption 1% Tm^{3+} in $LuPO_4$	Crystal field fit 1% Tm^{3+} in $LuPO_4$	Electronic Raman $TmPO_4$
Γ_1	0	0	0
Γ_5	25	22	30
Γ_3	80	90	86
Γ_5	125	132	138
Γ_2	a	183	a
Γ_1	a	248	a
Γ_4	a	254	a
Γ_5	a	281	280
Γ_3	a	303	a
Γ_4	a	321	a

a: not observed.

electronic transition at 5688 cm^{-1} is very close to a plasma line, however, its identification is rendered unambiguous by using excitation at 488.0 nm, for which there is no near-lying plasma line.

Table 4.1 summarizes the electronic energy level structure of the $^3H_6$ multiplet and lists the energy values from the optical absorption measurements and crystal field fits for 1% Tm^{3+} in $LuPO_4$ [1], and the values obtained for $TmPO_4$ from the electronic Raman spectra. For the $^3H_6$ multiplet, the optical absorption measurements are based upon excited state absorption spectra taken at 77 K, so that if there are any shifts in energy between 4.2 and 77 K, they will be reflected by the optical absorption values quoted in Table 4.1. Table 4.2 summarizes the electronic energy level structure and measurements for the $^3F_4$ multiplet. The experimental error on the electronic Raman energy values is ± 1 cm^{-1}.

The electronic Raman values of Table 4.1 agree with those reported by Guha, the only difference being that he erroneously identified the line at 86 cm^{-1} as being of symmetry Γ_4, due to neglect of the 45° rotation of the D_{2d} symmetry axes relative to the crystallographic axes (described in section 3.1.3).

Table 4.2: Energy level values for the Tm^{3+} $^3F_4$ multiplet.

	Energy (cm^{-1})		
Symmetry	Optical Absorption 1% Tm^{3+} in $LuPO_4$	Crystal field fit 1% Tm^{3+} in $LuPO_4$	Electronic Raman $TmPO_4$
Γ_3	a	5587	5602
Γ_5	5674	5682	5688
Γ_1	a	5700	5676
Γ_2	a	5735	a
Γ_4	5763	5769	a
Γ_5	5842	5844	a
Γ_1	a	5857	5870

a: not observed.

Raman spectra were also taken for the crystals 20% Tm^{3+} in $LuPO_4$, 10% Tm^{3+} in $LuPO_4$ and YPO_4, and 2% Tm^{3+} in $LuPO_4$ and YPO_4. The peaks are much weaker in intensity for the diluted crystals. The strong Γ_3 line in the 80 cm^{-1} region is clearly observed in all the diluted crystals. Figure 4.3 shows the Raman spectra of 20% Tm^{3+} in $LuPO_4$ at ~4.2 K with excitation at 514.5 nm, with an average power of 30 mW at the sample. The Γ_3 transition at 82 cm^{-1} is very strong but broader than in the 100% crystal. The Γ_5 line at 286 cm^{-1} is still visible but that at 138 cm^{-1} is no longer present and is possibly obscured by phonon E_g^1. The B_g^1 phonon peak is leakage from the (XX) and (YY) polarizations. Phonon E_g^1 is not perfectly symmetric, probably because of internal crystal strains (see section 3.2.2).

Table 4.3 summarizes the line positions observed for the electronic Raman transitions from the ground state to the levels of the $^3H_6$ multiplet for the various concentration crystals. The linewidth has been indicated in parenthesis for those transitions for which it is measurable to a reasonable degree of accuracy. The linewidth given is the full width at half maximum and has an uncertainty of ± 1 cm^{-1}. Since the ground state has by definition zero linewidth, the linewidth of the electronic Raman transitions that originate in the initial state is the linewidth of the level which is the final state. The 280 cm^{-1} region transition is quite broad and for the diluted crystals it is difficult to accurately pinpoint the center of

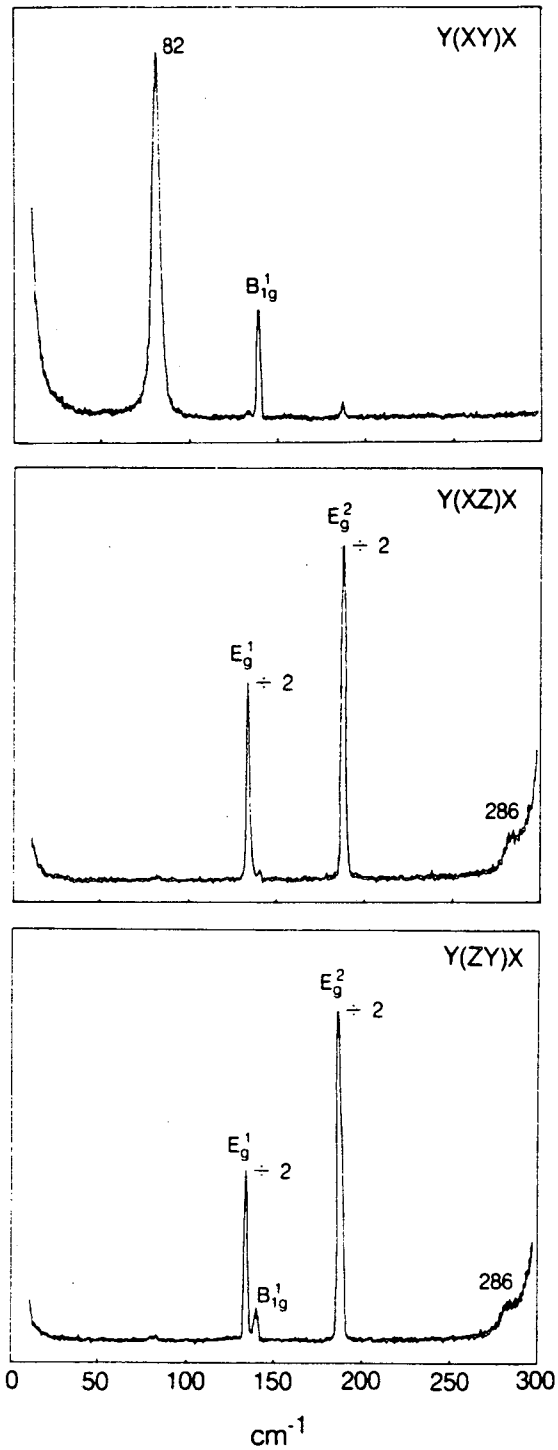

Figure 4.3: 20% Tm^{3+} in $LuPO_4$ Raman spectra at ~4.2 K in the 0-300 cm^{-1} region. The full scale is 1,000 counts per second in all polarizations and the E_g^1 and E_g^2 phonon peaks have been reduced in intensity by a factor of two. The spectrometer bandpass is 2.5 cm^{-1}.

this transition.

Table 4.3: Frequencies and linewidths γ (in parenthesis, when measurable) of the $^3H_6$ crystal field levels observed via electronic Raman scattering in Tm^{3+} doped phosphate crystals, in cm^{-1}.

	Γ_5	Γ_3	Γ_5	Γ_5
$TmPO_4$	30 ($\gamma = 3$)	86 ($\gamma = 3$)	138 ($\gamma = 6$)	280 ($\gamma = 8$)
20% Tm^{3+}:$LuPO_4$	a	82 ($\gamma = 5$)	a	286
10% Tm^{3+}:$LuPO_4$	a	81 ($\gamma = 6$)	a	286
2% Tm^{3+}:$LuPO_4$	a	82 ($\gamma = 5$)	a	a
10% Tm^{3+}:YPO_4	a	77 ($\gamma = 6$)	a	281
2% Tm^{3+}:YPO_4	a	76 ($\gamma = 6$)	a	a

a: not observed.

The Γ_3 line in the 80 cm^{-1} region has a Gaussian profile at T≃4.2 K for the 100, 20, and 10% Tm^{3+} crystals, where its linewidth is mostly inhomogeneous. In the 2% crystals the line appears to be homogeneously broadened, with a Lorentzian profile. The inhomogeneous linewidth of an electronic line comes from variations in the crystal field from site to site. These have their origin either in configurational disorder, as is the case for the mixed crystals, or from strains and defects. Crystals with roughly the same amount of Tm^{3+} and Lu^{3+} should show the greatest amount of disorder induced inhomogeneous broadening of the electronic levels, since it is for these crystals that the environment of Tm^{3+} can vary the most. The very concentrated or very dilute crystals should show the least amount of disorder induced inhomogeneous broadening. The 10% and 20% crystals indeed show large linewidths for the Γ_3 (80 cm^{-1}) transition, however, those of the 2% crystals are also observed to be quite large, albeit with a homogeneous line profile. The linewidth of the transition at 280 cm^{-1} is clearly mostly homogeneous, as its lineshape is Lorentzian in character. It has a large homogeneous linewidth since it can decay via the emission of phonons to the various crystal field states that lie below it in energy, thereby reducing its lifetime. For a discussion of line broadening mechanisms, see Hüfner [4, chapter 4].

Spectra taken at higher temperatures show that the electronic Raman peaks broaden significantly with temperature, and also that they shift slightly in energy. Figure 4.4 shows

the 77 K spectra for $TmPO_4$ in the 0-300 cm^{-1} region, taken with excitation at 514.5 nm. The Γ_3 peak is now at 82 cm^{-1}. The transition at 138 cm^{-1}, which at T≃4.2 K is noticeably stronger than phonon E_g^1, is now a weak shoulder. A broad peak centered at 108 cm^{-1} is observed in the (XY) and (ZZ) polarizations. It represents the transition $\Gamma_5(30\ cm^{-1}) \longrightarrow \Gamma_5(138\ cm^{-1})$. The polarization selection rules are satisfied for this transition as $\Gamma_5 \otimes \Gamma_5 = \Gamma_1 + \Gamma_2 + \Gamma_3 + \Gamma_4$. This peak appears only at higher temperatures since the 30 cm^{-1} state needs to be thermally populated for the transition to take place. The B_g^1 phonon, which has a frequency nearly identical to the electronic transition at 138 cm^{-1}, leaks through in the ZY polarization a little bit more than in the XZ polarization. Since at T=77 K the electronic transition is broad and weak, the phonon leakage is clearly superimposed upon it, giving rise to a a sharper peak in ZY polarization. At 4.2 K the 138 cm^{-1} electronic transition is strong and sharp enough that the phonon leakage is a negligible perturbation on its lineshape. The insets in Figure 4.4 show the 138 and 280 cm^{-1} transitions at T=35 K.

The strength of the $TmPO_4$ Raman transition at 86 cm^{-1} allows a detailed study of the temperature dependence of its frequency and linewidth. Figure 4.5 shows the lineshape of this transition at selected temperatures between ~4.2 and 295 K. The intensity of the transition decreases with temperature as the the ground state, which is the initial state, depopulates and the excited crystal field states become populated. Even at room temperature, a faint trace of the signal is still visible as a broad bump. Figure 4.6 displays the linewidth of this transition, measured as the full width at half maximum, as a function of temperature. Figure 4.7 graphs the position of this line as a function of temperature for both $TmPO_4$ and 20% Tm^{3+} in $LuPO_4$. The vertical bars represent the experimental uncertainties on the frequencies and linewidths. It is interesting to note that while for $TmPO_4$ there is a marked decrease in the frequency of the line no such effect occurs for the diluted crystal, at least up to 140 K. Since the temperature dependence of both linewidths and energy position shifts of lanthanide electronic states in crystals depend on the specifics of the electron-phonon coupling mechanisms, this indicates that the coupling is perhaps different for the concentrated and diluted crystals.

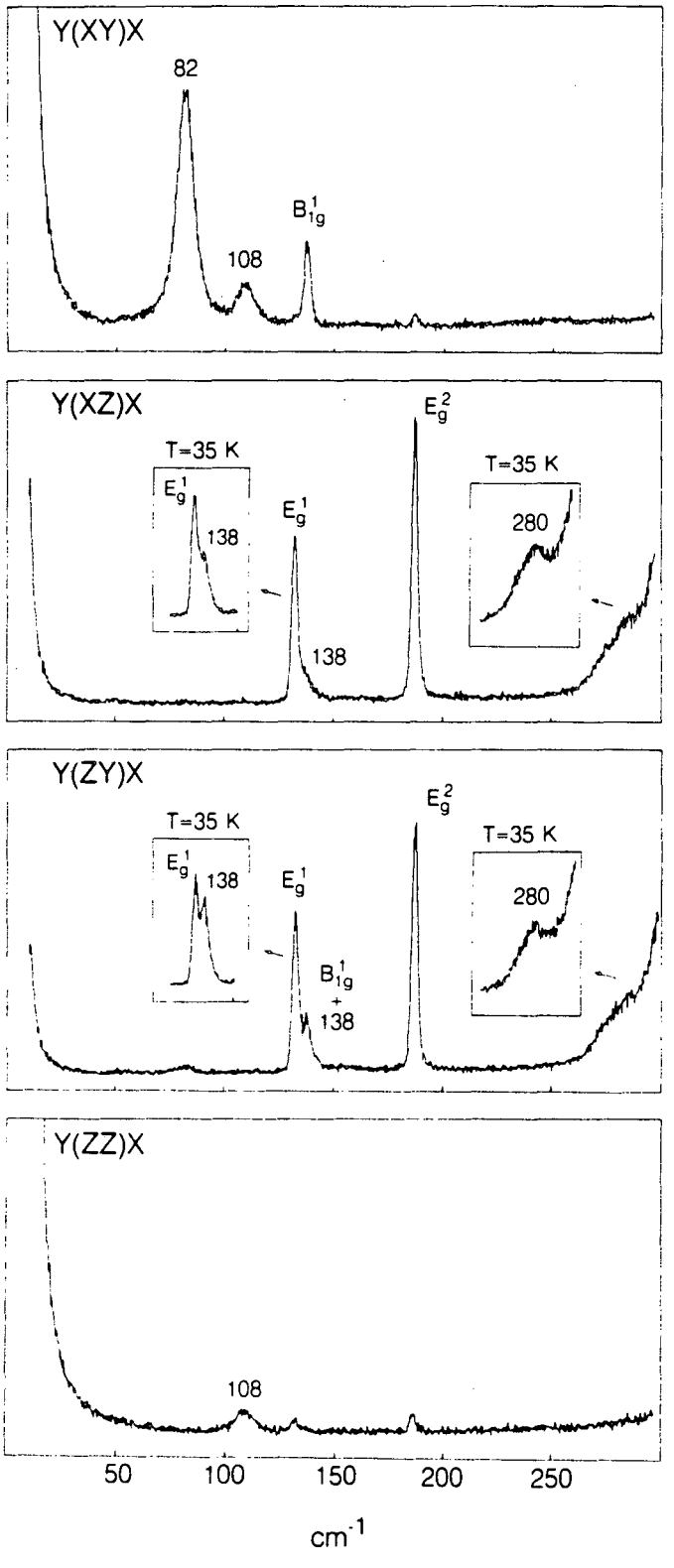

Figure 4.4: $TmPO_4$ polarized Raman spectra at 77 K in the 0-300 cm^{-1} region. The full scale is 1,000 counts per second in all polarizations. The full scale on the 35 K insets is 500 cps. The spectrometer bandpass is 2.5 cm^{-1}.

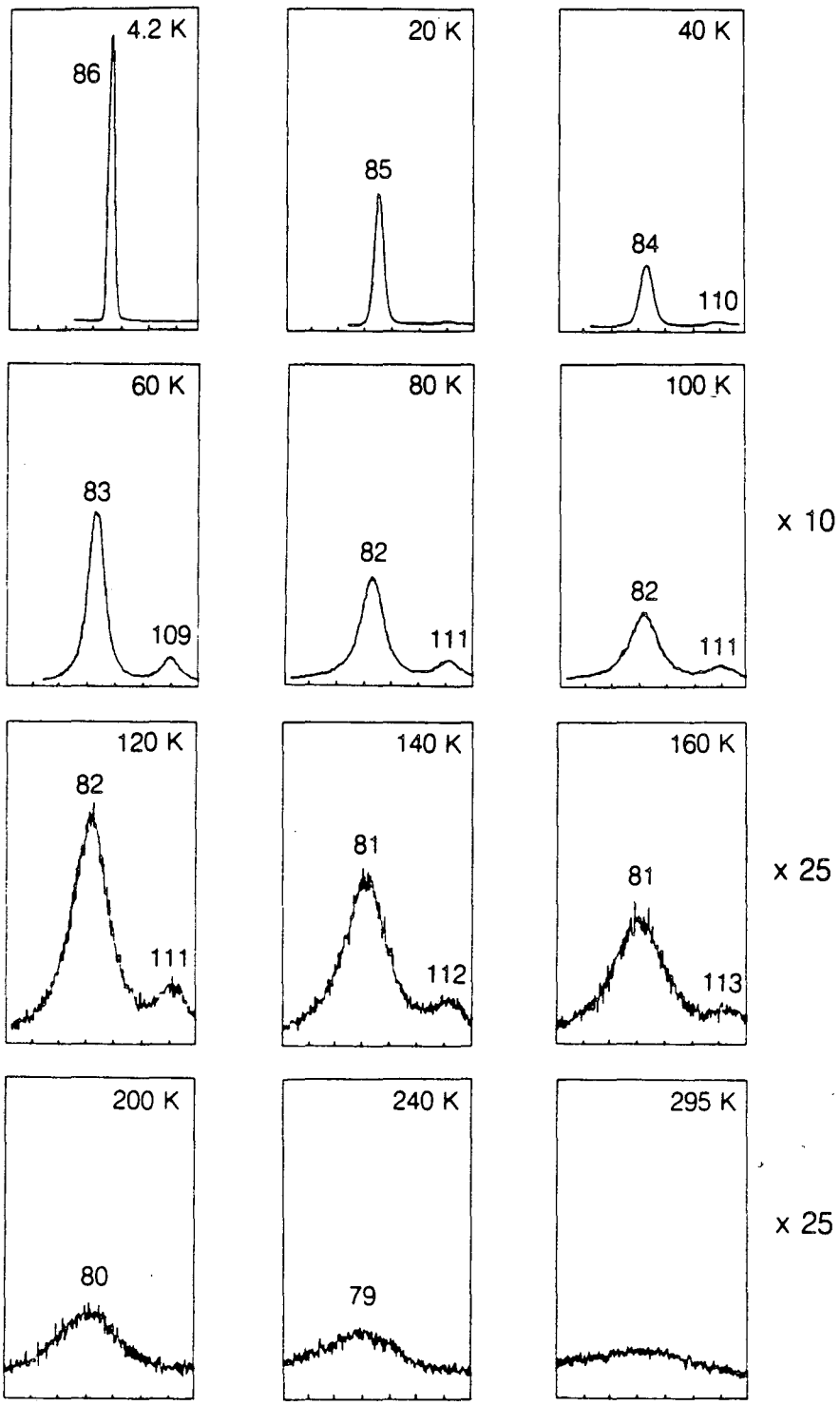

Figure 4.5: Evolution of the $TmPO_4$ 86 cm^{-1} electronic Raman transition as a function of temperature (scattering geometry Y(XY)X). The full scale is 25,000 counts per second for the top row, 2,500 cps for the second row, and 1,000 cps for the two bottom rows. The spectrometer bandpass is 2.5 cm^{-1}. The temperatures are indicated in the upper right hand corners.

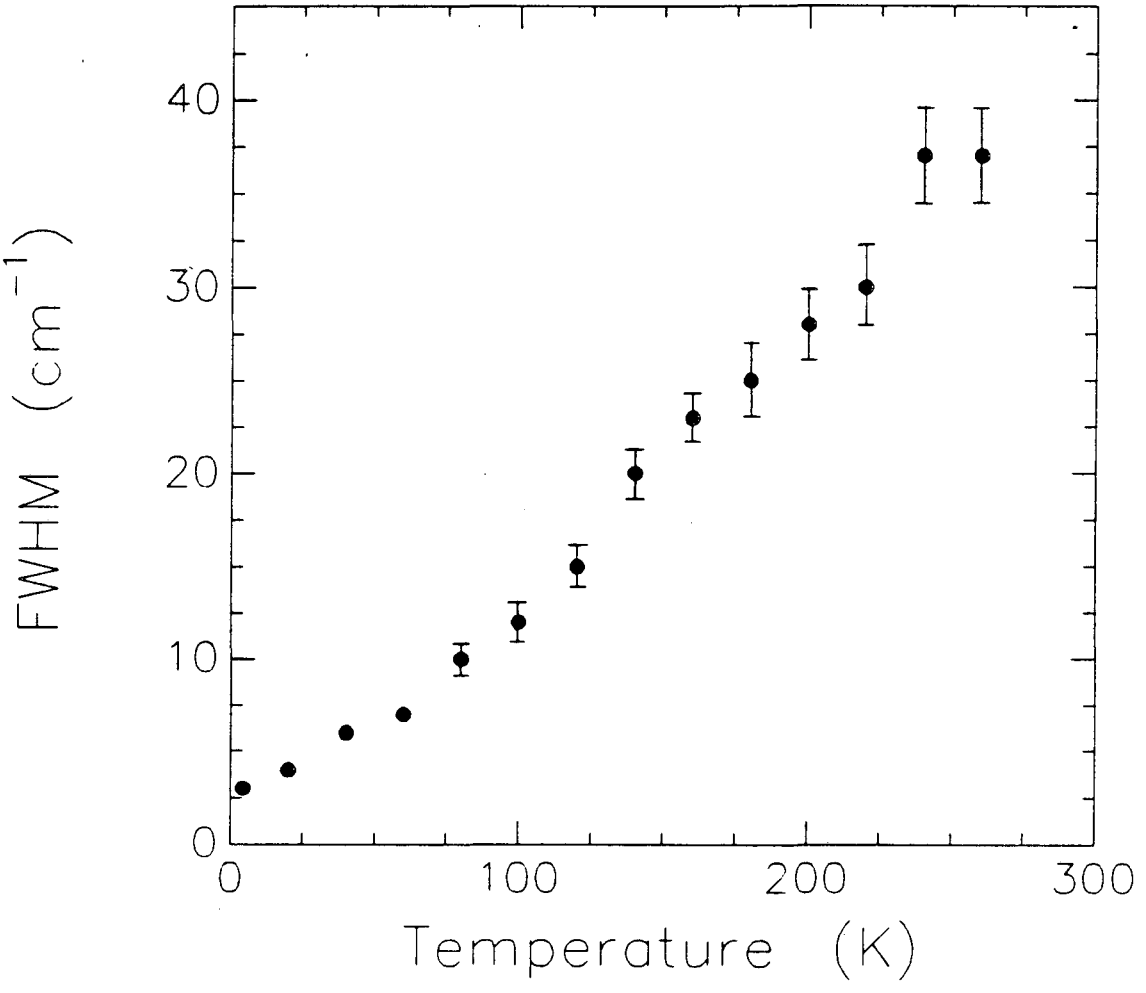

Figure 4.6: Linewidth (in cm^{-1}) of the $TmPO_4$ 86 cm^{-1} region electronic Raman transition as a function of temperature.

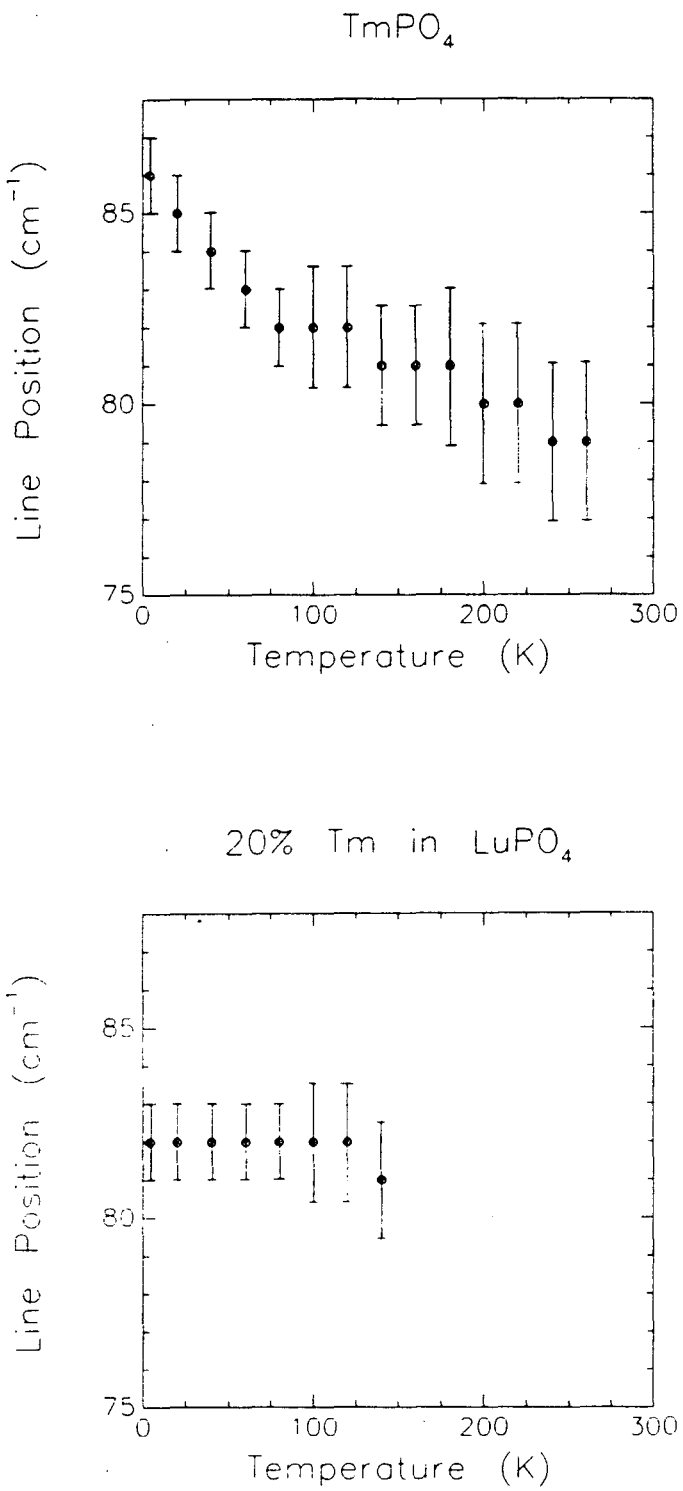

Figure 4.7: Frequency (in cm^{-1}) of the Γ_3 80 cm^{-1} region electronic Raman transition as a function of temperature for $TmPO_4$ and 20% Tm^{3+} in $LuPO_4$.

4.3 Experimental Raman Spectra of Er^{3+} in Tetragonal Phosphate Hosts

4.3.1 Er^{3+} - Selection Rules

Er^{3+} has the open shell configuration $4f^{11}$ which is formally equivalent to the f^3 system Nd^{3+}. Er^{3+} has an odd number of electrons so that the electronic states are labeled by the irreducible representations Γ_6 and Γ_7. All the Er^{3+} electronic levels are thus doubly degenerate Kramer's states. The optical absorption spectrum and crystal field fit of Er^{3+} doped at low concentrations ($\sim$ 1%) in $LuPO_4$ have been reported by Hayhurst *et al* [5], and that of Er^{3+} in YPO_4 by Kuze [6]. The crystal field fit and energy level structure of Er^{3+} in $LuPO_4$ have been summarized in appendix A, section A3.

The ground multiplet of Er^{3+} is $^4I_{15/2}$. Electronic Raman transitions were observed between the ground state and the excited crystal field states of the ground multiplet. The next highest multiplet is $^4I_{13/2}$ at roughly 6,500 cm^{-1} above the ground state. Electronic Raman transitions to the $^4I_{13/2}$ multiplet were searched for but were not observed (with nonresonant excitation). The decomposition of the ground multiplet into irreducible representations is given by $4\Gamma_6 + 4\Gamma_7$. The ground crystal field state has the symmetry Γ_7. We can calculate the selection rules for Raman transitions from the Γ_7 ground state to the other states by taking the direct product of Γ_7 with the irreducible representation of the final state. We obtain the following symmetries for the allowed scattering tensors:

transition	scattering tensor symmetry
$\Gamma_7 \longleftrightarrow \Gamma_6$	$\Gamma_3 + \Gamma_4 + \Gamma_5$
$\Gamma_7 \longleftrightarrow \Gamma_7$	$\Gamma_1 + \Gamma_2 + \Gamma_5$

The electronic scattering tensors for each symmetry have been listed in Table 3.2. The only real selection rule that arises is that $\Gamma_7 \longleftrightarrow \Gamma_7$ transitions are not allowed in (ZZ) polarization. All the transitions will appear in the Γ_5 symmetry scattering geometries and can exhibit asymmetry with respect to interchange of the polarizations of the incident and scattered photons.

4.3.2 Er^{3+} - Experimental Raman Spectra

The low temperature experimental Raman spectrum of $ErPO_4$ has been published previously by Becker *et al* [3]. The spectra obtained for $ErPO_4$ at ~4.2 K in the 0-300 cm^{-1} region are shown in Figure 4.8. Four electronic Raman transitions are observed at 33, 53, 105, and 145 cm^{-1}. The excitation is with the 514.5 nm line of the argon-ion laser, with an average power of 40 mW at the sample. Raman spectra taken with excitation at 476.5 and 457.9 nm are identical to those shown in Figure 4.8. Excitation with the line at 488.0 nm results in strongly enhanced resonant spectra. The resonance scattering results are discussed in detail in chapter 5. The two transitions at 33 and 53 cm^{-1} show very large amounts of asymmetry when the (XZ) and (ZY) spectra are compared (X and Y are equivalent so that XZ≡YZ and ZX≡ZY). The 33 cm^{-1} transition is much stronger in (XZ) than in (ZY), whereas the 53 cm^{-1} transition is much stronger in (ZY) than in (XZ). The transition at 145 cm^{-1} is also asymmetric but it is very weak so that the experimental uncertainty renders the measurement of its asymmetry inaccurate. The strongest transition observed in the $ErPO_4$ spectra is the 33 cm^{-1} transition in (XY) polarization. Nevertheless, it is ten times weaker than the (XY) 86 cm^{-1} transition in $TmPO_4$. In the 250-300 cm^{-1} region there are some broad and weak features that might be electronic Raman transitions from the ground state to the three highest states of the ground multiplet. The extra peak at 284 cm^{-1} is not a Raman peak and is probably due to fluorescence, perhaps of an impurity. It is present in all the erbium doped samples (with excitation at 514.5 nm). Table 4.4 summarizes the electronic energy level structure of the $^4I_{15/2}$ multiplet and lists the energy values from the optical absorption measurements and crystal field fits for 1% Er^{3+} in $LuPO_4$ [5], and the values obtained for $ErPO_4$ from the electronic Raman spectra. The experimental uncertainty of the electronic Raman frequencies is ±1 cm^{-1}.

At higher temperatures excitation at 514.5 nm produces fluorescence from the $ErPO_4$ sample. This fluorescence obscures the real Raman signals. The temperature dependence of the electronic Raman peaks can, however, be tracked up to room temperature with excitation at 476.5 and 457.9 nm. Figure 4.9 shows the Y(XZ)X spectrum in the 0-150 cm^{-1} region at various temperatures between 4.2 and 295 K and the behaviour of the electronic transitions at 33 and 53 cm^{-1}, with excitation at 476.5 nm. The temperature broadening of the electronic lines in the temperature range 0-80 K appears to be significantly less rapid than for $TmPO_4$. The line positions do not appear to shift with temperature. At

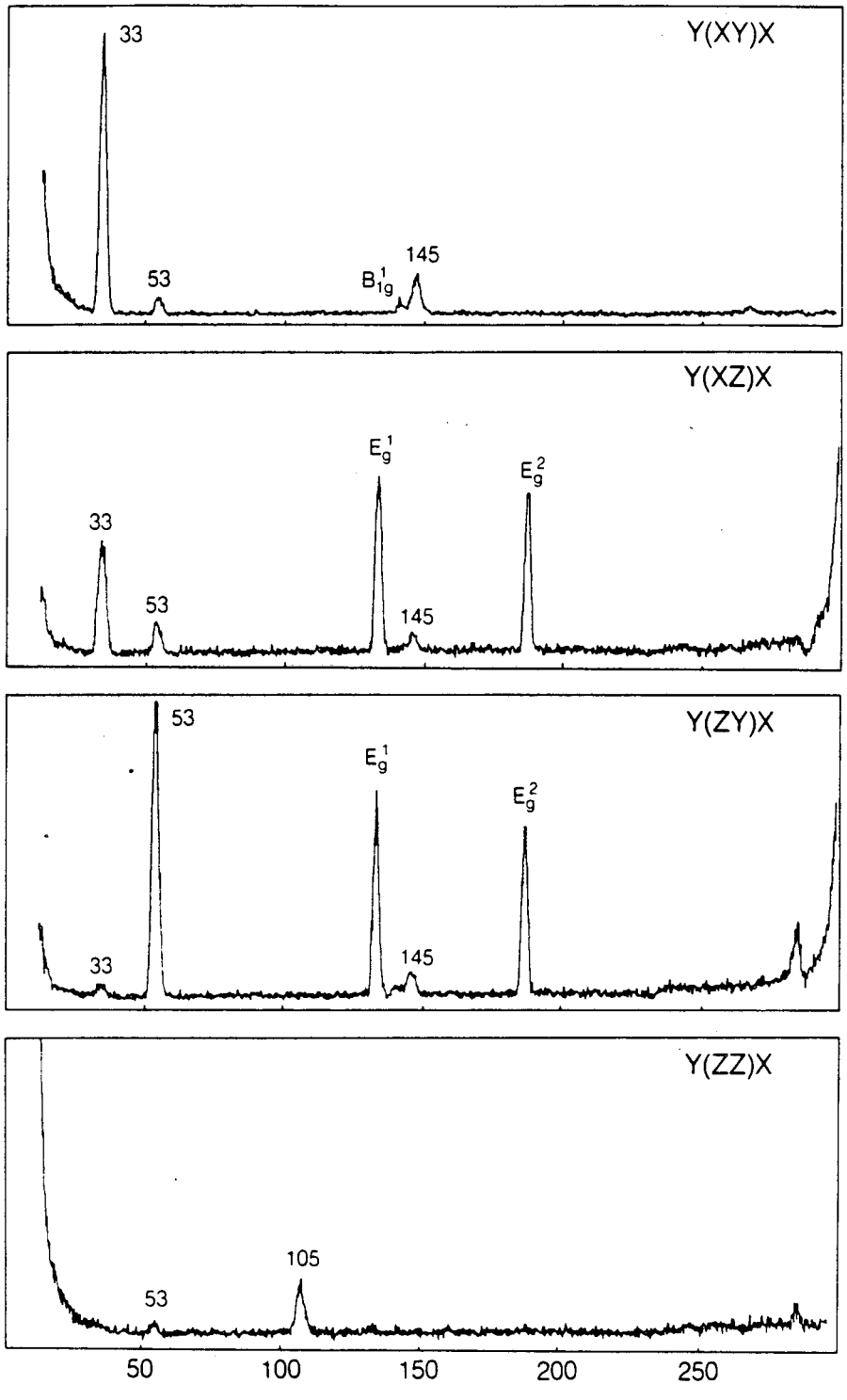

Figure 4.8: $ErPO_4$ polarized Raman spectra at ~4.2 K in the 0-300 cm^{-1} wavenumber region. The full scale is 1,000 counts per second for the Y(XY)X polarization, and 500 cps for the other polarizations. The spectrometer bandpass is 2.5 cm^{-1}.

Table 4.4: Energy level values for the Er^{3+} $^4I_{15/2}$ multiplet.

	Energy (cm^{-1})		
Symmetry	Optical Absorption 1% Er^{3+} in $LuPO_4$	Crystal field fit 1% Er^{3+} in $LuPO_4$	Electronic Raman $ErPO_4$
Γ_7	0	0	0
Γ_6	36	36	33
Γ_7	53	50	53
Γ_7	98	101	105
Γ_6	a	133	145
Γ_6	a	230	a
Γ_7	a	247	a
Γ_6	a	287	a

a: not observed.

higher temperatures, a weak peak appears at 20 cm^{-1} in the Y(XY)X spectrum which is the excited state transition 33 cm^{-1} $\longrightarrow$ 53 cm^{-1}.

Raman spectra were also taken of erbium diluted at concentrations of 50, 20, 10, and 1% in $LuPO_4$, and 10% and 1% in YPO_4. The frequencies and linewidths of the electronic Raman transitions from the ground state to the crystal field states of the $^4I_{15/2}$ multiplet are given in Table 4.5. The 1% crystals are not included as the electronic Raman peaks are too weak to be clearly identified. The experimental uncertainty on the linewidths is ± 1 cm^{-1}.

4.3.3 Er^{3+} - Anti-Stokes Raman Spectra

Up to now we have been discussing Stokes Raman transitions, for which the scattered photon has a lower energy than the incident photon. In an anti-Stokes Raman transition, the scattered photon has a *higher* energy than the incident photon. This is due to the fact that the transition originates in an excited state and terminates in a state lower in energy than the initial state, usually the ground state. This is shown pictorially in Figure 4.10.

The anti-Stokes transitions can be observed only at higher temperatures since the excited crystal field states need to be thermally populated for the process to occur. The anti-Stokes

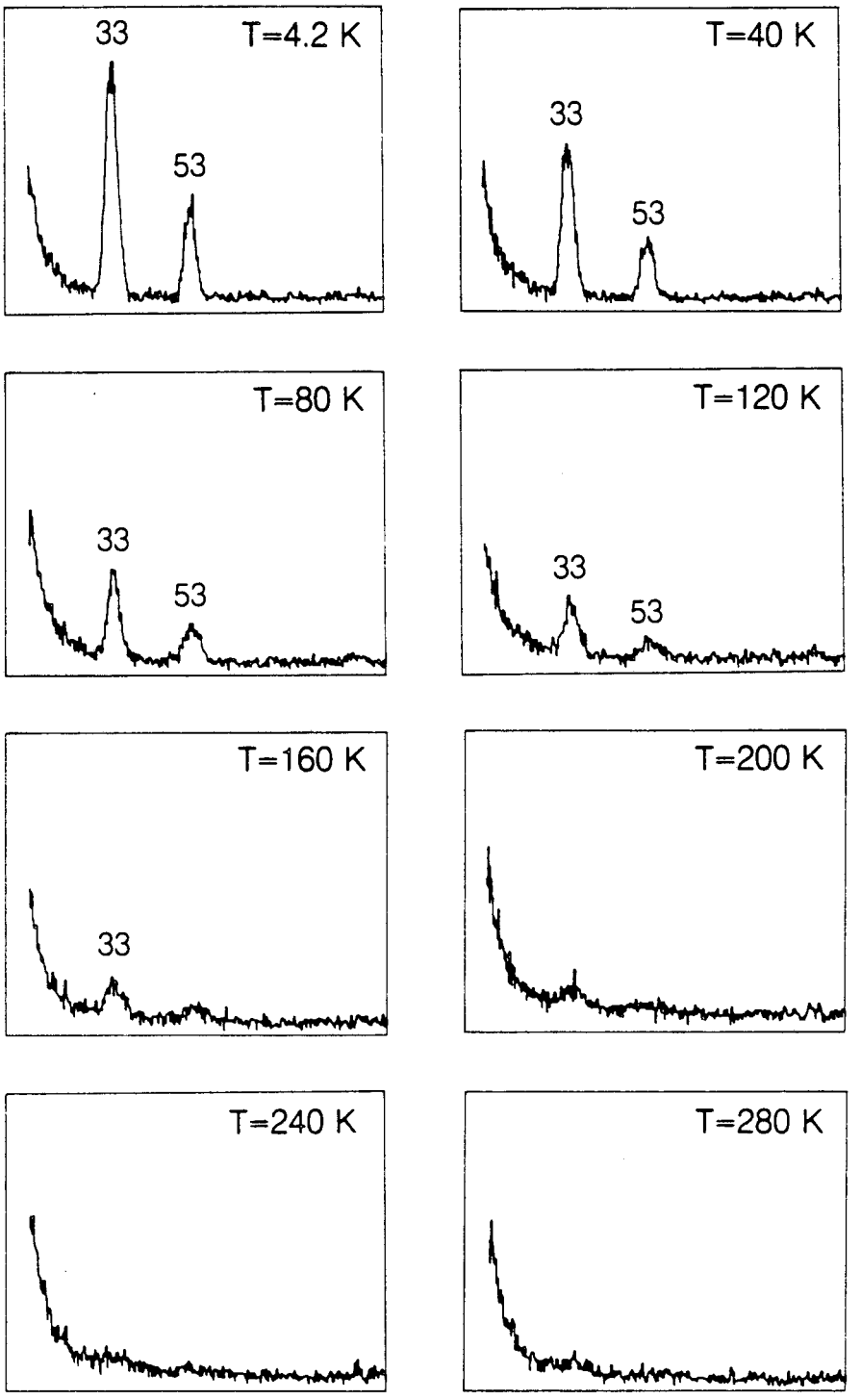

Figure 4.9: Temperature evolution of the electronic Raman lines of Er^{3+} in $ErPO_4$ in the 0-150 cm^{-1} range, with excitation at 476.5 nm. The scattering geometry is Y(XZ)X and the full scale is 250 counts per second.

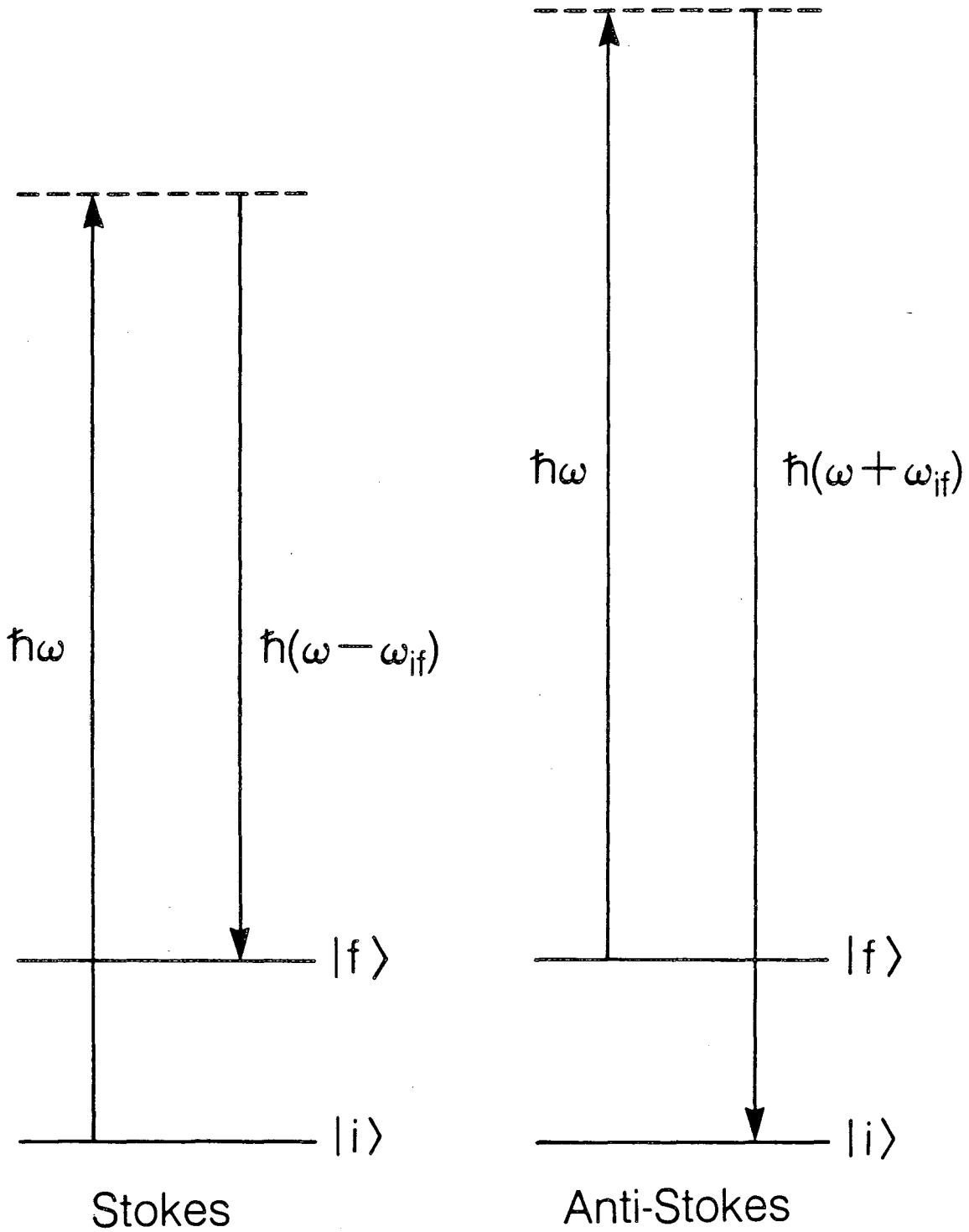

Figure 4.10: Stokes and anti-Stokes Raman transitions between two states $|i\rangle$ and $|f\rangle$.

Table 4.5: Frequencies and linewidths γ (in parenthesis, when measurable) of the $^4I_{15/2}$ multiplet crystal field levels observed via electronic Raman scattering in Er^{3+} doped phosphate crystals, in cm^{-1}.

	Γ_6	Γ_7	Γ_7	Γ_6
$ErPO_4$	33 ($\gamma = 2$)	53 ($\gamma = 2$)	105 ($\gamma = 3$)	145 ($\gamma = 3$)
50% Er^{3+}:$LuPO_4$	33 ($\gamma = 3$)	52 ($\gamma = 3$)	100 ($\gamma = 6$)	148 ($\gamma = 6$)
20% Er^{3+}:$LuPO_4$	36 ($\gamma = 3$)	54 ($\gamma = 3$)	100 ($\gamma = 5$)	152 ($\gamma = 5$)
10% Er^{3+}:$LuPO_4$	36 ($\gamma = 3$)	53 ($\gamma = 3$)	99 ($\gamma = 4$)	152 ($\gamma = 5$)
10% Er^{3+}:YPO_4	33 ($\gamma = 3$)	53 ($\gamma = 3$)	107	145

a: not observed.

electronic Raman peaks were studied as a function of temperature and the results are shown in Figure 4.11.

It is interesting to note that the asymmetry for the anti-Stokes transitions is reversed compared to that for the corresponding Stokes transition. Indeed, if we write the amplitude for the Stokes transition from $|i\rangle$ to $|f\rangle$ as follows:

$$\sum_j \frac{\langle f|D_\rho|j\rangle\langle j|D_\sigma|i\rangle}{E_j - \hbar\omega} + [\rho \leftrightarrow \sigma] \tag{4.1}$$

and that for the anti-Stokes amplitude:

$$\sum_j \frac{\langle i|D_\rho|j\rangle\langle j|D_\sigma|f\rangle}{E_j - \hbar\omega} + [\rho \leftrightarrow \sigma] \tag{4.2}$$

for a particular polarization combination($\rho\sigma$), then it is easy to see that the asymmetry has been reversed. In fact, one must have $I_{\rho\sigma}$ (Stokes) = $I_{\sigma\rho}$ (anti-Stokes) for a particular transition $|i\rangle \longrightarrow |f\rangle$. Indeed, Figure 4.11 shows that in the anti-Stokes spectrum the 33 cm^{-1} transition is stronger in ZY, and the 53 cm^{-1} transition is stronger in XZ, which is the reverse of what happens in the Stokes spectrum. The actual amount of asymmetry is the same when measured in either the Stokes or the anti-Stokes spectrum, taking into account the polarization reversal.

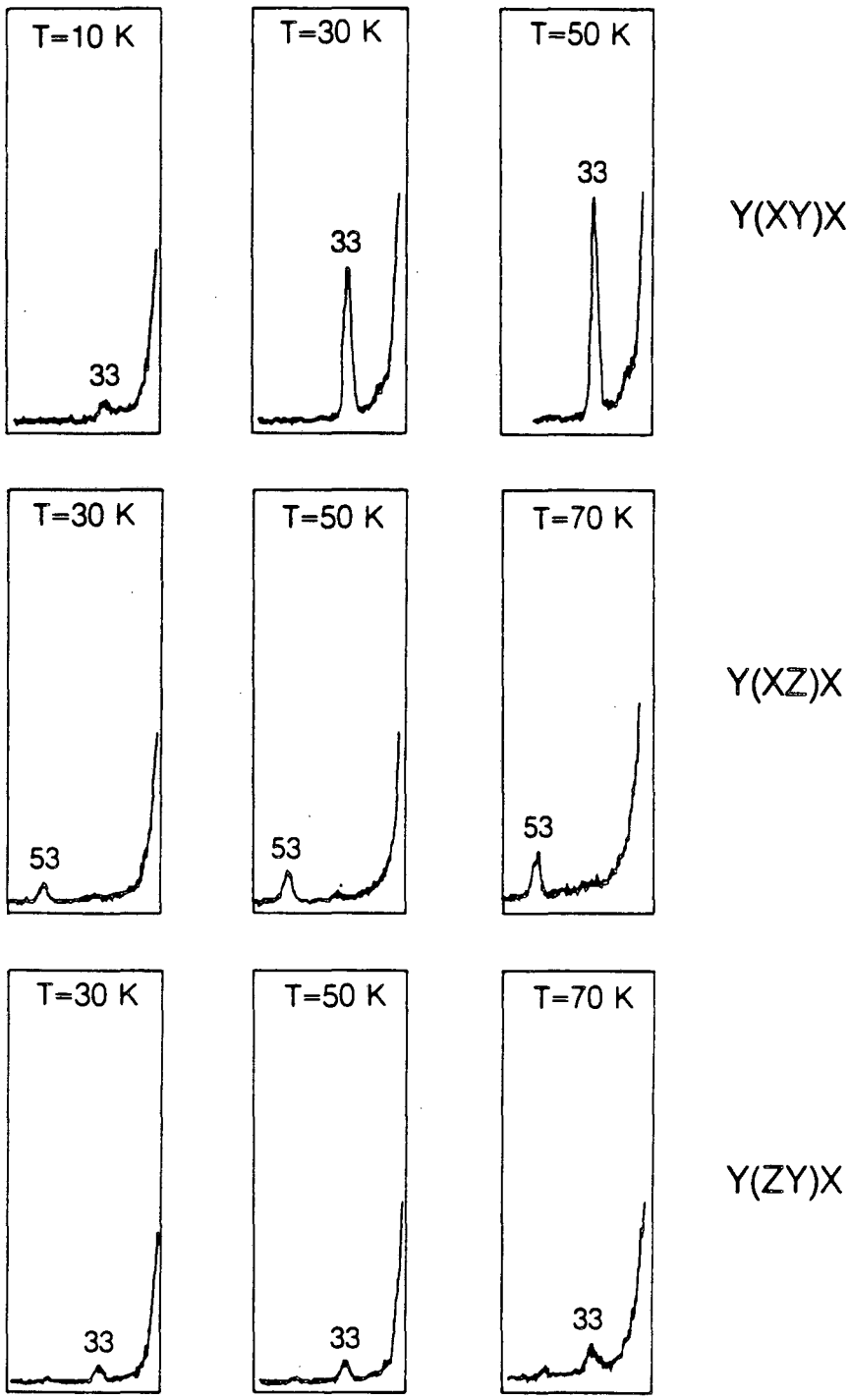

Figure 4.11: Polarized anti-Stokes Raman spectra of the 33 and 53 cm^{-1} transitions of Er^{3+} in $ErPO_4$ as a function of temperature, with excitation at 476.5 nm. The full scale is 1,000 counts per second for all the scans and the spectrometer bandpass is 2.5 cm^{-1}.

4.4 Experimental Raman Spectra of $HoPO_4$

4.4.1 Ho^{3+} - Selection Rules

The electronic Raman scattering results reported here represent the first reported observation of electronic Raman transitions in Ho^{3+}. The electronic Raman peaks are, however, extremely weak. They are an order of magnitude less intense than in Tm^{3+} or Er^{3+}. Ho^{3+} has the open shell configuration $4f^{10}$. Ho^{3+} thus has an even number of electrons and the electronic states are labeled by the irreducible representations Γ_1, Γ_2, Γ_3, Γ_4, and Γ_5. The optical absorption spectrum and crystal field fit of Ho^{3+} doped at low concentrations ($\sim$ 1%) in $LuPO_4$ and YPO_4 have been studied by Edelstein and Shalimoff and are as yet unpublished [7]. Some transitions have also been reported for Ho^{3+} in YPO_4 by P.J. Becker [8]. The crystal field fit and energy level structure of Ho^{3+} in $LuPO_4$ has been summarized in appendix A, section A4. Only the pure crystal $HoPO_4$ was available for the Raman scattering experiments.

The ground multiplet of Ho^{3+} is $^5I_8$. Electronic Raman transitions were observed between the ground state and the excited crystal field states of the ground multiplet. The decomposition of the ground multiplet into irreducible representations is given by $3\Gamma_1 + 2\Gamma_2 + 2\Gamma_3 + 2\Gamma_4 + 4\Gamma_5$. The ground crystal field state has the symmetry Γ_5 and is thus doubly degenerate. We can calculate the selection rules for Raman transitions from the Γ_5 ground state to the other states by taking the direct product of Γ_5 with the irreducible representation of the final state. We summarize the selection rules for the Raman transitions originating in the ground state:

transition	scattering tensor symmetry
$\Gamma_5 \longleftrightarrow \Gamma_1$	Γ_5
$\Gamma_5 \longleftrightarrow \Gamma_2$	Γ_5
$\Gamma_5 \longleftrightarrow \Gamma_3$	Γ_5
$\Gamma_5 \longleftrightarrow \Gamma_4$	Γ_5
$\Gamma_5 \longleftrightarrow \Gamma_5$	$\Gamma_1 + \Gamma_2 + \Gamma_3 + \Gamma_4$

The scattering tensors are listed in Table 3.2. Asymmetric transitions originating in the ground state will occur for all final states except those of symmetry Γ_5.

4.4.2 Ho^{3+} - Experimental Raman Spectra

The spectra obtained for $HoPO_4$ at ~4.2 K in the low wavenumber region 0-300 cm^{-1} are shown in Figure 4.12. Five electronic Raman transitions are observed at 68, 82, 92, 193, and 251 cm^{-1}. The Y(ZZ)X spectrum is not shown since it is featureless in the 0-300 cm^{-1} region, except for some slight polarization leakage. In Figure 4.12 the excitation is with the 514.5 nm line of the argon-ion laser, with an average power of 40 mW at the sample. Raman spectra taken with excitation at 488.0 and 496.5 nm are identical to those shown in Figure 4.12. The transitions at 68 and 82 cm^{-1} are seen to be very strongly asymmetric. They are quite intense in (XZ) polarization and totally absent in (ZY). The transition at 193 cm^{-1} also shows a large amount of asymmetry, however, the transition at 251 cm^{-1} shows little asymmetry.

Table 4.6 summarizes the electronic energy level structure of the $^5I_8$ multiplet and lists the energy values from the optical absorption measurements and crystal field fits for 1% Ho^{3+} in $LuPO_4$, and the values obtained for $HoPO_4$ from the electronic Raman spectra. The experimental uncertainty on the electronic Raman frequencies is ± 1 cm^{-1}.

The low wavenumber Raman spectrum of $HoPO_4$ was also taken at 77 and 295 K with green excitation at 514.5 nm. The line at 488.0 nm can no longer be used at temperatures above 4.2 K as it excites strong fluorescence from the sample. The 68 and 82 cm^{-1} electronic Raman transitions were tracked as a function of temperature and their frequencies were found to vary very little between 4.2 and 80 K. Above 100 K the two lines are too weak and broad to be clearly identified.

The phonon spectrum of $HoPO_4$ displays some peculiarities. The E_g^2 phonon decreases in frequency from 184 cm^{-1} at room temperature, to 180 cm^{-1} at ~4.2 K. This is opposite to the behaviour of that phonon in the other tetragonal rare earth phosphates (see Table 3.2). This might be an indication of coupling with the nearby electronic level at 193 cm^{-1}.

Table 4.6: Energy level values for the Ho^{3+} $^5I_8$ multiplet.

Symmetry	Energy (cm^{-1})		
	Optical Absorption 1% Ho^{3+} in $LuPO_4$	Crystal field fit 1% Ho^{3+} in $LuPO_4$	Electronic Raman $HoPO_4$
Γ_5	0	0	0
Γ_1	72	68	a
Γ_4	67	72	68
Γ_3	81	84	82
Γ_5	89	88	92
Γ_4	160	150	a
Γ_2	188	195	193[b]
Γ_1	a	196	a
Γ_5	a	225	a
Γ_3	250	245	251
Γ_5	279	276	a
Γ_2	a	277	a
Γ_1	a	300	a

a: not observed.

b: could also be assigned to $\Gamma_1(196\ cm^{-1})$.

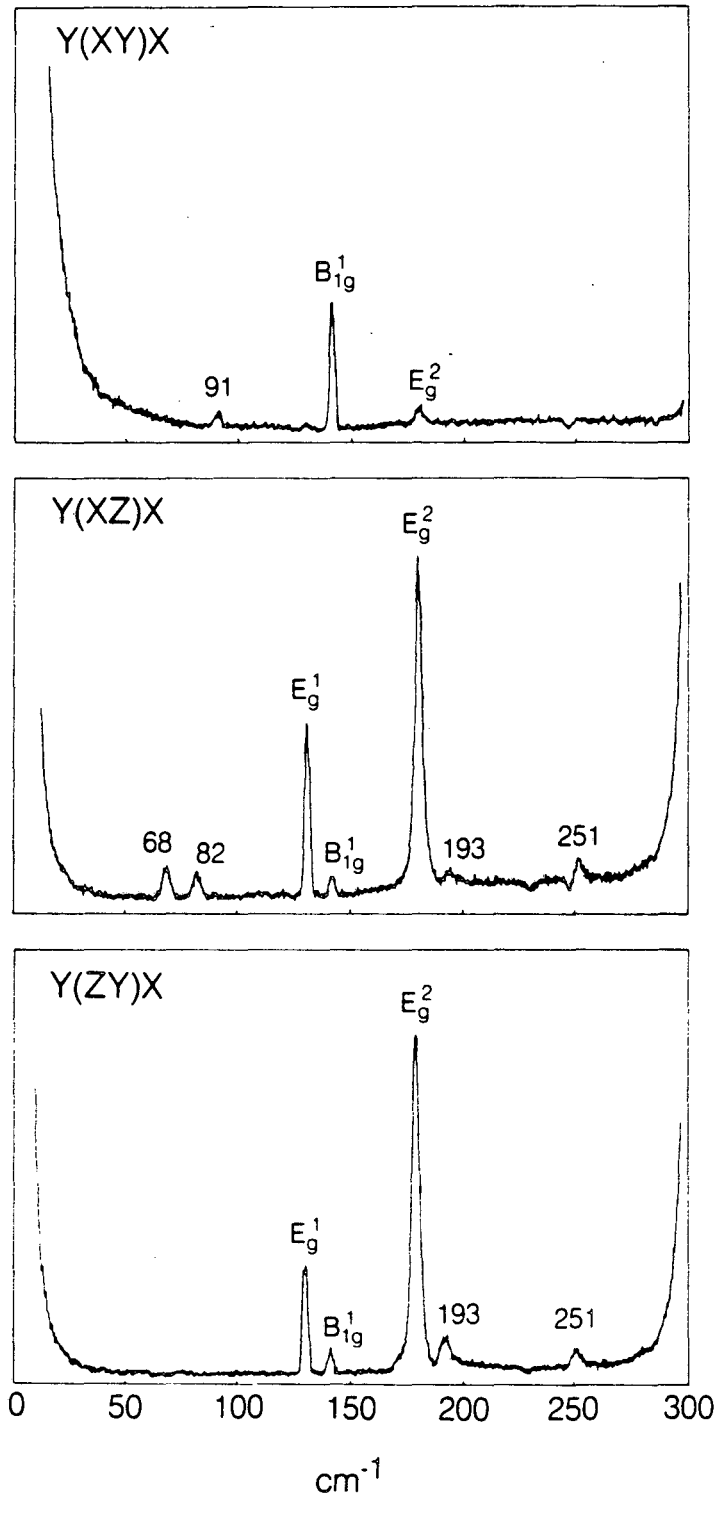

Figure 4.12: $HoPO_4$ polarized Raman spectra at ~4.2 K in the 0-300 cm^{-1} region. The full scale is 2,000 counts per second in all polarizations. The spectrometer bandpass is 2.5 cm^{-1}.

References

[1] P.C. Becker, T. Hayhurst, G. Shalimoff, J.G. Conway, N. Edelstein, L.A. Boatner, and M.M. Abraham, J. Chem. Phys. **81**, 2172 (1984).

[2] S. Guha, Phys. Rev. B **23**, 6790 (1981).

[3] P.C. Becker, N. Edelstein, G.M. Williams, J.J. Bucher, R.E. Russo, J.A. Koningstein, L.A. Boatner, and M.M. Abraham, Phys. Rev. B **31**, 8102 (1985).

[4] S. Hüfner, *Optical Spectra of Rare Earth Compounds* (Academic Press, New York, 1978).

[5] T. Hayhurst, G. Shalimoff, N. Edelstein, L.A. Boatner, and M.M. Abraham, J. Chem. Phys. **74**, 5449 (1981).

[6] D. Kuze, Z. Phys. **203**, 409 (1967).

[7] N. Edelstein and G. Shalimoff, Lawrence Berkeley Laboratory, unpublished results.

[8] P.J. Becker, phys. stat. sol. **38**, 379 (1970).

Chapter 5

Electronic Raman Scattering in Tm^{3+}, Er^{3+}, and Ho^{3+} in Tetragonal Phosphate Crystal Hosts - Intensity Analysis

This chapter compares the calculated and observed electronic Raman transition intensities for transitions between individual crystal field states for the ions Tm^{3+}, Er^{3+}, and Ho^{3+} in tetragonal phosphate crystals. The Judd-Ofelt closure approximation is applied to two-photon processes in lanthanide ions to obtain the predicted intensities. It is shown that d orbital intermediate states fail to correctly explain the data, and that intermediate states with g orbital character seem to play a significant role. Several discrepancies still remain, even with the inclusion of g orbital intermediate states.

An important foundation of the calculations presented here is provided by the crystal field fits, based upon optical absorption measurements, of the ions Tm^{3+}, Er^{3+}, and Ho^{3+} diluted to a few percent in $LuPO_4$ and YPO_4. These fits yield a precise picture of the electronic energy level structure along with the wavefunctions necessary for the Raman transition intensity calculations. Chapter 3, section 3.3, outlines the general theory of these intensities within the Judd-Ofelt framework.

5.1 Comparison of Calculated and Observed Electronic Raman Transition Intensities

The spherical and Cartesian scattering tensors for the transitions of interest to this study between the crystal field states of the ions Tm^{3+}, Er^{3+}, and Ho^{3+} are listed in

appendix B. The tensor elements are a function of the parameters F_1 and F_2, which in turn depend upon the nature of the intermediate states. There is only one adjustable parameter available, namely F_1/F_2, since once this ratio is set the intensities are all proportional to $(F_2)^2$. The relative intensities are then uniquely determined.

It is interesting to compare the calculated and observed asymmetry of the Γ_5 transitions. As mentioned previously, the observation of such asymmetries is one of the more unique features of electronic Raman scattering. In addition, it is a sensitive probe of the theory used to calculate the transition intensities. We measure the asymmetry of a transition by the ratio of its intensity in XZ (≡ YZ) polarization to that in ZX (≡ ZY). Under the assumption that the dominant intermediate states belong to the configuration $4f^{N-1}5d$, we obtain from the calculations of section 3.3.5 the following ratio:

$$F_1/F_2 = 1.3 \times \frac{\hbar\omega}{E_{4f-5d}} \tag{5.1}$$

where $\hbar\omega$ is the excitation energy and E_{4f-5d} the average energy of the $4f^{N-1}5d$ configuration relative to the ground state. The numerical factors come from the 6-J symbols, the radial matrix elements having canceled out. With $\hbar\omega \sim 20{,}000$ cm^{-1} and $E_{4f-5d} \sim 100{,}000$ cm^{-1}, this ratio is predicted to be 0.25. The following sections, which compare the observed and calculated intensities for Tm^{3+}, Er^{3+}, and Ho^{3+} in tetragonal phosphate hosts, will test whether this assumption is correct.

The experimental intensities are averaged from the data for different excitation wavelengths, different crystal samples, and different crystal orientations. For each scan, the polarization characteristics of the phonon lines were checked to ensure that the crystal was properly aligned, and the intensity measurements were retained only for those scans for which the phonon selection rules were obeyed. In particular, the Raman tensor of the E_g phonon lines were checked for symmetry ($I_{XZ} = I_{YZ} = I_{ZX} = I_{ZY}$), since the measurement of the asymmetry of the electronic lines is one of the more important results of this work. As mentioned in section 3.2, the most significant polarization leakage is between the Γ_3 and Γ_4 symmetries. This does not affect the asymmetry measurements, which are contained in transitions of Γ_5 symmetry. The relative uncertainty of the experimental intensities is ±20%, and the relative uncertainty of the experimental asymmetry ratios is ±40%.

5.1.1 Review of Previous Intensity Comparisons

There has not been, to date, very much systematic work done in comparing experimental and calculated electronic Raman intensities. The first comparison, mainly qualitative, was done by Axe for multiplet to multiplet transitions in $PrCl_3$ [1]. The agreement was good. Some work was also done by Koningstein [2,3]. For transitions between individual crystal field levels in $PrCl_3$, he finds some discrepancies [3]. Wadsack *et al* compared the intensities for transitions in Dy garnets and found only qualitative agreement [4]. There have been no detailed studies of the asymmetries of the transitions and their relationship to the intensity theory. Obviously, there is room for a quite a bit of work to be done in his area.

5.1.2 Tm^{3+} in Tetragonal Phosphate Crystals

The electronic Raman scattering tensors for Tm^{3+} are calculated using the theory described in section 3.3.6 and the wavefunctions listed in appendix A2. The necessary unit tensors for the transitions within the ground multiplet are:

$$\begin{aligned} \langle {}^3H_6||\mathbf{U}^{(1)}||{}^3H_6\rangle &= 2.113 \\ \langle {}^3H_6||\mathbf{U}^{(2)}||{}^3H_6\rangle &= -1.108 \end{aligned} \tag{5.2}$$

and those for transitions from the ground multiplet to the first excited multiplet are:

$$\begin{aligned} \langle {}^3F_4||\mathbf{U}^{(1)}||{}^3H_6\rangle &= 0 \\ \langle {}^3H_4||\mathbf{U}^{(1)}||{}^3H_6\rangle &= 0 \\ \langle {}^3F_4||\mathbf{U}^{(2)}||{}^3H_6\rangle &= -0.913 \\ \langle {}^3H_4||\mathbf{U}^{(2)}||{}^3H_6\rangle &= -0.046 \end{aligned} \tag{5.3}$$

The ${}^3F_4$ excited multiplet has a small amount of ${}^3H_4$ components, which contribute only negligibly to the electronic Raman amplitudes. The spherical and Cartesian scattering tensors for the transitions from the Γ_1 ground state to the crystal field states of the ${}^3H_6$ and ${}^3F_4$ multiplets are listed in appendix B, section B1.

We first study the ground multiplet Γ_5 asymmetric transitions, of which there are three, all observed experimentally. Since the intensities are proportional to the square of F_1/F_2, two values for F_1/F_2 can be extracted from the experimental asymmetry for a particular transition, using the calculated scattering matrix elements. For the transition at 30 cm^{-1}, we have:

$$I_{xz}/I_{zx} = \frac{(-.183F_1 + .020F_2)^2}{(.183F_1 + .020F_2)^2} = 3.0 \tag{5.4}$$

Table 5.1: Comparison of observed and predicted asymmetry ratios $I_{xz,zy}/I_{zx,zy}$ for the electronic Raman transitions of $TmPO_4$.

	Transition		
	30 cm^{-1}	138 cm^{-1}	280 cm^{-1}
Observed asymmetry	3.0	0.9	1.2
Predicted asymmetry with $F_1/F_2 = 0.25$	0.1	5.8	0.5
Predicted asymmetry with $F_1/F_2 = -0.03$	3.1	0.8	1.1

which leads to the following possible values of F_1/F_2:

$$\begin{cases} F_1/F_2 = -.03 \\ F_1/F_2 = -.4 \end{cases} \tag{5.5}$$

For the transition at 138 cm^{-1} the asymmetry is:

$$I_{xz}/I_{zx} = \frac{(.063F_1 + .035F_2)^2}{(-.063F_1 + .035F_2)^2} \tag{5.6}$$

while for the transition at 280 cm^{-1} it is:

$$I_{xz}/I_{zx} = \frac{(-.021F_1 + .029F_2)^2}{(.021F_1 + .029F_2)^2} \tag{5.7}$$

Experimentally, the lines at 138 and 280 cm^{-1} exhibit no asymmetry, within experimental error, so that it is not possible to extract a value for F_1/F_2 from these transitions.

In Table 5.1 we compare the calculated and experimental asymmetries for both $F_1/F_2 = 0.25$ ($4f^{11}5d$ as the only intermediate configuration), and $F_1/F_2 = -.03$, the more "acceptable" of the two parameters predicted by the experimental transition at 30 cm^{-1}. The value $F_1/F_2 = -.03$ works surprisingly well in predicting that the two transitions at 138 and 280 cm^{-1} will have a very small amount of asymmetry. We test this value further, as opposed to $F_1/F_2 = 0.25$, by checking the relative intensities for all the transitions, given in Table 5.2. The calculated relative intensities are in units of $(F_2)^2 \times 10^{-4}$ and the observed values are scaled so that the predicted and observed intensities for the 86 cm^{-1} transition are equal. The energy levels are either the Raman values for $TmPO_4$ or, if these are not available, the crystal field fit values from Table 4.1. This table was published by Becker *et al* [5], with a

Table 5.2: Predicted and observed intensities of the electronic Raman transitions from the ground state to the crystal field levels of the $^3H_6$ multiplet of $TmPO_4$. The calculated intensities are in units of $(F_2)^2 \times 10^{-4}$.

Transition	Polarization	Observed intensity	Predicted intensity $F_1/F_2 = 0.25$	Predicted intensity $F_1/F_2 = -0.03$
30 cm^{-1}	XZ,YZ	3.7	13.2	13.0
	ZX,ZY	1.2	86.4	4.2
86 cm^{-1}	XY,YX	228.0	228.0	228.0
138 cm^{-1}	XZ,YZ	21.6	51.6	22.0
	ZX,ZY	24.0	7.4	27.2
183[b] cm^{-1}	XY,YX	a	11.1	0.2
248[b] cm^{-1}	XX,YY	a	10.2	10.2
	ZZ	a	41.0	41.0
254[b] cm^{-1}	XX,YY	a	47.6	47.6
280 cm^{-1}	XZ,YZ	23.4	11.2	17.6
	ZX,ZY	20.3	23.4	16.0
303[b] cm^{-1}	XY,YX	a	0.4	0.4
321[b] cm^{-1}	XX,YY	a	7.8	7.8

a: not observed.

b: from the crystal field fit, Table 4.1.

factor of two missing from the calculated values for the Γ_5 transitions. This omission was corrected in a later article [6]. For the experimental intensities, the excitations used were the 514.5, 488.0, and 476.5 nm lines of the argon-ion laser. Note that the transitions at 248 and 245 cm^{-1} were not observed experimentally. In the XX,YY polarizations the only electronic transition observed was leakage from the XY,YX components of the 86 cm^{-1} transition.

There is much better agreement for $F_1/F_2 = -.03$ than for $F_1/F_2 = 0.25$. Nevertheless, a major problem is the absence in the experimental spectrum of the transitions at 248 and 254 cm^{-1}. They are predicted to be extremely strong. The intensities of these transitions

is governed only by F_2^2, so that changing F_1/F_2 has no influence on the predicted intensity of these lines.

The experimental and calculated electronic Raman transition intensities were also compared for the transitions from the ground state to the first excited multiplet $^3F_4$. Since only $\alpha^{(2)}$ contributes to the transition amplitudes F_1 does not play any role and all the intensities are proportional to F_2^2 and are fixed relative to each other. The results are shown in Table 5.3. The scaling of the observed intensities is the same as for those of Table 5.1 so that the intensities of the $^3H_6$ multiplet can be directly compared to those of the $^3F_4$ multiplet. It was not possible to accurately measure the XX and YY intensities of the 5676 and 5870 cm^{-1} lines due to polarization leakage,

Table 5.3 is identical to Table VIII of Becker *et al* [5] with some corrections. A missing factor of two for the Γ_5 transitions has now been included. The factor of two comes from the double degeneracy of the Γ_5 states which was not taken into account in [5] for the calculated values. The experimental intensities for the $^3F_4$ transitions were normalized by a factor of $(\frac{\omega_0}{\omega_S})^2$ (ω_0: incident light frequency; ω_S: scattered light frequency) so as to take into account the ω_S^3 drop in intensity of the Raman signal (see section 3.3.3) for the $^3F_4$ transitions versus those for $^3H_6$. For the $^3H_6$ multiplet transitions, it was assumed that $\omega_s \approx \omega_0$. Note that it is the relative values of $|\alpha_{\rho\sigma}|^2$ that are listed in Tables 5.1 and 5.3. The photomultiplier tube is a photon counting detector and the signal it produces is proportional to the intensity of the light incident upon it divided by the energy of a light quantum, hence the loss of one power of the frequency in the frequency dependence of the Raman signal coming from the photomultiplier tube. The $(\frac{\omega_0}{\omega_S})^2$ factor is 2.0 for the $^3F_4$ transitions. The difference in spectral response of the spectrometer and photomultiplier tube between the various ω_S also needs to be taken into account and contributes a significant correction. In Table VIII of [5] a factor of $(\frac{\omega_0}{\omega_S})^4$ was assumed for the frequency dependence of the Raman signal because the semi-classical expression for the Raman intensity was used and also because the photon counting character of the detection system was not recognized. It is seen in Table 5.3 that the predicted intensities are quite a bit stronger than the observed intensities, except for the line at 5602 cm^{-1} for which there is good agreement.

Table 5.3: Predicted and observed intensities of the electronic Raman transitions from the ground state to the crystal field levels of the $^3F_4$ multiplet of $TmPO_4$. The calculated intensities are in units of $(F_2)^2 \times 10^{-4}$.

Transition	Polarization	Observed intensity	Predicted intensity
5602 cm^{-1}	XY,YX	19.7	30.3
5676 cm^{-1}	XX,YY	a	10.9
	ZZ	4.6	43.6
5688 cm^{-1}	XZ,YZ,ZX,ZY	5.0	48.0
5735[b] cm^{-1}	XY,YX	a	0.0
5763 cm^{-1}	XY,YX	a	2.0
5842[b] cm^{-1}	XZ,YZ,ZX,ZY	a	1.0
5870 cm^{-1}	XX,YY	a	13.0
	ZZ	10.5	51.8

a: not observed.

b: from the crystal field fit, Table 4.1.

5.1.3 Er^{3+} in Tetragonal Phosphate Crystals

The electronic Raman scattering tensors for Er^{3+} are calculated with the wavefunctions listed in appendix A2. The necessary unit tensors for the ground multiplet transitions are:

$$\begin{aligned} \langle {}^4I_{15/2}||\mathbf{U}^{(1)}||{}^4I_{15/2}\rangle &= 2.774 \\ \langle {}^4I_{15/2}||\mathbf{U}^{(2)}||{}^4I_{15/2}\rangle &= -0.469 \end{aligned} \tag{5.8}$$

The spherical and Cartesian scattering tensors for the transitions from the Γ_7 ground state to the crystal field states of the ${}^4I_{15/2}$ multiplet are listed in appendix B, section B2.

All the transitions are predicted to have Γ_5 components, since Er^{3+} is an odd electron system. The transitions at 33, 53, and 145 cm^{-1} are experimentally observed to be asymmetric (see Figure 4.8). This is especially true for the two lines at 33 and 53 cm^{-1} which exhibit very sharp asymmetries. The line at 145 cm^{-1} is quite weak and the asymmetry is within the experimental error. The asymmetric transitions can be used to calculate the value of F_1/F_2. For the transition at 33 cm^{-1}, we have:

$$I_{xz}/I_{zx} = \frac{(.209F_1 + .016F_2)^2}{(-.209F_1 + .016F_2)^2} = 5.3 \tag{5.9}$$

which leads to the following possible values of F_1/F_2:

$$\begin{cases} F_1/F_2 = .20 \\ F_1/F_2 = .03 \end{cases} \tag{5.10}$$

For the transition at 53 cm^{-1} the asymmetry is:

$$I_{xz}/I_{zx} = \frac{(.158F_1 - .026F_2)^2}{(-.158F_1 - .026F_2)^2} = 0.2 \tag{5.11}$$

which leads to the following possible values of F_1/F_2:

$$\begin{cases} F_1/F_2 = .37 \\ F_1/F_2 = .07 \end{cases} \tag{5.12}$$

The experimental relative uncertainty on the 145 cm^{-1} line does not allow an accurate determination of F_1/F_2, as the transition is very weak. We compare in Table 5.4 the calculated and experimental asymmetries for both $F_1/F_2 = 0.25$ ($4f^{11}5d$ as the only intermediate configuration) and for $F_1/F_2 = .03$, which is pointed to by the experimental asymmetries and actually yields a better fit to the data. It is interesting to note that again, a value of F_1/F_2 close to zero is more accurate in predicting the experimental asymmetries than the

Table 5.4: Comparison of observed and predicted asymmetry ratios $I_{XZ,ZY}/I_{ZX,ZY}$ for the electronic Raman transitions of $ErPO_4$.

	Transition		
	33 cm^{-1}	53 cm^{-1}	145 cm^{-1}
Observed asymmetry	5.3	0.2	0.6
Predicted asymmetry with $F_1/F_2 = 0.25$	3.5	0.04	1.9
Predicted asymmetry with $F_1/F_2 = 0.03$	5.2	0.5	1.1

expected value of 0.25. The relative intensities for all the transitions observed in $ErPO_4$ are displayed in Table 5.5. The energy levels are either the Raman values for $ErPO_4$ or, if these are not available, the crystal field fit values from Table 4.4. The calculated relative intensities are in units of $(F_2)^2 \times 10^{-4}$ and the observed values are scaled so that the predicted and observed intensities for the XY,YX components of the 33 cm^{-1} transition are equal. Excitation with the 514.5, 476.5, and 457.9 nm lines of the argon-ion laser was used to obtain the experimental intensities. Both $F_1/F_2 = 0.25$ and $F_1/F_2 = 0.03$ are used for the calculated values. $F_1/F_2 = 0.03$ gives a much better fit to the experimental data, especially for the 33 cm^{-1} transition. The three highest states of the multiplet are included even though they cannot be clearly identified in the experimental spectra. This table has been published previously in two separate parts [5,6]. It should be pointed out that it was not possible to obtain good quality XX or YY spectra from the $ErPO_4$ crystals, the polarization leakage always being to high to allow an accurate measurement of the electronic Raman intensities. Thus the 33 cm^{-1} transition had a rather strong XX intensity (although less than its XY intensity) which could have been leakage from XY into XX.

Table 5.5: Predicted and observed intensities of the electronic Raman transitions from the ground state to the crystal field levels of the $^4I_{15/2}$ multiplet of Er^{3+}. The calculated intensities are in units of $(F_2)^2 \times 10^{-4}$. The XX and YY intensities could not be accurately measured.

Transition	Polarization	Observed intensity	Predicted intensity $F_1/F_2 = 0.25$	Predicted intensity $F_1/F_2 = 0.03$
33 cm^{-1}	XX,YY	a	0.6	0.6
	XY,YX	15.2	15.2	15.2
	XZ,YZ	3.0	46.6	5.0
	ZX,ZY	0.6	13.1	0.9
53 cm^{-1}	XX,YY	a	0.04	0.04
	ZZ	a	0.2	0.2
	XY,YX	0.9	14.6	0.2
	XZ,YZ	0.9	1.8	4.5
	ZX,ZY	6.1	42.9	9.4
105 cm^{-1}	XX,YY	a	2.0	2.0
	ZZ	1.5	7.8	7.8
	XY,YX	a	1.7	0.02
	XZ,YZ	a	0.6	0.5
	ZX,ZY	a	0.4	0.5
145 cm^{-1}	XX,YY	a	0.2	0.2
	XY,YX	1.8	8.4	8.4
	XZ,YZ	0.6	4.9	3.8
	ZX,ZY	0.9	2.5	3.5

a: not observed.

Table 5.5 (continued):

229[b] cm^{-1}	XX,YY	a	4.4	4.4
	XY,YX	a	0.2	0.2
	XZ,YZ	a	0.8	0.04
	ZX,ZY	a	0.5	$5\ 10^{-5}$
246[b] cm^{-1}	XX,YY	a	0.2	0.2
	ZZ	a	0.8	0.8
	XY,YX	a	0.6	0.6
	XZ,YZ	a	0.3	0.3
	ZX,ZY	a	0.2	0.2
286[b] cm^{-1}	XX,YY	a	0.5	0.5
	XY,YX	a	0.3	0.3
	XZ,YZ	a	0.2	0.1
	ZX,ZY	a	0.03	0.1

a: not observed.

b: from the crystal field fit, Table 4.4.

5.1.4 Ho^{3+} in Tetragonal Phosphate Crystals

The electronic Raman scattering tensors for Ho^{3+} are calculated using the theory described in section 3.3.6 and the wavefunctions listed in appendix A4. The necessary unit tensor matrix elements for the ground multiplet are:

$$\begin{aligned} \langle {}^5I_8||\mathbf{U}^{(1)}||{}^5I_8\rangle &= 2.86 \\ \langle {}^3K1_8||\mathbf{U}^{(1)}||{}^3K1_8\rangle &= 3.77 \\ \langle {}^3K2_8||\mathbf{U}^{(1)}||{}^3K2_8\rangle &= 3.77 \\ \langle {}^3K2_8||\mathbf{U}^{(1)}||{}^3K1_8\rangle &= 0 \end{aligned} \tag{5.13}$$

for $\mathbf{U}^{(1)}$, and

$$\begin{aligned} \langle {}^5I_8||\mathbf{U}^{(2)}||{}^5I_8\rangle &= 0.48 \\ \langle {}^3K1_8||\mathbf{U}^{(2)}||{}^3K1_8\rangle &= -0.71 \\ \langle {}^3K2_8||\mathbf{U}^{(2)}||{}^3K2_8\rangle &= -0.46 \\ \langle {}^3K2_8||\mathbf{U}^{(2)}||{}^3K1_8\rangle &= 0.48 \end{aligned} \tag{5.14}$$

for $\mathbf{U}^{(2)}$. The major part of the ground multiplet wavefunctions is ${}^5I_8$, with smaller amounts of ${}^3K1_8$ and ${}^3K2_8$ (an additional quantum number is needed to distinguish the different ${}^3K_8$

multiplets, the notation used is that of Nielson and Koster [7]). The spherical and Cartesian scattering tensors for the transitions from the doubly degenerate Γ_5 ground state to the crystal field states of the ground $^5I_8$ multiplet are listed in appendix B, section B3.

The asymmetry of several of the Ho^{3+} Γ_5 transitions is quite spectacular. The transitions at 68 and 82 cm^{-1} are present in XZ ($\equiv$ YZ) polarization and, within experimental error, absent in ZY ($\equiv$ ZX). Their asymmetry ratio I_{xz}/I_{zx} is thus, strictly speaking, equal to infinity. This means that for these two transitions the symmetric and antisymmetric contributions to I_{zx} must exactly cancel each other. The transition at 193 cm^{-1} is also very asymmetric and is at least ten times stronger in ZY than in XZ. The weak transition at 251 cm^{-1} is only slightly asymmetric.

Using the scattering tensors listed in appendix B3, it is possible to calculate the values of F_1/F_2 predicted by the Γ_5 transitions. Since the equation for the 68 and 82 cm^{-1} transitions will be $I_{zx} = 0$, we will obtain only one value of F_1/F_2 from these two transitions. For the 68 cm^{-1} transition we have:

$$\begin{aligned} I_{zx} &= (.084F_1 + .021F_2)^2 + (-.095F_1 - .019F_2)^2 = 0 \\ &\Longrightarrow (.084F_1 + .021F_2) \approx (-.095F_1 - .019F_2) \approx 0 \end{aligned} \tag{5.15}$$

which implies that:

$$F_1/F_2 = -0.23 \tag{5.16}$$

For the 82 cm^{-1} transition we have:

$$\begin{aligned} I_{zx} &= (-.094F_1 - .023F_2)^2 + (.109F_1 + .022F_2)^2 = 0 \\ &\Longrightarrow (-.094F_1 - .023F_2) \approx (.109F_1 + .022F_2) \approx 0 \end{aligned} \tag{5.17}$$

which also implies that:

$$F_1/F_2 = -0.22 \tag{5.18}$$

This is a very surprising but consistent result which does not agree with the assumption that d orbital wavefunctions are the intermediate states. The line at 193 cm^{-1} is also strongly asymmetric. There are two possible lines from the crystal field fit that it can be identified with, namely 195 and 196 cm^{-1} (see Table 4.6). The two lines might actually be so close together so as to be experimentally unresolvable. At any rate, the question of which of the two levels corresponds to the 193 cm^{-1} transition is somewhat academic since both levels

are predicted to have almost identical Raman scattering tensors, regardless of the value of F_1/F_2. We arbitrarily assign the 193 cm^{-1} line to the transition from the ground state to the 195 cm^{-1} level. We then have for the asymmetry:

$$I_{xz}/I_{zx} = \frac{(-.073F_1 - .021F_2)^2 + (-.077F_1 - .017F_2)^2}{(.073F_1 - .021F_2)^2 + (.077F_1 - .017F_2)^2} = 0.15 \tag{5.19}$$

which leads to the following values of F_1/F_2:

$$\begin{cases} F_1/F_2 = -0.11 \\ F_1/F_2 = -0.58 \end{cases} \tag{5.20}$$

The results are different than for the 68 and 82 cm^{-1} transitions, but again the negative values of F_1/F_2 indicates the strong presence of g orbitals. The line at 251 cm^{-1} is only slightly asymmetric and is very weak, so that the relative uncertainty of its experimental intensity is too large to allow an accurate determination of F_1/F_2.

The observed and calculated asymmetry ratios for the Γ_5 electronic Raman transitions of Ho^{3+} are shown in Table 5.6 for both $F_1/F_2 = -0.22$ and for $F_1/F_2 = +0.25$ (mainly d orbitals for the intermediate states). It is quite clear that $F_1/F_2 = 0.25$ fails miserably to explain the experimental asymmetry ratios. In contrast, $F_1/F_2 = -0.22$ is in excellent agreement for the 68 and 82 cm^{-1} transitions. Unfortunately it is off by a factor of ten for the 193 cm^{-1} transition, and by a factor of a hundred for the 251 cm^{-1} transition. Choosing F_1/F_2 close to zero would result in asymmetry ratios of nearly unity.

Table 5.7 compares the experimental and calculated intensities for the three values $F_1/F_2 = -0.22$, 0, and 0.25. It was not possible, due to polarization leakage, to obtain accurate values for the XX and YY intensities. $F_1/F_2 = -0.22$ is correct in predicting that the XZ intensities of the 68 and 82 cm^{-1} transitions are roughly equal. For the other lines, however, it has serious flaws. The 92 cm^{-1} transition is experimentally 40 times stronger than predicted. Since its intensity is proportional to F_2^2, changing F_1/F_2 does not affect its calculated intensity. The 150 cm^{-1} transition, seen at 160 cm^{-1} in the 1% Ho^{3+}:$LuPO_4$ optical absorption spectra should be present but is not observed. The 251 cm^{-1} intensities are not well reproduced by any of the values of F_1/F_2.

Table 5.6: Comparison of observed and predicted asymmetry ratios $I_{XZ,YZ}/I_{ZX,ZY}$ for the $^5I_8$ electronic Raman transitions of Ho^{3+} in $HoPO_4$.

	Transition			
	68 cm^{-1}	82 cm^{-1}	193 cm^{-1}	251 cm^{-1}
Observed asymmetry	∞	∞	0.15	0.75
Predicted asymmetry with $F_1/F_2 = -0.22$	$2.1\,10^2$	$4.3\,10^2$	0.01	0.01
Predicted asymmetry with $F_1/F_2 = 0.25$	$4.9\,10^{-3}$	$6.1\,10^{-3}$	$2.3\,10^2$	$4.9\,10^{-3}$

5.1.5 Comparison of the Relative Multiplet → Multiplet Scattering Strengths of Tm^{3+}, Er^{3+}, and Ho^{3+}

It is interesting to compare the relative multiplet → multiplet electronic Raman scattering strengths from ion to ion. To accomplish this we sum the experimental intensities observed for all the transitions between individual crystal field states for a specific multiplet to multiplet transition, in all polarizations. In the second order theory, it was shown by Axe that this total intensity is proportional to the reduced matrix elements of the unit tensors $U^{(1)}$ and $U^{(2)}$ between the initial and final multiplets [1]:

$$I_{\text{total}} \propto F_1^2 \langle 4f^N \alpha' S L' J' || U^{(1)} || 4f^N \alpha S L J \rangle^2 + F_2^2 \langle 4f^N \alpha' S L' J' || U^{(2)} || 4f^N \alpha S L J \rangle^2 \quad (5.21)$$

We choose $F_1/F_2 = 0$ for Tm^{3+} and Er^{3+} and $F_1/F_2 = -0.22$ for Ho^{3+}, since these are the values indicated by the data. We also assume that the energy denominators and matrix elements that enter the expression for F_2 are the same for the different ions.

To obtain the experimental scattering intensities in a way that is consistent with comparing the scattering strengths of one ion relative to another, which requires that the differences in scattering efficiencies and input powers be corrected for, we reference all the intensities to a common scattering intensity for phonon E_g^5. This calibrates the observed intensities that come from different spectra. The XX and YY intensities have not been included in the experimental total since they are not accurately measured, however, this should not induce a very large error in the experimental scattering strengths. The observed intensities are correct to within ±50%. As an example of the absolute scattering strengths, for the

Table 5.7: Predicted and observed intensities of the electronic Raman transitions from the ground state to the crystal field levels of the $^5I_8$ multiplet of Ho^{3+}. The calculated intensities are in units of $(F_2)^2 \times 10^{-4}$.

Transition	Polarization	Observed intensity	Predicted intensity $F_1/F_2 = -0.22$	Predicted intensity $F_1/F_2 = 0$	Predicted intensity $F_1/F_2 = 0.25$
68[b] cm^{-1}	all	a	0	0	0
68 cm^{-1}	XZ,YZ	31.2	31.5	8.0	0.2
	ZX,ZY	0	0.1	10.1	45.9
82 cm^{-1}	XZ,YZ	23.6	40.2	10.1	0.3
	ZX,ZY	0	0.1	10.1	45.9
92 cm^{-1}	XX,YY XY,YX	20.0	0.5	0.5	0.5
150[b] cm^{-1}	XZ,YZ	a	11.0	2.9	0.02
	ZX.ZY	a	0.01	2.9	12.5
193 cm^{-1}	XZ,YZ	6.4	0.2	7.3	28.5
	ZX,ZY	40.8	25.8	7.3	0.1
196[b] cm^{-1}	XZ,YZ	a	0.2	7.2	28.6
	XZ,ZY	a	25.3	7.2	0.1
225[b] cm^{-1}	XX,YY XY,YX	a	4.5	4.5	4.5
251 cm^{-1}	XZ,YZ	18.0	2.0	0.5	0.01
	ZX,ZY	23.6	$7\ 10^{-5}$	0.5	2.3
276[b] cm^{-1}	XX,YY XY,YX	a	0.3	0.3	0.3
277[b] cm^{-1}	XZ,YZ	a	$2\ 10^{-3}$	0.2	0.7
	ZX.ZY	a	0.6	0.2	0
300[b] cm^{-1}	all	a	0	0	0

a: not observed.

b: from the crystal field fit, Table 4.6

Table 5.8: Comparison of the relative multiplet → multiplet electronic Raman scattering intensities, for multiplet to multiplet transitions, for Tm^{3+}, Er^{3+}, and Ho^{3+}.

	Tm^{3+} $^3H_6 \rightarrow {}^3H_6$	Tm^{3+} $^3H_6 \rightarrow {}^3F_4$	Er^{3+} $^4I_{15/2} \rightarrow {}^4I_{15/2}$	Ho^{3+} $^5I_8 \rightarrow {}^5I_8$
calculated intensity	100	67	18	51
observed intensity	100	12	39	4

intensities reported here the peak height of phonon E_g^5 is 17,000 counts per second, that of the Tm^{3+} 86 cm^{-1} transition (in XY) is 18,000 counts per second, that of the Er^{3+} 33 cm^{-1} transition (in XY) is 4,800 cps and that of the Ho^{3+} 68 cm^{-1} transition (in XZ) is 200 cps.

The comparison is summarized in Table 5.8, where for convenience Tm^{3+} has been given a total scattering strength of 100 for the transition $^3H_6 \longrightarrow {}^3H_6$ for both calculated and experimental values.

The intensities for Tm^{3+} and Er^{3+} are in fairly good agreement, although the Tm^{3+} $^3H_6 \rightarrow {}^3F_4$ transition is much weaker experimentally than expected. The biggest discrepancy is for Ho^{3+}, which is observed to be ten times weaker than predicted. This weakness of the Ho^{3+} electronic Raman transitions probably accounts for the fact that there have been no previously published electronic Raman spectra of Ho^{3+} in the literature.

5.2 Summary of the Results for Tm^{3+}, Er^{3+}, and Ho^{3+}

In the preceding sections, a comparison was made of the experimental and calculated electronic Raman transition intensities of Tm^{3+}, Er^{3+}, and Ho^{3+} in the tetragonal rare earth phosphate crystals $(RE)_xLu_{1-x}PO_4$. For Tm^{3+}, experimental spectra were obtained for $x = 1, .2, .1, .01$; for Er^{3+} $x = 1, .5, .2, .1, .01$; and for Ho^{3+} only $x = 1$ was used. Some crystals of the type $(RE)_xY_{1-x}PO_4$) were also studied, but the experimental spectra were of distinctly lower quality then the lutetium phosphate crystal hosts. Spectra were taken for all the polarization combinations of the incident and scattered light allowed by the scattering geometry, so as to construct the Raman scattering matrix $|\alpha_{\rho\sigma}|^2$.

The first immediate result is that electronic Raman scattering, as a spectroscopic technique, allows the measurement of the frequencies, linewidths, and symmetries of some of the crystal field levels of the ground multiplet and, in some cases, of the first excited multiplet. These levels are often not observable by other means and can in addition be tracked as a function of temperature.

The second interest for this study is the comparison of the experimental and calculated electronic Raman transition intensities. This is a test of the second-order Judd-Ofelt theory applied to two-photon transitions in trivalent lanthanides, to date a relatively unexplored area as opposed to one-photon transitions such as absorption or fluorescence. It was found that for Tm^{3+}, Er^{3+}, and Ho^{3+} there are large discrepancies between the experimental and predicted Raman transition intensities for transitions between individual crystal field levels. The asymmetry of the transitions, a unique feature of electronic Raman scattering, was used to highlight the role of the intermediate states. The phenomenological parameter F_1/F_2, which governs the amount of asymmetry, was adjusted to find the best fit of the experimental to calculated intensities. The character of the intermediate states that contribute to the Raman amplitudes can be inferred from the value of F_1/F_2. The usual assumption that the $4f^{N-1}5d$ configuration is responsible for the bulk of the transition amplitude leads to $F_1/F_2 \approx 0.25$.

For Tm^{3+} it was found that a value of F_1/F_2 close to zero yielded the best fit for the asymmetries and intensities. $F_1/F_2 = 0.25$ was in obvious contradiction with the experimental intensities. This implies that g orbitals contribute a significant portion of the electronic Raman amplitudes (in section 3.3.4 it was shown that d and g orbitals have opposite sign

contributions to the antisymmetric component of the scattering tensor). This is a surprising result in view of the high energy of g orbital configurations in the free ions. Tm^{3+} has nevertheless two glaring discrepancies in the experimental absence of the two transitions at 248 and 254 cm^{-1}, predicted to be very strong irrespective of the value of F_1/F_2.

For Er^{3+}, $F_1/F_2 \approx 0.25$ gave a better fit than in the case of Tm^{3+}, but again a value of F_1/F_2 close to zero gave an even better fit for both the asymmetry ratios and the relative intensities. With $F_1/F_2 = 0.03$ there are no major discrepancies in the case of Er^{3+}.

Ho^{3+} provides the most intriguing results of the study. The asymmetries of the transitions at 68 and 82 cm^{-1} indicate a complete dominance of g orbitals for the intermediate states, since they predict $F_1/F_2 \approx -0.22$. This value works noticeably less well, however, for the two transitions at 193 and 251 cm^{-1}. There are other discrepancies for Ho^{3+}, in particular the unexpected relative experimental strength of the 92 cm^{-1} transition.

The main results of the intensity studies is the experimental observation of the importance of g orbitals in mediating two-photon transitions. How g orbital intermediate configurations, or states that mimic the angular properties of g orbital states, could play a role in determining the electronic Raman amplitudes is still an unresolved question. The g orbital intermediate states need to be quite low in energy to be able to compete so effectively, as they do, with the d orbital intermediate states.

The results also seem to be sensitive to the particular lanthanide ion used, which indicates that the details of the electronic energy level structure and of the interactions with the host lattice are important in determining the intensities. For Tm^{3+} and Er^{3+} the study of the diluted crystals did not reveal any concentration dependence of the electronic Raman intensities, at least down to a 10% concentration of the optically active ion. The fact that the spectra remained the same with different excitation frequencies shows that no resonance effects are coming into play.

The comparison of the multiplet $\rightarrow$ multiplet scattering strengths of the different ions studied also revealed discrepancies, notably in the case of Ho^{3+} where there is a discrepancy of one order of magnitude. It is quite possible that this is telling us that the relevant intermediate states are different for Ho^{3+} than for the other ions, or more generally that the transition intensities are in some way sensitive to the particular ion involved.

In the next sections, we investigate in more detail the question of the role played by g orbitals and the implications for the lanthanide ion-host lattice and lanthanide ion-radiation

field interactions. We also briefly discuss some of the other effects that might come into play, such as higher order terms, ion-ion correlations, and vibronic coupling.

5.3 The Role of g Electrons in Trivalent Lanthanide Optical Transition Intensities

5.3.1 Review of the Literature for One-Photon Transition Intensities

There is substantial evidence that the consideration of only the $4f^{N-1}5d$ configuration as the intermediate state for second order optical processes in trivalent lanthanide ions does not suffice to explain the experimental results. As discussed in section 1.2.2, one-photon "forbidden electric dipole" transitions in rare earth ions arise from a second order process involving the product of the matrix elements of the odd parity terms of the crystal field $\langle \Psi' | V_{odd} | 4f^N \rangle$ and the matrix elements of the dipole operator $\langle \Psi' | \vec{D} | 4f^N \rangle$, weighted by the energy denominator $E(\Psi') - E(4f^N)$. The excited intermediate states $|\Psi'\rangle$ belong to configurations of oppposite parity to $4f^N$, that is $4f^{N-1}d$ or $4f^{N-1}g$ configurations. A calculation of the one-photon transition intensities is parameterized by the three Judd-Ofelt parameters, which contain the contributions of the various intermediate states. The rest of the intensity is determined by the angular properties of the initial and final states and the values of the odd parity crystal field parameters. The intermediate configurations contribute to the Judd-Ofelt parameters via two separate quantities; first, through their radial matrix elements with the $4f^N$ configuration, and second, through their energy difference with the $4f^N$ configuration. In the electric dipole approximation, an intermediate configuration Ψ' will have a contribution commensurate with the size of the quantity:

$$\frac{\langle \Psi' | r | 4f^N \rangle}{E(\Psi') - E(4f^N)} \tag{5.22}$$

The radial matrix element is defined by the following integral:

$$\langle \Psi' | r | 4f^N \rangle = \int_0^\infty P_{\Psi'}(r) r P_{4f^N}(r) dr \tag{5.23}$$

where the $P_{nl}(r)$ are the radial distribution functions defined by Cowan [8].

The Judd-Ofelt parameters are usually determined by making a least-squares fit of the calculated to the observed intensities. Except in the case of the hypersensitive transitions,

this usually gives an excellent account of the experimental intensities. The empirical parameters can then be compared to their theoretical expressions. Quite unexpectedly, such a comparison reveals that g orbital wavefunctions make a large contribution to the one-photon intensities. This is very surprising, as the g orbital wavefunctions are significantly higher in energy than the $4f^{N-1}5d$ configuration and their overlap with the 4f wavefunctions considerably smaller.

Axe [1] was the first to realize the importance of g orbital contributions in determining the radiative transition intensities of Eu^{3+} in europium ethylsulfate. From his determination of the Judd-Ofelt parameters necessary to accurately reproduce the observed intensities, he comes to the conclusion that "g orbitals make an important, if indeed not a dominant, contribution to the configurational mixing responsible for electric dipole transition strengths".

Krupke [9] studied the radiative transition transition intensities of selected rare earths in Y_2O_3 and LaF_3. He found that g orbitals contribute more than is expected fron the free ion picture, and that the $4f^{N-1}5d$ configuration contributes to the observed intensities an order of magnitude less than is indicated by the free ion calculations. Modifying the free ion radial matrix elements so as to include the effects of the lattice leads to the conclusion that the bulk of the Judd-Ofelt parameters originates from g orbital configurations. With a certain amount of prescience, Krupke notes that "this conclusion is of importance in estimating the electronic Raman cross sections for spontaneous and stimulated scattering by rare earth ions in solids".

P.J. Becker [10] studied the optical absorption intensities of Ho^{3+} in YPO_4. He found that g orbital contributions are of the same order of magnitude as the d orbital contributions. This is extremely interesting in light of the fact that the Raman studies reported here indicate the major effect of g orbitals in also mediating the electronic Raman transitions of Ho^{3+}. Surprisingly enough, Becker also calculated that the core excitation configurations, $4f^{N+1}3d^9$ and $4f^{N+1}3d^9$, outweigh the $4f^{N-1}5d$ configuration in determining the Judd-Ofelt parameters.

More recently, Hasunama *et al* [11] investigated the fluorescence of Eu^{3+} in europium tris(bromate) enneahydrate. From their calculation of the Judd-Ofelt parameters necessary to fit the experimental data they found that g orbitals were responsible for most of the electric dipole intensities.

The conclusion is then that the bulk of the published studies of the one-photon radiative

transition intensities indicates that g orbitals make a significant if not dominant contribution to the configurational mixing responsible for the intensities. This is extremely surprising in view of the fact that for the free ion the contribution of the g orbitals would be expected to be entirely negligible. In light of the above conclusions, it is not all too unexpected that we find that g orbitals contribute significantly to two-photon radiative transition intensities.

5.3.2 The Role of g Electrons in Electronic Raman Transition Intensities in Rare Earth Phosphate Crystals

The study of the electronic Raman data for Tm^{3+}, Er^{3+}, and Ho^{3+}, in tetragonal phosphate crystals, clearly highlights the importance of the role played by g orbitals in mediating the two-photon transitions of these ions. The data for Tm^{3+} and Er^{3+} indicates that d and g orbitals play comparable roles, whereas the asymmetry of the transitions in Ho^{3+} tends to indicate that g orbitals play the dominant role.

A simple argument, originally due to Judd, can be made to justify *a priori* the comparable importance of d and g orbitals as intermediate states in the electronic Raman process. Consider the expression for the two-photon scattering amplitude $\alpha_{\rho\sigma}$ for a transition from state $|i\rangle$ to state $|f\rangle$:

$$(\alpha_{\rho\sigma})_{if} = -\frac{1}{\hbar}\sum_j \left[\frac{\langle f|D_\rho|j\rangle\langle j|D_\sigma|i\rangle}{\omega_{ji}-\omega} + \frac{\langle f|D_\sigma|j\rangle\langle j|D_\rho|i\rangle}{\omega_{jf}+\omega}\right] \tag{5.24}$$

where $\mathbf{D}$ is the electric dipole operator, ρ and σ denote Cartesian coordinates, $\hbar\omega_{ji}$ and $\hbar\omega_{jf}$ are, respectively, the energy differences $E_j - E_i$ and $E_j - E_f$, and ω is the frequency of the incident radiation. This equation is equivalent to equation 3.22 if one assumes that $|i\rangle$ is the ground state (so that $\hbar\omega_{ji} = \hbar\omega_j$), and also uses the fact that $\hbar\omega_j + \hbar\omega_s = \hbar\omega_j + \hbar\omega - \hbar\omega_f = \hbar\omega_{jf} + \hbar\omega$.

Grouping the sum over intermediate states into a sum over intermediate configurations, each one of which is assumed to be at the degenerate energy $E_{\Psi'}$, we have for the antisymmetric part of the scattering tensor:

$$-\sum_{\Psi', j \text{ in } \Psi'} [\langle f|D_\rho|j\rangle\langle j|D_\sigma|i\rangle - \langle f|D_\sigma|j\rangle\langle j|D_\rho|i\rangle]\frac{\hbar\omega}{E^2_{\Psi'}} \tag{5.25}$$

If we make the hypothesis that $E_{\Psi'}$ is the same for all the intermediate configurations, then we can pull out the energy denominator from the sum and perform a full closure over both

angular and radial variables. The term in square brackets then becomes:

$$\langle f|D_\rho D_\sigma - D_\sigma D_\rho|i\rangle = 0 \tag{5.26}$$

since the components of **D** commute with one another. An alternate way to view this would be with equations 3.45 and 3.46, which show that apart from the energy denominators and dipole matrix elements, the d and g orbitals have contributions that are identical in absolute value and opposite in sign. Setting $E_{df} \approx E_{gf} \approx \bar{E}$, where $\bar{E}$ is some average energy, and using the fact that $\sum_{n'd}\langle 4f|r|n'd\rangle^2 = \sum_{n'g}\langle 4f|r|n'g\rangle^2 = \langle 4f|r^2|4f\rangle$, equations 3.45 and 3.46 then imply that the d and g orbital contributions to the antisymmetric tensor will exactly cancel out. The assumption that d and g orbitals are at roughly the same energy is not at all expected from the free ion picture and, if indeed true, indicates that the presence of the crystalline environment substantially modifies the free ion wavefunctions and optical transition mechanisms.

5.3.3 g and d Orbital Wavefunctions and Electric Dipole Matrix Elements

The free ion wavefunctions, energies, and electric dipole matrix elements provide an important starting point for describing trivalent lanthanide ions in a crystal host. This section describes the results of Hartree-Fock calculations of the free ion states that can serve as intermediate states in a second order one-photon or two-photon transition by a lanthanide ion. The work presented here is the result of computer calculations performed by N. Edelstein.

The lowest energy d configuration is $4f^{N-1}5d$. It is usually assumed that it is the dominant $4f^{N-1}nd$ ($n \geq 5$) configuration as far as optical transition intensities are concerned. The core excitation d configurations, $4f^{N+1}3d^9$ and $4f^{N+1}4d^9$ are very high in energy. Table 5.9 summarizes the energies of the d configurations and their dipole matrix elements with the 4f configuration, from free ion Hartree-Fock calculations. Figure 5.1 shows the radial distribution functions for these configurations, for the ion Tm^{3+}.

Similar calculations can be done for the g orbital configurations. The results are shown in Table 5.10. Figure 5.2 shows the radial distribution functions for these configurations, for the ion Tm^{3+}.

The free ion energies and dipole matrix elements clearly indicate that the $4f^{N-1}5d$ ex-

Table 5.9: Energies and dipole matrix elements of excited d orbital configurations of Tm^{3+} (from Hartree-Fock calculations).

Configuration Ψ'	Energy (cm^{-1})	Dipole Matrix Element $\langle\Psi'\|r\|4f\rangle$
$4f^{11}5d$	81,000	0.54
$4f^{13}3d^9$	11,956,000	0.12
$4f^{13}4d^9$	1,465,000	−0.57

a: not available.

Table 5.10: Energies and dipole matrix elements of excited g orbital configurations of Tm^{3+} (from Hartree-Fock calculations).

Configuration Ψ'	Energy (cm^{-1})	Dipole Matrix Element $\langle\Psi'\|r\|4f^N\rangle$
$4f^{11}5g$	173,000	0.06
$4f^{11}8g$	316,000	0.04
$4f^{11}10g$	326,000	0.03

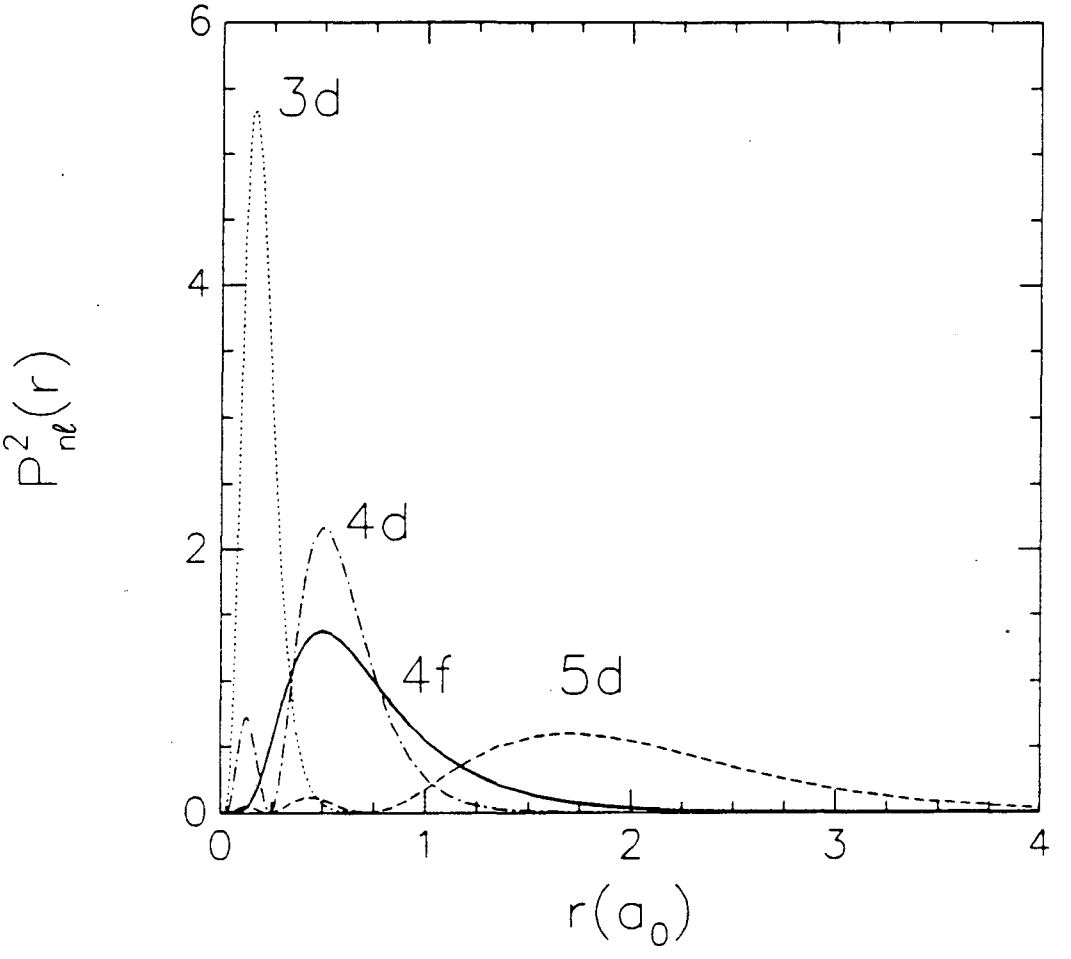

Figure 5.1: Radial distribution functions of the 4f orbital of $4f^{12}$, and of the d orbitals of $4f^{11}5d$, $4f^{13}3d^9$, and $4f^{13}4d^9$.

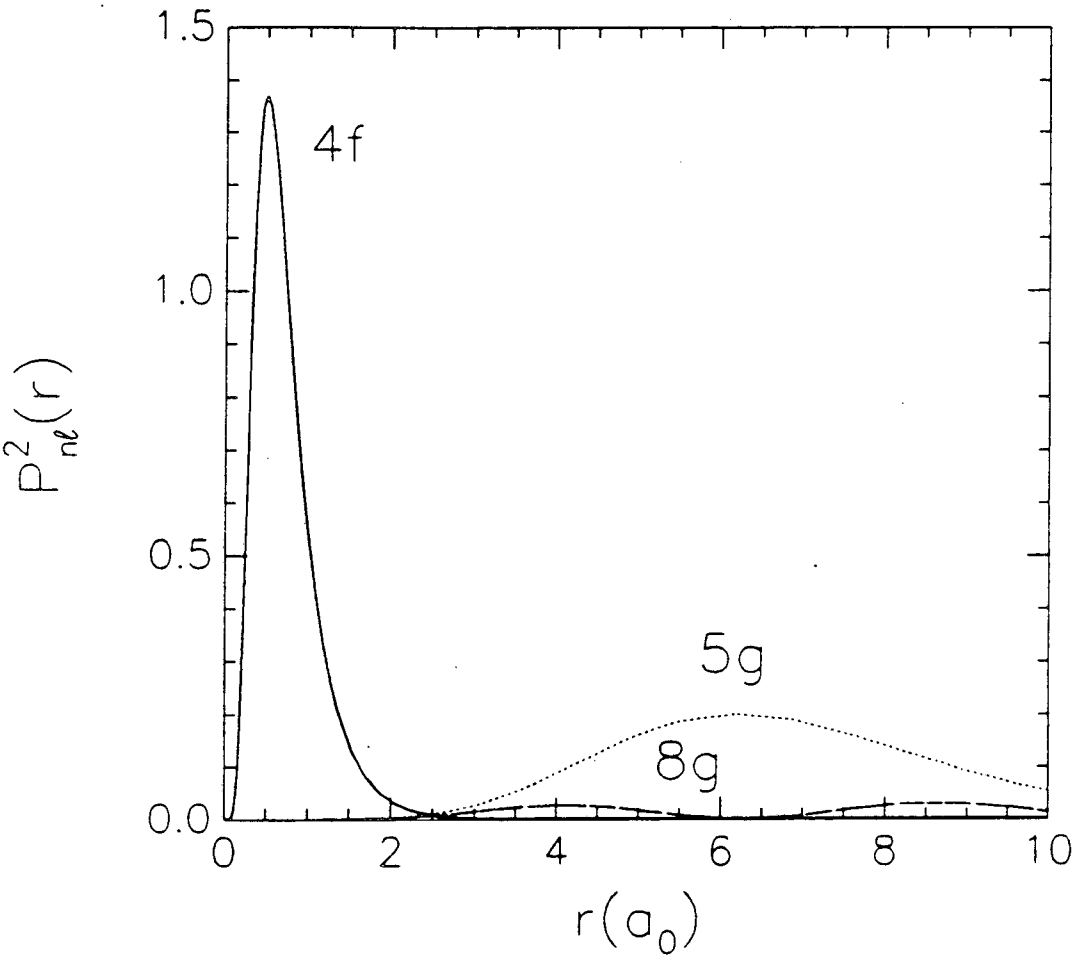

Figure 5.2: Radial distribution functions of the 4f orbital of $4f^{12}$, and of the g orbitals of $4f^{11}5g$ and $4f^{11}8g$.

cited configuration must be the preponderant intermediate state for two-photon transitions in trivalent lanthanide ions. It has the lowest energy and the largest dipole matrix element of any of the excited configurations of the free ion. The bound g configurations, which have energies close to the ionization limit, have only negligible dipole matrix elements with $4f^N$ due to the small overlap of the f and g orbitals. To bring in the first node of the g orbitals close enough to the nucleus to obtain a large overlap with the f orbitals requires $4f^{N-1}g$ configurations that are well into the continuum and have very high energies. Whether these continuum wavefunctions are indeed playing a role in the electronic Raman transitions is still an unanswered question. The main conclusion of this section, and of the preceding ones, is that the free ion numbers fail to explain the radiative transition intensities of rare earth ions in crystals, even though the crystal field is only a weak perturbation on the $4f^N$ states which are participating in the electronic Raman transitions.

5.3.4 The Free Ion Picture vs. Molecular Orbitals

The approach used so far to calculate the optical transition intensities of the lanthanide ions has been an atomic one, in the sense that the wavefunctions used are those of the free ions. In the crystal, the neighbouring ions (the ligands), are considered to produce only a small perturbation which serves to lift the degeneracy of the atomic multiplets. Clearly. this free ion picture is not sufficient to explain the mechanics of the two-photon transitions between the crystal field states.

The ligands are usually not assumed to participate in the radiative processes of the lanthanide ion. This is an extremely static view of the role played by the ligands and is certainly not very close to reality. While for a treatment of the energy level structure of the ground $4f^N$ configuration this model might be a good approximation, for the case of radiative transitions via highly excited virtual intermediate states this can no longer be true. The intermediate states, configurations such as $4f^{N-1}5d$, are no longer localized near the lanthanide nucleus as the $4f^N$ states are, but instead overlap quite significantly the neighbouring ligands. As such, they can no longer be considered pure states of the lanthanide ion but must be combined with the wavefunctions of the neighbouring ions to form molecular orbitals. It is here that the free ion model breaks down and g orbital like wavefunctions can now acquire much more importance than in the free ion.

There is experimental proof for the importance of the ligand effects in the observation

of the so-called *charge transfer* states in absorption or emission spectra [12,13]. These involve the passage of a ligand electron to the lanthanide ion. In molecular orbital language one would say that the electron goes from a predominantly s or p orbital to a bound lanthanide orbital. The observed charge transfer bands lie in the same energy region as the $4f^N$-$4f^{N-1}5d$ transitions. The presence of these charge transfer bands with oscillator strengths comparable to the $4f^N$-$4f^{N-1}5d$ transitions underlines the shortcomings of the free ion model.

A radiative process such as electronic Raman scattering, even though it starts and ends on a state of the $4f^N$ configuration, makes virtual transitions through these excited states or molecular orbitals. In the event that the bulk of the transition amplitude is provided by $4f^N$ intermediate states this problem would not arise as much since the $4f^N$ states in the crystal are still very much like the free ion states. However, for allowed electric dipole transitions the intermediate states must belong to excited d or g orbital configurations. Electronic Raman scattering, with an excitation energy on the order of 20,000 cm^{-1} thus serves, paradoxically enough, as a sensitive probe of physical states that lie much higher in energy than the lower lying $4f^N$ states.

The immediate surroundings of the lanthanide ion is constituted by eight O^{2-} oxygen ions. The oxygen ions have the configuration $(1s)^2(2s)^2(2p)^6$. The valence electrons of the oxygen ion are thus s and p electrons. When considering the construction of the molecular orbitals, it is thus necessary to "hybridize" [14] the nd and ng orbitals of the lanthanide ion on the one hand, and the 2s and 2p orbitals of the oxygen ion on the other. For the ground configuration $4f^N$ one would use the 4f orbitals of the rare earth ion but since they have such a small overlap with the neighbouring ions, the hybridization can be expected to be very weak. The effect of molecular orbitals on crystal field parameters has been a subject of study for quite some time [15,16,17,18,19,20]. Molecular orbitals in tetragonal rare earth vanadates and phosphates have been considered by Gubanov *at al* [21,22]. An actual numerical calculation of the electronic Raman intensities, within the framework of this model, thus requires the calculation of the molecular orbitals for the lanthanide nd and ng orbitals, and perhaps also for the 4f states. The consideration of molecular orbitals for the intermediate states could presumably increase the role played by g orbitals (or orbitals which transform according to their symmetry properties) relative to d orbitals. A recent calculation of the effect of the ligands (the so called ligand polarization effects) in governing

the intensities of two photon transitions has been done by Sztucki and Stręk [24], based on a suggestion by Reid and Richardson [25]. It would be very interesting to to apply their results to the electronic Raman intensity problem.

5.4 Beyond the Single Ion

5.4.1 The Problem of the Missing Tm^{3+} Electronic Raman Transitions

The most glaring discrepancy between the calculated and observed electronic Raman intensities occurs for the Tm^{3+} Γ_1 and Γ_4 transitions predicted by crystal field calculations to be at 248 and 254 cm^{-1}, respectively. Their scattering intensity is calculated to be of the same order of magnitude as that of the line at 86 cm^{-1}, which itself is comparable in strength to the intense 1000 cm^{-1} region phonons. The 248 and 254 cm^{-1} transitions were searched for in the XX, YY, and ZZ polarizations and were found to be completely absent. Their experimental intensity must thus be at least 10^3 to 10^4 times weaker than their predicted intensity.

The interesting point to note about these two transitions is that their calculated intensity is proportional to F_2^2, that is they contain no antisymmetric component. As a result, the g electron theory outlined in the preceding sections cannot provide a direct explanation for the absence of these lines. The g electron theory serves principally to explain the values obtained for the ratio F_1/F_2 which governs the asymmetry of the transitions which have both symmetric and antisymmetric components. Changing F_1/F_2 will not change the intensities of the 248 and 254 cm^{-1} transitions relative to that at 86 cm^{-1}, since all three are proportional to F_2^2 (see appendix B). The inclusion of ligand polarization effects can, however, affect the relative intensities of these three transitions.

One should note that the wavefunctions given in Appendix A would need to be drastically modified in terms of their Russell-Saunders components if one were trying to fit the intensity data. The calculation, for example, of the amplitude of the 248 cm^{-1} electronic Raman intensity shows that the amplitude does not depend on the difference of two large numbers. It can be argued that there is no reason to expect that wavefunctions obtained from an energy level fit will explain optical transition intensities. This should not be taken to mean that their Russell-Saunders components are necessarily incorrect, rather, this should be interpreted as telling us that the wavefunctions are incomplete (e.g. ligand or vibronic

components might be missing), which has an effect on the transition intensities but not on the energy levels and so are not detected by the parametric Hamiltonian fitting procedure.

The lines at 248 and 254 cm^{-1} are predicted to be so strong, and their absence so conspicuous, that one is drawn to the conclusion that perhaps some kind of unsuspected selection rule must be the reason for their disappearance.

5.4.2 Third Order Terms

The inclusion of third order terms in the perturbation expansion for two-photon processes in lanthanide ions was found by Downer to be indispensable in explaining his experimental two-photon absorption data [23]. The third order terms in essence correct the Judd-Ofelt approximation used in the second order term, but is nevertheless smaller than the second order term, as in any "standard" perturbation expansion. Downer's experimental situation was such that the second order term was inordinately small for the lanthanide ions he was studying, making the higher order terms observable. In the case of the electronic Raman transitions studied here the second order term is selection rule allowed and no higher order terms are *a priori* necessary to explain the experimental intensity.

The third order term for electronic Raman scattering has the following form:

$$\sum_{jk}\left[\frac{\langle f|\vec{D}\cdot\vec{E}_1|k\rangle\langle k|V|j\rangle\langle j|\vec{D}\cdot\vec{E}_2|i\rangle}{(\mathrm{E}_j-\hbar\omega_1)(\mathrm{E}_k-\hbar\omega_1)}+\frac{\langle f|\vec{D}\cdot\vec{E}_2|k\rangle\langle k|V|j\rangle\langle j|\vec{D}\cdot\vec{E}_1|i\rangle}{(\mathrm{E}_j+\hbar\omega_2)(\mathrm{E}_k+\hbar\omega_2)}\right] \tag{5.27}$$

where ω_1 is the frequency of the incident photon, ω_2 that of the scattered photon, and V the static perturbation considered in the excited state. Clearly, the ratio of the third order term to the second order one is given by the size of $\frac{\langle k|V|j\rangle}{(\mathrm{E}_k-\hbar\omega_1)}$.

There are three types of third order terms, depending on which perturbation is considered for the intermediate states. The spin-orbit Hamiltonian is the weakest of the three and, barring some selection rule breakdown, can be neglected. For the $4f^{N-1}5d$ configuration the spin-orbit parameter is a couple of thousand wavenumbers in energy units, which is very small compared to the average energy denominator of 100,000 cm^{-1}.

Using the crystal-field perturbation in the excited intermediate states leads to a ratio of the third-order term to the second order one of roughly $\frac{\mathrm{B}_q^{(k)}}{\mathrm{E}_j}$, where the $\mathrm{B}_q^{(k)}$ are the crystal field parameters for the excited states. Taking for example the $4f^{N-1}5d$ configuration, the crystal field parameters are on the order of 20,000 cm^{-1} and the energy denominator is 100,000 cm^{-1}, which yields a value of 0.2 for the magnitude of the third-order term relative

to the second order one. This means that it will not have a very large effect on Raman transition intensities that are allowed in second order. It is perhaps of some interest to calculate the third-order term for electronic Raman scattering, with V being the crystal field Hamiltonian. We can basically extend with some slight modifications the results of Downer for two-photon absorption. A calculation of the third order crystal field correction in the case of $TmPO_4$ showed that it produced an effect of at most 10%.

It might be expected that the strongest static perturbation in the third order term would be provided by the electrostatic interaction. Since the intermediate states are of the form $4f^{N-1}nl$, this excited configuration can be pictured as consisting of a $4f^{N-1}$ core and an outer nl electron. The electrostatic interaction is then separated into two pieces; one which represents the repulsion between the the 4f electrons of the core, and one for the interaction betweeen the core and the nl electron. The electrostatic repulsion between the 4f electrons is quite large, on the order of the Slater F^k parameters (10,000 to 100,000 cm^{-1}).

However, a calculation of the third order term with the electrostatic repulsion between the (N-1) 4f electrons of the $4f^{N-1}nl$ configuration as the middle matrix element of equation 4. 5.27 yields identically zero. This can be shown diagramatically using many-body atomic theory [26]. We conclude that third order effects that involve perturbations in the intermediate states, and thus attempt to correct for the closure approximation, do not appear to have a bearing on the problems discussed here.

5.4.3 Vibronic Effects

A further improvement upon the theory considered so far is the inclusion of the lattice and its vibrational modes as participants in the radiative process. There are two distinct regimes of vibromic effects; the strong coupling case and the weak coupling case. It is usually the weak coupling case that is assumed for lanthanide ions doped in crystals, and we will treat this case first. There is growing experimental evidence for strong coupling and this case will be discussed in turn at the end of this section.

The wavefunctions are written in the Born-Oppenheimer approximation as the product of an electronic wavefunction and a vibrational wavefunction:

$$|i\rangle = |g\rangle|m\rangle \tag{5.28}$$

where $|g\rangle$ is an electronic state and m represents vibrational quantum numbers, as the vi-

brational quantum states can be classified by the phonon occupation numbers. A transition between two states thus involves a change in either the electronic state or the vibrational state, or both. It is common to use the notation n-m for a particular electronic transition to specify the phonon occupancy numbers of the initial and final states. The phonon occupancy numbers should be thought of in the general sense as being the ocupation numbers for all the phonon modes allowed by symmetry. The vast majority of the rare earth phosphate 4f-4f absorption and emission lines observed are 0-0 lines, that is they are purely electronic lines and do not involve any phonon excitations. The transitions from the $4f^{N-1}5d$ to the $4f^N$ states, however, can involve the excitation of one or more phonons. This comes from the fact that the $4f^N$ states, which have strong atomic identity, have a relatively weak coupling with the phonons, but excited configurations such as $4f^{N-1}5d$ have a large overlap with the neighbouring ligands and have significant vibronic coupling.

The effect of vibronic coupling can be visualized best by means of the *configuration coordinate model* [27]. The effect of the lattice vibrations is represented by a harmonic oscillator potential for the electronic states, which is a function of the generalized coordinates Q of the ions of the lattice. The potential energy minima of the $4f^N$ states are all at about the same normal coordinate, whereas the potential minima of the excited configurations are then shifted relative to those of the ground state. The Franck-Condon principle then implies that transitions between ground and excited configurations involve the excitation of one or more vibrational quanta. This is the cause of the large Stokes shift between absorption and fluorescence frequencies in 4f-5d rare earth ion transitions and the presence of strong vibronic sidebands. More detailed discussions of vibronic effects in lanthanide ion one-photon spectra can be found in Imbusch and Kopelman [27] and Englman [28].

The calculation of the Raman transition amplitudes in the framework of the Born-Oppenheimer approximation is well known, at least in the formal sense [29]. It makes use of the expansion of the dipole operator of the electronic system as a function of the normal coordinates of the lattice ions (the Hertzberg-Teller expansion). The importance of the vibronic effects is measured by the size of $\frac{\partial D_\rho}{\partial Q}$, where D_ρ is the dipole operator and Q represents the normal coordinates of the ions. It turns out that because of the sum over intermediate states that occurs in the expression for the Raman amplitude, closure can be performed over the vibrational wavefunctions and thus in zeroth order the effects of vibronic coupling in the intermediate states, characterized for example by the displacement in the

potential energy minima between $4f^N$ and $4f^{N-1}5d$ states, have no effect on the Raman amplitudes [29]. As a result, vibronic coupling in the excited states is not an explanation for the unexpected electronic Raman intensities obtained for Tm^{3+}, E^{3+}, and Ho^{3+} in the tetragonal phosphate crystals. Only a difference in vibronic coupling between initial and final states will produce an effect (in zeroth order). This is not expected to occur for $4f^N$ states.

The higher order terms in the Raman amplitude result in vibroelectronic Raman transitions that involve the simultaneous change in both electronic and vibrational states. These would appear in the Raman spectra as sidebands akin to the sidebands observed in fluorescence or absorption. No vibroelectronic Raman peaks were observed in this study. The electronic Raman transitions are thus of the 0-0 type which is not to surprising since the one-photon $4f^N$ transitions are of the 0-0 type.

The above discussion tends to indicate that vibronic coupling effects can be neglected for $4f^N$ states. On the other hand, there is growing indication of strong electron-phonon coupling that involves specific $4f^N$ crystal field electronic states and phonons, in a number of rare earth crystals. The first example of this is provided by the cooperative Jahn-Teller transitions in the rare earth vanadates [30]. Another category of effects are the magetoelastic and anticrossing effect studied by Schaack and his collaborators over the years [31,32,33,34,35]. Chapter 6 of the present work provides evidence for extremely strong electron-phonon coupling in $YbPO_4$. The conclusion is that in spite of the atomic nature of the $4f^N$ states there can nevertheless be strong coupling between the electronic and vibrational states. Whether this occurs on a localized or delocalized scale, and why it occurs only for certain crystals and certain states is still a matter for speculation.

The wavefunctions of such strongly coupled states must be treated according to the precepts of quantum mechanics for strongly interacting states, i.e. a Hamiltonian needs to be diagonalized, perturbation theory is no longer valid, and the new eigenstates are hybrid modes that can no longer be called electronic or phonon modes. As far as our calculated Raman intensities are concerned, this means that our wavefunctions are missing components that arise out of this hybridization. These components contribute to the transition intensity quite drastically since the phonons have such strong Raman scattering strengths, but not very much to the energies, at least not on the scale of a crystal field fit. One could for example hypothesize that since phonon scattering is symmetric the effect of the coupling

might be to "symmetrize" the electronic Raman transitions. This could hold for the 138 and 280 cm^{-1} transitions of Tm^{3+} and the 193 and 251 cm^{-1} transition of Ho^{3+} which are near E_g phonons (of the right symmetry for coupling to Γ_5 electronic transitions). Only in the case of phonon E_g^2 of Ho^{3+} is there any indication of the anomalous frequency shifts (of either the electronic or vibrational states) that are direct evidence of electron-phonon coupling.

5.4.4 Concentration Effects and Ion-Ion Correlations

Concentration effects are well known to be extremely important in rare earth systems. Fluorescence quenching and cooperative phenomena are two examples of these types of phenomena [15,36]. It is important to note that so far our approach has dealt only with single ions, which is the most natural conceptual starting point. It has been found that the forbidden electric dipole matrix elements of trivalent lanthanide ions do not vary much with concentration, so it is not unreasonable to expect the same of the Raman transition intensities. The observed nonresonant relative intensities of the electronic Raman transitions studied in Tm^{3+}:$LuPO_4$ and Er^{3+}:$LuPO_4$ were found to remain the same, within experimental error, when the optically active lanthanide ion of the rare earth phosphate crystal was diluted from a 100% constituent to 10%. 1% Tm^{3+} in $LuPO_4$ was also studied and did not contradict the data of the higher concentration crystals in that the missing lines at 248 and 254 cm^{-1} did not appear, even though the 86 cm^{-1} transition was clearly observable and the missing lines are predicted to be of the same order of magnitude as that line.

When the interaction between neighbouring ions is sufficiently strong, then transfer of electronic excitation can occur from ion to ion and these excitations, no longer localized on a specific ion, are more appropriately called *excitons*. Electronic Raman scattering probes excitons with wavevector $\vec{q} = 0$. The symmetry properties of the excitons can be treated in a similar fashion as that of the phonons. Their symmetry is determined by the crystal space group. At $\vec{q} = 0$ the appropriate group to describe either the vibrational or electronic excitations is the factor group, which is the point group of the crystal. The factor group is also the invariance group of the primitive cell. Since there are two ions in the primitive cell, the passage from the site symmetry group to the factor group is the result of "turning on" the interaction between the two ions. The interaction splits into two the excited single ion states, the splitting being known as the *Davydov splitting* [37]. For rare

earth ions the Davydov splitting of the $4f^N$ states is usually quite small as the interaction between neighbouring lanthanide ions is weak. This originates from the small overlap of their respective 4f orbitals.

The factor group for the tetragonal phosphate crystals is D_{4h}, which can be considered to be the direct product of D_{2d} and the inversion group. Each irreducible representation of D_{2d} now has a label that indicates whether it has even or odd parity under the inversion operation. The wavefunctions of the coupled ions are thus symmetric and antisymmetric linear combinations of the products of the wavefunctions for each of the two ions. The only new selection rule that has been introduced by this is that the electronic Raman transition must conserve parity. No group theoretical selection rule has arisen that would forbid the 248 and 254 cm^{-1} transitions. Thus it is not immediately apparent how ion-ion correlations would solve the problem of the missing lines. However, since the experiments were not done in extremely dilute crystals which would prevent ion-ion coupling from occuring, the possibility of a concentration effect cannot be completely ruled out.

5.5 Future Directions

It is clear that electronic Raman scattering has uncovered a new perspective on optical transition mechanisms in rare earth ions in crystals. The fact that orbitals with g electron characteristics can play an important role in governing these transitions seems to recur in a number of experiments. It would be worthwhile to do electronic Raman scattering in a different type of crystal, LaF_3 for example, and see whether changing the ligands has any kind of influence on the Raman intensity pattern. From the experimental point of view, it might be advantageous to attack the problem using a technique such as stimulated Raman scattering.

Another interesting avenue of research would be to use the excited state Raman effect [38,39,40]. One can populate an excited state and observe Raman scattering from it, and repeat the intensity calculations for transitions that originate considerably higher in energy than the ground state and are closer to the possible intermediate states.

References

[1] J.D. Axe, J. Chem. Phys. **39**, 1154 (1963).

[2] J.A. Koningstein and O.S. Mortensen, Phys. Rev. **168**, 75 (1968).

[3] J.A. Koningstein, J. Chem. Phys. **51**, 1163 (1969).

[4] R.L. Wadsack, J.L. Lewis, B.E. Argyle, and R.K. Chang, Phys. Rev. **3**, 4342 (1971).

[5] P.C. Becker, N. Edelstein, G.M. Williams, J.J. Bucher, R.E. Russo, J.A. Koningstein, L.A. Boatner, and M.M. Abraham, Phys. Rev. B **31**, 8102 (1985).

[6] P.C. Becker, N. Edelstein, B.R. Judd, R.C. Leavitt, and G.M.S. Lister, J. Phys. C **18**, L1063 (1985).

[7] C.W. Nielson and G.F. Koster, *Spectroscopic Coefficients for the p^n, d^n, and f^n Configurations* (The M.I.T. Press, Cambridge, Massachussetts, 1963).

[8] R.D. Cowan, *The Theory of Atomic Structure and Spectra* (University of California Press, Berkeley, 1981).

[9] W.F. Krupke, Phys. Rev. **145**, 325 (1966).

[10] P.J. Becker, Phys. Stat. Sol. (b) **43**, 583 (1971).

[11] M. Hasunama, K. Okada, and Y. Kato, Bull. Chem. Soc. Jpn. **57**, 3036 (1984).

[12] R. Reisfeld and C.K. Jørgensen, *Lasers and Excited States of Rare Earths* (Springer-Verlag, Berlin, 1977). see in particular chapter 1, section D.

[13] E. Nakazawa and F. Shiga, J. of Lumin. **15**, 255 (1977).

[14] C.J. Ballhausen and H.B. Gray, *Molecular Orbital Theory* (The Benjamin/Cummings Publishing Company, Frontiers in Chemistry Series, Reading, Massachussetts, 1964).

[15] S. Hüfner, *Optical Spectra of Rare Earth Compounds* (Academic Press, New York, 1978).

[16] C.K. Jørgensen, R. Pappalardo, and H-H Schmidtke, J. Chem. Phys. **39**, 1422 (1963).

[17] G. Burns and J.D. Axe, in *Optical Properties of Ions in Crystals*, H.M. Crosswhite and H.W. Moos, eds. (Interscience, John Wiley and Sons, New York, 1966), p.53.

[18] W. Urland, Chem. Phys. **14**, 393 (1976).

[19] W. Urland, Chem. Phys. Lett. **77**, 58 (1981).

[20] D. Garcia and M. Faucher, J. Chem. Phys. **82**, 5554 (1985).

[21] V.A. Gubanov, M.V. Ryzhkov, and V.P. Zhukov, Opt. Spectrosc. **45**, 177 (1977).

[22] V.A. Gubanov, D.E. Ellis, and A.A. Fotiev, J. Sol. St. Chem. **21**, 303 (1977).

[23] M.C. Downer, Ph.D. thesis, Harvard University, Cambridge, 1983 (unpublished).

[24] J. Sztucki and W. Stręk, Phys. Rev. B **34**, 3120 (1986).

[25] M.F. Reid and F.S. Richardson, Phys. Rev. B **29**, 2830 (1984).

[26] R.P. Leavitt, Johns Hopkins University, unpublished results.

[27] G.F. Imbusch and R. Kopelman, in *Laser Spectroscopy of Solids*, W.M. Yen and P.M. Selzer, eds. (Springer-Verlag, Berlin, 1981), p. 1.

[28] R. Englman, *Non-Radiative Decay of Ions and Molecules in Solids* (North-Holland Publishing Co., Amsterdam, 1979). see in particular chapter 19 on rare earth ions.

[29] R.J.H. Clark and T.J. Dines, in *Advances in Infrared and Raman Spectroscopy*, Vol. 9, R.J.H. Clark and R.E. Hester, eds. (Heyden, London, 1982), p. 282.

[30] R.J. Elliott, R.T. Harley, W. Hayes, and S.R.P. Smith, Proc. Roy. Soc. Lond. A **328**, 217 (1972).

[31] H. Gerlinger and G. Schaack, Phys. Rev. B **33**, 7438 (1986).

[32] M. Dahl and G. Schaack, Z. Phys. B **56**, 279 (1984).

[33] K. Ahrens, H. Gerlinger, H. Lichtblau, G. Schaack, G. Abstreiter, and S. Mroczkowski, J. Phys. C **13**, 4545 (1980).

[34] K. Ahrens and G. Schaack, Phys. Rev. Lett. **42**, 1488 (1979).

[35] H. Gerlinger and G. Schaack, Phys. Rev. B **33**, 7438 (1986).

[36] F.E. Auzel, Proc. IEEE **61**, 758 (1973).

[37] W. Hayes and R. Loudon, *Scattering of Light by Crystals* (Wiley, New York, 1978).

[38] B. Halperin and J.A. Koningstein, J. Chem. Phys. **69**, 3302 (1978).

[39] M. Asano, D. Mongeau, D. Nicollin, R. Sasseville, and J.A. Koningstein, Chem. Phys. Lett. **65**, 293 (1979).

[40] B. Halperin and J.A. Koningstein, Can. J. Chem. **59**, 2792 (1981).

Chapter 6

Resonant Electronic Raman Scattering in Erbium Phosphate Crystals - Experimental Results and Discussion

This chapter describes and analyzes the observation of resonance enhancement factors of 10 to 100 of the electronic Raman transitions within the ground $^4I_{15/2}$ multiplet of Er^{3+} in concentrated and dilute erbium phosphate crystals [1]. The energy of the 488.0 nm argon-ion laser line which is used for the excitation is almost coincident in energy with the transitions between the crystal field levels of the $^4F_{7/2}$ excited multiplet and the $^4I_{15/2}$ ground level. Particular attention is paid to demonstrating the point that in $ErPO_4$ one is observing resonance Raman scattering and not fluorescence. The spectra of $ErPO_4$ and 10% Er in $LuPO_4$ are compared and contrasted.

6.1 Introduction - Resonance Enhancement of Electronic Raman Scattering in Rare Earth Crystals

The enhancement of electronic Raman scattering transitions can occur via different types of resonances. Usually, the resonance enhancement of a nonlinear optical process is mediated by an allowed electric dipole transition. In the case of trivalent lanthanide ions, this implies that strong resonance enhancement of electronic Raman transitions occurs for excitation very close in energy to that of a $4f^N \longrightarrow 4f^{N-1}5d$ transition. This requires ultraviolet excitation, an experimental complication, since most tunable lasers operate in the visible region of the spectrum. Resonance enhancement in the visible can occur via a

$4f^N \longrightarrow 4f^N$ transition, however, since the oscillator strengths of such transitions are very weak, the effect is expected to be quite small.

The Raman scattering tensor that arises in the second order calculation of the Raman transition amplitude between $4f^N$ states has the form:

$$(\alpha_{\rho\sigma})_{if} = -\sum_j \left[\frac{\langle f|D_\rho|j\rangle\langle j|D_\sigma|i\rangle}{E_{ji} - \hbar\omega + i\Gamma_j} + \frac{\langle f|D_\sigma|j\rangle\langle j|D_\rho|i\rangle}{E_{jf} + \hbar\omega + i\Gamma_j} \right] \tag{6.1}$$

for a transition from state $|i\rangle$ to state $|f\rangle$, where D_ρ is the electric dipole operator, ρ and σ are Cartesian coordinates, $|j\rangle$ is the intermediate state, and Γ_j is a damping factor that is inversely proportional to the dephasing lifetime of the radiative state [2,3]. The damping factor is necessary to prevent the expression from going to infinity in cases where the excitation energy exactly or almost exactly matches the transition between two states of the system. The damping factor is usually small compared to the real part of the energy denominator and can be neglected unless the excitation is very close to resonance. In the nonresonant situations discussed in chapters 4 and 5, no damping factors are needed and the intermediate states are all considered to belong to excited configurations of opposite parity to $4f^N$. However, if the energy of the exciting radiation is very close to that of a $4f^N$-$4f^N$ transition, then the energy denominator of the first term of equation 6.1 is very small and this compensates for the weakness of the $4f^N$-$4f^N$ matrix elements. Therefore, one may expect a noticeable change to occur in the electronic Raman intensity pattern with respect to the polarizations of the incident and scattered photons, as opposed to the pattern with nonresonant excitation.

A simple order of magnitude estimate can be made of the resonance enhancement that such a mechanism will produce [4]. We consider first the nonresonant contribution of the higher energy opposite parity configurations. For the sake of simplicity the $4f^{N-1}5d$ configuration will be used as the dominant intermediate state. The first term of the Raman tensor can be symbolically represented as:

$$\frac{\langle f|D_\rho|4f^{N-1}5d\rangle\langle 4f^{N-1}5d|D_\sigma|i\rangle}{E_{5d4f} - \hbar\omega} \tag{6.2}$$

where E_{5d4f} is the average energy difference between the $4f^N$ and $4f^{N-1}5d$ configurations. The product of the two matrix elements in the numerator is proportional to the oscillator strenth of 4f-5d transitions, which since they are electric dipole allowed are on the order of 0.1 to 1. In units of oscillator strength per cm^{-1} the order of magnitude of the nonresont

Raman amplitude is thus:

$$\frac{10^{-1} \text{ to } 1}{10^5} = 10^{-6} \text{ to } 10^{-5} \tag{6.3}$$

Now, for a resonance with a 4f-4f transition we might have an energy mismatch of 1 to 10 cm^{-1} between the excitation energy and that of the transition, and the oscillator strengths of the 4f-4f forbidden electric dipole are known to be about 10^{-6} to 10^{-7}. The order of magnitude of the Raman tensor is then estimated to be (only the first term in equation 5.1 is important with resonant excitation):

$$\frac{10^{-6} \text{ to } 10^{-5}}{1 \text{ to } 10} = 10^{-7} \text{ to } 10^{-5} \tag{6.4}$$

The resonant contribution is seen to be comparable in amplitude to the nonresonant contribution, especially if the excitation is only a few wavenumbers away from the transition.

Nevertheless, with the exception of the work of Nicollin and Koningstein [5] and of Wadsack and Chang [6], there are few reports of resonance electronic Raman scattering in trivalent rare earth doped crystals. In the resonance Raman studies noted above, enhancement factors that were of the order of 5 at most were reported, whereas in the erbium phosphate studies reported here the enhancement factors are on the order of 10 to 100. Somewhat similar resonance effects have been observed for other nonlinear optical processes, such as four wave mixing phenomena [7,8], in rare earth crystals.

6.2 Overview of the Situation in Erbium Phosphate Crystals

6.2.1 Electronic Energy Level Structure of Er^{3+}

The absorption studies and crystal field fits performed on 1% Er^{3+} doped in $LuPO_4$ and YPO_4 allow the construction of the electronic energy level diagram of the erbium ion. The atomic multiplets are split into crystal field levels characterized by the irreducible representations of D_{2d} according to which they transform. This diagram is shown in Figure 6.1 for the energy range 0 to 27,000 cm^{-1}. The atomic multiplets are labeled by their dominant Russell-Saunders components and their widths represent the crystal field splitting. It is based on the data of Hayhurst *et al* [9] and on wavefunction calculations using the parameters they report. Also indicated is the 488.0 nm line of the argon ion laser which is resonant with the $^4I_{15/2} \longrightarrow {}^4F_{7/2}$ transitions.

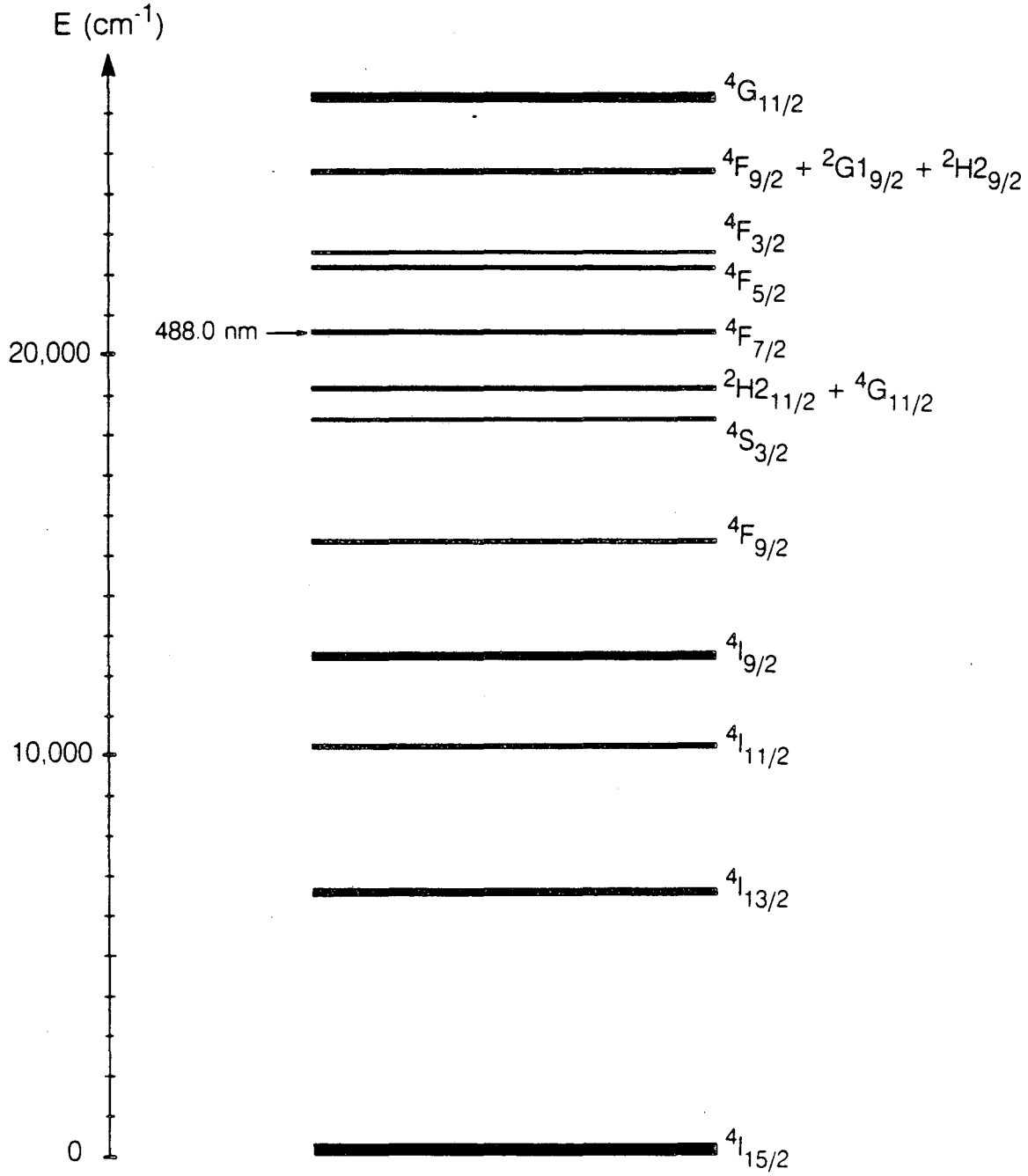

Figure 6.1: Electronic energy level diagram of Er^{3+} doped in $LuPO_4$, from 0 to 27,000 cm^{-1}. The widths of the manifolds indicate the crystal field splittings. The resonant excitation 488.0 nm line of the argon-ion laser is shown.

6.2.2 Absorption Studies of the Resonant $^4F_{7/2}$ Multiplet

The precise locations of the crystal field levels of the $^4F_{7/2}$ and $^4I_{15/2}$ multiplets need to be known for an accurate understanding of the resonance Raman phenomena in the erbium phosphate crystals. For the $^4F_{7/2}$ multiplet there are four levels, two of Γ_6 symmetry and two of Γ_7 symmetry. The levels were located by taking absorption spectra at both 4.2 and 77 K, this last temperature allowing the observation of the excited crystal field states of the ground state, with photographic plates taken with a 3.4 m Ebert spectrograph (see Chapter 2). Figure 6.2 shows the energies of the crystal field levels of the $^4F_{7/2}$ multiplet of the Er^{3+} ion for the various crystals $Er_xLu_{1-x}PO_4$, with x = 1; 0.5; 0.2; 0.1; 0.01, and also for 1% Er^{3+} in YPO_4. The spectrometer has an accuracy of ± 0.1 cm^{-1}, however the levels have a certain breadth and the centers of the lines need to be estimated. As a result, the uncertainty of the energy values given in Figure 6.2 is ± 0.25 cm^{-1}. The lower Γ_7 level (20,485 cm^{-1} in $ErPO_4$) is somewhat more uncertain since only in the case of $ErPO_4$ and 1% Er^{3+} in $LuPO_4$ was it directly observed in the absorption spectra. For the other concentration crystals it is too close to the lower Γ_6 level which has extremely strong absorption intensities. For the 10%, 20%, and 50% Er^{3+} in $LuPO_4$ crystals the value of the lower Γ_7 energy level needs to be inferred from T=77 K absorption transitions that originate in excited crystal field levels of the ground multiplet. It is usually averaged from three different transitions and has an uncertainty on the order of ± 0.5 cm^{-1}. The energy values of the $^4I_{15/2}$ excited crystal field levels are listed as the need arises in tables in the following sections.

Unfortunately, the photographic plates do not give the linewidths of the states since the plates do not have a linear response to the amount of light incident upon them. To determine these linewidths, which play an important role in determining the resonant electronic Raman spectra, absorption measurements were taken with a tungsten lamp. These measurements were also repeated with a pulsed dye laser [10]. The tungsten lamp output was loosely focussed on the crystal and the transmitted light was analyzed with the SPEX double monochromator and the collection optics used for the Raman experiments (see chapter 2). The current supplied to the tungsten lamp was kept low to prevent heating of the sample. The output of the tungsten lamp is relatively flat over the 100 cm^{-1} span of the $^4F_{7/2}$ multiplet. To measure the narrower linewidths it was necessary to take spectra with the spectrometer entrance and exit slits closed down to 35μ. The tungsten lamp absorption spectra of $ErPO_4$, taken at T$\approx$4.2 K (the temperature is measured at the tip of the cold

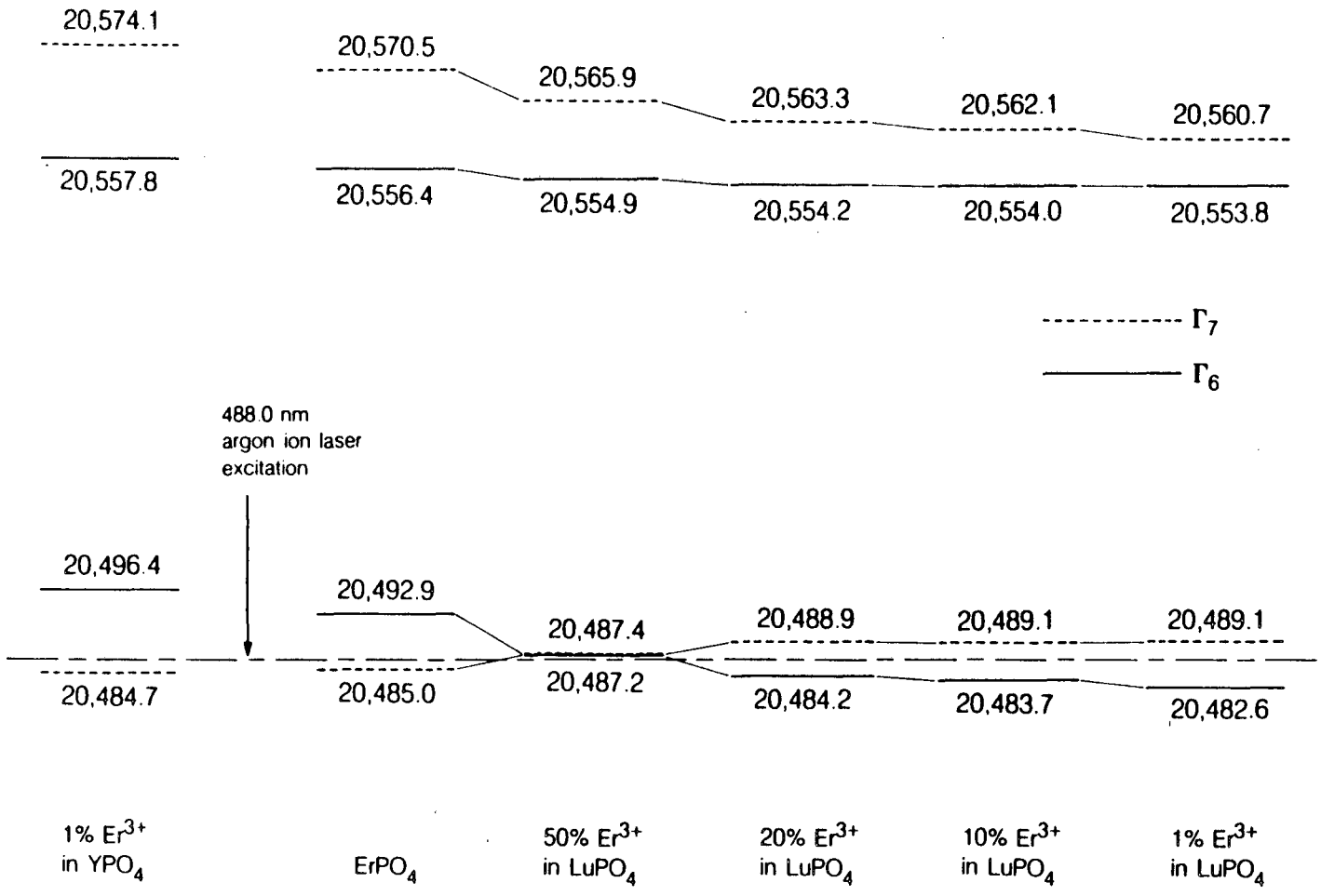

Figure 6.2: Crystal field levels of the $^4F_{7/2}$ manifold of Er^{3+} for varying concentration erbium phosphate crystals. All energy values are in vacuum wavenumbers. The 488.0 nm line of the argon-ion laser is at 20,486.7 cm^{-1} (in vacuum).

finger), are shown in Figure 6.3. This figure gives a clear picture of the relative intensities of the various absorption transitions. It is important to notice that for the lower Γ_6 and Γ_7 levels, which are the ones directly involved in the enhancement process, the oscillator strength of the transition to the Γ_6 level is much stronger than that to the Γ_7 level. The lower Γ_6 level will thus play the dominant role in the enhancement of the electronic Raman transitions. Tungsten lamp absorption measurements taken at higher temperatures allow the observation of transitions that originate in excited crystal field states of the ground multiplet. It was also observed that the crystal transmits roughly twice as much light in π polarization (Z polarized light) as opposed to σ (X,Y polarized light) polarization, which is due to the fact that the crystal is birefringent and has two different indices of refraction.

The linewidths, measured as the full width at half maximum, are listed in Table 6.1. The main problem is that the absorptions are so strong that the crystal usually absorbs 100% of the light incident upon it in a small wavelength region near the peak of the absorption. This can artificially distort the lineshapes and broaden the lines. The $ErPO_4$ sample was available as a very thin platelet so that its spectra appeared to be much more distortion free than those of the 10% Er^{3+} in $LuPO_4$ crystal which was comparatively thick. The problem is more acute in σ polarization then in π polarization since the absorption is significantly stronger in the former. When possible, the π polarization absorptions are used to measure the linewidths. Linewidths that are potentially overestimated by a one or two cm^{-1} are indicated in Table 6.1 by a dagger. The other linewidths are accurate to ± 0.5 cm^{-1} and those of the 1% Er^{3+} doped crystal are accurate to ± 0.25 cm^{-1}. Even though the lower Γ_7 level could not be observed with the tungsten lamp absorption measurements its linewidth can be estimated to be at the most 1 cm^{-1} (from photographic plates and pulsed dye laser absorption).

6.2.3 Fluorescence Studies of Erbium Doped Phosphate Crystals

The fluorescence spectrum of the Er^{3+} manifolds can be studied by exciting the crystal with one of the argon-ion laser lines. For the multiplets of interest here we use the lines that lie above the 488.0 nm line (476.5 nm, etc.). The main conclusion of these studies is that the $^4F_{7/2}$ and $^2H_{11/2}$ multiplets fluoresce extremely weakly whereas the $^4S_{3/2}$ and $^4F_{9/2}$ multiplets fluoresce extremely strongly. This is similar to the findings of Reed and Moos [11] in their study of multiphonon relaxation of excited states of rare earth ions in YPO_4 (see

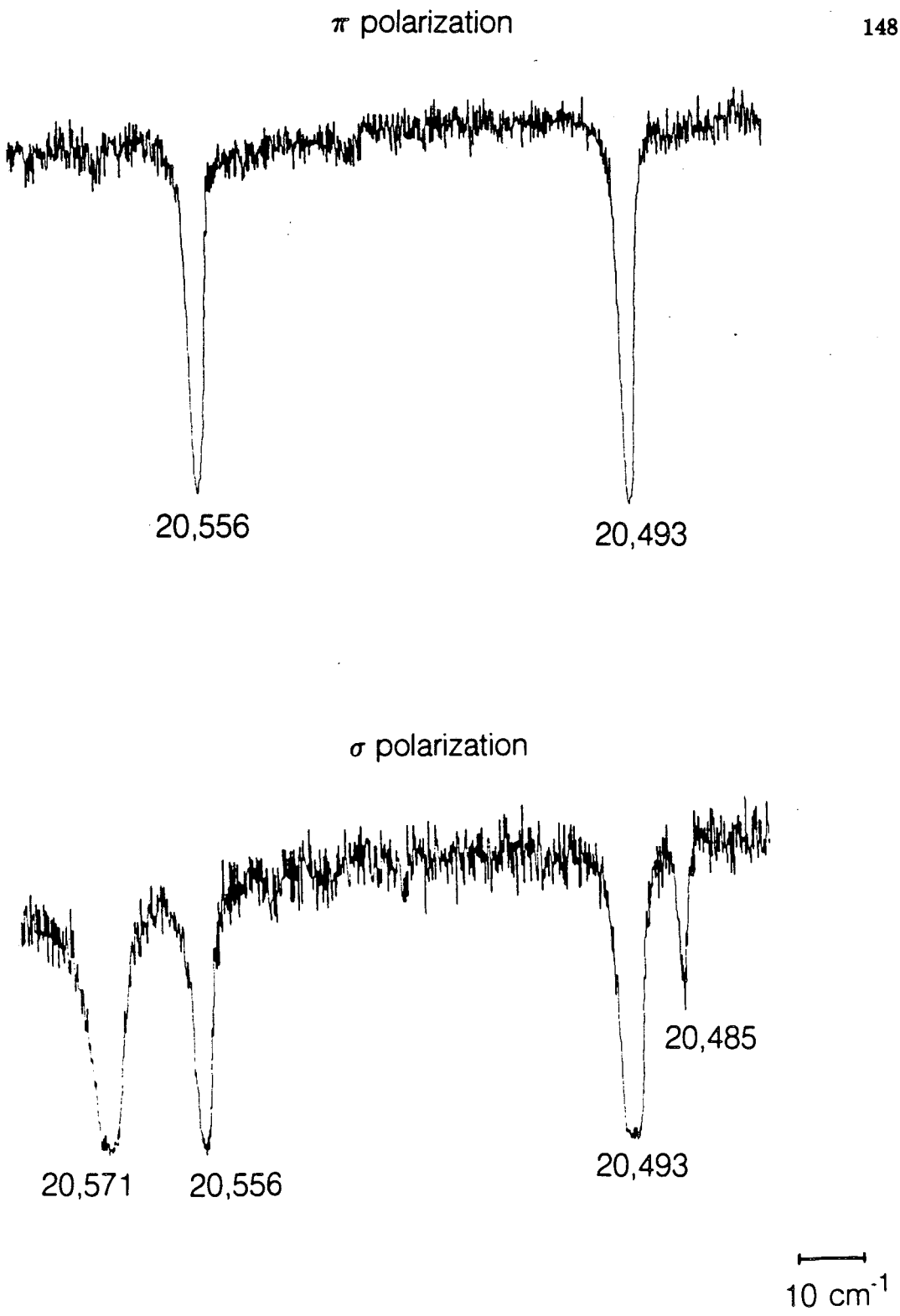

Figure 6.3: Absorption spectra at T≈4.2 K of the $^4F_{7/2}$ multiplet of Er^{3+}. The crystal sample is $ErPO_4$. The spectrometer slit settings are 35-100-100-35 μ and the spectral bandpass is 0.5 cm^{-1}.

Table 6.1: Linewidths in cm^{-1} of the $^4F_{7/2}$ multiplet crystal field levels as measured photometrically. See Figure 6.2 for the energy level values for the crystals listed.

	higher Γ_7 level	higher Γ_6 level	lower Γ_6 level	lower Γ_7 level
$ErPO_4$	5.5†	2.5	2.5	1.5
10% Er^{3+} in $LuPO_4$	8.5†	3.5	6.5†	not observed
1% Er^{3+} in $LuPO_4$	1.5	1.0	1.0	not observed

†: Could be overestimated due to strong absorption.

in particular their Figure 2). The physical processes that are thought to be occuring are depicted in Figure 6.4. Ions excited to the $^4F_{7/2}$ and $^2H_{11/2}$ manifolds decay nonradiatively in cascade fashion to the $^4S_{3/2}$ and $^4F_{9/2}$ states, with a fast enough decay rate that the $^4F_{7/2}$ and $^2H_{11/2}$ states can fluoresce only weakly. Very strong fluorescence then occurs from the $^4S_{3/2}$ and $^4F_{9/2}$ multiplets. The energy gap between the $^4F_{7/2}$ multiplet and the $^4S_{3/2}$ multiplet can be bridged almost exactly with two 1000 cm^{-1} region optical phonons, which is perhaps one of the reasons that the nonradiative decay between those two multiplets is so strong. The fluorescence spectrum of $ErPO_4$ excited with the 476.5 nm line of the argon-ion laser is shown at four different temperatures in Figure 6.5 across the spectral range from 21,000 to 15,000 cm^{-1}. The relative intensity of the phonon and fluorescent peaks can be clearly followed. The fluorescence spectrum of 1% Er^{3+} in $LuPO_4$ excited at 476.5 nm is quite similar, the transitions from the $^4S_{3/2}$ and $^4F_{9/2}$ multiplets decreasing in absolute intensity by one or two orders of magnitude relative to $ErPO_4$. The only differences are that in the 1% crystal there is a slight change in the relative intensities of these fluorescent transitions. For both $ErPO_4$ and Er^{3+} diluted in $LuPO_4$ some extraneous fluorescent peaks that appear to be due to Pr^{3+} and/or Eu^{3+} impurities can be observed in the spectra.

A study was made of the fluorescence from the $^4F_{7/2}$ multiplet using the 476.5 nm exciting line and the $ErPO_4$ crystal. It is several orders of magnitude weaker than the $^4S_{3/2}$ and $^4F_{9/2}$ fluorescence. The spectra obtained are shown in Figure 6.6. The fluorescence observed at 4.2 K is from the Γ_6 level at 20,493 cm^{-1} to the two excited levels at 33 and

53 cm^{-1}. These are the two lines at 20,466 and 20,446 cm^{-1} (air values directly measured from the spectrometer). It is important to notice that the line at 20,466 disappears at T≈7 K, whereas the line at 20,446 cm^{-1} disappears by T≈15 K. It seems reasonable to infer that the fluorescence is being quenched by inter-ionic energy transfer or reabsorption of the emitted light by a neighbouring ion (see Figure 6.7(e) and the accompanying discussion in the text), which of course occurs at a lower temperature for the transitions involving the 33 cm^{-1} state since it needs less thermal energy to be populated as opposed to the 53 cm^{-1} state. The actual values of the temperature at which the quenching takes place are slightly different than those listed in Figure 6.6 since the temperature is measured at the tip of the cold finger and not at the sample, which causes errors at low temperature.

Instead of fluorescent peaks one can often see at higher temperatures dips in the spectrum which correspond to absorption of scattered light at the frequencies corresponding to the energies of the transitions from the $^4F_{7/2}$ levels to the levels at 33 and 53 cm^{-1}. For transitions involving the ground state these absorption dips can be seen at 4.2 K. This effect is most pronounced in XY polarization. We conclude that resonant inter-ion energy transfer quenches the fluorescence that might occur from the $^4F_{7/2}$ multiplet and which is already quite weak due to nonradiative relaxation to the lower multiplets.

6.2.4 Light Scattering Mechanisms Under Resonant Excitation

The light scattering that is of interest here is the inelastic scattering of a monochromatic light wave with the appearance of lanthanide ion dependent peaks in the frequency spectrum of the scattered light. The two main mechanisms of light scattering that enter into play in this study are fluorescence and Raman scattering. A number of different processes enter one of these two categories, their relevance depending on the nature of the electronic energy level structure and phonon density of states of the rare earth crystal, the excitation wavelength of the incident light, and also the temperature. It is important to distinguish which particular process is responsible for the observed light scattering spectrum. The various mechanisms that are important are depicted pictorially in Figure 6.7 and are briefly described here. References are given to previous studies of these processes, in which much more detailed information can be found. For the sake of simplicity, only a few levels are depicted. The real situation is of course much more complicated.

Figure 6.7(a) shows the process of fluorescence with nonresonant excitation. The excita-

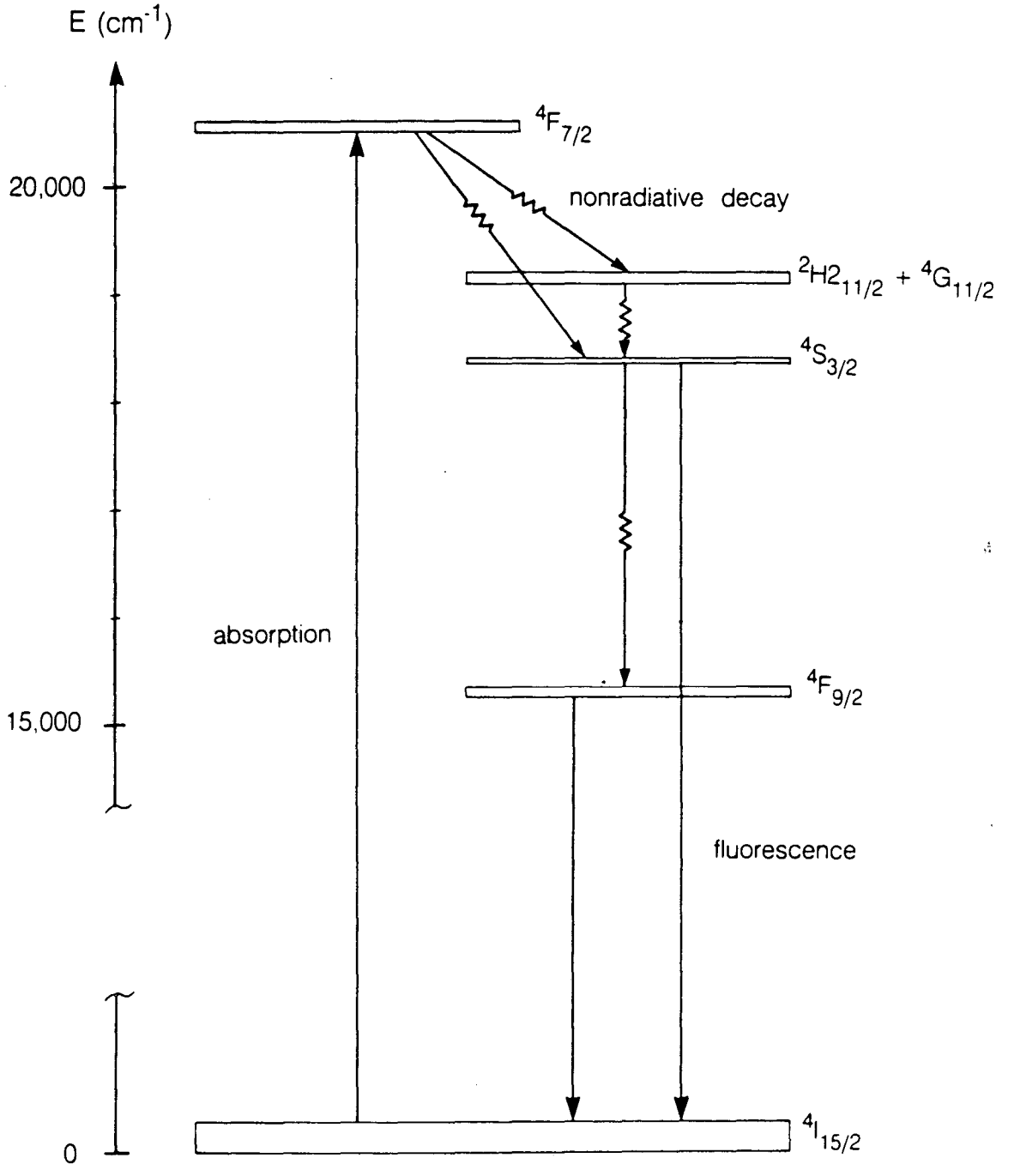

Figure 6.4: Fluorescence of the Er^{3+} ion in $ErPO_4$ and Er^{3+} doped $LuPO_4$.

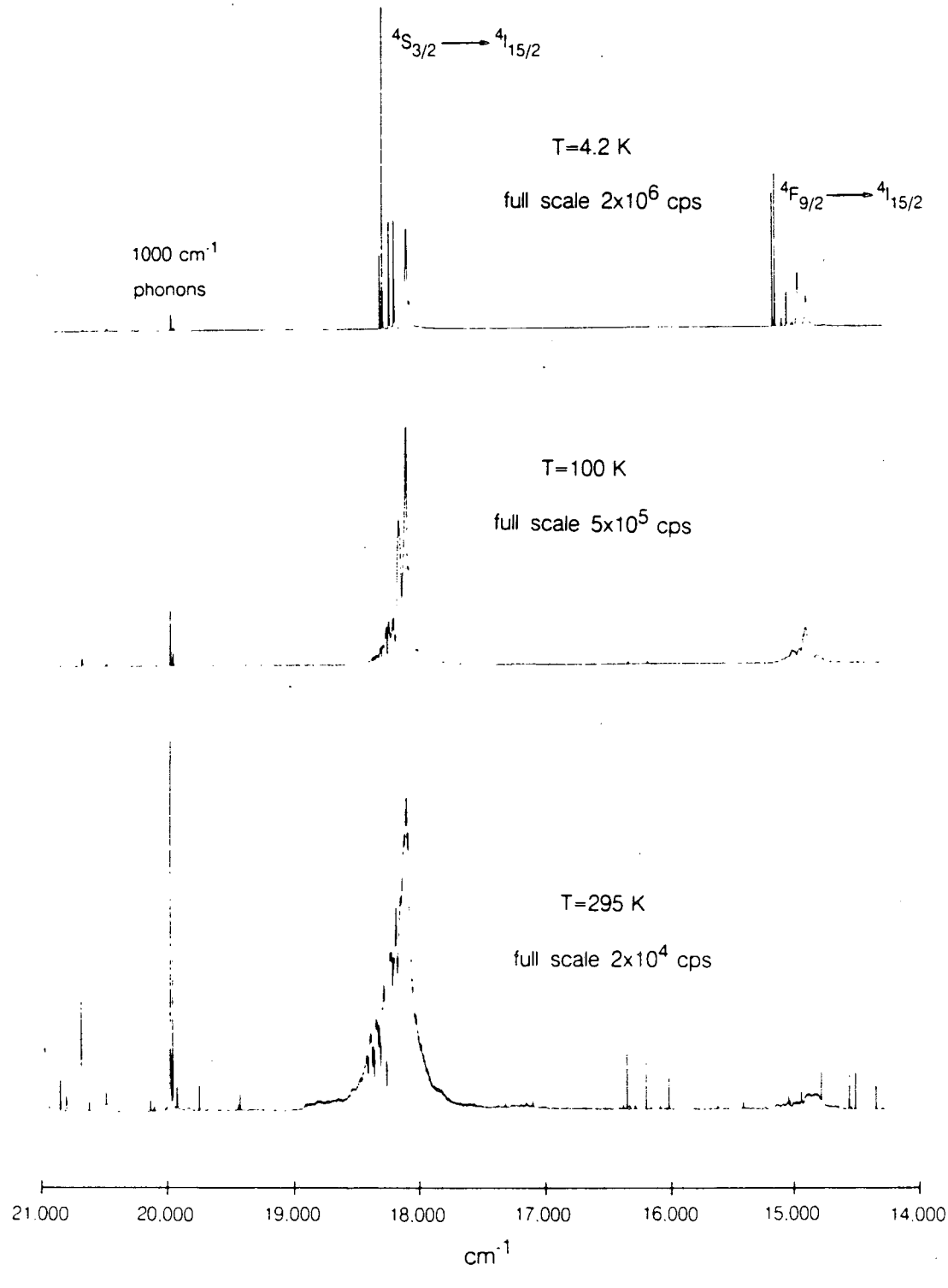

Figure 6.5: Fluorescence of Er^{3+} in $ErPO_4$ with excitation at 476.5 nm, for T=4.2, 100, and 295 K. The full scale is indicated in counts per second.

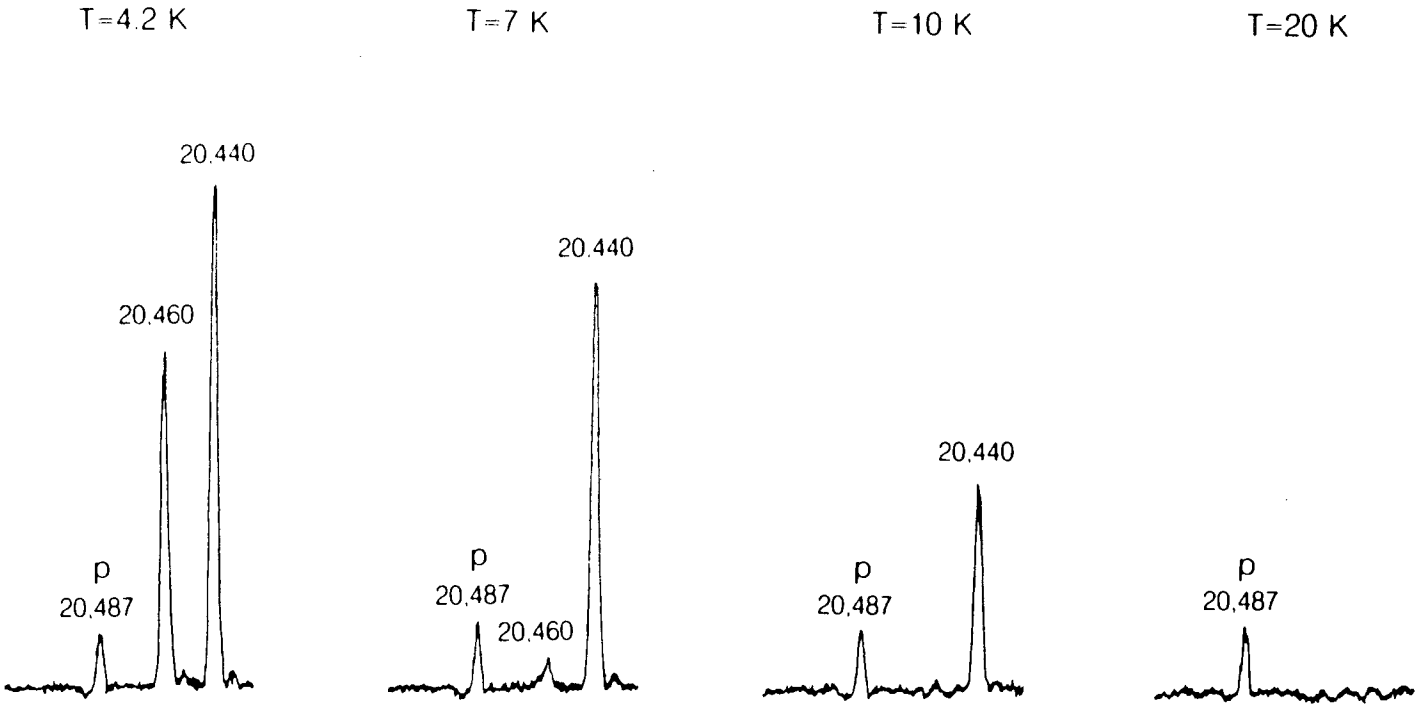

Figure 6.6: Fluorescence of the $^4F_{7/2}$ manifold of Er^{3+} in $ErPO_4$ as a function of temperature with excitation at 476.5 nm. The full scale is 1,000 counts per second. The 20,487 cm^{-1} transition is a laser plasma line. The lines at 20,460 and 20,440 cm^{-1} represent, respectively, the transitions from the 33 and 53 cm^{-1} states to that at 20,493 cm^{-1}. The temperature values are approximate since the sample is cooled in a cold finger dewar (see section 2.1.2).

tion is not necessarily directly populating the initial level of the fluorescent transition, and there has been loss of phase relationship between the incident and scattered light waves. To conserve energy in this process, another excitation needs to be created or destroyed. In the case of rare earth crystals it is usually a phonon which assists the process, depicted in Figure 6.7 by a broken arrow. This mechanism allows one to observe fluorescence from many levels that are not resonant with the exciting radiation. This is well known to occur for rare earth crystals and both Stokes and anti-Stokes fluorescence can be observed from levels that are several thousands of wavenumbers away from the exciting line. Figure 6.7(a) shows a Stokes process since the fluorescence is of a lower energy than the excitation. The intensity of this process depends on the temperature, the phonon density of states, and the position of the exciting line relative to the energy levels. Usually it can be characterized by the fact that the polarization properties of the fluorescent light are independent of the polarization of the incident light, since the assistance of the phonon essentially negates the selection rules that exist for the direct absorption process. Studies of this type of light scattering are especially due to Auzel [12,13]. The intensity of the fluorescence depends on the rate at which the level is being populated and the strength of the various radiative and nonradiative decay channels.

Figure 6.7(b) depicts fluorescence with resonant excitation. This process is also sometimes referred to as hot luminescence. There is loss of phase relationship between the incident and emitted light wave, which is indicated by the horizontal broken arrow. However, there are now strict selection rules for the absorption of the incident light, and there is a selection rule dependent relationship between the polarizations of the incident and scattered light beams. The intensity of the fluorescence depends on the absorption strength and the competition between the various decay channels.

Figure 6.7(c) depicts Raman scattering with nonresonant excitation. Comparing it with Figure 6.7(b) it is clear that there is a frequency difference between fluorescent and Raman transitions to the same final level. The polarization and parity selection rules are different for the two processes. Also, for Raman scattering, the phase of the scattered light is fixed relative to that of the incident light wave.

Figure 6.7(d) depicts Raman scattering with resonant excitation. Resonant Raman scattering is usually much stronger in intensity than nonresonant Raman scattering. There is now, however, a problem in distinguishing the scattered resonant Raman light from the

fluorescent light of Figure 6.7(c), since they are of the same frequency. Distinguishing resonance Raman scattering from hot luminescence has been the subject of heated debate in the literature. Of particular interest is the theoretical work of Shen [2] and the experimental work of Yu and Shen [14] followed by that of Weiner [15] on semiconductors, and that of Rousseau *et al* on molecular systems [16]. Basically, the two processes can be distinguished by their different time evolution patterns. The Raman light decays with a lifetime governed by the T_2 dephasing lifetime and the fluorescent light decays with the T_1 lifetime of the initial state, which is convoluted from its radiative and nonradiative decay rates. The difference between the two temporal evolution patterns was illustrated for the case of electronic energy levels in rare earth crystals by Nicollin and Koningstein [5].

Figures 6.7(e) and 6.7(f) show several energy loss mechanisms that can impact the intensities of the radiative transitions. Figure 6.7(e) depicts a nonradiative transition from the populated upper level to a nearby lower level. The transition involves the emission of a phonon. In general there can be a number of levels available as pathways for nonradiative relaxation. There is an extensive wealth of literature on nonradiative transitions in rare earth crystals [17,18,19,20,21]. The important variables are the temperature and the phonon density of states. The nonradiative decay rate from an upper level to a lower level has the functional dependence:

$$W^{NR} = W_0^{NR}(1 - exp(-\frac{\hbar\omega}{kT}))^n \text{ with } W_0^{NR} \propto exp(-\frac{\Delta E}{\hbar\omega}) \tag{6.5}$$

where n is the number of phonons of energy needed to bridge the energy gap ΔE between the two levels [22]. Nonradiative decay rates in the phosphate crystals are significantly higher than in most other crystals since the maximum phonon energy in the phosphates is 1070 cm^{-1} as opposed for instance to 175 cm^{-1} for $LaBr_3$, 260 cm^{-1} for $LaCl_3$, and 350 cm^{-1} for LaF_3, so that less phonons are required to bridge a given energy gap.

Figure 6.7(f) is a trapping mechanism that operates by resonant inter-ion energy transfer. The deexcitation of ion 1 is accompanied by the excitation of ion 2. Such mechanisms "capture" the energy available for the radiative transition in the form of an itinerant electronic excitation. Note that this process can occur in a variety of ways (dipole-dipole interaction, phonon exchange, absorption by ion 2 of the photon emitted by ion 1, etc.). This process depends on both the temperature and the rare earth ion concentration. Note that if the final state of the deexcitation transition is an excited state, then it needs to be

thermally populated for ion 2 to be able to resonantly absorb that energy. There is a large amount of literature on energy transfer and its various embodiments for rare earth ions [22,23,24,25,26,27]. The mechanism shown in Figure 6.7(f) appears to be the most relevant for the erbium phosphate crystals studied here.

6.2.5 Importance of the Inhomogeneous and Homogeneous Linewidths - Site Selective Fluorescence

The energy levels of rare earth ions in crystals do not have Dirac delta-function lineshapes. In Figure 6.7 the levels are drawn with with zero width only for the sake of simplicity. In fact, as in any other quantum system, the energy levels have a finite linewidth. There are two types of line broadening. The inhomogeneous linewidth of a particular level comes from the distribution of slightly different sites that the ion can occupy in the crystal. These sites have approximately the same site symmetry, but have microscopic differences in the positions of the ligands and the resulting crystal field parameters. The slight changes in the crystal field parameters between these different sites, which occur because the crystal is not perfectly homogeneous, are responsible for the inhomogeneous spread of the energy levels, with a Gaussian lineshape. The homogeneous linewidth is the natural linewidth of the level for an individual site. It is determined by the lifetime of the state and its dephasing time. The homogeneous lineshape is a Lorentzian curve. In general, for the lowest energy level of a crystal field split multiplet of a lanthanide ion in a crystal, the inhomogenous linewidth is quite a bit larger than the homogeneous linewidth, as shown in Figure 6.8.

The inhomogeneous linewidth can be resolved by the technique of site selective fluorescence or fluorescence line narrowing. This was first applied to impurity ions in solids by Szabo [28] in his study of ruby and was followed by a large amount of work on rare earth ions doped in various concentrations in insulating crystals [29,30,31]. If the excitation is of narrow enough bandwidth (significantly smaller than the inhomogeneous linewidth) then only the ions that have an energy within the bandwidth of the excitation will absorb the radiation and be excited to their excited state. Their subsequent fluorescence will then only exhibit a homogenous broadening. Barring spectral diffusion from ion-ion energy transfer or phonon assisted transfer, this technique allows the isolation of a small set of identical sites occupied by the rare earth ions in the crystals, among the whole collection of sites responsible for the inhomogeneous linewidth. The linewidth of the argon ion laser is 0.1

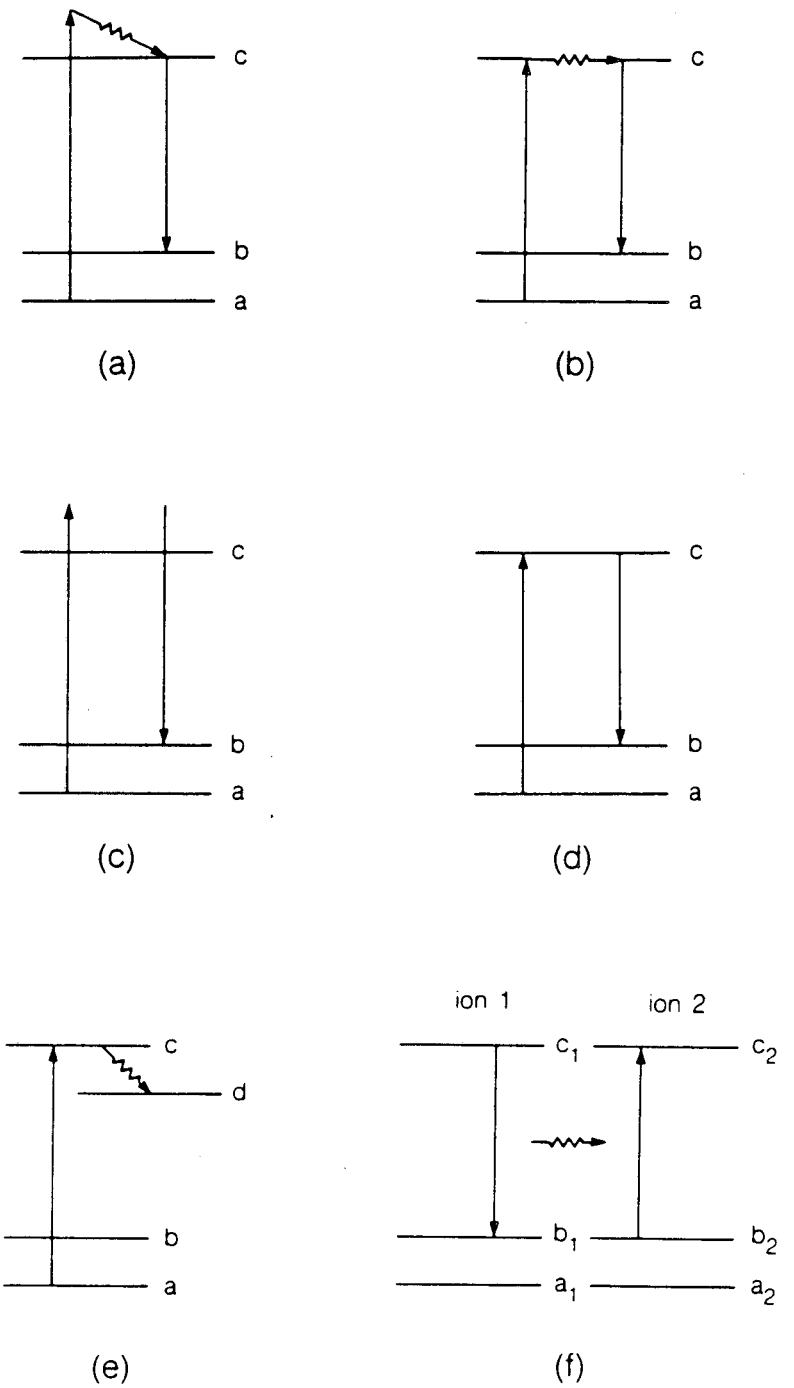

Figure 6.7: Light scattering and energy loss mechanisms relevant to the resonant Raman studies of the Er^{3+} ion. See explanations in the text, section 6.2.4.

cm^{-1} so that excitation within the inhomogeneous linewidths of the $^4F_{7/2}$ energy levels, which appear to be at least 1 cm^{-1}, can definitely excite site selective fluorescence from these levels. The intensity of this fluorescence will depend on the competition between the the radiative and nonradiative decay channels.

6.2.6 Amplitude Interference Effects in the Resonant Raman Spectrum

The intensities of the electronic Raman transitions will not be the same under resonant excitation as opposed to nonresonant excitation. The amplitude of the Raman transition is the sum of the amplitudes contributed by the different quantum mechanical channels via which the process can take place. These channels are shown in Figure 6.9. The nonresonant contribution to the amplitude, which was studied in detail in Chapter 4, arises from the high energy intermediate configurations $4f^{N-1}nd$, $4f^{N-1}ng$, and core excitation d configurations. These are the dominant nonresonant intermediate states since they have parity allowed electric dipole matrix elements with the $4f^N$ states. The resonant contribution to the Raman amplitude comes from the "forbidden electric dipole" matrix elements between the $^4F_{7/2}$ and $^4I_{15/2}$ states, that come into play only because the exciting laser line is so close in energy to these transitions. We write the total amplitude for the electronic Raman transition from state $|n\rangle$ to state $|k\rangle$ as the sum of the nonresonant and resonant amplitudes:

$$\begin{aligned}(\alpha_{\rho\sigma})_{nk} &= (\alpha_{\rho\sigma})_{nk,res.} + (\alpha_{\rho\sigma})_{nk,nonres.} \\ &= -\sum_{^4F_{7/2}} \frac{\langle k|D_\rho|r\rangle\langle r|D_\sigma|n\rangle}{E_{rn} - \hbar\omega + i\Gamma_r} + (\alpha_{\rho\sigma})_{nk,nonres.} \end{aligned} \tag{6.6}$$

where the sum in the resonant term is over the crystal field states $|r\rangle$ belonging to the $^4F_{7/2}$ multiplet. Only the first term of equation (5.1) has been kept for the resonant term since it is the only one that is enhanced by the resonance effect. The Γ_r damping constant is inversely proportional to the T_2 lifetime of the state r [2,3]. The intensity of the Raman transition is proportional to the absolute square of this Raman amplitude:

$$I_{nk} \propto \left| -\sum_{^4F_{7/2}} \frac{\langle k|D_\rho|r\rangle\langle r|D_\sigma|n\rangle}{E_{rn} - \hbar\omega + i\Gamma_r} + (\alpha_{\rho\sigma})_{nonres.} \right|^2 \tag{6.7}$$

There can thus be interference between the terms that contribute to the intensity. There can be interference between the the resonant amplitude and the nonresonant amplitude and there can also be interference between the individual terms that contribute to the resonant

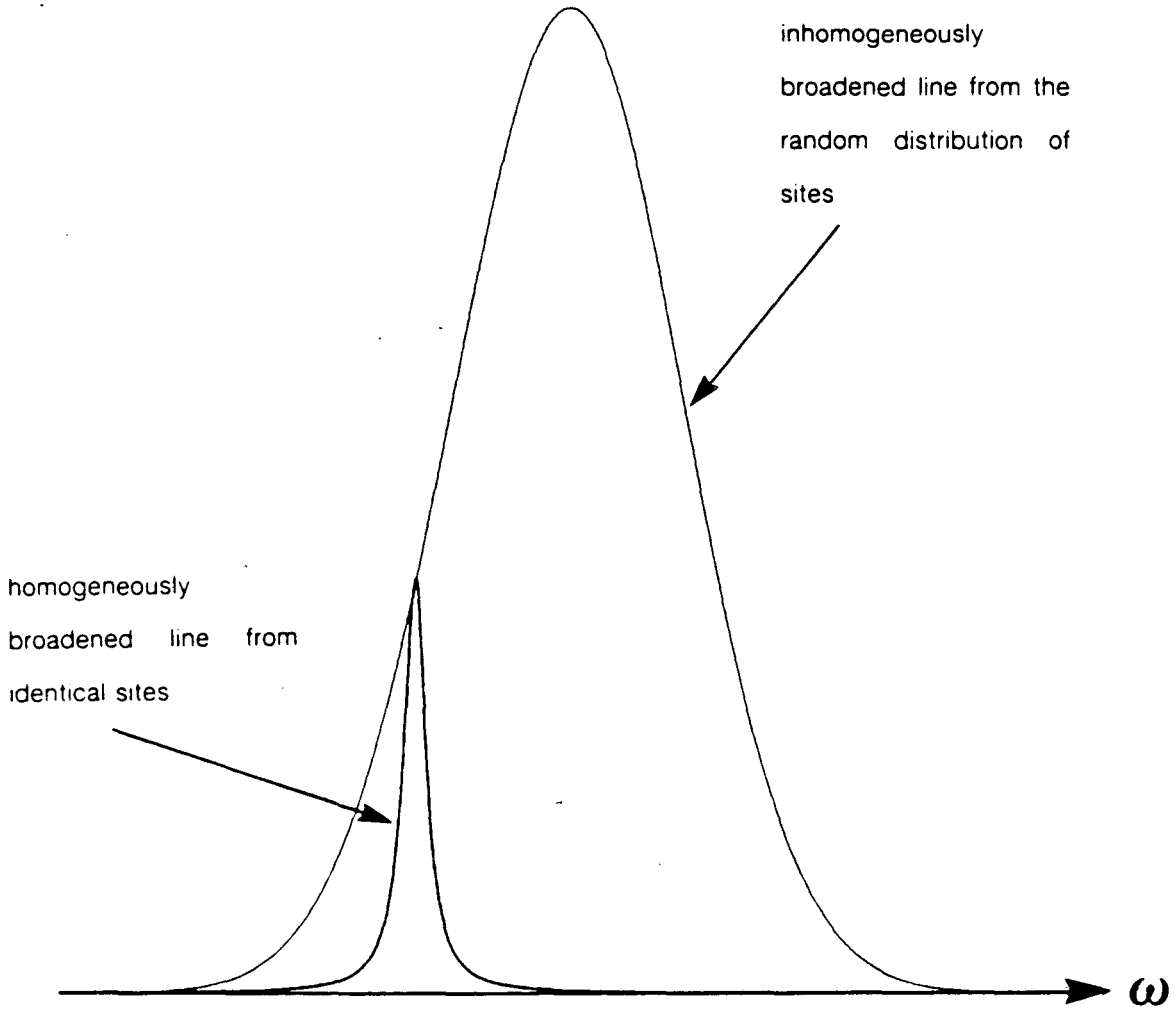

Figure 6.8: Lineshape of a lanthanide ion energy level in a crystal host.

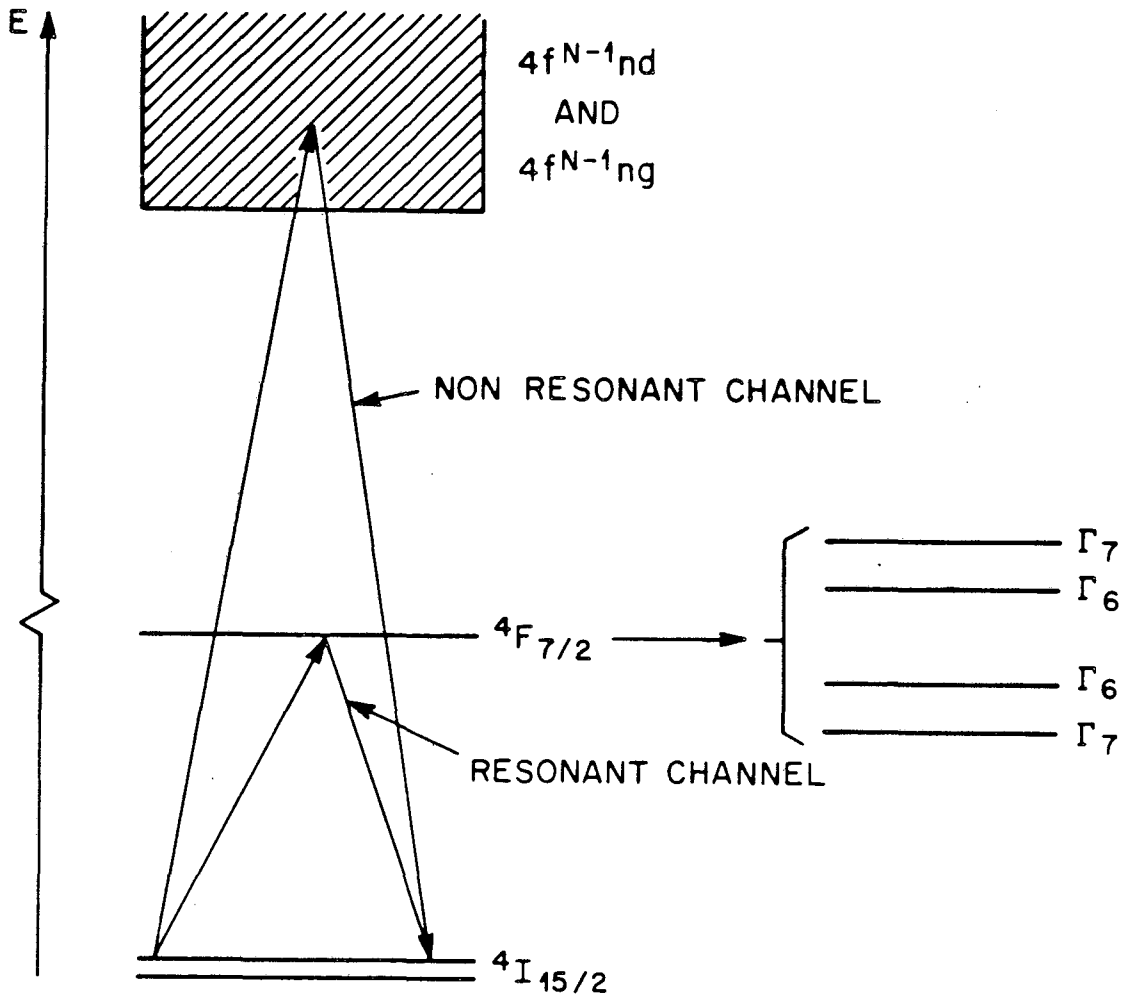

$$|\alpha_{\rho\sigma}|^2 = |\alpha_{\rho\sigma}\,(\text{RESONANT}) + \alpha_{\rho\sigma}\,(\text{NON RESONANT})|^2$$

Figure 6.9: Electronic Raman intensity channels of Er^{3+} with excitation resonant with the $^4I_{15/2} \longrightarrow {}^4F_{7/2}$ transitions.

amplitude. This is a purely quantum mechanical effect which arises from the fact that we cannot distinguish between the various intermediate states via which the process can take place. This is exactly similar to the problem of electron diffraction by a double slit [32]. Since the resonant energy denominator is extremely sensitive to the difference $E_{rn} - \hbar\omega$, the amplitudes and interferences will be different for the different concentration Er^{3+} crystals. A glance at Figure 6.2 shows that the energy levels actually cross the laser line somwhere around 50% Er^{3+} doped $LuPO_4$, resulting in a change in sign of the energy denominator and a reversal of the interference! This shows up in the experimental spectra as a significant change in the relative intensities of the electronic Raman transitions as the doping amount of Er^{3+} is changed.

One final point needs to be made, which is that the intensity we have just written is valid only for a single site. Since the crystal has imperfections, there is actually a distribution of sites which results in an inhomogeneously broadened line for a specific transition. The intensity of the Raman signal from the crystal as a whole is a convolution of the signals from the various sites. We must thus integrate the intensity caculated above over the inhomogeneous linewidth. It is in this case the intensities and not the amplitudes which must be summed since ions at different sites can be distinguished. We denote the different sites by the suffix j, the frequency of the transition from state $|r_j\rangle$ to state $|n_j\rangle$ by $\omega_j(rn)$, the damping function at site j by $\Gamma_j(r)$, and the distribution function of sites j by $g(j)$. We can write the Raman intensity in a somewhat formal fashion as:

$$I_{total} = \sum_j \left| - \sum_{^4F_{7/2}} \frac{\langle k_j|D_\rho|r_j\rangle\langle r_j|D_\sigma|n_j\rangle}{\hbar\omega_j(rn) - \hbar\omega + i\Gamma_j(r)} + (\alpha_{\rho\sigma})_{nonres.} \right|^2 g(j) \tag{6.8}$$

and the distribution function is normalized by:

$$\sum_j g(j) = 1 \tag{6.9}$$

Consider the case of a single resonant line. If the line is centered at some average frequency ω_0 and $\hbar\omega_j(rn) - \hbar\omega \approx \hbar\omega_0 - \hbar\omega$, and the homogeneous linewidth is the same at all the sites, then the energy denominator can be pulled out from the sum and replaced by the average value $(\hbar\omega_0 - \hbar\omega + i\Gamma_r)^{-1}$. The matrix elements can also be assumed to be independent of the sites. The integration over the distribution function then yields one. The argument is easily generalized to the case of several resonant lines to give the following result, valid to

a good approximation when the exciting line is at least one linewidth away from the center of any given resonance line:

$$I_{total} = \left| - \sum_{^4F_{7/2}} \frac{\langle k|D_\rho|r_0\rangle\langle r_0|D_\sigma|n\rangle}{\hbar\omega_0(rn) - \hbar\omega + i\Gamma_r(0)} + (\alpha_{\rho\sigma})_{nonres.} \right|^2 \tag{6.10}$$

where $\omega_0(rn)$ is the center frequency of the transition from r to n. This calculation and the case where the approximations it involves break down will be discussed in more detail in the following chapter. It is useful for quantitative comparisons of experimental and calculated relative intensities.

6.3 The Resonant Electronic Raman Spectra of $ErPO_4$ - The Case of Near Resonant Excitation

6.3.1 Experimental Spectra at T=4.2 K

The experimental Raman spectra of $ErPO_4$, excited with the 488.0 nm line of the argon ion laser, show extremely strong enhancements of the intensities of the electronic Raman peaks, compared to the nonresonant spectra taken with the 514.5 or 476.5 nm lines. The enhancement factors of the electronic peaks are on the order of 10 to 100, depending on the polarizations of the incident and scattered light. The phonon peaks, however, show no change in intensity. Thus the increase in intensity of the electronic Raman transitions is due to resonance enhancement. In fact, the phonon intensities can be used to calibrate and correct for different scattering efficiencies (as in chapter 5) and for the absorption of the incident light for the strong resonance situations that occur when the excitation overlaps the lineshape of a transition (which is the case for the 50%, 20%, and 10% Er^{3+} doped $LuPO_4$ crystals). The spectra at T=4.2 K are shown in Figures 6.10 and 6.11. Both the resonant and nonresonant spectra are simultaneously displayed so as to bring out the resonance enhancements. Note in particular the change in scales between the resonant and nonresonant spectra, and the relative intensities of the electronic and vibrational transitions.

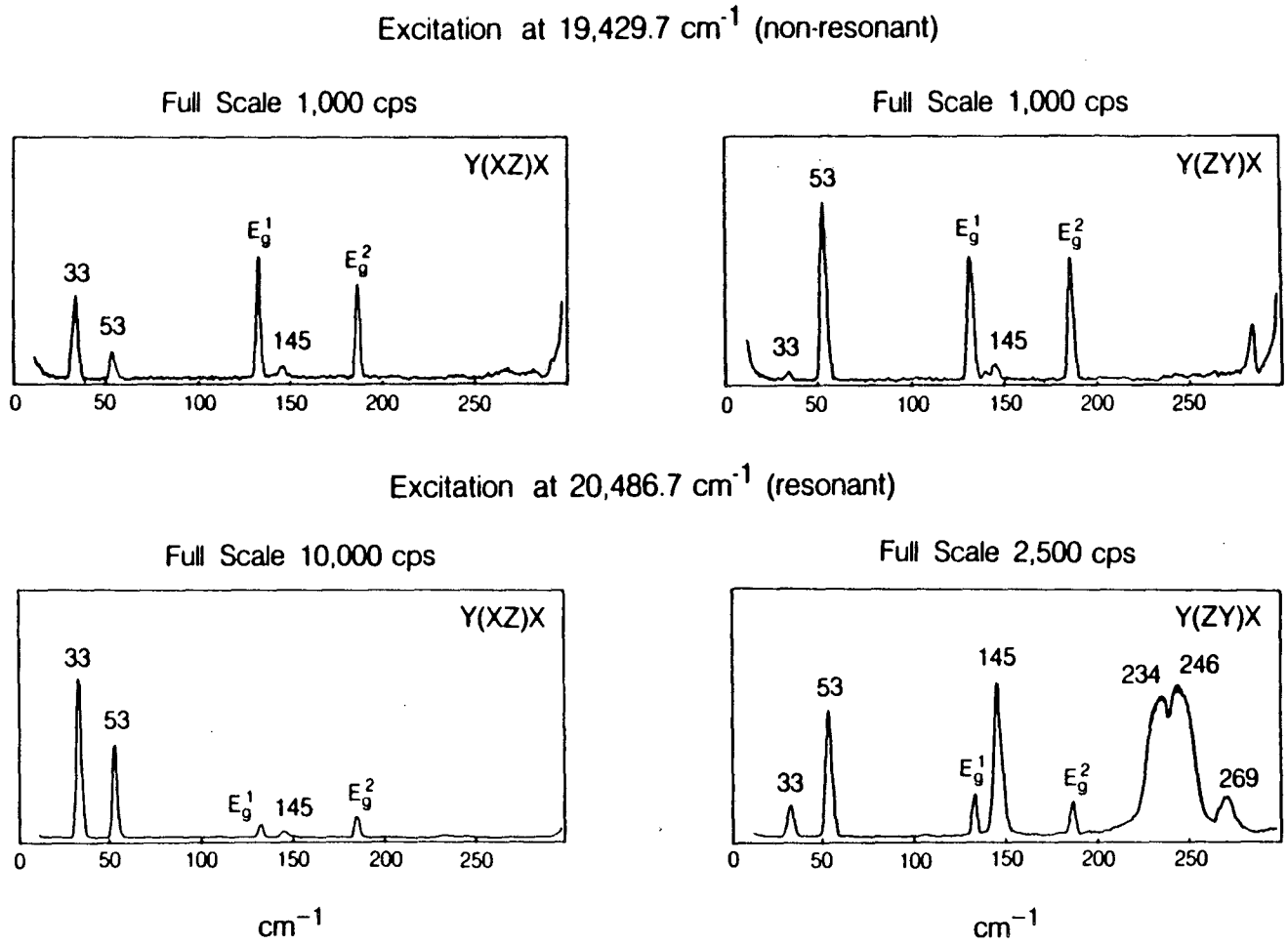

Figure 6.10: Experimental Raman spectra of $ErPO_4$ at T=4.2 K for both nonresonant excitation at 514.5 nm and resonant excitation at 488.0 nm. The scattering geometries are Y(XZ)X and Y(ZY)X. The wavenumbers of the exciting lines are given in vacuum. The spectral bandwidth of the spectrometer is set to 2.5 cm^{-1}. Note the change in scales between the resonant and nonresonant spectra.

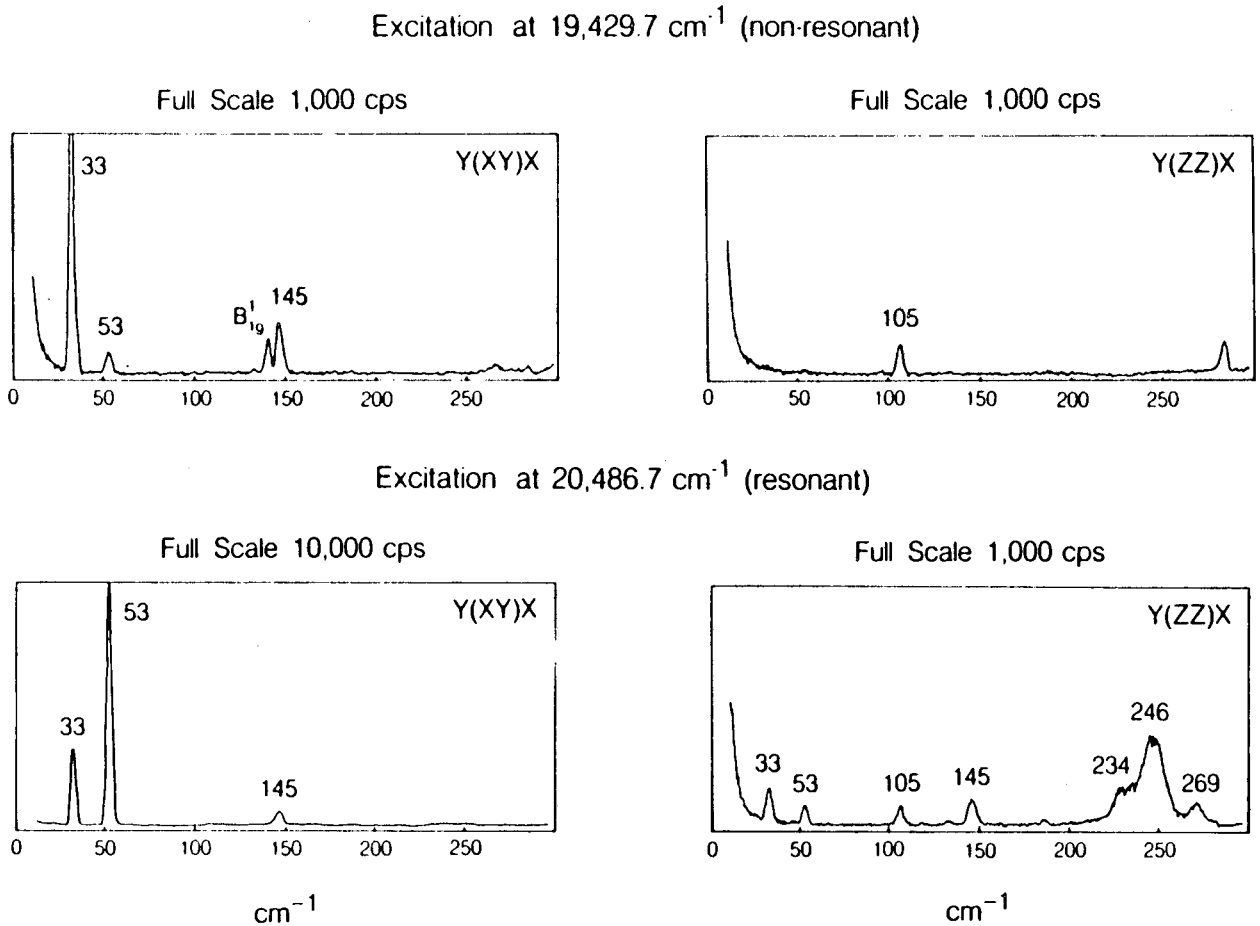

Figure 6.11: Experimental Raman spectra of $ErPO_4$ at T=4.2 K for both nonresonant excitation at 514.5 nm and resonant excitation at 488.0 nm. The scattering geometries are Y(XY)X and Y(ZZ)X. The wavenumbers of the exciting lines are given in vacuum. The spectral bandwidth of the spectrometer is set to 2.5 cm^{-1}. Note the change in scales between the resonant and nonresonant spectra.

6.3.2 Temperature Dependence of the Resonant Stokes Spectra

The temperature evolution of the resonance Raman spectra can be used to explore more fully the mechanism of the enhancement process and also to bring out the difference between Raman and fluorescence transitions. In this section we study the temperature dependence of the Stokes spectra, more particularly the temperature quenching of the Raman peaks and the appearance of a resonantly enhanced transition at 20 cm^{-1} originating in the 33 cm^{-1} state and terminating in the 53 cm^{-1} state.

Figure 6.12 shows the temperature evolution of the Stokes XY spectrum in the 10 to 60 cm^{-1} range. The temperature range is 4.2 to 60 K. The full scale is 10,000 counts per second. Phonon E_g^3 in ZY polarization, located at 303 cm^{-1} at 4.2 K, is displayed at each temperature to show the increasing absorption of X and Y polarized light with temperature. The peak at 20 cm^{-1}, which corresponds to the 33 $\longrightarrow$ 53 cm^{-1} transition, grows steadily with temperature as the population of the 33 cm^{-1} state increases. The intensity of this transition is roughly an order of magnitude larger than with nonresonant excitation. Measurements of the electric dipole oscillator strengths indicate that the matrix elements $|\langle\Gamma_6(33\,cm^{-1})|X,Y|\Gamma_6(20,493\,cm^{-1})\rangle|^2$ and $|\langle\Gamma_7(53\,cm^{-1})|X,Y|\Gamma_6(20,493\,cm^{-1})\rangle|^2$ are quite large (see chapter 7). The Raman transition between the 33 and 53 cm^{-1} states will have a resonant contribution proportional to the product of these two matrix elements and as a consequence the enhancement will be large. The size of the matrix elements makes up for the relatively large value of the energy denominator $\Delta E = (20,493 - 33) - 20,487 = -24\,cm^{-1}$. The 20 cm^{-1} transition is also observed in ZY polarization with a much weaker intensity than in XY. It is not observed in the nonresonant ZY spectra. The temperature evolution of the ZY spectra in the 10 to 60 cm^{-1} range, from T=4.2 to T=60 K, are shown in Figure 6.13.

There are two reasons for the overall decrease in scattering intensity with increasing temperature, quite visible for the 33 and 53 cm^{-1} transitions in XY polarization. First of all, as the temperature is increased, it is observed that the phonon intensities drop. This arises from increasing absorption of the incident laser radiation. Phonon E_g^3 was tracked as a function of temperature for all the temperature evolution scans so as to be able to correct the electronic Raman intensities for the absorption of the incident light, since the scattered phonon intensity is proportional to the effective incident intensity. The absorption increases with temperature as the energy levels broaden with temperature and start overlapping the

incident frequency to a larger degree thereby increasing its absorption. Phonon assisted absorption will also become greater at higher temperatures. The first explanation seems more reasonable as the absorption of the incident light occurs preponderantly for Y polarized light. Thus the drop in intensity of phonon E_g^3 is much more marked in ZY polarization than in XZ (where the drop in intensity is barely noticeable for $ErPO_4$) since the absorption of Z polarized light is much weaker.

Figure 6.14 is a semi-log graph of the relative intensities of several transitions as a function of temperature. The temperature values should be treated with caution since the sample is in a cold finger dewar and the temperature is measured at the tip of the cold finger. In fact, there is some evidence of local heating due to the absorption of some of the laser radiation which increases the temperature by at least a few degrees Kelvin. The drop in intensity of phonon E_g^3 is seen to be much stronger in ZY than in XZ. Spectra taken at higher temperature show that the intensity of E_g^3 falls off at a much slower rate above 80 K (in ZY polarization), than the initial fast exponential decay seen in Figure 6.14 from 4.2 to 60 K. The intensities of the electronic transitions were corrected for the absorption of the incident light by multiplying them by the ratio $I_{4.2K}(E_g^3)/I_T(E_g^3)$.

The drop in intensity of the 33 and 53 cm^{-1} transitions as the temperature is raised is due to reabsorption of the Raman scattered light which, as the energy levels broaden with temperature, is increasingly resonant with an actual transition orginating in one of the excited crystal field states (the reabsorption process is similar to the one shown in Figure 6.7(f)). For instance the electronic Raman transition at 33 cm^{-1} corresponds to light of wavenumber 20,453.7 cm^{-1} which can be reabsorbed by either the transition 33 $\longrightarrow$ 20,485 cm^{-1} (which is the closest in energy) or the transition 33 $\longrightarrow$ 20,493 cm^{-1}. The situation is entirely the same for the 53 cm^{-1} transition.

Figure 6.15 displays tungsten lamp absorption spectra taken at T=25 and 50 K, in both π and σ polarization. Transitions originating out of the excited states at 33 and 53 cm^{-1} are clearly visible and have large intensities. The Stokes peaks at 20, 33, and 53 cm^{-1}, and the anti-Stokes peak at 33 cm^{-1}, with resonant excitation at 488.0 nm, are shown on these spectra at their absolute wavenumber position so as to make apparent which peaks are the most affected by the reabsorption process. Most of the peaks are clearly within the linewidth of absorption transitions which why these Raman peaks are so affected by the reabsorption that occurs at higher temperatures. The 33 cm^{-1} transition drops in intensity

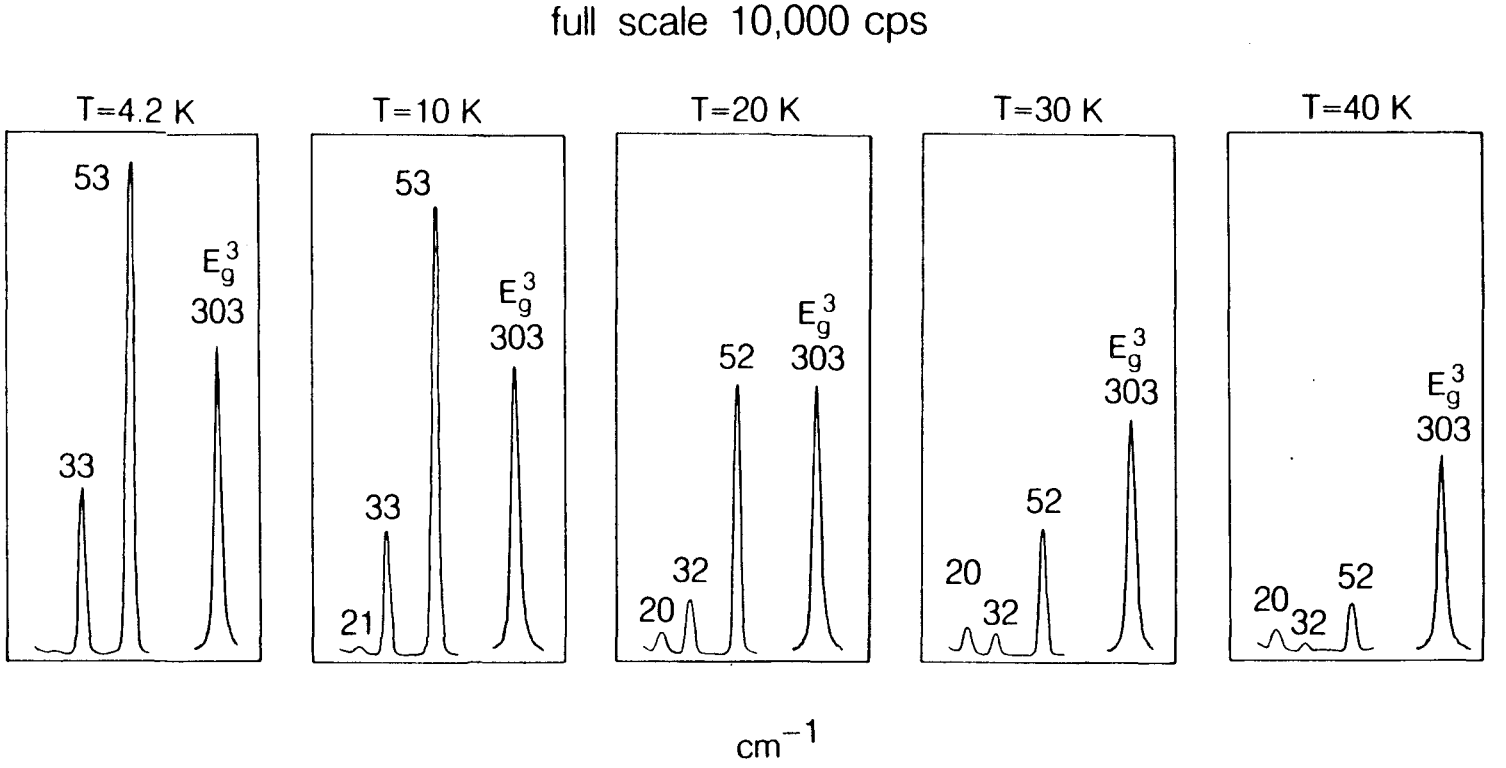

Figure 6.12: Experimental Raman spectra of $ErPO_4$ in XY polarization in the 10-60 cm^{-1} range as a function of temperature. The E_g^3 phonon at 303 cm^{-1} is shown in the right of each frame in ZY polarization to track the increasing absorption of the laser light with temperature.

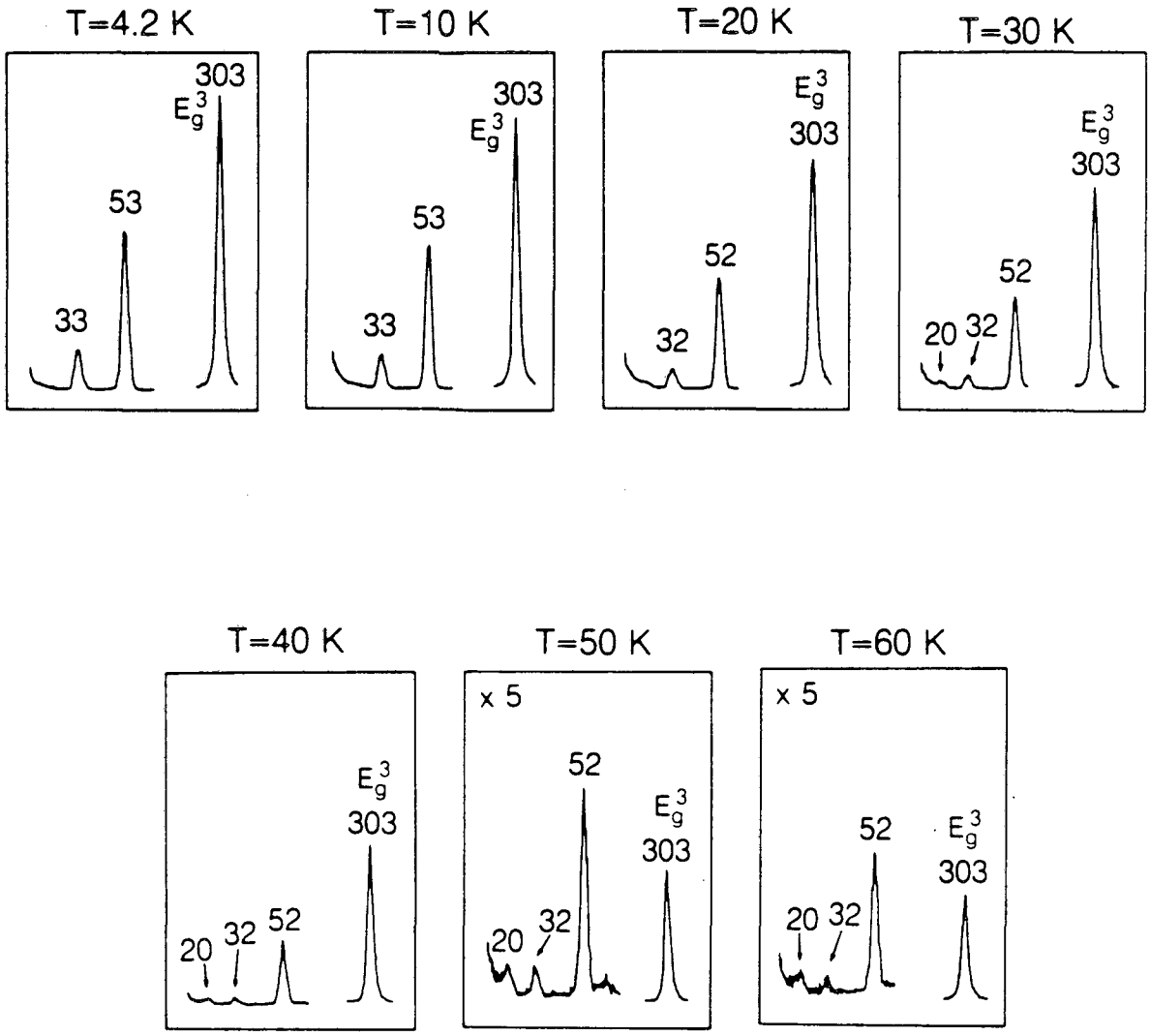

Figure 6.13: Temperature evolution of the experimental Raman spectra of $ErPO_4$ in ZY polarization in the 10 to 60 cm^{-1} range. Phonon E_g^3 at 303 cm^{-1} is also shown. For the electronic transitions the full scale is 2,500 counts per second from 4.2 to 40 K and 500 cps at 50 and 60 K. The phonon peak is at 5,000 cps at 4.2 K.

before the 53 cm^{-1} transition does since the 33 cm^{-1} state becomes thermally populated at a lower temperature than the 53 cm^{-1} state. The reabsorption is either a direct process or a phonon assisted process. The direct absorption process seems to be indicated by the data since the 33 and 53 cm^{-1} transitions drop off at a much slower rate in ZY polarization. The phonon assisted reabsorption would not distinguish between the polarizations of the Raman scattered radiation whereas the direct absorption does. The 53 cm^{-1} transition drops off very slowly in ZY (compared to the 33 cm^{-1} transition) which comes from the fact that the 33 $\longrightarrow$ 20,485 cm^{-1} transition is forbidden in Z polarization. In fact the 53 cm^{-1} (ZY) transition is the only low wavenumber transition still visible up to temperatures in the 100-150 K range. Figure 6.15 shows that the ZY(53 cm^{-1}) transition is not reabsorbed, which is why it persists until high temperatures.

If the power of the laser is turned down to a very low value the XY intensity of the 33 cm^{-1} transition goes up by about 10% compared to the 53 cm^{-1} (XY) transition which indicates that at higher powers there is local heating which populates the 33 cm^{-1} state and allows reabsorption even at T $\approx$ 4.2 K (measured at the cold finger tip).

The intensity of the 20 cm^{-1} transition increases initially as the population of the 33 cm^{-1} state rises with temperature. At about 30 K it begins to be reabsorbed since in absolute wavenumbers it is at 20,466.7 cm^{-1} which is close in energy to the transition 33 $\longrightarrow$ 20,493 cm^{-1}. The slope of the initial rise in intensity of the 20 cm^{-1} transition is slightly less than what one would expect from the Boltzmann factor governing the thermal population of the 33 cm^{-1} state.

The 145 and 234 cm^{-1} transitions initially rise in intensity from T=4.2 to 30 K by about 10% in XY and 30% in ZY (corrected for incident light absorption). They then start gradually dropping in intensity, especially in ZY. Since the 145 and 234 cm^{-1} transitions do not start getting populated until higher temperatures, the reabsorption does not occur at low temperatures. The matrix elements of Z between the 145 and 234 cm^{-1} states on the one hand, and the 20,485 cm^{-1} state on the other, are observed from the absorption spectra to be very high. When the 145 and 234 cm^{-1} become thermally populated, the direct reabsorption process will be very efficient for Z scattered light. The temperature effects for the 244 and 265 cm^{-1} transitions are much less pronounced. They initially rise slightly in intensity, then stay at roughly the same level until T $\simeq$ 150 K at which point they start dropping in intensity as the crystal appears to be absorbing most of the scattered

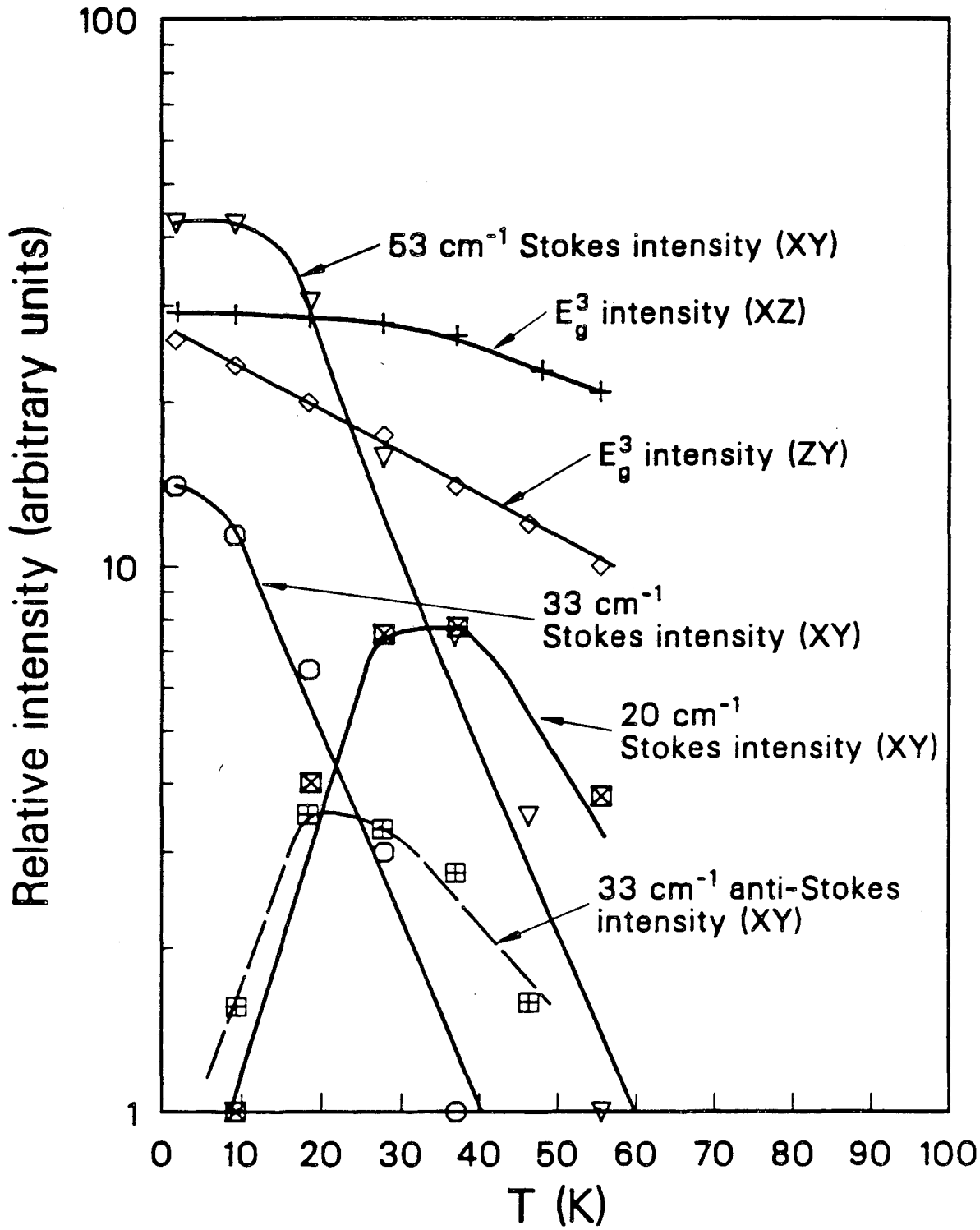

Figure 6.14: Temperature evolution of relative electronic Raman transition intensities of Er^{3+} (in $ErPO_4$) with resonant excitation at 488.0 nm. The electronic Raman transitions have been normalized to the ZY intensity of phonon E_g^3.

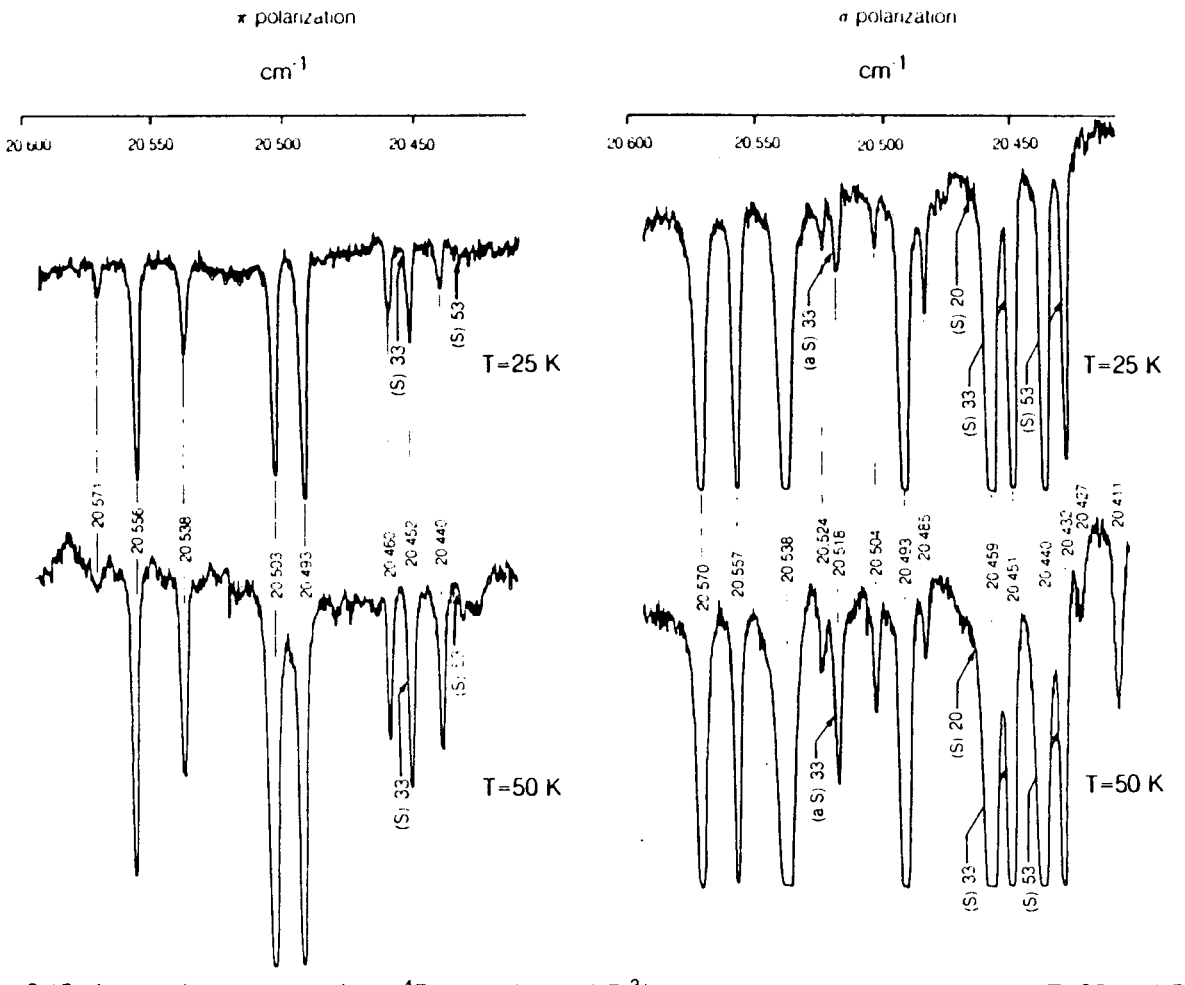

Figure 6.15. Absorption spectra of the $^4F_{7/2}$ multiplet of Er^{3+} (taken with a tungsten lamp) at T=25 and 50 K. The crystal sample is $ErPO_4$. The spectrometer slit settings are 35-100-100-35 μ and the spectral bandwidth is 2.5 cm^{-1}. The positions of selected Stokes and anti-Stokes Raman transitions relative to absorption peaks are indicated so as to show the possible reabsorption of the Raman scattered light that can occur in the crystal at higher temperatures.

light in the vicinity of that spectral region.

6.3.3 Resonance Enhancement of the Anti-Stokes Spectrum

Several strong lines are observed in the anti-Stokes Raman spectra with excitation at 488.0 nm. The anti-Stokes spectrum in XY polarization as a function of temperature is displayed in Figure 6.16. The temperature range is 4.2 to 60 K. In the XY spectrum a transition appears at 33 cm^{-1}. It is slightly visible even at T≈4.2 K and grows rapidly in intensity as the temperature is raised from T≈4.2 to T=30 K. This transition is the resonantly enhanced anti-Stokes Raman transition corresponding to the Stokes Raman peak at 33 cm^{-1}. The fact that it appears at T≈4.2 K (measured at the cold finger tip) supports the observation that the laser light is locally heating the sample and raising its temperature above the nominal value of 4.2 K. Its intensity as a function of temperature, corrected for the absorption of incident laser light, is plotted in Figure 6.14. Its initial rise in intensity is parallel to that of the Stokes 20 cm^{-1} transition, which agrees with the assumption that both of their intensities are proportional to the population of the 33 cm^{-1} state. It starts dropping off in intensity at T= 40 K which probably comes from the fact that it is being reabsorbed since it is very near in energy to the transitions 33 $\longrightarrow$ 20,556 cm^{-1} and 53 $\longrightarrow$ 20,570 cm^{-1}. A peak at 20 cm^{-1} also appears in the XY anti-Stokes spectrum which corresponds to the Raman transition 53 $\longrightarrow$ 33 cm^{-1}. It starts appearing at T=10 K and slowly grows in intensity. The 33 cm^{-1} transition is roughly ten times stronger with resonant excitation than with nonresonant excitation. The 20 cm^{-1} transition is actually not observed with nonresonant excitation. Its resonance enhancement might be coming at least partially from the two higher energy levels of the $^4F_{7/2}$ multiplet.

In ZY polarization no new features are observed. The 53 cm^{-1} transition appears weakly with a strength comparable to its nonresonant intensity. In the XZ anti-Stokes spectrum the 33 and 20 cm^{-1} transitions are weakly observed with maximum intensity at about T=40 K. In the ZZ anti-Stokes spectrum nothing is observed.

6.3.4 The Problem of Raman vs. Fluorescence Transitions

In the case of excitation very close in energy to an actual transition of the lanthanide ion under study, the question naturally arises whether the light inelastically scattered by that ion comes from an electronic Raman transition or a fluorescent one. In the case of $ErPO_4$,

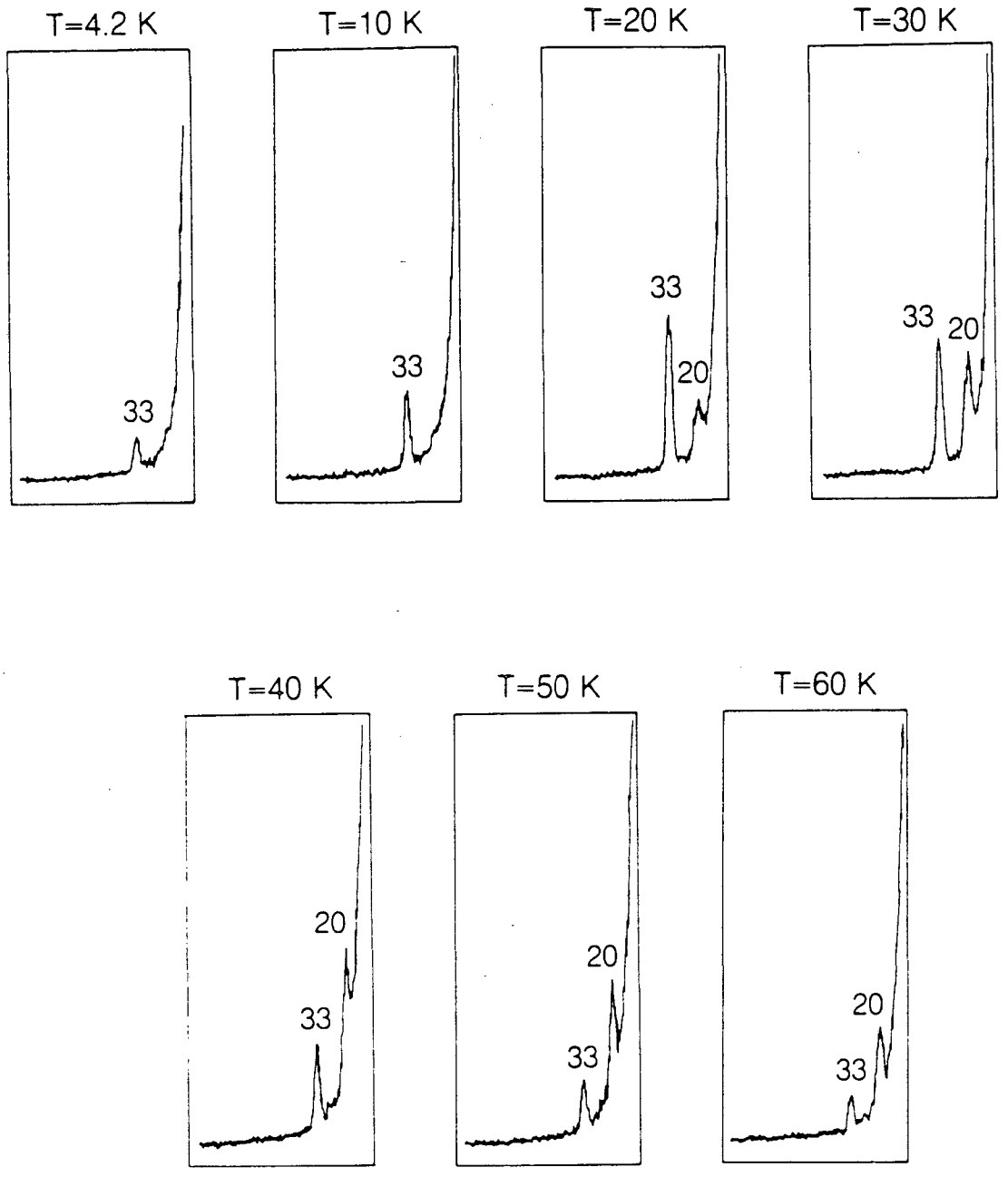

Figure 6.16: Experimental anti-Stokes Raman spectra of $ErPO_4$ in XY polarization in the temperature range 4.2 to 60 K with resonant excitation. The full scale is 500 counts per second. The absorption of the incident laser light that accompanies the increase in temperature can be followed by tracking the intensity of phonon E_g^3, shown in Figures 6.12 or 6.13.

for which the spectra have been described and interpreted in the previous sections, several arguments can be made to justify the claim that resonance electronic Raman scattering is indeed being observed from the crystal. A glance at the tungsten lamp absorption spectra of Figure 6.3 and the linewidth data of Table 6.1 shows that the excitation clearly does not overlap the lineshapes of the two lower $^4F_{7/2}$ levels.

1. Since the excitation is not exactly resonant with an actual transition, there will be a difference in energy between an electronic Raman transition and an incoherent fluorescent transition originating in either the lower Γ_6 or Γ_7 level (a transition similar to that shown in Figure 6.7(a)). Fluorescent transitions are always at the same frequency relative to the exciting frequency and shift in absolute value as the exciting frequency is changed. The lower Γ_6 level at 20,493 cm^{-1} has much stronger oscillator strengths for transitions to the ground multiplet than the lower Γ_7 level at 20,485 cm^{-1}. Fluorescence from the lower Γ_6 level would thus show up as peaks shifted by $\approx 20,493 - 20,487 = 7$ cm^{-1} from the Raman frequency. Fluorescence from the lower Γ_7 level would be shifted by ≈ 2 cm^{-1}, which might be hard to resolve experimentally, but which in any case cannot account for the strength of certain transitions, for instance 53 cm^{-1} in XY, since the transition $20,485 \longrightarrow 53$ cm^{-1} is strictly forbidden in σ polarization (X and Y polarized light) by the electric dipole selection rules.

   For the first four transitions at 33, 53, 105, and 145 cm^{-1}, it is found that there are no shifts in the Raman frequencies of these transitions to within an accuracy of $\pm$ 0.5 cm^{-1}. The slits of the spectrometer were closed down to 80-150-150-80 μ and scans were taken of these transitions for excitation at both 514.5 nm (nonresonant) and 488.0 nm (resonant). Scans were simultaneously taken of phonon E_g^3 so as to allow the measurement of the position of the electronic transitions relative to the phonon and correct for any difference in calibration of the spectrometer between the two spectral regions. No shifts in frequencies were observed. With resonant excitation at 488.0 nm, the linewidths of the two transitions were found to be respectively 1.8 and 1.9 cm^{-1}, with an error of $\pm$ 0.5 cm^{-1}. The same values are obtained, within the experimental uncertainty, with nonresonant excitation at 514.5 nm.

   Absorption measurements were also taken at T=4.2 and 77 K on photographic plates using an Ebert 3.4 m spectrometer. This allowed the determination of the frequencies

of the 33, 53, 105, and 145 cm^{-1} levels with an accuracy of $\pm$ 0.25 cm^{-1}, and of the two levels at 232 and 243 cm^{-1} with an accuracy of $\pm$ 1 cm^{-1} (these two levels are quite broad). The results agree with the frequencies measured in the resonant and nonresonant Raman spectra.

We conclude that with resonant excitation the transitions at 33, 53, 105, and 145 cm^{-1} are resonantly enhanced electronic Raman peaks and not fluorescent transitions from the inhomogeneously broadened levels at 20,493 and 20,485 cm^{-1}. The argument cannot be applied to the levels at 234, 244, and 269 cm^{-1} in the resonant excitation spectra since these are not conclusively observed in the nonresonant Raman spectra. Table 6.2 summarizes the various frequencies measured from the resonant and nonresonant Raman spectra, and the frequencies measured from optical absorption data.

2. With excitation near resonance, and the known ability of lanthanide ions to efficiently emit Stokes or anti-Stokes luminescence (see Figure 6.7(a)), it would be expected that two peaks should appear, one corresponding to fluorescence and one corresponding to Raman. However, in the experimental spectra, only one peak is observed for each level of the $^4I_{15/2}$ multiplet. There is no evidence of any kind of doublet structure. Even with no resonance enhancement, the nonresonant electronic Raman intensities are large enough that these Raman peaks should appear with excitation at 488.0 nm. There is no reason to expect the Raman transitions to all disappear, so the conclusion is that it is the fluorescent transitions which for some reason are missing. As discussed in section 5.2.3, the fluorescence from the $^4F_{7/2}$ multiplet in $ErPO_4$, excited with the argon-ion laser line at 476.5 nm, is extremely weak and and is quenched at low temperatures by energy transfer. Paradoxically enough, excitation at 488.0 nm might not even be able to excite as much fluorescence from the lower levels of the $^4F_{7/2}$ multiplet as excitation at 476.5 nm, and in any case the nonradiative relaxation to the lower multiplets and the energy transfer quenching appear to preclude any radiative transition that has a chance of occuring from these levels. Instead of producing observable fluorescence from the sample, it appears that the transitions between the lower $^4I_{15/2}$ crystal field levels and the $^4F_{7/2}$ levels are acting as traps for radiation of energy equal to the energy differences between these levels. Light scattered at

Table 6.2: Frequencies (in cm^{-1}) of the electronic levels of the $^4I_{15/2}$ crystal field levels, measured using Raman scattering with resonant excitation at 488.0 nm, Raman scattering with nonresonant excitation at 514.5 nm, and 77 K absorption absorption data.

Symmetry	Crystal Field Fit for 1% Er in $LuPO_4$	Optical Absorption Measurements $ErPO_4$	Resonance Raman Measurements $ErPO_4$	Nonresonance Raman Measurements $ErPO_4$
Γ_7	0	0	0	0
Γ_6	36	33	33	33
Γ_7	50	53	53	53
Γ_7	101	105	105	105
Γ_6	133	145	145	145
Γ_6	230	232	234	a
Γ_7	247	244	246	a
Γ_6	287	a	269	a

a: not observed.

those frequencies is reabsorbed by the crystal. The higher temperature Stokes spectra have evidence of absorption dips at the frequencies where the fluorescent transition is expected to occur. The reabsorption also explains the drop in intensity of the Stokes Raman lines at 33 and 53 cm^{-1} as the temperature rises. The drop in intensity of these lines is much slower than that observed for the fluorescent transitions excited with the 476.5 nm line (see Figure 6.6) since the Raman lines are not in exact resonance with the transitions between the energy levels.

3. The possibility of site selective fluorescence, occuring at the same frequency as the Raman transition, would arise if there were frequency overlap between the excitation bandwidth (0.1 cm^{-1} for the argon-ion laser) and the inhomogeneously broadened line. However, as mentioned before, this does not occur for $ErPO_4$, making it a rather simple system to study from the point of view of Raman scattering with the 488.0 nm line since site selective fluorescence is expected to be either nonexistent or extremely weak.

4. The Stokes electronic Raman peaks are not the only transitions that are observed to be resonantly enhanced by the 488.0 nm excitation. In the Stokes spectra, the 20 cm^{-1} line is at the same frequency but ten times more intense than the corresponding Raman peak with nonresonant excitation. In absolute wavenumbers its position is $20,487 - 20 = 20,467$ cm^{-1} which does not correspond to any fluorescent transition. The closest one would be $20,493 \longrightarrow 33$ cm^{-1} which is 7 cm^{-1} away in frequency. However, the transition $33 \longrightarrow 20,493$ contributes to reabsorption of the 20 cm^{-1} Stokes transition (at higher temperatures). Also, the polarization in which it appears, XY, is the one for which its enhancement is predicted to be the strongest.

   On the anti-Stokes side, the transition at 33 cm^{-1} is also observed to be very strongly enhanced. In absolute wavenumbers this transition is at 20,520 cm^{-1}. The closest transitions are $20,556 \longleftrightarrow 33$ (= 20,523 cm^{-1}) and $20,570 \longleftrightarrow 53$ (= 20,517 cm^{-1}). The resulting 3 cm^{-1} frequency shift between fluorescence and Raman is not observed to occur. Thus the 33 cm^{-1} anti-Stokes transition must be the anti-Stokes Raman transition of the 33 cm^{-1} Stokes electronic transition. Again, the XY polarization is the polarization in which the most resonance enhancement of this transition is expected to occur. However, as the temperature rises, the two direct transitions just

mentioned will act to quench the 33 cm^{-1} anti-Stokes line, in the same fashion as the quenching of the 33 and 53 Stokes transitions. A resonantly enhanced anti-Stokes transition at 20 cm^{-1} is also observed in the XY spectrum.

5. Finally, another argument for the presence of resonant Raman scattering is to observe more closely the relative intensity pattern of the 33 and 53 cm^{-1} transitions. The ratios of the resonant to nonresonant scattering intensities of the 33 and 53 cm^{-1} transitions are summarized in Table 6.3. Some of the lines, for instance 33 cm^{-1} in ZY and XZ, or 53 cm^{-1} in XY and XZ, have greatly increased in intensity (by a factor of ten to a hundred) whereas 33 cm^{-1} in XY and 53 cm^{-1} in ZY have barely increased in intensity. These last two transitions are actually quite strong with nonresonant excitation and thus have the posiibility of exhibiting significant destructive inteference with the resonant amplitudes, leading to a much smaller intensity for these transitions compared to the others such as 53 cm^{-1} in XY which will have mostly a resonant contribution, its nonresonant amplitude being quite small. Also, if it were fluorescence which were taking place, one would expect that for example the 33 cm^{-1} transition intensities should be comparable in XY and in XZ (if not larger in XY). This comes from the fact that the overall fluorescence intensity can be written as the product of the two dipole absorption and emission intensities so that the two transitions would differ only in that absorption of X polarized light is taking place vs. absorption of Z polarized light. The ion would then emit X polarized light. For the two lower levels of the $^4F_{7/2}$ multiplet the X absorption is much stronger, in fact direct Z absorption is forbidden for the lower Γ_7 level. Experimentally, one observes that the XZ component of the 33 cm^{-1} transition is roughly twenty times stronger than the XY component. Any reabsorption or nonradiative decays would be exactly the same for the emitted light in both cases since it is of the same frequency and polarization. Thus the relative intensities do not at all fit the fluorescence explanation but rather the amplitude interference of the resonant Raman effect explanation.

Having established the presence of strong resonance enhancement of the electronic Raman transitions in $ErPO_4$, a number of interesting investigations can be pursued. Scanning a tunable dye laser through the $^4F_{7/2}$ multiplet would allow a detailed study of the relative intensity pattern as a function of excitation frequency and would perhaps elucidate with

Table 6.3: Ratio of the resonant to nonresonant scattering intensities of the 33 and 53 cm^{-1} Raman transitions in various polarizations. Phonon E_g^3 was used as an internal standard to normalize the spectra to a common scattering efficiency.

	Polarization			
	XY	ZY	XZ	ZZ
33 cm^{-1} transition	1.8	80.0	18.1	a
53 cm^{-1} transition	124.8	1.9	29.1	a

a: ZZ transitions are absent or weak.

more specificity the problem of the missing fluorescent transitions from the lower $^4F_{7/2}$ levels to the 33 and 53 cm^{-1} levels. Another route was pursued here to allow the the continued use of the cw Raman photon counting system, which was to study the varying concentration $Er_xLu_{1-x}PO_4$ crystals using the 488.0 nm line. The energy levels in these crystals shift relative to that line in a way that mirrors the tuning of a dye laser across a system of fixed energy levels. Other effects also arise that are discussed in the next sections. Finally, one should mention that if a pulsed dye laser is available it is possible to study the Raman peaks in a time resolved fashion. The laser pulse needs to be quite short since the $^4F_{7/2}$ lifetimes appear to be extremely small. An estimate of the characteristic lifetime is made in chapter 7.

6.4 The Resonant Electronic Raman Spectra of 10% Er^{3+} in $LuPO_4$ - The Case of Resonant Excitation at the Half Maximum of the Line

In 10% Er^{3+} in $LuPO_4$ the lower Γ_6 level is at 20,483.7 cm^{-1} and has a linewidth which was observed to be 6.5 cm^{-1}. This last value might be slightly overestimated due to the difficulty of measuring the linewidth of strongly absorbing transitions. At any rate, taking this linewidth as a rough estimate, this implies that the argon-ion laser excitation, 20,486.7

cm^{-1} (vacuum value), is at the half maximum of the line since it is half a linewidth away from the center of the line. This has several important consequences:

- There is absorption of the incident laser light. This absorption is observed to be stronger in X,Y polarized light than in Z polarized light, since the absorption strengths are larger for the former. The absorption of the incident light decreases the amount of light available for producing Raman scattered radiation, be it vibrational or electronic Raman scattering. In addition, there can be local heating of the sample due to the absorption.

- Site selective fluorescence can potentially be excited from the sample and since it has exactly the same frequency as the Raman scattered light it is not possible to distinguish between the two forms of scattering with a cw Raman system.

- A calculation of the intensities of the lines can no longer make use of the simplifying assumption which replaces the inhomogeneous lineshape with a Dirac delta fuction positioned in frequency at the center of the line. The intensity calculation must now be performed as an integration over the inhomogeneous lineshape and must include the imaginary part of the energy denominator which is proportional to the dephasing time T_2.

6.4.1 Experimental Spectra at T=4.2 K - Description and Interpretation

The experimental spectra observed at T=4.2 K are shown in Figure 6.17. It is apparent from the intensity scales indicated on the figure that the signal from the electronic peaks is significantly larger than that obtained for $ErPO_4$, even though the Er^{3+} concentration has been diluted by a factor of ten. For example, the XY intensities of the 35 and 53 cm^{-1} transitions are on the order of 20,000 counts per second whereas for $ErPO_4$ the same transitions are on the order of 10,000 cps. This translates to an increase in signal *per ion* of a factor of twenty. The intensities of the phonons are comparable for the two crystals so that this increase cannot be explained as coming from an experimental parameter such as crystal length or collection efficiency, but must have something to do with the interaction between the laser radiation and the Er^{3+} $^4F_{7/2}$ energy levels.

Another interesting point is that the intensity of phonon E_g^3 is twice as large in XZ than in ZY. This confirms the fact that there is now overlap between the laser frequency and the lower Γ_6 level at 20,484 cm^{-1}. There is substantial absorption of the laser radiation and since the oscillator strength of the transition from the ground state to the 20,484 cm^{-1} state is larger in X or Y polarized light than in Z, the ZY and XY intensities will be reduced compared to the XZ znd ZZ intensities. A phonon such as E_g^3, which should have symmetrical Raman transition intensities, will thus produce a reduced signal in ZY polarization. As was done for the higher temperature data for $ErPO_4$, this polarization dependent reduction in phonon intensity can be used can be used to correct the electronic intensities for the absorption of incident light. Visually observing the laser beam after it traverses the crystal sample, it is apparent that the absorption of X,Y polarized light is larger than that of Z polarization. One can also see a yellow-green fluorescence which is the signature of the $^4S_{3/2} \longrightarrow {}^4I_{15/2}$ radiative transitions.

In Table 6.1, the linewidth of the lower Γ_6 state was given as 6.5 cm^{-1} although this might be a slightly overestimated value as discussed in section 6.2.2. Nevertheless, if we consider this value as accurate, it tells us that the laser frequency is right at the half maximum of the line which agrees with the experimental observation that strong absorption is taking place. A smaller value of the linewidth would place the laser frequency at a different position relative to the center of the line, but at any rate it is quite clear that it is well within the inhomogeneous lineshape of the lower Γ_6 level at 20,484 cm^{-1}.

Another interesting point that can be observed in the T=4.2 K spectra is that the relative intensities of the 35 and 53 cm^{-1} transitions in various polarizations have changed compared to those seen in $ErPO_4$. An obvious example is given by the XY spectrum. In $ErPO_4$ the 53 cm^{-1} transition is twice as strong as that at 33 cm^{-1}. In the 10% Er^{3+} in $LuPO_4$ crystal, the situation is reversed, the 35 cm^{-1} transition is now stronger than the one at 53 cm^{-1}. Barring strong site selective fluorescence, this is an indication of the change in Raman amplitude interferences dicussed in section 6.2.6 that occurs when the resonating energy levels shift relative to the laser line as they do in going from the pure erbium crystal to the 10% one. The intensities of the 33 cm^{-1} transition should, however, be treated with caution since the absorption of the laser radiation is quite strong and can result in local heating and hence reabsorption of the 33 cm^{-1} Raman scattered light.

The 35 and 53 cm^{-1} transition line centers were measured to within ± 0.5 cm^{-1} with

both resonant and nonresonant excitation, using the slit widths 80-120-120-80 μ. They were found to be at the same position relative to phonon E_g^3, within experimental error. However, their linewidths appear to be 25% to 35% larger with resonant excitation. This might be an indication of site selective fluorescence.

The intensities of the higher lying lines have also changed quite substantially. For the transitions at 152, 242, 257, and 275 cm^{-1}, the ZY intensities are equal to those in ZZ. The per ion intensities are also two orders of magnitude larger than those for $ErPO_4$. This tends to support the hypothesis that these transitions are actually fluorescence resulting from the radiative decay of the population of the 20,483 cm^{-1} level. This level absorbs roughly twice as much light in X than in Z. The intensity of the Z fluorescence will not depend on whether the incident excitation is X or Z polarized if the polarization characteristic of the absorbed light is lost either by phonon assisted absorption or ion-ion energy transfer. Both of these processes produce spectral diffusion of the frequency of the incident radiation and allow radiative transitions from sites that are not exactly resonant with the exciting frequency.

The appearance of the strong ZZ intensities for the 152 and 242 cm^{-1} transitions also violates the electronic Raman selection rule $\Gamma_7 \longrightarrow \Gamma_6$ transitions forbidden in ZZ (in the electric dipole approximation). The only way these transitions can be allowed in ZZ is via magnetic dipole transitions through the intermediate states. The resonance enhancement might make such transitions observable, but since magnetic dipole transitions are much weaker than electric dipole transitions this could not account for the high strength of the 152 and 242 cm^{-1} transitions in ZZ. This again supports the argument that these higher transitions are actually incoherent fluorescence. Only the 152 cm^{-1} transition appears (weakly) in the nonresonant Raman spectra so that it is not possible to check whether the transitions are at the same Raman frequency with nonresonant excitation.

A comparison of the XZ and XY spectra shows that there are differences between the relative intensities of the 33 and 53 cm^{-1} in XZ versus those in XY. If these two transitions were fluorescent, their relative intensities would be the same in XZ as in XY, since, as argued in the previous paragraphs, the relative intensities of the two X polarized fluorescent transitions do not depend on whether the original excitation was X or Z polarized. The overall intensities of the two transitions might be stronger in XZ than in ZY, or vice versa, if there are differences in absorption between Z and Y. Thus, this is an indication that resonant electronic Raman transitions are participating in the lines at 33 and 53 cm^{-1}.

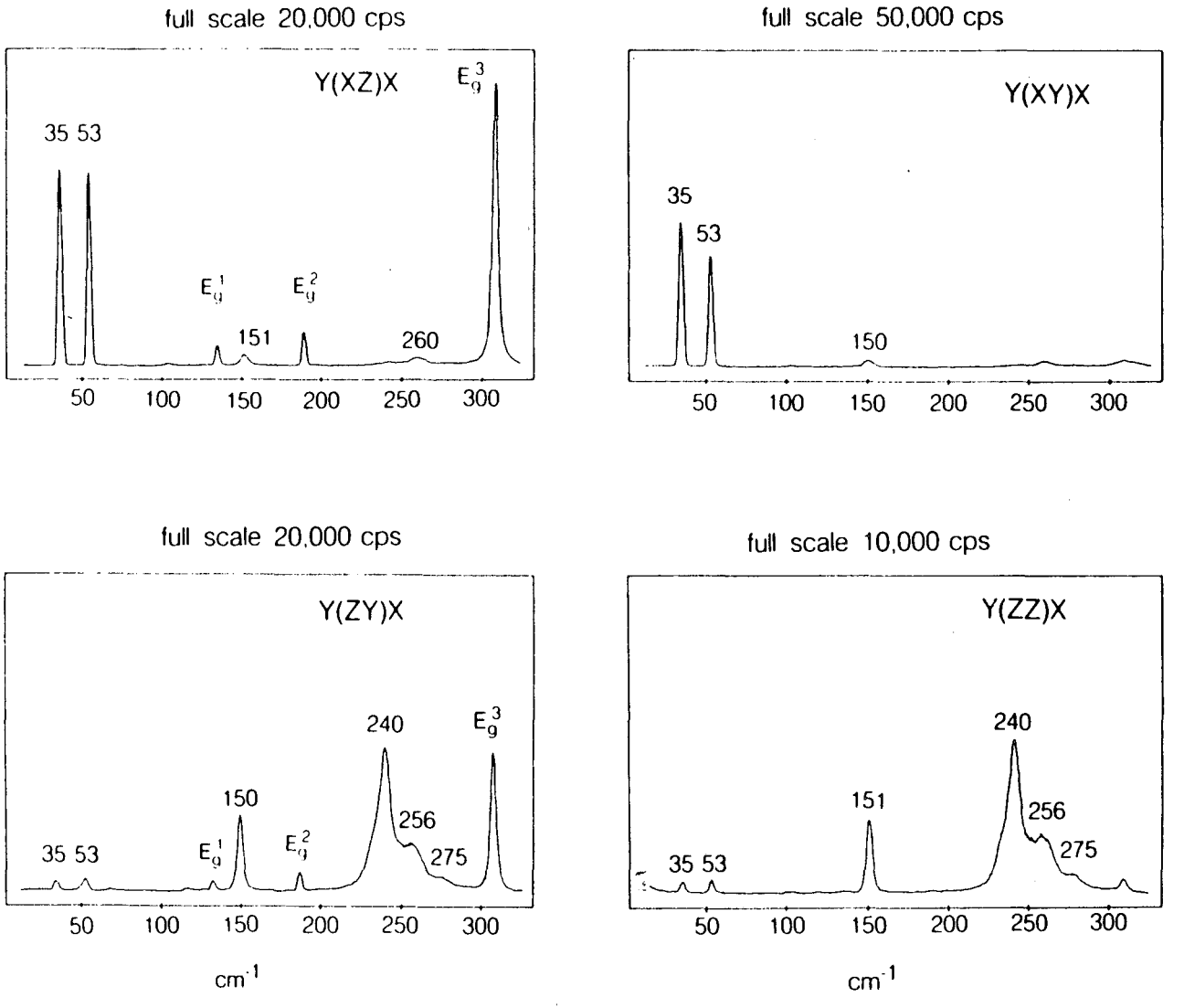

Figure 6.17: Experimental Raman spectra of 10% Er^{3+} in $LuPO_4$ at T=4.2 K with resonant excitation at 488.0 nm. The spectral bandwidth of the spectrometer is set to 2.5 cm^{-1}.

6.4.2 Temperature Dependence of the Stokes Raman Spectrum

The resonant Raman spectra can be recorded as a function of temperature, in a similar fashion to $ErPO_4$. The results are different than those for $ErPO_4$ and are quite enlightening. The tenfold dilution of erbium not only shifts the energy levels but also affects the rate at which the Raman scattered light is reabsorbed. Thus the high temperature spectra are simpler to interpret than those of $ErPO_4$.

Figure 6.18 shows the temperature evolution of the XY and ZY spectra in the low wavenumber region. Phonon E_g^3 at 307 cm^{-1} is also shown so that the intensities at different temperatures can be normalized to a common scattering efficiency. The interesting point to note about Figure 6.18 is the shift that occurs in the XY spectrum between 100 and 150 K. The transitions at 35 and 53 cm^{-1} steadily decrease in intensity from 4.2 to 100 K as the scattered light is reabsorbed by the crystal in the same fashion as for $ErPO_4$. At 100 K slight absorption dips begin appearing that become quite strong by 150 K and render the 35 and 53 cm^{-1} transitions unobservable. At 100 K the absorption peak centers are shifted relative to the 35 and 53 cm^{-1} transitions, which can be understood from the fact that the level which is absorbing is 3 cm^{-1} away from the exciting laser line and thus shifted relative to the potential Raman lines. In contrast, in the ZY spectrum, the reabsorption is much weaker due to selection rules and small oscillator strengths so that the 35 and 53 cm^{-1} transitions are still observed all the way up to room temperature. Thus the crystal does not fluoresce but instead absorbs the scattered light in the ${}^4F_{7/2} \longleftrightarrow {}^4I_{15/2}$ transition region, with a strength that depends on the polarization of the light. One can thus reason that the 35 and 53 cm^{-1} transitions are electronic Raman transitions that are reabsorbed in XY but not in ZY because the erbium ion is sufficiently diluted. It is thus quite possible that the 10% Er^{3+} crystal allows the observation of resonantly enhanced electronic Raman transitions up to room temperature.

6.5 Future Directions

The next step in the resonant Raman studies of the erbium phosphate crystals is to study the resonance effect as the laser excitation is tuned across the levels of the ${}^4F_{7/2}$ multiplet. It will then be easy to clearly distinguish between Raman and fluorescence transitions and observed quantitatively the enhancement pattern. There are also other erbium levels, such

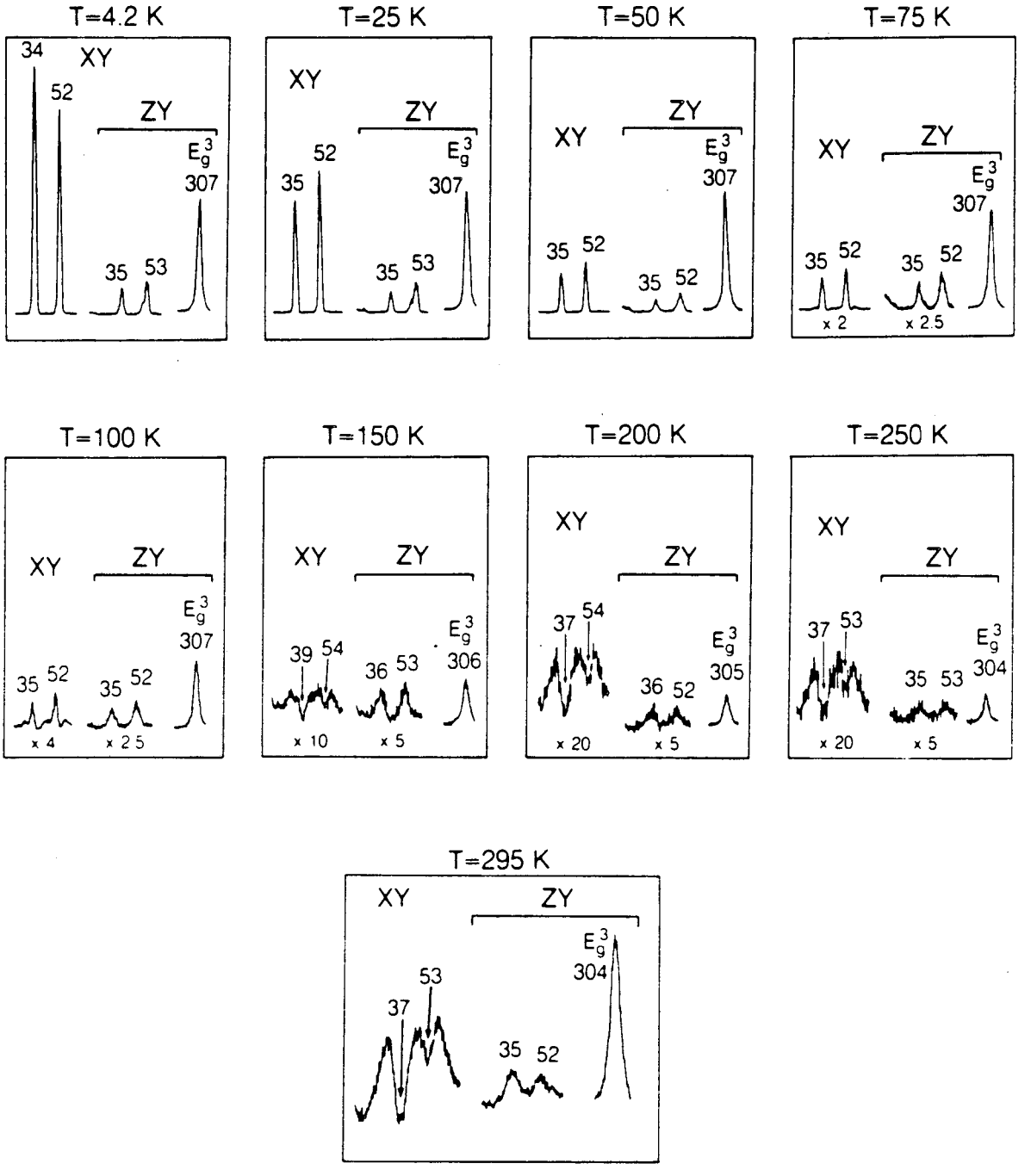

Figure 6.18: Temperature evolution of the low-wavenumber resonant Raman spectra of 10% Er^{3+} in $LuPO_4$. Full scale at 4.2 K is 20,000 cps in XY and ZY(E_g^3), and 5,000 cps for the ZY electronic transitions. Changes in scale are indicated up to 250 K. At room temperature (separate scan) full scale is 2,000 cps for the elctronic transitions and 5,000 cps for E_g^3.

as $^4S_{3/2}$, that are promising candidates for resonance enhancement studies of the electronic Raman transitions. The same types of studies can also be carried out in other rare earth ions.

References

[1] P.C. Becker, G.M. Williams, R.E. Russo, N. Edelstein, J.A. Koningstein, L.A. Boatner, and M.M. Abraham, Opt. Lett. **11**, 282 (1986).

[2] Y.R. Shen, Phys. Rev. B **9**, 622 (1974).

[3] D. Lee and A.C. Albrecht, in *Advances in Infrared and Raman Spectroscopy*, Vol. 12, R.J.H. Clark and R.E. Hester, eds. (Wiley Heyden, London, 1985), p.179.

[4] P. Grünberg and J.A. Koningstein, J. Chem. Phys. **53**, 4584 (1970).

[5] D. Nicollin and J.A. Koningstein, Chem. Phys. **49**, 377 (1980).

[6] R.L. Wadsack and R.K. Chang, Solid State Commun. **10**, 45 (1972).

[7] D.A. Ender, M.S. Otteson, R.L. Cone, and M.B. Ritter, Opt. Lett. **7**, 611 (1982).

[8] M.L. Shand, J. Appl. Phys. **52**, 1470 (1981).

[9] T. Hayhurst, G. Shalimoff, N. Edelstein, L.A. Boatner, and M.M. Abraham, J. Chem. Phys. **74**, 5449 (1981).

[10] G. Williams, Lawrence Berkeley Laboratory, unpublished results.

[11] E.D. Reed and H.W. Moos, Phys. Rev. B **8**, 980 (1973).

[12] F. Auzel, in *Luminescence of Inorganic Solids*, B. Di Bartolo, ed. (Plenum Press, New York, 1978), p.67.

[13] F. Auzel, Phys. Rev. B **13**, 2809 (1976).

[14] P.Y. Yu and Y.R. Shen, Phys. Rev. B **12**, 1377 (1975), and Phys. Rev. B **17**, 4017 (1978).

[15] J. Weiner, Ph.D. thesis, University of California, Berkeley, 1983 (unpublished).

[16] D.L. Rousseau, J.M. Friedman, and P.F. Williams, in *Raman Spectroscopy of Gases and Liquids*, A. Weber, ed. (Springer-Verlag, New York, 1979), p. 203.

[17] M.J. Weber, Phys. Rev. **157**, 262 (1967).

[18] M.J. Weber, Phys. Rev. **171**, 283 (1968).

[19] L.A. Riseberg and H.W. Moos, Phys. Rev. Lett. **19**, 1423 (1967).

[20] L.A. Riseberg and H.W. Moos, Phys. Rev. **174**, 429 (1968).

[21] L.A. Riseberg and M.J. Weber, Relaxation phenomena in rare earth luminescence, in *Progress in Optics*, vol. XIV, E. Wolf, ed. (North-Holland Publishing Co., Amsterdam, 1976), p. 91.

[22] S. Hüfner, *Optical Spectra of Rare Earth Compounds* (Academic Press, New York, 1978), chapter 5.

[23] J.C. Wright, in *Topics in Applied Physics*, F.K. Fong, ed. (Springer-Verlag, Berlin, 1976), p. 239.

[24] R. Reisfeld, Structure and Bonding **30**, 65 (1976).

[25] R. Orbach, in *Optical Properties of Ions in Solids*, B. Di Bartolo, ed. (Plenum Press, New York, 1975), p. 355.

[26] R.K. Watts in *Optical Properties of Ions in Solids*, B. Di Bartolo, ed. (Plenum Press, New York, 1975), p. 307 and p. 337.

[27] R.L. Cone and R.S. Meltzer, J. Chem. Phys. **62**, 3573 (1975).

[28] A. Szabo, Phys. Rev. Lett. **25**, 924 (1970).

[29] L.E. Erickson, Phys. Rev. B **11**, 77 (1975).

[30] D.S. Hamilton, P.M. Selzer, and W.M. Yen, Phys. Rev. B **16**, 1858 (1977).

[31] W.M. Yen and P.M. Selzer, in *Laser Spectroscopy of Solids*, W.M. Yen and P.M. Selzer, eds. (Springer-Verlag, Berlin, 1981), p. 141.

[32] R.P. Feynmann, R.B. Leighton, and M. Sands, *The Feynmann Lectures on Physics*, Vol. III (Addison-Wesley Publishing Co., Reading, MA, 1965), chapter 1.

[33] P.C. Becker, N. Edelstein, G.M. Williams, J.J. Bucher, R.E. Russo, J.A. Koningstein, L.A. Boatner, and M.M. Abraham, Phys. Rev. B **31**, 8102 (1985).

[34] P.C. Becker, N. Edelstein, B.R. Judd, R.C. Leavitt, and G.M.S. Lister, J. Phys. C **18**, L1063 (1985).

Chapter 7

Calculation of the Resonant Raman Intensities in Erbium Phosphate Crystals - Interference Effects and Estimate of T_2

It is possible to estimate numerically the relative intensities of the electronic Raman transitions if the different quantities that enter the expression for the Raman amplitude are known. Expression 6.7 can be used for this purpose if values are obtained for the following quantities:

- the resonant matrix elements $\langle j|D_\rho|i\rangle$, where the crystal field states $|j\rangle$ and $|i\rangle$ belong to the ${}^4F_{7/2}$ and ${}^4I_{15/2}$ multiplets, and D_ρ is the electric dipole operator for the polarization ρ;
- the energy differences $E_{ji} - \hbar\omega$ where E_{ji} is the energy difference between the intermediate state $|j\rangle$ and the initial state $|i\rangle$, and $\hbar\omega$ is the excitation energy (in vacuum wavenumbers);
- the nonresonant amplitudes $\alpha_{\rho\sigma}$.

In the following section we list the values of these quantities and the method by which they were obtained. The relative intensities of the resonantly enhanced electronic Raman transitions are then calculated using these values and compared to the experimentally observed intensities. This work was done only for the Stokes transitions at 33 and 53 cm^{-1} since these transitions in various polarizations in the different concentration Er^{3+} doped phosphate crystals provide a large amount of data that can be used to test the accuracy of the calculations performed here and the underlying asumptions. It is also fairly easy to obtain the relevant matrix elements involving the 33 and 53 cm^{-1} states.

The spectra and the calculations show that strong quantum mechanical interference effects appear in determining the resonance Raman intensities. These interference effects have been observed before in various systems [1,2,3].

7.1 Resonant Matrix Elements

The resonant matrix elements can be obtained via normalized absorption measurements as a function of frequency. For a given crystal of length l, at a frequency ω where the absorption coefficient is $\alpha(\omega)$, the transmitted intensity is equal to:

$$I(\omega) = I_0(\omega)\exp(-\alpha(\omega)l) \tag{7.1}$$

where $I_0(\omega)$ is the incident light intensity. Thus if the percentage of light absorbed by the crystal at a particular frequency is determined experimentally one can extract the absorption coefficient $\alpha(\omega)$. The absorption coefficient of a particular transition is itself proportional to the oscillator strength of that transition which in turn is proportional to the square of the matrix element of the radiative multipole operator which connects the two states. In the transitions considered here the absorption transitions observed all appear to be electric dipole transitions.

The tungsten lamp absorption measurements reported in section 6.2 for T=4.2 K and in section 6.3 for T=25 and 50 K give an idea of the strength of the various transitions. The T=4.2 K transitions originate all in the ground state, whereas the higher temperature spectra exhibit transitions that originate in the excited 33 and 53 cm^{-1} states. Normalized absorption measurements of the two $^4F_{7/2}$ lower levels in both 1% Er^{3+} in YPO_4 and $ErPO_4$ were performed with an Nd:YAG pumped pulsed dye laser [4]. The resulting oscillator strengths, calculated from William's data [4], are listed in Table 7.1. It is assumed that the oscillator strengths are the same for any given concentration of Er^{3+} doped in $LuPO_4$. This assumption is supported by absorption measurements done with photographic plates and a tungsten lamp on the various concentration Er^{3+} in $LuPO_4$ and YPO_4 crystals. All the transitions appear with approximately the same relative intensities for all the crystals. The reason for this is that the relative intensities are mainly governed by the Judd-Ofelt parameters, and these, like the even parity crystal field parameters which determine the energy levels, vary very little among the various members of the erbium phosphate family.

Table 7.1: Oscillator strengths of the transitions between the 0, 33, and 53 cm^{-1} levels of the $^4I_{15/2}$ multiplet and the 20,485 and 20,493 cm^{-1} levels of the $^4F_{7/2}$ multiplet of $ErPO_4$, from Nd:YAG pulsed laser absorption measurements.

$\langle\Gamma_7(20,485)\|Z\|\Gamma_7(0)\rangle^2 = 0$	$\langle\Gamma_7(20,485)\|X,Y\|\Gamma_7(0)\rangle^2 = 0.02$
$\langle\Gamma_7(20,493)\|Z\|\Gamma_7(0)\rangle^2 = 0.3$	$\langle\Gamma_7(20,493)\|X,Y\|\Gamma_7(0)\rangle^2 = 0.6$
$\langle\Gamma_7(20,485)\|Z\|\Gamma_6(33)\rangle^2 = 0.1$	$\langle\Gamma_7(20,485)\|X,Y\|\Gamma_6(33)\rangle^2 = 1.5$
$\langle\Gamma_7(20,493)\|Z\|\Gamma_6(33)\rangle^2 = 0$	$\langle\Gamma_7(20,493)\|X,Y\|\Gamma_6(33)\rangle^2 = 5.0$
$\langle\Gamma_7(20,485)\|Z\|\Gamma_7(53)\rangle^2 = 0$	$\langle\Gamma_7(20,485)\|X,Y\|\Gamma_7(53)\rangle^2 = 1.0$
$\langle\Gamma_7(20,493)\|Z\|\Gamma_7(53)\rangle^2 = 0.03$	$\langle\Gamma_7(20,493)\|X,Y\|\Gamma_7(53)\rangle^2 = 3.2$

The strongest transitions are by far those from the 33 and 53 cm^{-1} states to those at 20,485 and 20,493 cm^{-1}, in X,Y polarization. This explains why the 20 cm^{-1} Stokes transition is so strong in XY polarization, since its resonant amplitude is proportional to the resonant matrix element products $\langle 53|X|20,485\rangle\langle 20,485|Y|33\rangle$ and $\langle 53|X|20,493\rangle\langle 20,493|Y|33\rangle$, which are the largest amplitude channels in this system of levels.

The oscillator strengths being proportional to the squares of the matrix elements, one can take the square roots of the values given in Table 7.1 and obtain (in arbitrary units) the relative dipole matrix elements of the various transitions. The amplitudes of the resonance parts of the Raman tensor can be obtained by forming the products $\langle f|D_\rho|j\rangle\langle j|D_\sigma|i\rangle$ where the initial state $|i\rangle$ is the ground state, the final state $|f\rangle$ is either the 33 or 53 cm^{-1} state, and the intermediate state $|j\rangle$ is the 20,485 or 20,493 cm^{-1} state. These products yield the strengths of the two resonant amplitude channels which go through either the 20,485 or 20,493 cm^{-1} states. Table 7.2 lists the values of these amplitudes. Since there is an indeterminancy in the absolute phases of the matrix elements (the square root can be taken to be positive or negative) there is a $\pm$ in front of each value.

Several conclusions can be drawn from Table 7.2.

- The Γ_7 state at 20,485 cm^{-1} is an extremely weak channel for resonance amplification and will not contribute significantly to the resonant Raman signal unless the exciting line is very close in energy to that transition.

- The strongest resonant amplitudes of the Stokes transitions that originate in the

Table 7.2: Amplitudes of the resonant matrix element products involving ${}^4F_{7/2}$ multiplet intermediate states.

$\langle\Gamma_6(33)\|X\|\Gamma_7(20,485)\rangle\langle\Gamma_7(20,485)\|Y\|\Gamma_7(0)\rangle = \pm 0.10$
$\langle\Gamma_6(33)\|Z\|\Gamma_7(20,485)\rangle\langle\Gamma_7(20,485)\|Y\|\Gamma_7(0)\rangle = \pm 0.02$
$\langle\Gamma_6(33)\|X\|\Gamma_7(20,485)\rangle\langle\Gamma_7(20,485)\|Z\|\Gamma_7(0)\rangle = 0$
$\langle\Gamma_6(33)\|Z\|\Gamma_7(20,485)\rangle\langle\Gamma_7(20,485)\|Z\|\Gamma_7(0)\rangle = 0$
$\langle\Gamma_6(33)\|X\|\Gamma_6(20,493)\rangle\langle\Gamma_6(20,493)\|Y\|\Gamma_7(0)\rangle = \pm 1.0$
$\langle\Gamma_6(33)\|Z\|\Gamma_6(20,493)\rangle\langle\Gamma_6(20,493)\|Y\|\Gamma_7(0)\rangle = 0$
$\langle\Gamma_6(33)\|X\|\Gamma_6(20,493)\rangle\langle\Gamma_6(20,493)\|Z\|\Gamma_7(0)\rangle = \pm 0.71$
$\langle\Gamma_6(33)\|Z\|\Gamma_6(20,493)\rangle\langle\Gamma_6(20,493)\|Z\|\Gamma_7(0)\rangle = 0$
$\langle\Gamma_7(53)\|X\|\Gamma_7(20,485)\rangle\langle\Gamma_7(20,485)\|Y\|\Gamma_7(0)\rangle = \pm 0.08$
$\langle\Gamma_7(53)\|Z\|\Gamma_7(20,485)\rangle\langle\Gamma_7(20,485)\|Y\|\Gamma_7(0)\rangle = 0$
$\langle\Gamma_7(53)\|X\|\Gamma_7(20,485)\rangle\langle\Gamma_7(20,485)\|Z\|\Gamma_7(0)\rangle = 0$
$\langle\Gamma_7(53)\|Z\|\Gamma_7(20,485)\rangle\langle\Gamma_7(20,485)\|Z\|\Gamma_7(0)\rangle = 0$
$\langle\Gamma_7(53)\|X\|\Gamma_6(20,493)\rangle\langle\Gamma_6(20,493)\|Y\|\Gamma_7(0)\rangle = \pm 0.80$
$\langle\Gamma_7(53)\|Z\|\Gamma_6(20,493)\rangle\langle\Gamma_6(20,493)\|Y\|\Gamma_7(0)\rangle = \pm 0.08$
$\langle\Gamma_7(53)\|X\|\Gamma_6(20,493)\rangle\langle\Gamma_6(20,493)\|Z\|\Gamma_7(0)\rangle = \pm 0.57$
$\langle\Gamma_7(53)\|Z\|\Gamma_6(20,493)\rangle\langle\Gamma_6(20,493)\|Z\|\Gamma_7(0)\rangle = \pm 0.05$

ground state are those of the 33 and 53 cm^{-1} transitions in XY and XZ polarization. This occurs via the Γ_6(20,493 cm^{-1}) intermediate state. For these lines there can be significant interference between the resonant and nonresonant amplitudes.

- The 33 cm^{-1} transition in ZZ polarization has zero resonance amplitude. In fact, based on one-photon electric dipole selection rules, the 0 to 33 cm^{-1} Raman transition is forbidden in ZZ polarization. This is valid for any $\Gamma_6 \longleftrightarrow \Gamma_7$ Raman transition. Any ZZ intensity for this type of transition must either come from polarization leakage or an intensity mechanism other than an electric dipole mediated Raman transition.

7.2 The Energy Denominators

The values of the energy levels of the two lower crystal field states of the $^4F_{7/2}$ multiplet are given in section 6.2. We assume that these two states are the only ones involved in the resonance enhancement of the the Stokes transitions that originate in the ground state, since the two higher levels of the $^4F_{7/2}$ multiplet are at least 60 cm^{-1} away from the exciting laser line. The energy differences between the lower Γ_6 and Γ_7 states of the $^4F_{7/2}$ resonant intermediate multiplet and the argon-ion laser line at 488.0 nm (20,486.7 cm^{-1}) are tabulated in Table 7.3, in vacuum wavenumbers. In all cases it is the center of the electronic line that is used to calculate the energy difference. The sign of the energy difference, or rather the change in sign of the energy denominator between different concentration Er^{3+} phosphate crystals, is responsible for the reversal of the Raman amplitude interference that results in significant variations in the relative intensity pattern of the resonant electronic Raman transitions in these crystals.

7.3 The Nonresonant Amplitudes

The nonresonant intensities can be experimentally obtained by exciting the crystal with the argon-ion laser lines at 514.5, 476.5, or 457.9 nm. One can then take the square root of these intensities to obtain the nonresonant amplitudes. The signs can be fixed by using the signs predicted by the theoretical calculations of Chapter 4 with $F_1/F_2 = 0.03$. This is a somewhat arbitrary choice which actually does not really matter since it is the relative phases of the nonresonant and resonant amplitudes which are important in determining the

Table 7.3: Energy differences between the exciting laser line and the two lower levels of the $^4F_{7/2}$ multiplet in various concentration Er^{3+} doped phosphate crystals.

	Lower Γ_6 level	Lower Γ_7 level
$ErPO_4$	6.2	−1.7
$Er_{.10}Lu_{.90}PO_4$	−3.0	2.4
$Er_{.01}Lu_{.99}PO_4$	−4.1	2.4

Table 7.4: Nonresonant Raman amplitudes for various polarizations of the incident and scattered light. The values are from experimental data and the signs are chosen in accordance with the signs predicted with $F_1/F_2 = 0.03$. The uncertainty is ±25% and the units are $(1{,}000\ \text{cps})^{\frac{1}{2}}$.

	Polarization			
	XY	ZY	XZ	ZZ
33 cm^{-1} transition	1.20	0.17	0.48	0
53 cm^{-1} transition	0.24	−0.70	−0.28	0

overall scattering amplitude. The nonresonant amplitudes are tabulated in Table 7.4 for selected polarization combinations of the incident and scattered light. They are averaged from several different scans with excitation at 514.5, 476.5, and 457.9 nm, and make use of more data than the intensities reported in Becker *et al* [5]. The amplitude values are in the "operational" units $(1{,}000\ \text{cps})^{\frac{1}{2}}$, where cps stands for counts per second. The intensity of phonon E_g^5, which will be used as a calibration standard to estimate the resonance enhancement, is 5,000 cps in the spectra that correspond to the amplitude values of Table 7.4. It is only necessary to square the amplitude values of Table 7.4 to obtain the nonresonant intensities.

The uncertainty on the amplitudes is ±25%. This is unfortunate as the interference between the resonant and nonresonant amplitudes is extremely sensitive to the ratio between the two amplitudes. We should therefore not expect that our calculations of the total intensity under resonant excitation be very accurate. Agreement to within a factor of

Table 7.5: Resonant Raman intensities for $ErPO_4$.

	Polarization			
	XY	ZY	XZ	ZZ
33 cm^{-1} transition	2.60	0.23	4.17	0.10
53 cm^{-1} transition	7.19	0.93	2.28	0.06

two would be quite reasonable given the assumptions and uncertainties involved in the calculations.

7.4 Experimental Resonant Intensities for the 100% and 10% Crystals

The resonant intensities can be tabulated for the various concentration erbium phosphate crystals. To facilitate the calculations and to allow comparison with the nonresonant intensities, the resonant intensities are given in units of (1,000 cps), phonon E_g^5 having the intensity 5,000 cps, as was the case for the nonresonant amplitudes reported in Table 7.4. This way the resonant and nonresonant intensities (obtained by taking the square of the values in Table 7.4) can be directly compared. By using the phonon intensity as a calibration, one can correct for possible differences in incident laser power and scattering efficiency. The resonant intensities for $ErPO_4$, averaged from several scans with excitation at 488.0 nm, are given below in Table 7.5.

Similarly, the resonant intensities for Raman scattering from 10% Er^{3+} doped in $LuPO_4$ are listed in Table 7.6. Phonon E_g^5 was normalized to 5,000 cps in the spectra that yielded these intensity values. Several scans using different samples were averaged to obtain the experimental intensities of Table 7.6. Since the concentration of Er^{3+} has decreased by a factor of ten compared to $ErPO_4$ it is necessary to multiply the intensities observed with the 10% Er^{3+} crystal by ten so as to allow a comparison with the $ErPO_4$ signal on a per ion basis. The values in Table 7.6 have been multiplied by this factor of ten.

The resonant intensity values of Tables 7.5 and 7.6 can be directly compared among one another since they are normalized to identical experimental conditions (scattering efficiency, incident power, etc.) by using the E_g^5 phonon standard. They are also given as per ion values

Table 7.6: Resonant Raman intensities for 10% Er^{3+} in $LuPO_4$.

	Polarization			
	XY	ZY	XZ	ZZ
35 cm^{-1} transition	129.4	3.3	39.5	1.0
53 cm^{-1} transition	98.9	3.9	39.6	1.3

so as to obtain a quantity that is indicative of the relative amplitudes of the resonant and nonresonant scattering channels and the dependence of the former on the location of the resonant energy levels.

It is apparent that as expected, the signal is largest for the 10% crystal, for which the excitation energy lies within the linewidth of the strongly resonant Γ_6 line at 20,483.7 cm^{-1}, as discussed in chapter 6. In addition, the reversal of the interference that results from the shift of the levels relative to the laser line will also have a significant impact on the relative intensities of the resonant electronic Raman transitions. This last effect appears to be occuring the most dramatically for the 33 cm^{-1} transition in XY polarization, which (on a per ion basis) differs by orders of magnitude between the 100% and 10% Er^{3+} crystals. Finally, one should be cautious in using the ZY and ZZ intensities in the 10% crystal since they are roughly two orders of magnitude weaker than the XY and XZ intensities and can thus partly arise from polarization leakage.

7.5 Calculation of the Resonant intensities - The Zero Linewidth Model

The total Raman amplitude is the sum of the nonresonant amplitude and the resonant amplitude. We can write the Raman amplitude for a transition between the ground state $|0\rangle$ and the final state $|f\rangle$ in the following form:

$$(\alpha_{\rho\sigma})_{0f} = (\alpha_{\rho\sigma})_{0f,nr} + k\left[\frac{P_{0f}(20,485\,\mathrm{cm}^{-1})}{-1.7} + \frac{P_{0f}(20,493\,\mathrm{cm}^{-1})}{6.2}\right] \qquad (7.2)$$

where P_{0f}(20,485 cm^{-1}) and P_{0f}(20,493 cm^{-1}) are the matrix element products for respectively the 20,485 and 20,493 cm^{-1} states, and the states and energy denominators are for Er^{3+} in $ErPO_4$. The matrix element products, which determine the strengths of the various

resonant amplitude channels, are listed in Table 7.2. The energy denominators are from Table 7.3. The constant k is needed because we have determined the relative nonresonant amplitudes from the nonresonant experimental spectra and not from first principles, so that it is not clear *a priori* what the proportion of the resonant to nonresonant amplitudes in the total Raman amplitude is. The parameter k must be calculated from the experimental resonant data so as to give an accurate account of the intensity pattern in both the 100% and 10% Er^{3+} crystals. Several simplifying assumptions have been made in writing equation 7.2:

- The resonant levels are assumed to have zero linewidth and have been "collapsed" to the center of the lines. This is valid if the exiting line is removed from the line, as in $ErPO_4$, but not when the excitation is within the linewidth of a transition, as in the 10% Er^{3+} crystal. Nevertheless, the shortcomings of the model in the 10% case will give us further clues as to the resonance enhancement mechanism.

- The imaginary part of the denominator, $i\Gamma_j$, has been neglected. Thus we assume that the homogeneous linewidth is small compared to the distance between the exciting line and the resonant level. This assumption is probably justified for $ErPO_4$, but again, probably not for 10% Er^{3+}.

For the calculation of the resonant intensities we first determine the constant k, and then the relative phases of the nonresonant and resonant amplitudes. It is found that a value of k can be found that gives a consistent picture of the relative intensity data for the 33 and 53 cm^{-1} transitions. The relative phases are calculated by looking at difference in the intensity predictions that result from using contructive vs. destructive interference between the nonresonant and resonant amplitudes. A confirmation of the following calculations can really only be accomplished by comparing the intensities they predict with an experimental excitation curve, that is a graph of the resonant intensity vs. excitation wavelength, since the calculations below are based on a very limited number of experimental data points. This necessitates a dye laser tunable in the $^4F_{7/2}$ region. In one of the following sections a calculation is made of Γ and the T_2 lifetime based on the resonant intensity data for the 10% crystal using a finite linewidth model.

XZ Spectrum

The XZ resonant amplitude arises only from the $\Gamma_6(20{,}493\ \mathrm{cm}^{-1})$ intermediate state since its matrix element with the Γ_7 ground state is electric dipole allowed in Z polarization whereas that of the $\Gamma_7(20{,}485\ \mathrm{cm}^{-1})$ intermediate state is forbidden. This renders the calculation of the intensities under resonant excitation somewhat easier. The XZ relative intensities of the 33 and 53 cm^{-1} transition in $ErPO_4$ will be used to estimate the parameter k. Neglecting the nonresonant contribution, the ratio of the 33 to 53 cm^{-1} transition intensity would be simply the ratio of the oscillator strengths of the respective matrix elements of these states with the 20,493 cm^{-1} state since the other matrix element that enters the Raman amplitude is that between the ground state and the 20,493 cm^{-1} state which is identical for the two transitions. The ratio of the oscillator strengths is $5.0/3.2 = 1.6$ whereas the observed ratio for $ErPO_4$ is 1.8. The difference is quite small, however, it could come from interference between the nonresonant and resonant amplitudes.

Requiring that k be positive we have the two following possibilities for the 33 cm^{-1} transition (using the amplitude values listed in the previous tables):

$$\begin{cases} \text{constructive interference :} & .48 + k \times .71/6.2 = \sqrt{4.2} \Rightarrow k = 13.7 \\ \text{destructive interference :} & .48 - k \times .71/6.2 = -\sqrt{4.2} \Rightarrow k = 22.1 \end{cases} \tag{7.3}$$

and for the 53 cm^{-1} transition we have:

$$\begin{cases} \text{constructive interference :} & -.28 - k \times .57/6.2 = -\sqrt{2.3} \Rightarrow k = 13.5 \\ \text{destructive interference :} & -.28 + k \times .57/6.2 = \sqrt{2.3} \Rightarrow k = 19.5 \end{cases} \tag{7.4}$$

The signs of the matrix element products are chosen in accord with whether the interference between nonresonant and resonant amplitudes is constructive or destructive. It is interesting to note that the two transitions predict remarkably similar values of k. At this point a choice needs to be made which value of k is best. An dispersion curve of the resonance intensities would allow an unequivocal choice of one of the two values, however, since we do not have this curve a choice has to be made based on the cw Raman data. The value $k = 13.6$ will be retained for the calculations in the remainder in this section since it appears to give better agreement for $ErPO_4$. The value $k \approx 21$ cannot be excluded until dispersion curve measurements are made. With $k = 13.6$ and constructive interference for the 33 and 53 cm^{-1} transitions we have for the predicted intensity of the 33 cm^{-1} transition in XZ:

$$(.48 + 13.6 \times .71/6.2)^2 = 4.2 \tag{7.5}$$

and for the intensity of the 53 cm^{-1} transition in XZ:

$$I_{XZ}(53\ cm^{-1}) = (-.28 - 13.6 \times .57/6.2)^2 = 2.3 \tag{7.6}$$

XY Spectrum

The XY intensity of the 33 cm^{-1} transition is complicated to compute since the three amplitudes that contribute to the total Raman intensity are of the same order of magnitude. However, this is the reason the XY intensity is so sensitive to interference. It seems apparent that in $ErPO_4$ there must be destructive interference between the amplitudes since relatively speaking the XY 33 cm^{-1} transition in $ErPO_4$ is weak. In 10% Er^{3+} in $LuPO_4$ its intensity goes up by two orders of magnitude. The 33 cm^{-1} intensity is given by:

$$I_{XY}(33\ cm^{-1}) = (1.2+13.6\times(\pm1.0/6.2\pm0.10/1.7))^2 = (1.2+13.6\times(\pm0.16\pm0.06))^2 \tag{7.7}$$

The two resonant channels have comparable amplitudes so that one cannot be neglected in front of the other. Overall, for destructive interference with the nonresonant amplitude, the resonant amplitude must be negative. The resonant amplitude can thus be -0.22 or -0.10. The second choice predicts an intensity of zero whereas the first predicts 3.2 which is quite close to the observed value. So to summarize, for the 33 cm^{-1} transition we have the following XY intensity:

$$I_{XY}(33\ cm^{-1}) = (1.2 + 13.6 \times (-0.16 - 0.06))^2 = 3.2 \tag{7.8}$$

Note that if one had chosen constructive interference between the nonresonant and resonant amplitudes the intensity would have been predicted to be 17.6, an order of magnitude stronger. The interference effects are thus very strong.

The 53 cm^{-1} transition has virtually no nonresonant amplitude. Its intensity in XY polarization is:

$$I_{XY}(53\ cm^{-1}) = (13.6 \times (\pm0.80/6.2 \pm 0.08/1.7))^2 = (13.6 \times (\pm0.13 \pm 0.05))^2 \tag{7.9}$$

Again, the resonant amplitudes differ by a factor of two depending on whether constructive or destructive interference is chosen between the two resonant channels. The smaller energy denominator of the 20,485 cm^{-1} intermediate state makes up to some extent for its weaker oscillator strengths. Constructive interference between the two yields better agreement with experiment. The XY intensity of the 53 cm^{-1} transition in $ErPO_4$ is thus predicted to be:

$$I_{XY}(53\ cm^{-1}) = (13.6 \times (0.13 + 0.05))^2 = 6.0 \tag{7.10}$$

ZY Spectrum

The resonance enhancement of the ZY intensities is not expected to be very large. For the 33 cm^{-1} line the only resonant channel is via the 20,485 cm^{-1} intermediate state and does not have much strength, and for the 53 cm^{-1} line the only resonant channel is via the 20,493 cm^{-1} state with again a relatively weak amplitude.

The 33 cm^{-1} transition has the following intensity:

$$I_{ZY}(33\ cm^{-1}) = (0.17 + 13.6 \times (0 \pm 0.02/1.7))^2 = (0.17 \pm 0.16)^2 \qquad (7.11)$$

Constructive interference gives an intensity of 0.10 and destructive interference gives an intensity of zero, so that the former choice appears to be more in line with the observed intensity.

The 53 cm^{-1} transition has the following intensity:

$$I_{ZY}(53\ cm^{-1}) = (-0.70 + 13.6 \times (0 \pm 0.08/6.2))^2 = (-0.70 \pm 0.18)^2 \qquad (7.12)$$

Constructive interference yields an intensity of 0.77 whereas destructive interference yields the value 0.27. In spite of the weakness of the resonant comtribution, there is a factor of three difference between the intensities predicted by the two different interference choices. Constructive interference gives a better agreement to the experimental data.

ZZ Spectrum

The ZZ intensities are extremely weak under resonant excitation. In fact, they are a only few percent of the XZ intensities and thus the slightest amount of leakage from XZ to ZZ polarization will affect them. The nonresonant amplitudes are zero. The resonant channels are both zero for the 33 cm^{-1} transition so that it should not have any intensity. The reason for this is that the electric dipole selection rules forbid the Raman transition $\Gamma_7(0\ cm^{-1}) \longrightarrow \Gamma_6(33\ cm^{-1})$ in ZZ polarization. The experimentally observed intensity of 0.10 is only 2% of the XZ intensity and so could be leakage. Alternatively, if there is some small amount of magnetic dipole transition intensity between the intermediate states on the one hand and the initial and final states on the other, the resonance enhancement might compensate for the weakness of the magnetic dipole matrix elements and render the ZZ intensity observable.

The 53 cm^{-1} transition has only the following resonant contribution to the total intensity:

$$I_{ZZ}(53\ cm^{-1}) = (\pm 13.6 \times 0.05/6.2)^2 = 0.01 \qquad (7.13)$$

Table 7.7: Resonant Raman intensities for $ErPO_4$.

	Polarization			
	XY	ZY	XZ	ZZ
33 cm^{-1} transition (observed)	2.60	0.23	4.17	0.10
33 cm^{-1} transition (calculated)	3.2	0.10	4.2	0
53 cm^{-1} transition (observed)	7.19	0.93	2.28	0.06
53 cm^{-1} transition (calculated)	6.0	0.77	2.3	0.01

This is smaller than the observed intensity of 0.06, which is however 3% of the XZ intensity and could be all leakage.

Summary

The agreement between calculated and observed intensities is quite good for $ErPO_4$. The relative intensities of the 33 and 53 cm^{-1} transitions in various polarizations in well accounted for with the single parameter $k = 13.6$ and the choice of the relative phases of the resonant and nonresonant amplitudes. A full confirmation of these calculations would be to compare the predicted to observed dispersion curves of the resonant intensities since the preceding calculations are based on a very limited number of experimental data points. Table 7.7 summarizes the calculated and observed intensities of the 33 and 53 cm^{-1} transitions in $ErPO_4$ under resonant excitation.

The calculations done above for $ErPO_4$ can be repeated for the 35 and 53 cm^{-1} transitions in the 10% Er^{3+} in $LuPO_4$ crystal. We assume that the matrix element products remain the same and that the only difference comes from the change in the energy denominators which embodies the amplitude interference reversal. The intensities calculated using the energy denominators for the 10% crystal and the value $k = 13.6$ are summarized in Table 7.8 along with the experimentally observed intensities. It is apparent that the intensities calculated for the 10% crystal all underestimate the observed intensities by factors that range from 3 to 7 for the XY and XZ intensities. The observed intensities in ZY and ZZ polarization are a few percent of the corresponding XY and XZ intensities and so could have a non negligible polarization leakage component. There are several reasons for the large discrepancies in the case of the 10% crystal, which we expected would occur.

Table 7.8: Resonant Raman intensities for 10% Er^{3+} in $LuPO_4$.

	Polarization			
	XY	ZY	XZ	ZZ
35 cm^{-1} transition (observed)	129.4	3.3	39.5	1.0
35 cm^{-1} transition (calculated)	39.7	0.10	7.5	0
53 cm^{-1} transition (observed)	98.9	3.9	39.6	1.3
53 cm^{-1} transition (calculated)	16.6	0.10	5.3	0.05

- The excitation energy is now well within the inhomogeneous linewidth of the Γ_6 level, situated at 20,483.7 cm^{-1} in the 10% crystal, with a full width at half maximum of roughly cm^{-1}. The zero linewidth model used in the calculations of this section thus totally breaks down. The real part of the energy denominator vanishes for the ions that have transition energies exactly at the laser line so that these ions contribute much more to the resonant Raman intensity than ions a few cm^{-1} away from the exciting line. In addition, for these ions the imaginary part of the energy denominator has to be taken into account.

- The possibility of site selective fluorescence is now present for those ions that are in exact resonance with the laser line. It is expected that this fluorescence is weak, due to the nonradiative decay and concentration quenching mechanisms that reduce the intensity of the $^4F_{7/2} \longrightarrow {}^4I_{15/2}$ radiative transitions. Nevertheless, any site selective fluorescence will be at the same frequency as the Raman transitions and will affect the relative intensities of the electronic transitions. The fluorescence and Raman components of a particular transition can be differentiated only by time resolved measurements.

- In the event of localized heating of the sample by the absorbed laser light, then the intensities of the 33 cm^{-1} transition can be reduced by the reabsorption of the Raman scattered light.

7.6 Calculation of the Resonant intensities-The Finite Linewidth Model

The intensities of the 35 and 53 cm^{-1} Raman transitions are quite different from the calculated values in the zero linewidth model described in the previous section. Since the exciting laser line is in the middle of the linewidth of the strongly resonating Γ_6 intermediate state it is obvious that the assumptions of the zero linewidth model are invalid for the 10% crystal.

As a first attempt to understand the intensities observed in the 10% crystal, we neglect the nonresonant contribution to the Raman amplitude since the resonance term now presumably greatly outweighs it due to the vanishing real energy denominator. The Raman amplitudes are then simply those arising from the single resonant intermediate channel $\Gamma_6(20{,}483.7\ cm^{-1})$. The resonant relative intensities are then proportional to the squares of the matrix element products of Table 7.2. The energy denominator, or rather the integral of the energy denominator over the inhomogeneous linewidth of the resonant line, is a common factor to all the intensities and drops out of any relative comparison. We thus obtain in Table 7.9 the predicted and observed resonant Raman intensities of the 35 and 53 cm^{-1} transitions in 10% Er^{3+} in $LuPO_4$. It should be kept in mind that site selective fluorescence and reabsorption of scattered light will affect the observed values and possibly distort the measurement of the resonant Raman intensities. To facilitate the comparison, in Table 7.9 the calculated relative intensities were scaled so that observed and calculated values are equal for the 53 cm^{-1} transition in XZ polarization.

The agreement is fairly good. The relative intensity of the XZ(35 cm^{-1}) transition has been somewhat overestimated and that of the XY (53 cm^{-1}) transition underestimated. We continue by calculating in a more correct fashion the resonance amplitude of the transitions taking into account the overlap between the laser line and the intermediate level.

The inhomogeneous linewidth is described by the following normalized Gaussian distribution function:

$$g(\omega) = \frac{1}{\sqrt{2\pi}\Delta} \exp\left(-\frac{(\omega - \omega_0)^2}{2\Delta^2}\right) \tag{7.14}$$

where ω_0 is the center of the line and Δ its inhomogeneous linewidth.

We can write the Raman intensity for a transition between the ground state $|0\rangle$ and the final state $|f\rangle$ in the following form (assuming that only the Γ_6 state contributes to the

Table 7.9: Relative resonant Raman intensities of the 10% crystal.

	XY	ZY	XZ	ZZ
35 cm^{-1} transition (observed)	129.4	3.3	39.5	1.0
35 cm^{-1} transition (calculated)	129.9	0	61.4	0
53 cm^{-1} transition (observed)	98.9	3.9	39.6	1.3
53 cm^{-1} transition (calculated)	78.0	0.8	39.6	0.3

intermediate resonance):

$$(\alpha_{\rho\sigma})_{0f}^2 = \int_{-\infty}^{+\infty} \left| (\alpha_{\rho\sigma})_{0f,nr} + k\frac{P_{0f}(\Gamma_6)}{\hbar\omega - \hbar\omega_l + i\Gamma} \right|^2 g(\omega)d\omega \tag{7.15}$$

where ω_l is the frequency of the laser, the parameter k is that of the previous section, and Γ is the homogeneous linewidth of the Γ_6 intermediate levels. That this is the correct expression can be verified by taking the limit where $\Delta \longrightarrow 0$. The distribution function becomes a Dirac delta function and by neglecting Γ in front of the real part of the energy denominator we recover the result of the last section providing we use the same parameter k. One caveat is that this expression assumes that the laser has an infinitely narrow linewidth. In reality, the laser linewidth is finite and its value Γ_l limits the measurement of Γ. In fact, it is the larger of Γ_l and Γ which enters the denominator of equation 7.15. If the laser linewith is narrower than the homogeneous linewidth then we will be able to measure Γ and hence T_2.

The integration in equation (7.15) was performed for the 35 and 53 cm^{-1} transitions in XY and XZ polarization , which allowed the determination of the homogeneous linewidth in the denominator of (7.15). The center of the line was taken to be at 20,483.7 cm^{-1} and its linewidth Δ was set at 6 cm^{-1}. As an example, the XZ intensity of the 53 cm^{-1} transition is given by:

$$I_{XZ}(53\ cm^{-1}) = \int_{-\infty}^{+\infty} \left| 0.48 + 13.6\frac{0.71}{\hbar\omega - 20,486.7 + i\Gamma} \right|^2 \frac{1}{\sqrt{2\pi}6} \exp\left(-\frac{(\hbar\omega - 20,483.7)^2}{18}\right)d\omega \tag{7.16}$$

Only one value of Γ yields agreement between calculated and observed Raman intensities for a particular transition in a selected polarization. It was found that indeed Γ is equal to the linewidth of the argon-ion laser ($\approx$0.1 cm^{-1}). Thus we have obtained a lower bound for T_2, and to improve this measurement we would need a narrower frequency laser. We find

that the following value:

$$T_2 \geq 100 \times 10^{-12} \text{ sec} = 100 \text{ psec} \tag{7.17}$$

7.7 Future Directions

The calculations that were outlined above show that strong quantum mechanical interference effects determine the relative resonant Raman intensities for the 33 and 53 cm^{-1} transitions. A dispersion curve of these intensities as a function of excitation energy, obtained by tuning a laser across the resonant energy levels, would allow a final determination of the signs of the interferences and a confirmation of the fact that such an effect is taking place.

The erbium phosphate crystals appear to be promising candidates for a study of the difference between fluorescence and resonance Raman, from the time resolved point of view. The lower bound of 100 psec obtained for T_2 is large enough that time resolved measurements could be made of the Raman transitions.

References

[1] J. Friedman and R.M. Hochstrasser, Chem. Phys. Lett. **32**, 414 (1975).

[2] D. Nicollin and J.A. Koningstein, Chem. Phys. **49**, 377 (1980).

[3] C. Hirlimann, M.P. dos Santos, and M. Balkanski, J. Phys. C **18**, 6297 (1985).

[4] G. Williams, Lawrence Berkeley Laboratory, unpublished results.

[5] P.C. Becker, N. Edelstein, G.M. Williams, J.J. Bucher, R.E. Russo, J.A. Koningstein, L.A. Boatner, and M.M. Abraham, Phys. Rev. B **31**, 8102 (1985).

Chapter 8

Raman Scattering Studies of Electron-Phonon Coupled Modes in Ytterbium Phosphate Crystals

The ytterbium phosphate crystals have a behaviour which departs considerably from that of the other crystals studied in this work, in terms of the Raman spectra observed with monochromatic laser excitation. The difference is observed in the 250 to 350 cm^{-1} region in the E_g symmetry spectra, that is with the XZ, YZ, ZX, and ZY polarization combinations. Figure 8.1 compares the spectra for $LuPO_4$, $TmPO_4$, and $YbPO_4$, at 295 and 4.2 K. It is quite clear that the spectra for $YbPO_4$ differ very markedly from those of the other crystals. The preponderant characteristic of the $YbPO_4$ Raman transitions in the 250-350 wavenumber region is that the narrow E_g^3 phonon no longer appears as it does in the spectra of the other tetragonal lanthanide phosphate crystals. At room temperature a surprisingly broad transition is observed in $YbPO_4$ at approximately 303 cm^{-1} with a linewidth of 50 cm^{-1}. Presumably, this transition is the Raman manifestation of phonon E_g^3, however, in the other lanthanide phosphate crystals E_g^3 is observed as a narrow transition with a linewidth of at most 7 cm^{-1} (at room temperature).

The temperature evolution of this transition in $YbPO_4$ is extremely dramatic, and again, different from what is seen in the other crystals. As the temperature is brought down from 295 to 4.2 K, the transition gradually splits up into several separate peaks with central frequencies and linewidths which depend on temeperature. The lineshapes observed are asymmetric. In the other crystals E_g^3 usually narrows down somewhat as the temperature drops, and if the ion does not have a full f shell the electronic Raman transitions can appear superimposed on the phonon spectrum, as occurs for $TmPO_4$ where a shoulder at 280 cm^{-1}

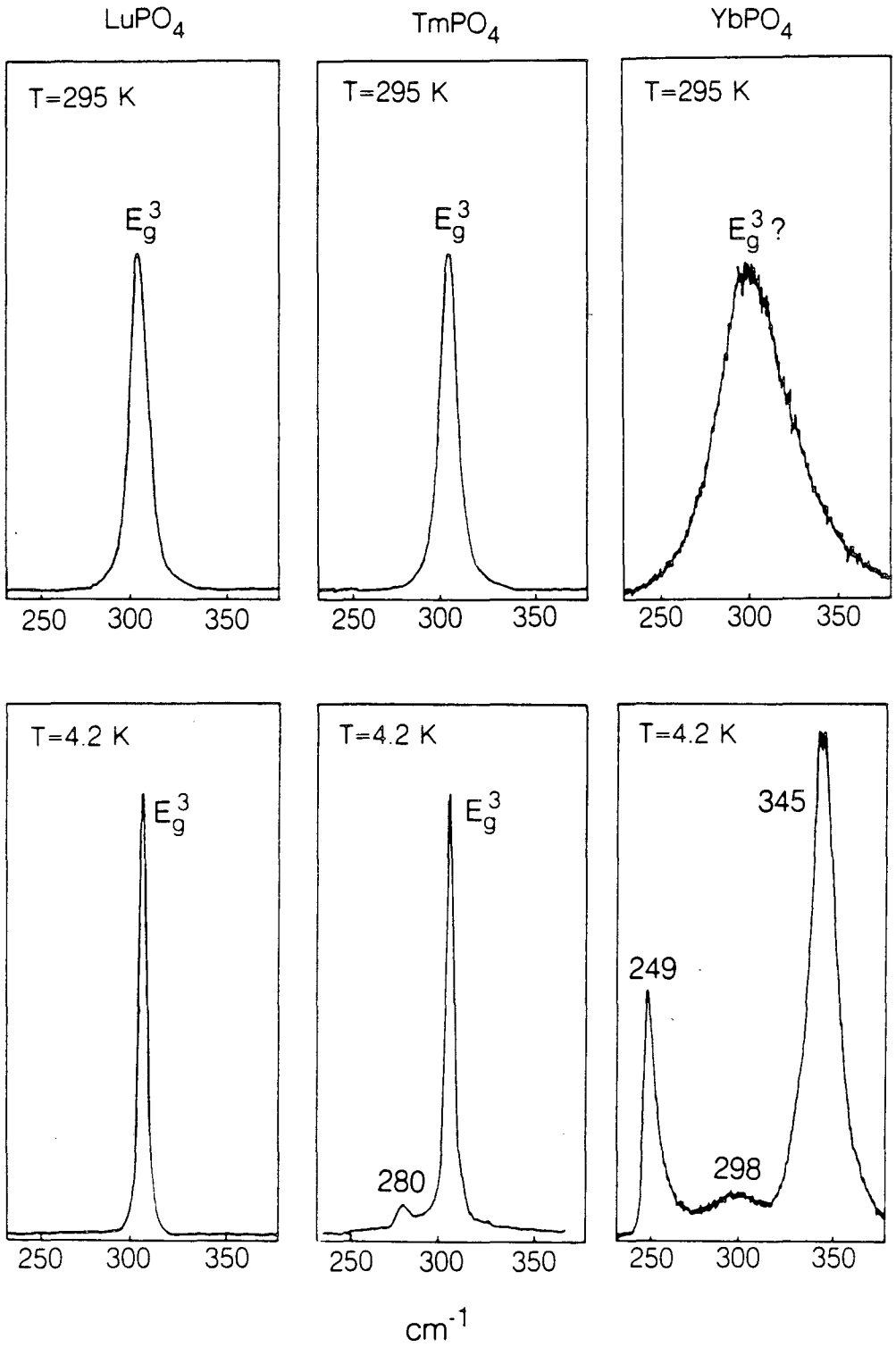

Figure 8.1: Experimental Raman spectra of $LuPO_4$, $TmPO_4$, and $YbPO_4$, in the Y(XZ)X scattering geometry in the 250-350 cm^{-1} region, at T=4.2 and 295 K.

is observed next to E_g^3.

It is concluded that in $YbPO_4$ there are strong electron-phonon coupling effects taking place due to the presence of two electronic transitions very close in energy to phonon E_g^3, leading to a resonance type interaction. This coupling affects the experimentally observed Raman spectra since the new eigenmodes of the system are no longer purely electronic or vibrational, but combinations of the two. There are also strong indications that the coupling is temperature dependent. Why this coupling occurs only in $YbPO_4$ and not in any of the other crystals investigated is still an unanswered question

In this chapter, the experimental Raman spectra of the $Yb_xLu_{1-x}PO_4$ crystals (x=1, 0.75, 0.50, 0.25, 0) and their temperature evolution are described. Attempts are made to model the electron-phonon coupled system and their lineshapes, and to obtain values for the electron-phonon coupling strengths.

A imposing body of work on electron-phonon coupling in rare earth crystals has been done by Schaack and his co-workers over the years [1,2,3,4,5] and by Thalmeier and Fulde [6]. There have also been detailed investigations of the Jahn-Teller effect (also due to electron-phonon coupling) by the experimental and theoretical groups at Oxford [7]. The only published work on $YbPO_4$ is by Nakazawa and Shionoya on cooperative luminescence [8].

8.1 Electronic Energy Level Structure of Yb^{3+}

The Yb^{3+} ion, an odd electron system, has the configuration f^{13}. This is formally equivalent to the configuration f^1 (Ce^{3+}) and is relatively easy to analyze. The energy level structure of the f^{13} configuration consists of two multiplets, $^2F_{7/2}$ and $^2F_{5/2}$, separated by roughly 10,000 cm^{-1}. The ground multiplet is $^2F_{7/2}$ (in Ce^{3+} it is $^2F_{5/2}$). This ground multiplet consists of four Kramers doublets, two of symmetry Γ_6 and two of symmetry Γ_7. The absorption spectra and crystal field fit of Yb^{3+} doped in $LuPO_4$ have been reported previously. The electronic energy level structure of the $^2F_{7/2}$ multiplet of Yb^{3+} in $LuPO_4$ is summarized in Table 8.1 (see appendix A1 for more details).

The energy levels of Yb^{3+} in $YbPO_4$ are probably much closer to those of Yb^{3+} doped in $LuPO_4$ than those of Yb^{3+} doped in YPO_4, since Yb^{3+} and Lu^{3+} have much closer atomic weights and ionic radii than Yb^{3+} and Y^{3+}. We thus retain for the general information we

Table 8.1: Electronic energy level structure of Yb^{3+} in $LuPO_4$.

symmetry	calc.	obs.
Γ_6	0.0	0.0
Γ_7	99.0	99.0
Γ_6	279.3	
Γ_7	288.6	
Γ_6	10244.7	10244.7
Γ_7	10271.8	10271.8
Γ_6	10475.5	10475.5

need about the energy levels and wavefunctions of Yb^{3+} in $YbPO_4$ the values obtained from the Yb^{3+} in $LuPO_4$ crystal field fit. The two higher energy levels of the $^2F_{7/2}$ multiplet, at 279 and 289 cm^{-1} (predicted values from the crystal field fit which could be off by at most 10 to cm^{-1}) are quite close in energy to phonon E_g^3. This opens up the possibility for coupling between the electronic transitions and the phonon via a resonance type interaction.

8.2 The Experimental Raman Spectra of $YbPO_4$

8.2.1 Experimental Raman Spectra at 295 and 4.2 K

The experimental Raman spectra of $YbPO_4$ at room temperature in the wavenumber region 10 to 400 cm^{-1} for the polarization combinations XZ and ZY are shown in Figure 8.2. In these polarization combinations the spectra should reveal only the E_g symmetry vibrational transitions since presumably at room temperature the electronic Raman transitions of Yb^{3+} are too broad and weak to be observed. Thus in this wavenumber region we expect to observe only the three phonons E_g^1, E_g^2, and E_g^3, as shown for example in Figure 3.2 for $LuPO_4$. The spectra of Figure 8.2 differ markedly from those of Figure 3.2 as regards phonon E_g^3. Phonons E_g^1 and E_g^2 have narrow lineshapes as in $LuPO_4$ and the other tetragonal rare earth phosphates, however, phonon E_g^3 is an order of magnitude broader than in any of the other crystals studied ($LuPO_4$, $TmPO_4$, $HoPO_4$, $DyPO_4$, and $HoPO_4$) as measured by the full width at half-maximum. We assume that this broad transition is intimately connected with E_g^3 since its center frequency of approximately 300 cm^{-1} is close to the frequency where

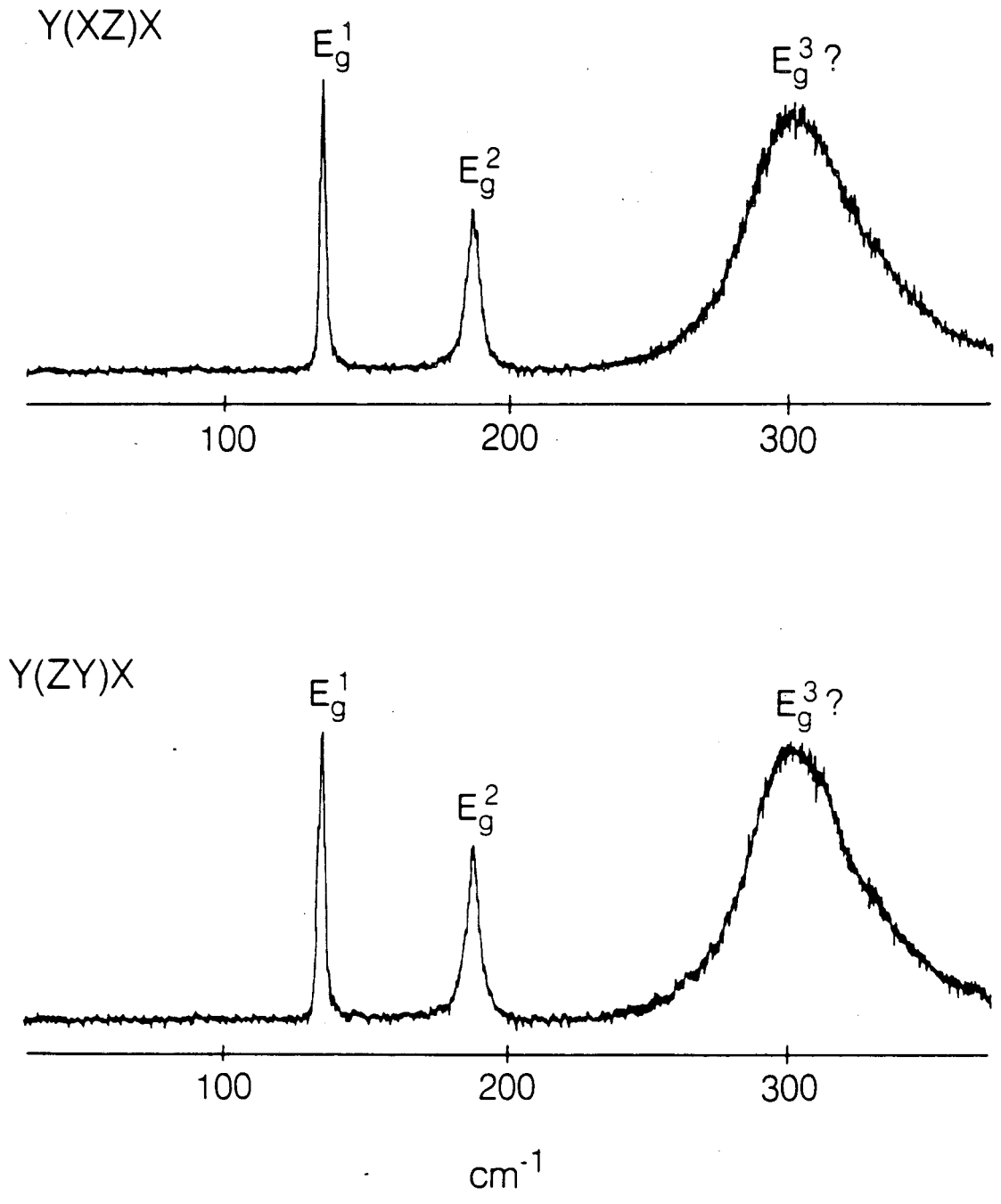

Figure 8.2: Experimental Raman spectra of $YbPO_4$ at 295 K in the Y(ZY)X and Y(XZ)X scattering geometries. The spectrometer bandpass is 2.5 cm^{-1}.

we expect E_g^3 to appear. Also, it appears only in the E_g symmetry spectra. The linewidth of roughly 50 cm^{-1} is uncharacteristically large. The room temperature scans in the other polarization combinations (XY, ZZ, etc.) exhibit no unusual features. A full list of the phonon frequencies of $YbPO_4$ can be found in Table 3.3 for 295, 77, and 4.2 K.

Upon cooling the sample to 4.2 K, one might perhaps expect the broad transition at 300 cm^{-1} to narrow down significantly. This is not the case. Figure 8.3 displays the XY, ZY, and XZ polarization Raman spectra of $YbPO_4$ at 4.2 K in the 20 to 380 cm^{-1} region.

It is seen in the XZ and ZY polarization spectra that the broad room temperature transition has been replaced by two sharp and intense peaks at 250 and 346 cm^{-1}, and a weak broad peak at roughly 298 cm^{-1}. This is the most surprising feature of the low temperature spectra.

In the XY spectrum, an electronic Raman transition appears at 93 cm^{-1} which is the transition from the Γ_6 ground state to the first excited Γ_7 state, observed at 99 cm^{-1} in the Yb^{3+} in $LuPO_4$ absorption spectra. The XY intensities should be treated with caution as there seems to be some amount of polarization leakage between the XY and XX,YY spectra, as evidenced by the appearance in XY of phonon B_{1g}^1 at 147 cm^{-1}. The XY spectrum also shows a distinct rise at about 250 cm^{-1} to a broad peak centered around 265 cm^{-1}. The scattered light level level dips only slightly following that peak and does not immediately drop down to the background level. There is still intensity in the 300 cm^{-1} region which could mean the presence of a second, broad transition near that frequency. The XY spectra of the mixed crystals $Yb_xLu_{1-x}PO_4$ also show these features, which narrow down as the concentration of Yb drops. The sharp strong transition is phonon B_{2g}^1.

The transitions at 250 and 346 cm^{-1} appear with some slight intensity in ZZ, however, this could be due to polarization leakage since the ZZ intensities of these two transitions are only about 1% of the respective XZ or ZY intensities.

8.2.2 Temperature Evolution of the E_g Symmetry Spectra

It is instructive to study the E_g symmetry spectra in the 250 to 350 cm^{-1} region as a function of temperature. In what fashion does the broad room temperature transition at 300 cm^{-1} in XZ and ZY split into the pattern observed at 4.2 K? The answer is provided by Figure 8.4, which shows the XZ spectra in this region at 40 K increments from 4.2 to 295 K. Several comments can be made about the distinct temperature evolution of the spectra.

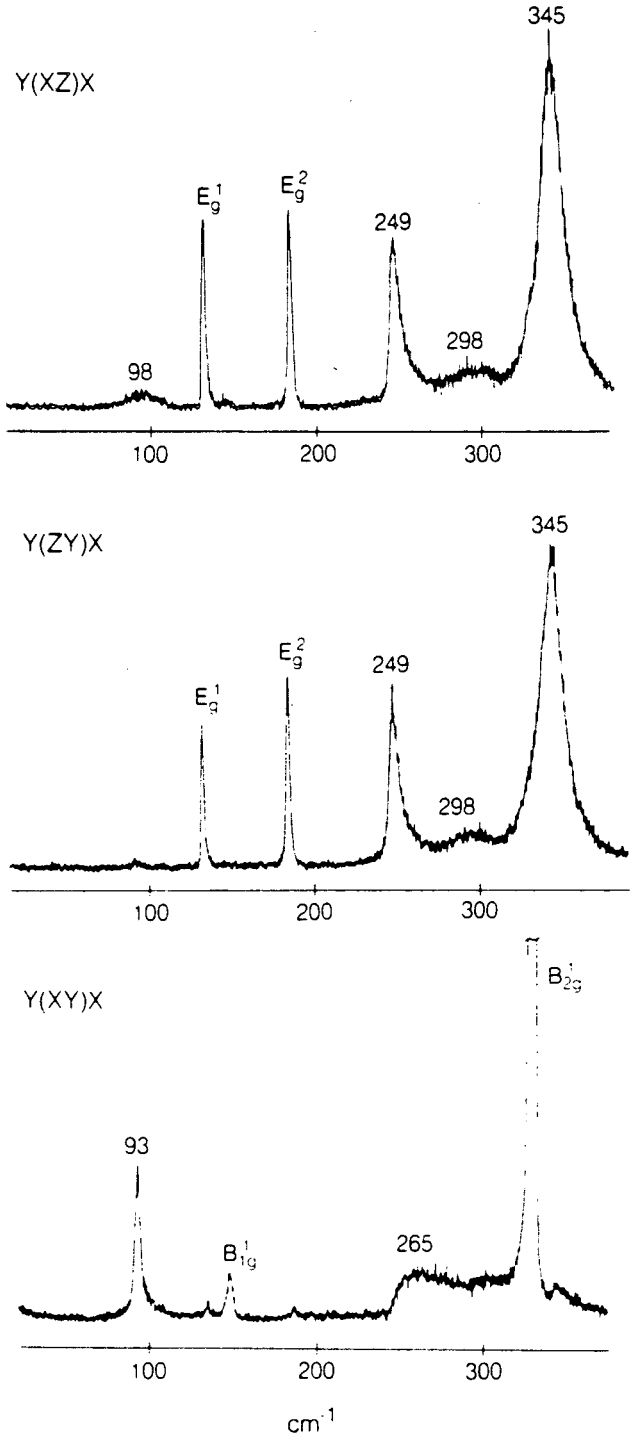

Figure 8.3: Experimental Raman spectra of $YbPO_4$ at 4.2 K in the Y(XY)X, Y(ZY)X, and Y(XZ)X scattering geometries. The spectrometer bandpass is 2.5 cm^{-1}.

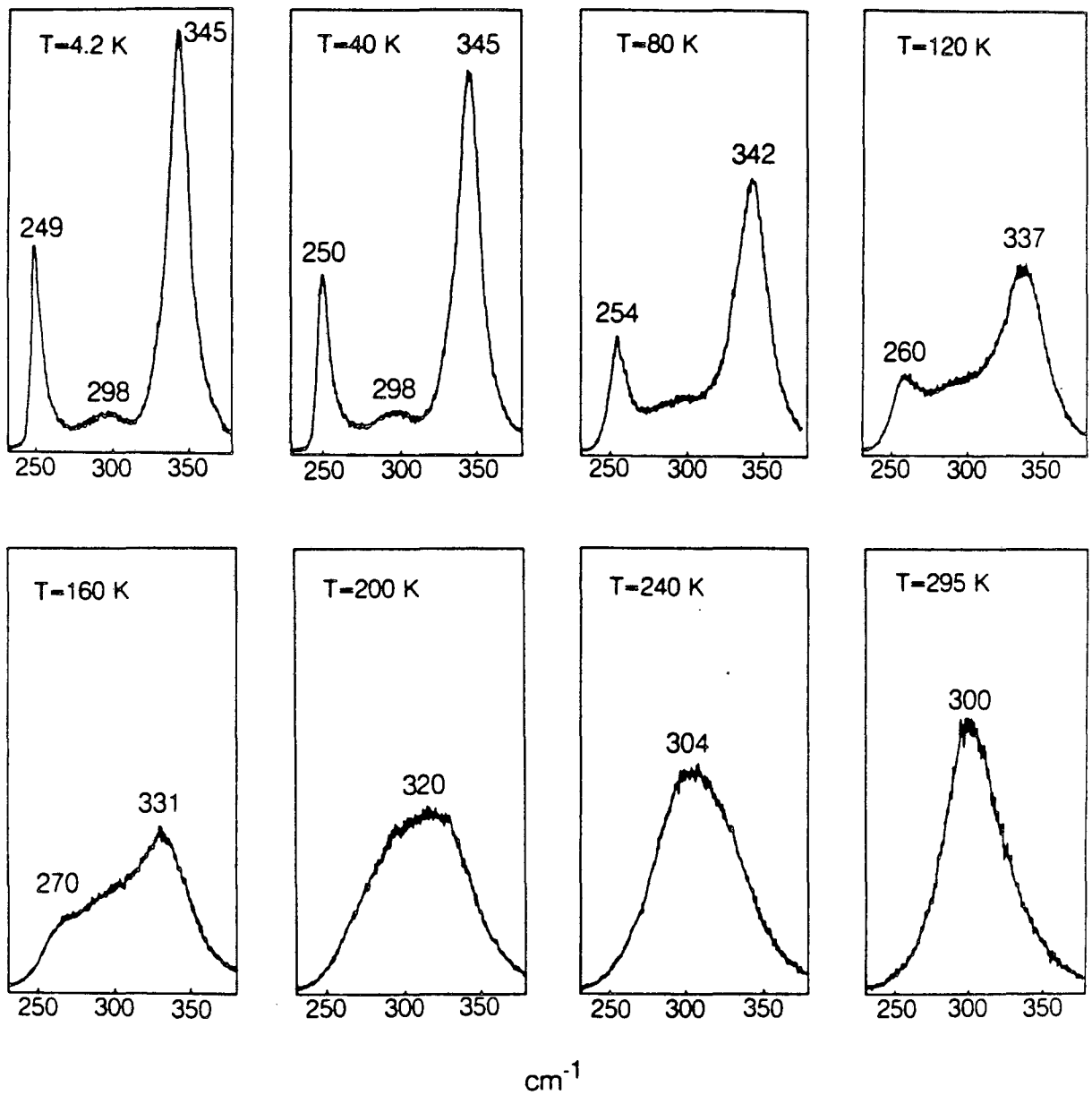

Figure 8.4: Temperature evolution of the $YbPO_4$ spectra in the 250 to 350 cm^{-1} region in XZ polarization.

- As the temperature is raised from 4.2 to 60 K the spectra do not change very much. It is in the 100 to 140 K temperature region that significant changes start occuring in the spectra.

- The two sharp peaks at 250 and 346 cm^{-1} at 4.2 K appear to gradually move closer together in frequency as the temperature is raised. Thus, at 100 K, for instance, the 250 cm^{-1} peak is at 257 cm^{-1} and the 345 cm^{-1} peak is at 340 cm^{-1}, a relative change in frequency of 10 to 20%. The 250 cm^{-1} peak can only be clearly followed up to at most 160 K, whereas the 346 cm^{-1} peak can be followed up to about 180 K. At this temperature the transitions blend into a very asymmetric and broad lineshape which narrows down somewhat as the temperature is raised to 295 K. At room temperature the lineshape, still somewhat asymmetric, looks like a single broad transition.

- As the temperature is raised, the two sharp outer peaks at 250 and 346 cm^{-1} not only move closer in frequency but also broaden. This linewidth broadening with increasing temperature is characteristic of rare earth ion electronic transitions.

- The intensity in the central region at 300 cm^{-1} is very small at 4.2 K but builds up gradually with temperature. At 140 K, for example, there is a significant amount of intensity under that peak. It does not appear that this intensity can be explained by the additive effect of the overlap of the tails of the lineshapes of the two outer transitions which are quite broad at higher temperatures.

8.2.3 Conclusion

It is apparent from even a cursory inspection of the E_g symmetry spectra (the XZ, YZ, ZX, and ZY polarizations) that the Raman scattering has uncovered phenomena previously unobserved in any of the other tetragonal lanthanide phosphate crystals. The only other effect that is somewhat similar to this is the decrease in energy of phonon E_g^2 (close in energy to an electronic transition) in $HoPO_4$, as the temperature drops (see Table 3.3) in contrast to all the other crystals where it increases in frequency.

The broad linewidth of what appears to be phonon E_g^3, and the behaviour as a function of temperature of this broad transition are extremely intriguing. The conclusion that one is naturally drawn to is that in the $YbPO_4$ crystal there are strong electron-phonon coupling effects occuring that are responsible for the surprising Raman spectra in the 250 to 350 cm^{-1}

region. Electron-phonon coupling effects have been observed previously in other tetragonal rare earth zircon like systems, and fall under the category of the cooperative Jahn-Teller effect [7]. However, the Raman spectra of these crystals all differ from those of $YbPO_4$ in one way or another. In $YbPO_4$ there is no phase transition that changes the lattice crystal structure, as is the case in the Jahn-Teller effect.

In the following sections we will describe two models of the electron-phonon coupled system of $YbPO_4$. The first, more simple, predicts only the eigenfrequencies of the coupled modes and their temperature evolution. The second, more complicated, attempts to quantitatively parameterize the Raman lineshapes observed experimentally. Both of these theories are to a large extent phenomenological. The important excitation picture of the Raman scattering process will be described first, since it provides the conceptual foundation upon which the ensuing discussion rests.

8.3 Electron-Phonon Coupled Modes in $YbPO_4$

8.3.1 The Excitation Picture at T=0 K

The situation in $YbPO_4$ is the following: two electronic levels, one of symmetry Γ_6 and one of symmetry Γ_7, are close in energy to phonon E_g^3. Raman transitions are allowed to all three of these states. In the usual case of decoupled electronic and vibrational states, the electronic Raman transitions are from the Γ_6 ground state (of a single ion) to the final electronic state of symmetry Γ_6 or Γ_7, and the vibrational Raman transitions are from the totally symmetric ground state of the crystal lattice, where all the phonon occupation numbers are zero, to a final state where one phonon has been created in the crystal. The vibrational excitations created by the laser excitation, the phonons, belong to the crystal as a whole. In order to approach in a more coherent and general fashion the electron-phonon coupling problem, we should treat the electronic transitions on an equal footing. Thus, we will speak of electronic transitions without specifying whether they are localized on a single ion or not. This does not involve any major changes in the symmetry labeling of the electronic states. We merely need to use the factor group representations that correspond to the site symmetry group representations Γ_6 and Γ_7. Theses are the D_{4h} representations Γ_6^+, Γ_7^+, Γ_6^-, and Γ_7^-. The electronic ground state will be Γ_6^+ and only Raman transitions

to Γ_6^+ and Γ_7^+ states are parity allowed.

The Raman scattered signal is created, in the semi-classical picture, by an oscillating polarization of the material. This oscillating polarization is induced by the incident laser radiation, which constitutes a harmonic driving field. The fluctuation-dissipation theorem provides the general setting for the calculation of the response of the medium to the incident field [9]. The induced polarizations, which also vary harmonically in time, have Raman shifted frequencies. Any observed Raman spectrum is produced by these oscillating polarizations and hence a coupled mode spectrum will be observed only if the polarizations are coupled. Since each Raman polarization corresponds to an excitation of the system, be it electronic or vibrational, one can equally well speak of coupled excitations. Thus the incident driving field is directly responsible for creating the excitations of the system and allowing them to couple. For example, when the polarization of the laser is such that phonon E_g^3 cannot be excited, then the electronic excitations and the corresponding polarizations of the medium are unaffected by the coupling and appear in the scattered frequency spectrum at their uncoupled position. However, when phonon E_g^3 is excited as well as the electronic excitations, a coupled mode spectrum will result. Thus the polarization of the laser is important in determining whether we see a coupled mode spectrum or not. This is an example of the quantum mechanical fact of life that any measurement inextricably links the outcome of the measurement with the actions of the observer.

The symmetry of the excitations involved is thus important in determining whether coupling is possible, and in which polarizations it can be observed. An electronic transition from the Γ_6^+ ground state to a Γ_6^+ final state has the symmetry $\Gamma_6^+ \otimes \Gamma_6^+ = \Gamma_1^+ + \Gamma_2^+ + \Gamma_5^+$. Thus four electronic excitations of symmetries Γ_1^+, Γ_2^+, and Γ_5^+ are produced. Similarly, in a transition from Γ_6^+ to Γ_7^+ the symmetries of the excitations produced are Γ_3^+, Γ_4^+, and Γ_5^+. The reason for the existence of four excitations comes from the fact that the YB^{3+} levels are Kramers doublets so that four transitions are possible at a given frequency.

Only the Γ_5^+ symmetry electronic excitations can couple to the E_g phonons ($\Gamma_5^+ \equiv E_g$) since the symmetries of the two excitations need to be identical for the two to couple. This comes from the fact that the coupling Hamiltonian must transform as the identity representation. Thus, of the four electronic excitations created by a Γ_6^+ to Γ_6^+ or Γ_6^+ to Γ_7^+ Raman transition, only two can couple to the phonon and produce a coupled mode spectrum. This occurs in the E_g symmetry spectra where both of these electronic and

vibrational excitations coexist. In contrast, in the A_{1g}, A_{2g}, B_{1g}, and B_{2g} spectra, only the uncoupled electronic excitations will appear. This is why the XY spectrum does not show the same scattering pattern in the 250-350 cm^{-1} region as the XZ or ZY spectra. Thus the somewhat broad peaks seen at 265 and perhaps 300 cm^{-1}, in XY symmetry, should be indicative of the uncoupled electronic excitations.

8.3.2 The Excitation Picture at Finite Temperatures, or Quantum Mechanics Revisited

At finite temperatures, the ytterbium ions are no longer all in their ground state. There is a finite probability that the higher excited states of the ion are occupied. When the ion is in an excited state, it can be argued that a resonance type interaction will no longer take place between an electronic Raman excitation, which necessarily originates in that excited state, and the E_g^3 vibrational excitation [10]. Consider for example that the ion is in the first excited state at 99 cm^{-1} (see Table 8.1). Raman transitions to the Γ_6 and Γ_7 states at respectively 279 and 289 cm^{-1} (calculated values) will correspond to excitations with energies 180 and 190 cm^{-1}. These are very far from resonance with the E_g^3 phonon at 310 cm^{-1} and hence a small coupling between these excitations will have a negligible effect on the eigenfrequencies. This situation is summarized in Figure 8.5.

The question may then be asked; will separate Raman spectra be observed for ions in their ground state (resulting in a coupled mode spectrum) and ions in an excited state (resulting in an uncoupled spectrum), or will some kind of averaging effect occur? The experimental data supports the second hypothesis, as witnessed by the temperature evolution of the E_g symmetry spectra of Figure 8.4. This can be understood from the fact that one cannot say that the ion is one state rather than another, without having made a measurement to determine this. Rather, one can only say that there are certain probabilities of occupation for each state of the ion, or that the electronic wavefunction is a superposition of these states. The physical mechanism by which such an equilibrium state is reached and attained is by the interaction of the ion with the lattice thermal bath of acoustic and optical phonons. We must thus treat the finite temperature problem by means of the density matrix. Note that even in the case where the electronic excitations are localized on one ion, this single ion can be treated by means of the density matrix since it is in equilibrium with the lattice thermal bath. Denoting the operator of the electron-phonon operator by V, the

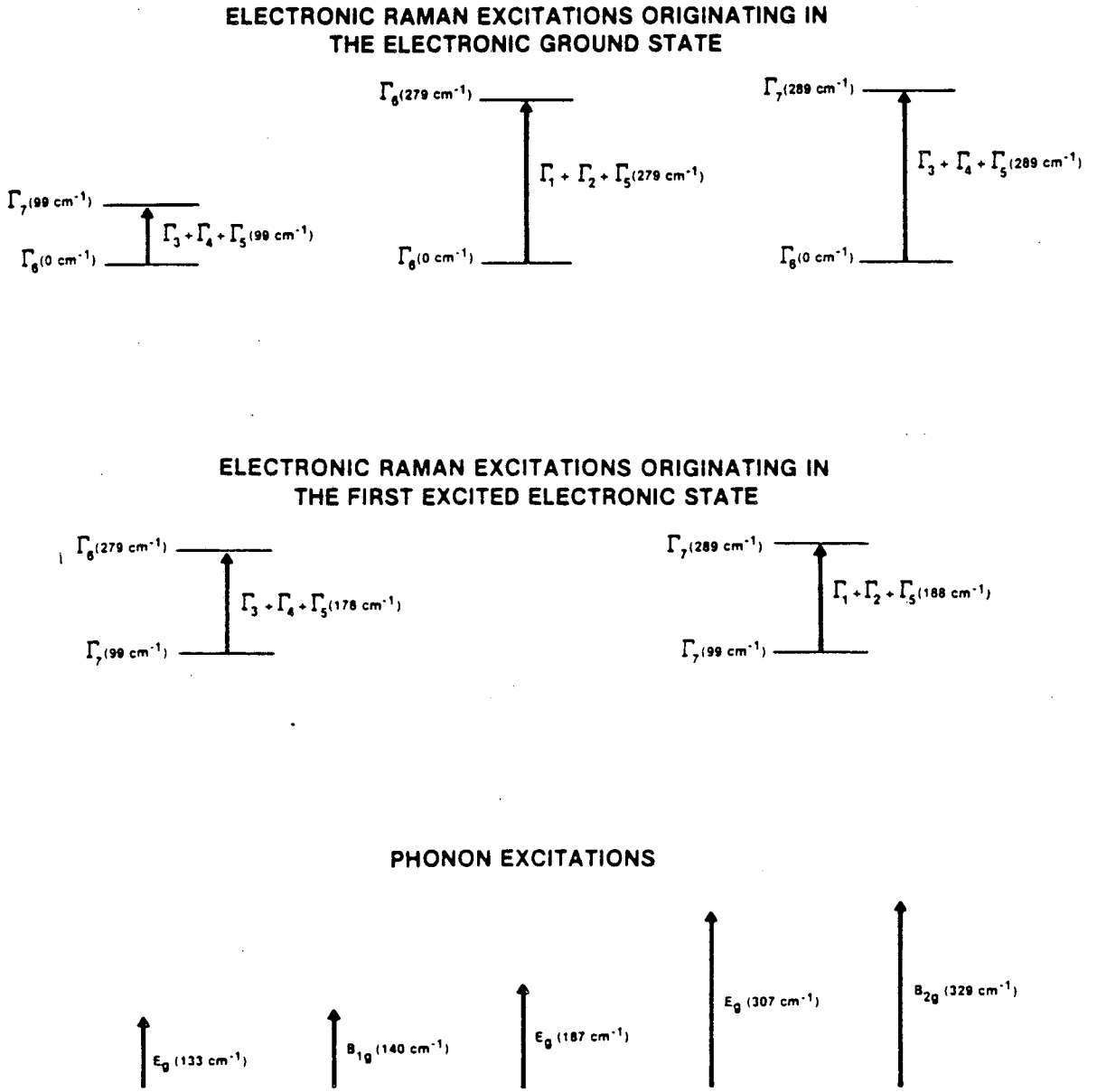

Figure 8.5: Low energy electronic and vibrational excitations in $YbPO_4$. Electronic excitations that originate in the first excited state are not resonant with the E_g phonon at 310 cm^{-1} and will not couple to it.

thermal average of V is thus given by:

$$\langle V \rangle = Tr(\rho V) \tag{8.1}$$

where ρ is the density matrix. Assuming that the only non-zero matrix element occurs for the ion's electronic ground state, then $\langle V \rangle$ is proportional to the ground state population Boltzmann factor.

8.4 Phenomenological Models of the Eigenfrequencies of the Electron-Phonon Coupled Modes

8.4.1 Coupled Mode Eigenfrequencies at T=4.2 K

The wavenumber region in which appears the electron-phonon coupled modes of $YbPO_4$ contains two electronic excitations and one phonon excitation. A priori, one would then expect a three level coupled system to be the physical foundation of the Raman spectra. This explanation makes apparent in a simple way why the low temperature (T=4.2 K) spectra show three distinct peaks. However, it cannot be immediately excluded that the system consists in reality of two coupled modes, one electronic and one phonon. In this latter case, the broad central feature at roughly 298 cm^{-1} has to be explained not as one of the coupled modes, but by some other reason such as the crystal not being exactly pure $YbPO_4$. It is better to treat both cases simultaneously so as to see which one is in better agreement with the data.

In what follows, we will use as basis states of the system products of the electronic wavefunctions and the phonon wavefunctions (defined by the phonon occupation numbers). The new coupled mode eigenfunctions will be linear combinations of these. The mode splitting occurs because of the near degeneracy of the state with an electronic ground state and one phonon E_g^3 and the states with either one of the two excited electronic states in the 300 cm^{-1} region and no phonon. The models below are somewhat of a simplification since both the electronic states and the phonon are doubly degenerate. However, the coupling cannot lift the Kramers degeneracy since it does not lift the time reversal symmetry so that there is no loss of generality in our treatment.

Consider two electronic excitations E_1 and E_2 with frequencies ω_{e1} and ω_{e2}. These correspond to the transitions from the electronic ground state to the two excited states in

the 300 cm^{-1} region. The frequencies ω_{e1} and ω_{e2} are known only approximately from the crystal field fit (see Table 8.1). The phonon frequency is $\omega_p \approx 310$ cm^{-1} (this is known from the $TmPO_4$ and $LuPO_4$ spectra and is also the position of the phonon in the $Yb_{.25}Lu_{.75}PO_4$ crystal). We introduce couplings V_1 and V_2 between the two electronic excitations and the phonon. These are phenomenological parameters. For a two level coupled system we keep only one of the electronic excitations and couple it to the phonon. The Hamiltonian matrix of a two level coupled system is as follows:

$$H_2 = \begin{pmatrix} \omega_{e1} & V_1 \\ V_1 & \omega_p \end{pmatrix} \tag{8.2}$$

For the three level coupled system it will be:

$$H_3 = \begin{pmatrix} \omega_{e1} & 0 & V_1 \\ 0 & \omega_{e2} & V_2 \\ V_1 & V_2 & \omega_p \end{pmatrix} \tag{8.3}$$

We have assumed in his latter model that there is no direct coupling between the two electronic excitations. However, they will be pushed apart via their common interaction with the phonon. This is a phonon mediated Davydov splitting of the two electronic excitations. H_2 and H_3 need to be diagonalized to yield the eigenfrequencies and eigenfunctions of the new coupled modes.

For the two level coupled system, we consider that there are two coupled mode eigenfrequencies, ω_- and ω_+. From the experimental Raman spectra at low temperatures, we select the two sharp and intense peaks at 250 and 346 cm^{-1} as the two coupled mode transitions:

$$\begin{cases} \omega_- = 250 \text{ cm}^{-1} \\ \omega_+ = 346 \text{ cm}^{-1} \end{cases} \tag{8.4}$$

The diagonalization of H_2 then yields the following values for ω_{e1} and V_1:

$$\begin{cases} \omega_{e1} = 290 \text{ cm}^{-1} \\ V_1 = 46 \text{ cm}^{-1} \end{cases} \tag{8.5}$$

The two modes split symmetrically about their center, $\frac{1}{2}(\omega_{e1}+\omega_{e2})$, and the total magnitude of the splitting is given by $\omega_+ - \omega_- = [(\omega_{e1} - \omega_p)^2 + 4V^2]^{1/2}$.

For the three level coupled system, we add to the sharp peaks at 250 and 346 cm^{-1} the broad central peak at about 298 cm^{-1} which in the three level model is considered to be

the third coupled mode. The three coupled mode eigenfrequencies are thus:

$$\begin{cases} \omega_- = 250\ \text{cm}^{-1} \\ \omega_+ = 346\ \text{cm}^{-1} \\ \omega_0 = 298\ \text{cm}^{-1} \end{cases} \tag{8.6}$$

There are now four parameters to be determined, ω_{e1}, ω_{e2}, V_1, and V_2, and only the three experimentally available values ω_+, ω_-, and ω_0. Thus, if we do not extract additional information from, for example, the relative intensities of the coupled mode peaks, only three of the four parameters mentioned above can be determined from the experimental spectra. Setting V_1/V_2 to some constant ratio allows the calculation of the electronic frequencies ω_{e1} and ω_{e2} and of the coupling strengths V_1 and V_2. The Hamiltonian matrix was diagonalized for various ratios V_1/V_2 and the resulting values of ω_{e1} and ω_{e2} are plotted in Figure 8.6.

The ratio $V_1/V_2 = 1.45$ is of particular interest since actual calculations of the relative coupling strengths between the two electronic excitations and the phonon by means of the electronic wavefunctions of Appendix A predict such a ratio (see next section). For $V_1/V_2 = 1.45$, we obtain:

$$\begin{cases} \omega_{e1} = 277\ \text{cm}^{-1} \\ \omega_{e2} = 301\ \text{cm}^{-1} \\ V_1 = 37\ \text{cm}^{-1} \\ V_2 = 24\ \text{cm}^{-1} \end{cases} \tag{8.7}$$

It is interesting to note that values of ω_{e1} and ω_{e2} predicted in this fashion are quite close to the values calculated in the crystal field fit and reported in Table 8.1. The coupling strengths predicted by either the two level or three level models are very strong, in fact they are an order of magnitude larger than previously observed electron- phonon coupling strengths in other rare earth compounds.

8.4.2 Calculation of the Relative Coupling Strengths

The relative coupling strengths of the two electronic excitations to the phonons can be estimated by using the wavefunctions for Yb^{3+} given in Appendix A. We assume that the electron-phonon coupling Hamiltonian can be written in the following form [1-6]:

$$H_{el-ph} = \sum_{\Gamma_\alpha} G_{\Gamma_\alpha} Q_{\Gamma_\alpha} O_{\Gamma_\alpha} \tag{8.8}$$

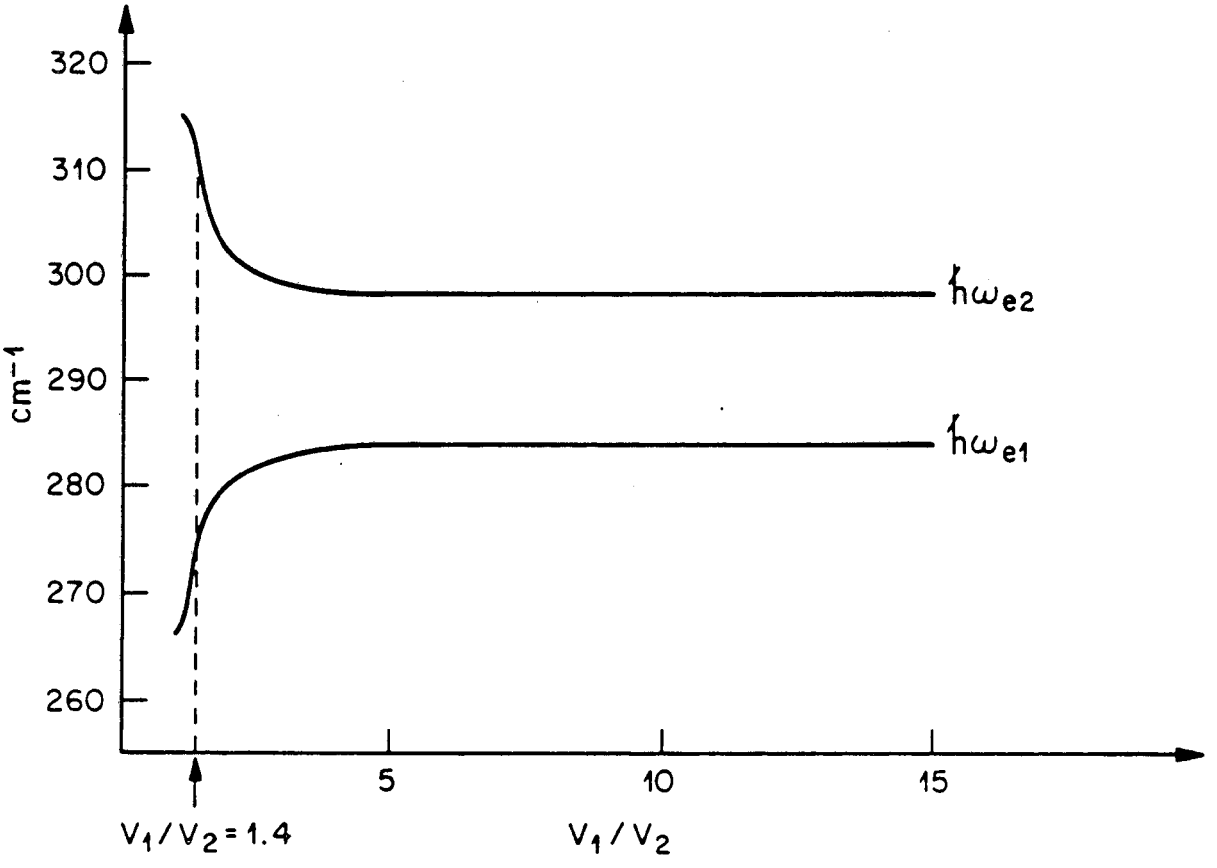

Figure 8.6: Energy values of the electronic excitations of $YbPO_4$ (in cm^{-1}) as a function of V_1/V_2, determined by the diagonalization of the three level energy matrix.

where the summation is over all the irreducible representations Γ and the suffix α is for the cases where the representations are degenerate. Q is the phonon amplitude and O is a quadrupolar electronic operator. The G are coupling constants. This expression comes from the differentiation of the crystal field Hamiltonian with respect to the ligand positions. In its above form it represents a local interaction, however, it can be summed over all the sites in the primitive cell if one wishes to extend the interaction to the level of the primitive cell. We consider only E_g symmetry, since this is where the coupling is taking place, and we have:

$$\begin{cases} O_{E_g(X)} = J_X J_Z + J_Z J_X \\ O_{E_g(Y)} = J_Y J_Z + J_Z J_Y \end{cases} \tag{8.9}$$

where we have used X and Y to distinguish the two modes of E_g symmetry. The matrix elements of these operators were calculated using the wavefunctions of the states of Yb^{3+}, given in Appendix A, and it was found that the ratio of the coupling strength of the Γ_6 level to that of the Γ_7 level is 1.4

8.4.3 Temperature Evolution of the Coupled Mode Eigenfrequencies

The conceptual reasoning underlying the temperature shift of the coupled mode eigenfrequencies, observed in Figure 8.4, was discussed in section 8.2.2. It now remains to be seen whether this temperature evolution can be incorporated into the phenomenological models with meaningful results. In section 8.2.2 it was argued that he electron-phonon coupling strength is proportional to the electronic ground state population factor. We thus have:

$$\langle V \rangle_T = \langle V \rangle_0 \frac{1}{Z} \tag{8.10}$$

where $\langle V \rangle_T$ is the coupling stregth at temperature T, $\langle V \rangle_0$ its value at T=0 K (we will assume $\langle V \rangle_0 = \langle V \rangle_4 .2$), and Z is the partition function. For a single Yb^{3+} ion we have:

$$Z = 1 + exp(-\frac{93}{kT}) + exp(-\frac{279}{kT}) + exp(-\frac{289}{kT}) \tag{8.11}$$

where kT is in wavenumber units, 93 cm^{-1} is the observed value of the first excited elctronic level of Yb^{3+} in $YbPO_4$ (from the electronic Raman spectra), and the two higher excited energy levels are taken from Table 8.1. The small differences between the actual energy values and those of Table 8.1 have a very weak impact upon the value of Z so that the above expression is accurate enough for our purposes. It is the 93 cm^{-1} line which has

the main effect on the temperature dependence. Figure 8.7 is a normalized plot of the splitting between the two sharp peaks at 250 and 346 cm^{-1} (at T=4.2 K), as a function of temperature.

The experimental splitting is shown up to T=160 K. Above that temperature the peaks are too broad to make an accurate measurement of their center feasible. The theoretical temperature evolution for two coupled modes is shown in Figure 8.7; it tends to fall off more rapidly than the experimental curve at low temperatures. The three level model curves are for $V_1/V_2 = 1.5; 1.3; 1.0$. The partition function of equation 8.9 was used to calculate the temperature evolution. The three level model curves are somewhat closer to the experimental one than that for the two level model, with the curve for $V_1/V_2 = 1.3$ offering perhaps the best average agreement in the low temperature and higher temperature regions.

Remarkably enough, the theoretical and experimental curves of Figure 8.7 are generally in good agreement. The experimental splitting starts showing a significant temperature decrease around T=120 K, which is the temperature at which we expect noticeable amounts of the ground state population to start appearing in the first excited electronic state at 93 cm^{-1}. Figure 8.7 thus confirms the arguments of section 8.2.2. Increasing the temperature effectively decreases the elctron-phonon coupling strength since on average the ion spends less time in its ground state and has a lower probability of creating an excitation resonant in energy with the phonon. This whole effect is profoundly quantum mechanical, since it is intimately linked with the experiment being performed and whether or not a measurement is made.

8.5 Phenomenological Models of the Raman Lineshapes of the Coupled Modes

8.5.1 Greens Functions and Response Theory of the Raman Lineshapes

The two level and three level phenomenological models described in the previous sections predict only the eigenfrequencies and eigenfunctions of the new coupled modes which are hybrid modes with both electronic and vibrational components. However, they do not say anything about the linewidths of the excitations involved or about the lineshapes of the Raman spectra. It is quite apparent from the spectra, especially those at higher tempera-

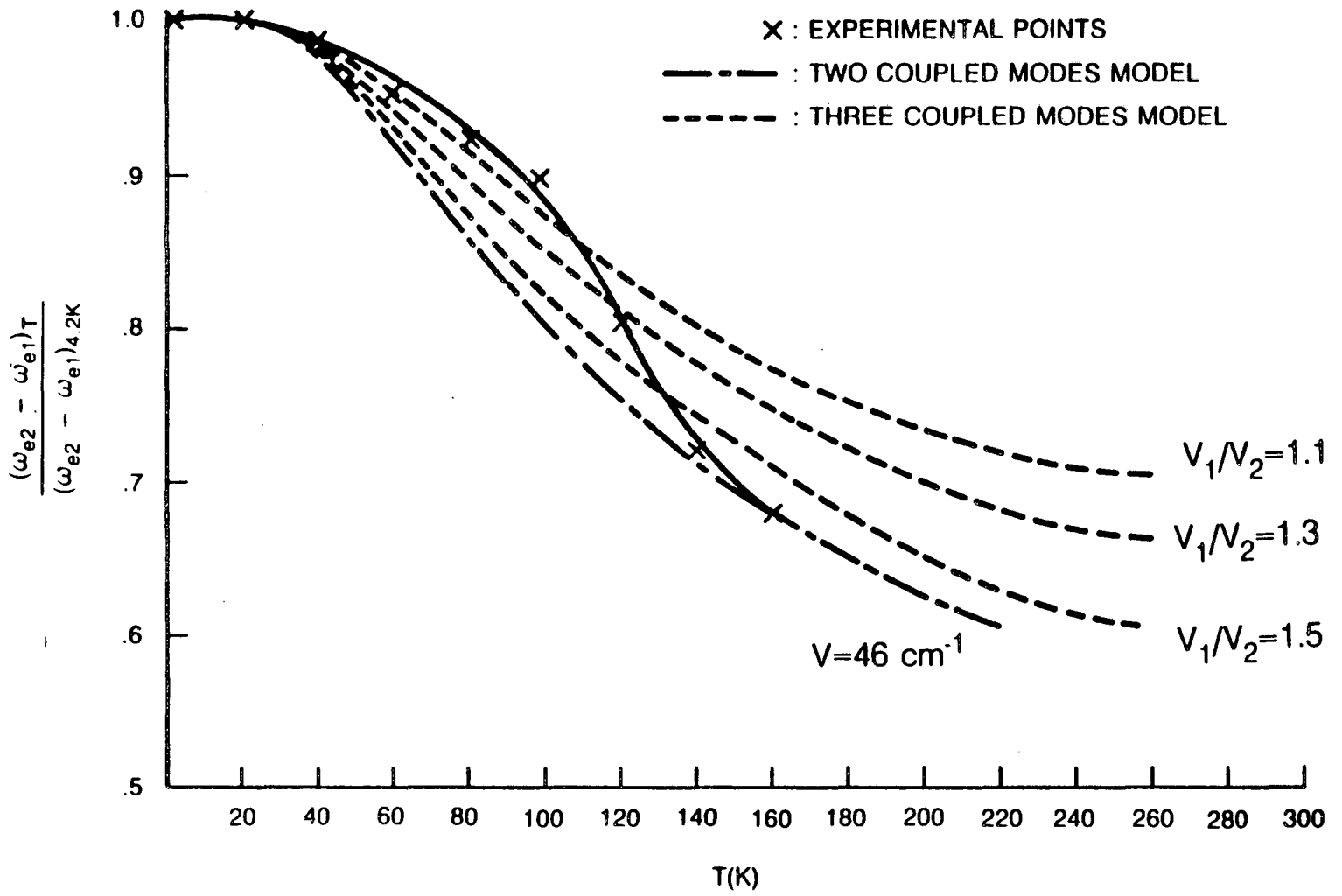

Figure 8.7: Splitting of the coupled modes of $YbPO_4$, as a function of temperature, in E_g symmetry (XZ or ZY polarization). Experimental and calculated curves are shown. ω_{e1}=249 cm^{-1} and ω_{e2}=345 cm^{-1} at T=4.2 K.

ture, that the Raman spectra are not the superposition of delta-function like peaks. The broadness of the spectral features stem from the large linewidths of the electronic excitations, which are in the range 10-20 cm^{-1} based on the observations made in other rare earth phosphate crystals. It is thus quite an oversimplification to reduce the interaction between a phonon at 300 cm^{-1} and an electronic excitation centered at 295 cm^{-1} with a linewidth of 20 cm^{-1} to a simple 2x2 energy matrix model like that of section 8.4.1 since the lineshape of the electronic excitation actually overlaps the phonon. This situation is somewhat akin to that of Fano resonances in solids, studied extensively in the 1970's [11,12,13].

The way to treat the interaction of broad and narrow excitations is to use the Greens function method [14][p.38], which actually dates back to the work of Barker and Hopfield [15]. Each excitation is treated as a harmonic oscillator with a complex energy which incorporates both its frequency and its natural linewidth. The harmonic oscillators are then coupled by phenomenological coupling parameters. For a system of coupled oscillators the Raman lineshape $S(\omega)$ as a function of frequency can be written:

$$S(\omega) = \bar{n}(\omega, \mathrm{T})\mathrm{Im}(\sum_{i,j} G_{ij}(\omega)\alpha_i\alpha_j) \tag{8.12}$$

where $\bar{n}$ is the Bose distribution function, the summation runs over the various modes that constitute the coupled system, the α_i are the scattering amplitudes of the modes, and G_{ij} is the Greens function matrix. For three coupled modes, G_{ij} is given by the following matrix:

$$G_{ij}^{-1}(\omega) = \begin{bmatrix} \omega_{e1}^2 - \omega^2 + i\Gamma_1\omega & 0 & V_1 \\ 0 & \omega_{e2}^2 - \omega^2 + i\Gamma_2\omega & V_2 \\ V_1 & V_2 & \omega_p^2 - \omega^2 \end{bmatrix} \tag{8.13}$$

where two electronic modes of frequencies ω_{e1} and ω_{e2}, and linewidths Γ_1 and Γ_2, have been coupled to a phonon of frequency ω_p assumed to have negligible linewidth. The model now incorporates the large linewidths of the electronic excitations, by means of Γ_1 and Γ_2. These linewidths will affect the positions of the peaks in the spectrum.

The lineshape model involves a fairly large number of phenomenological parameters; ω_{e1}, ω_{e2}, Γ_1, Γ_2, V_1, V_2, α_1, α_2, and α_3. Actually, since the Raman spectra intensities are in relative units only α_1/α_3 and α_2/α_3 need to be determined. All the parameters need to be fitted from the experimental spectra. However, we can use as a general guideline the values of ω_{e1} and ω_{e2} obtained from the simple eigenfrequency model discussed previously, and

also require that α_1/α_3 and α_2/α_3 be small since the phonon Raman scattering strength is presumably much stronger than the electronic ones.

8.5.2 Application to the $YbPO_4$ Spectra

The Greens function model was applied to the three level system and fitted to the $YbPO_4$ spectra at T≈4.2 K. The agreement is quite good, as shown by the experimental and calculated curves of Figure 8.8.

The values obtained for the various parameters are:

$$\begin{cases} \omega_{e1} = 273 \text{ cm}^{-1} \\ \omega_{e2} = 301 \text{ cm}^{-1} \\ \Gamma_1 = 14 \text{ cm}^{-1} \\ \Gamma_2 = 37 \text{ cm}^{-1} \\ \alpha_1 = \alpha_2 = 0.1\alpha_3 \\ V_1 = 15\ 10^3 \\ V_2 = 23\ 10^3 \end{cases}$$

These values are all quite reasonable. ω_{e1} and ω_{e2} are very close to those obtained from the simple eigenfrequency model. The linewidths are in good agreement with the XY spectrum transitions, the large value of Γ_2 explaining why the ω_{e2} transitions is so broad in that symmetry. V_1 and V_2 are comparable as was the case in the simple eigenfrequency model (although here V_1 is smaller than V_2). The two level model does not adequately predict the lineshapes for the $YbPO_4$ low temperature spectra, since it cannot reproduce the central bump at 298 cm^{-1}. By increasing the linewidths Γ_1 and Γ_2 with temperature, the three level model just outlined tracks fairly well the Raman lineshapes up to about 160 K at which point the values of the parameters begin to become unreasonable if one wishes to obtain a good fit to the experimental spectra. In fact, the broad peak at room temperature cannot be fitted in the three level model without using outlandishly large values of Γ_1 and Γ_2. The two level model can, however, replicate fairly well the room temperature spectra. The conclusion is that the three level model works well at low temperatures, but breaks down at high temperatures where the two level model seems to fit better. The theory just outlined is somewhat simple compared to the complexity of the system under study, especially at high temperatures where a multitude of interactions occur, so that we should not be surprised that it is only qualitatively correct over the full range of temperatures.

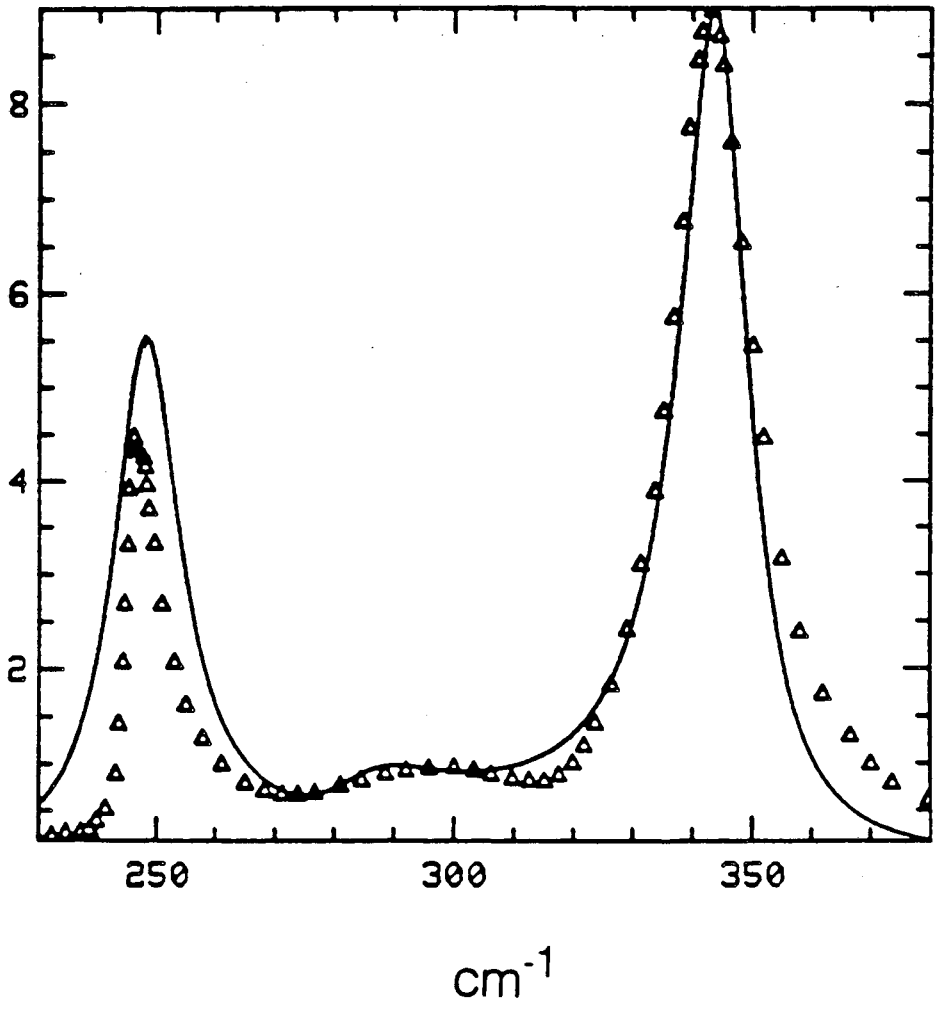

Figure 8.8: Fit of the three coupled modes Greens function model to the experimental (triangles) spectrum of $YbPO_4$ at 4.2 K in ZY polarization.

8.6 Spectra of the Mixed Ytterbium Lutetium Crystals

Raman spectra were taken of the mixed crystals $Yb_xLu_{1-x}PO_4$, with $x = 0.25; 0.50; 0.75$. These spectra were taken at ~4.2 K and also as a function of temperature in E_g symmetry in the 300 cm^{-1} region. The XZ polarization spectra at 4.2 K in the 300 cm^{-1} region are compared for all the crystals in Figure 8.9.

For $LuPO_4$ of course only the sharp phonon E_g^3 is present. It is then very interesting to see the evolution of the spectra as the concentration of Yb^{3+} is increased. As the proportion of Yb^{3+} to Lu^{3+} present in the crystal rises, two simultaneous effects start occuring. First, the intensity of phonon E_g^3 drops but it is nevertheless present. Second, the coupled modes begin appearing and start rising in intensity. Thus, it seems as if two spectra are present at the same time, which is somewhat reminiscent of the two mode phonon spectrum of alloy systems. One spectrum is just the "normal" phonon E_g^3, and the other is the coupled mode spectrum. This suggests that the electron-phonon interaction is localized and that spatial regions of the crystal that contain Lu^{3+} contribute to the "normal" E_g^3 phonon spectrum, and regions with Yb^{3+} contribute to the coupled mode spectrum. It is interesting to compare and contrast the effects of temperature vs. concentration on these Raman spectra. Whereas the temperature produces an averaging effect, the concentration seems to result in a superposition effect.

The temperature evolution of the XZ spectra for the 25%, 50%, and 75% Yb^{3+} crystals, in the 300 cm^{-1} region, is shown in Figures 8.10,8.11,and 8.12. At room temperature only one broad peak is present, and in Figure 8.13 the linewidth of that peak has been plotted as a function of Yb^{3+} concentration. The linewidth is roughly linearly proportional to the Yb^{3+} concentration.

The spectra of the mixed crystals are difficult to analyze in detail, since there are many lines wth overlapping lineshapes. In addition, these crystals have a configurational disorder. Thus, strictly speaking, they do not have translational symmetry and Raman scattering can occur from points in the Brillouin zone other than $\vec{k} = 0$.

8.7 Future Directions

The spectra of the ytterbium phosphate crystals seem to be extremely rich from both the experimental and the theoretical viewpoint. One experiment that naturally comes to

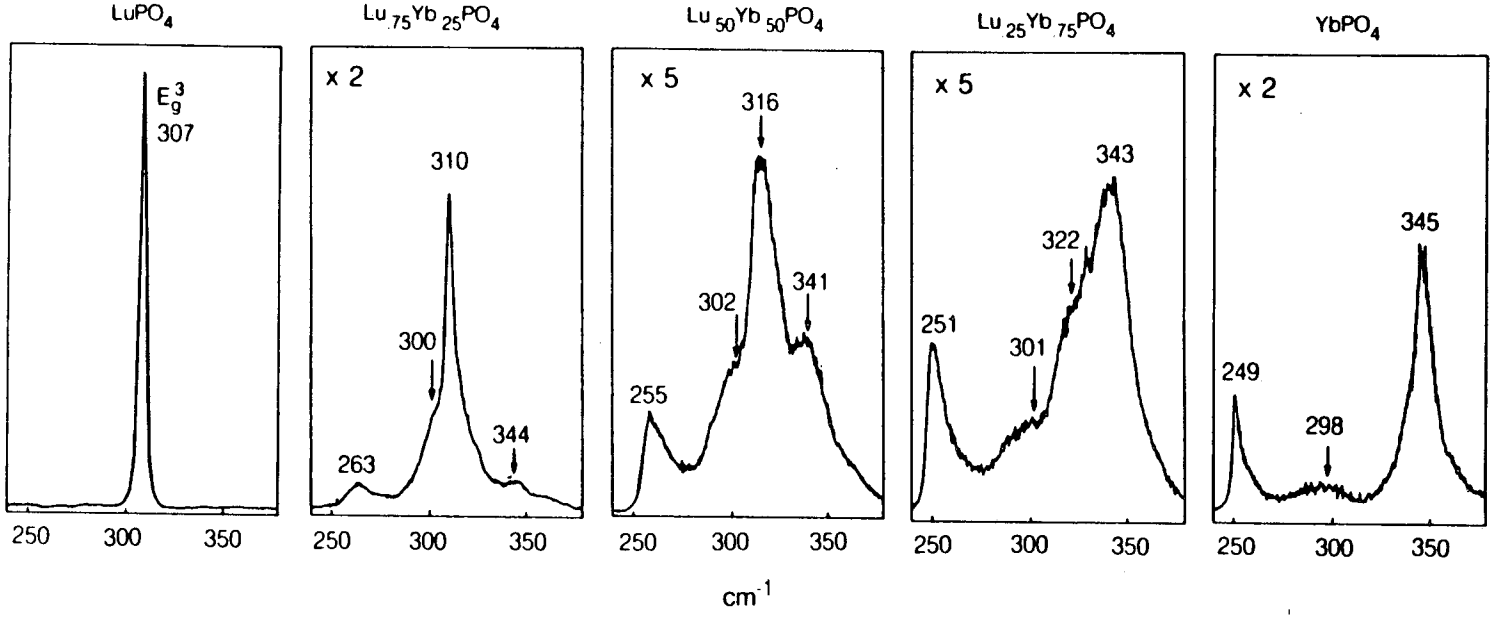

Figure 8.9: Experimental Raman spectra of the mixed ytterbium lutetium crystals at T=4.2 K in XZ polarization in the 250-350 cm^{-1} region.

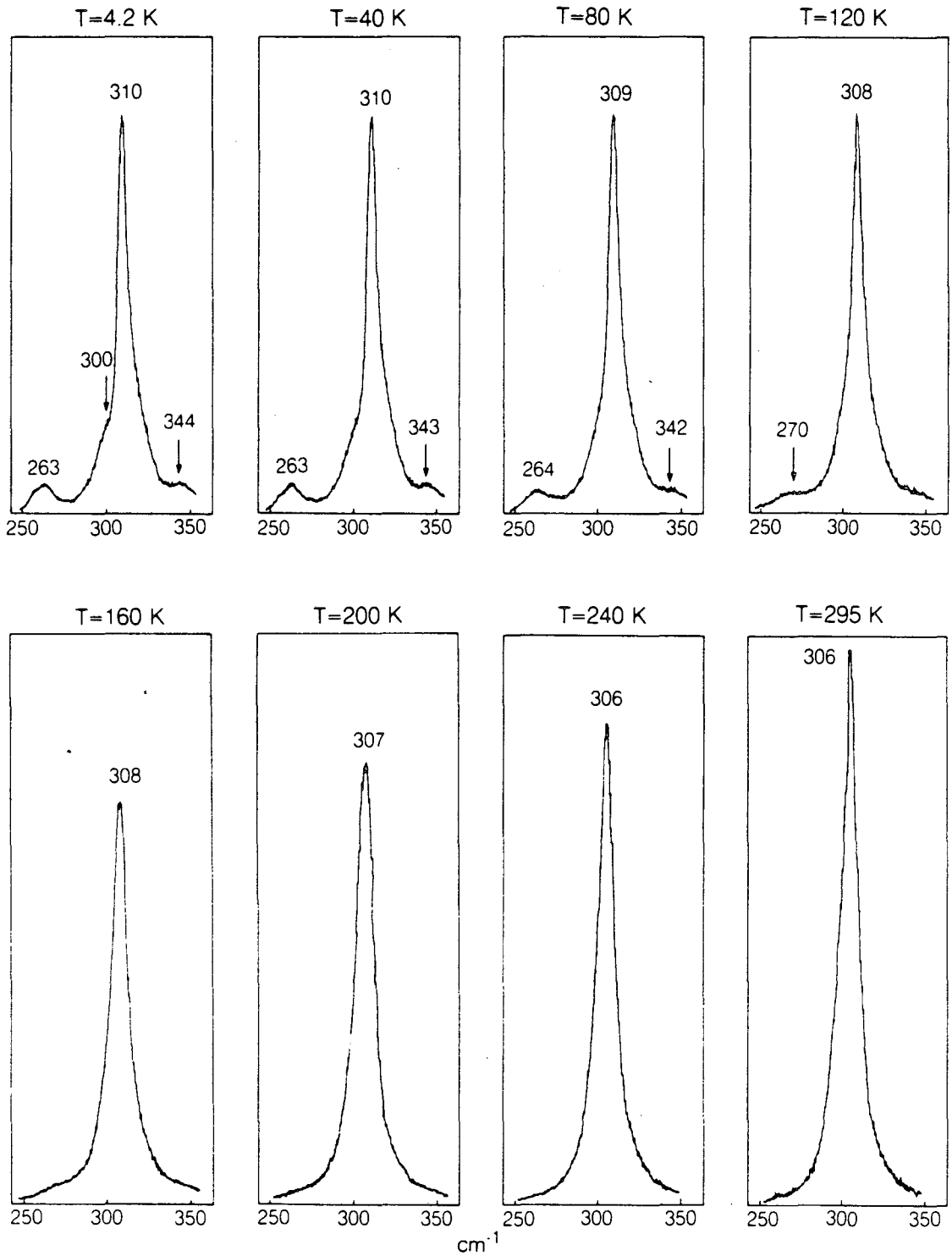

Figure 8.10: Temperature evolution of the XZ spectra of $Yb_{.25}Lu_{.75}PO_4$ in the 300 cm^{-1} region.

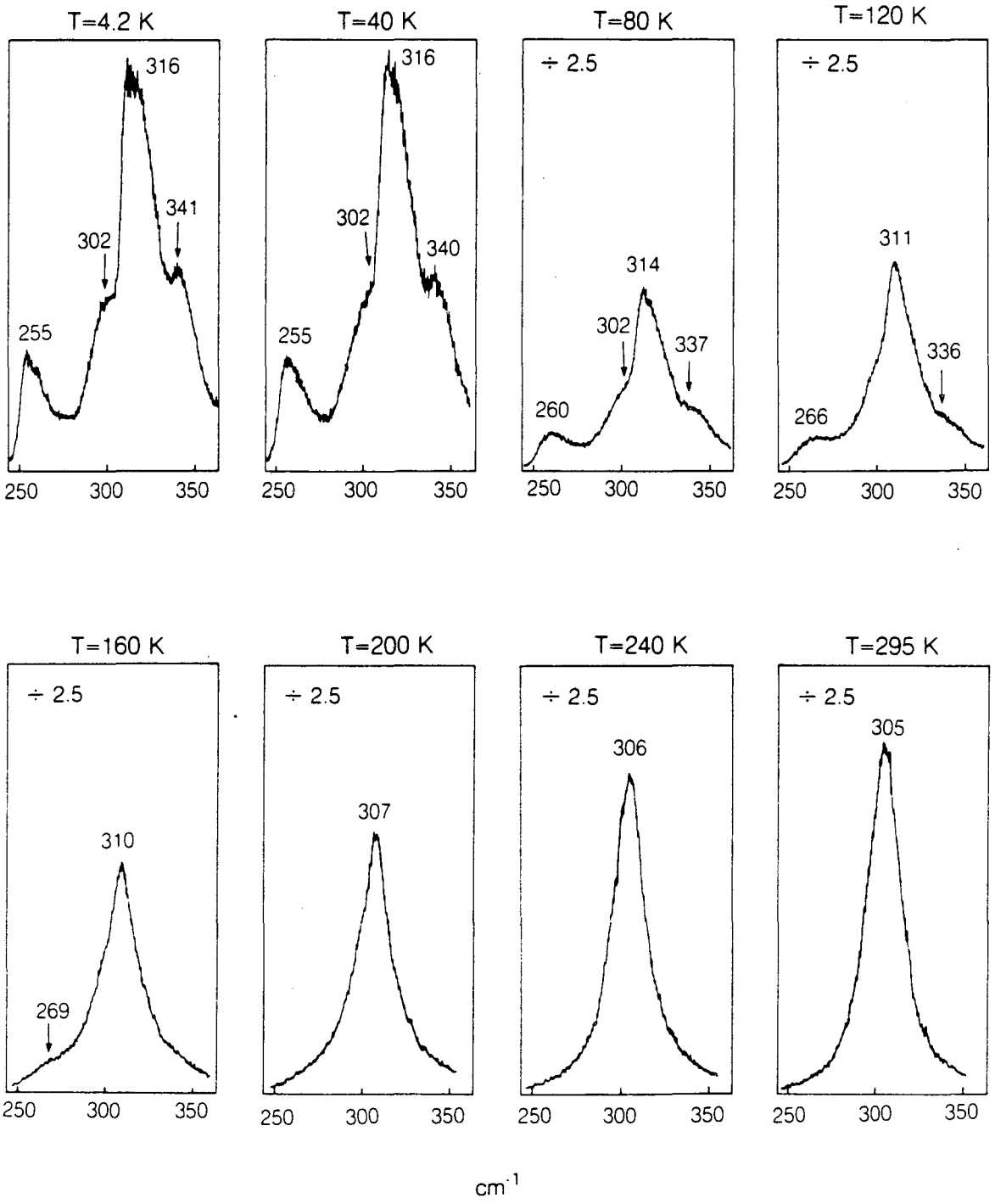

Figure 8.11: Temperature evolution of the XZ spectra of $Yb_{.50}Lu_{.50}PO_4$ in the 300 cm^{-1} region.

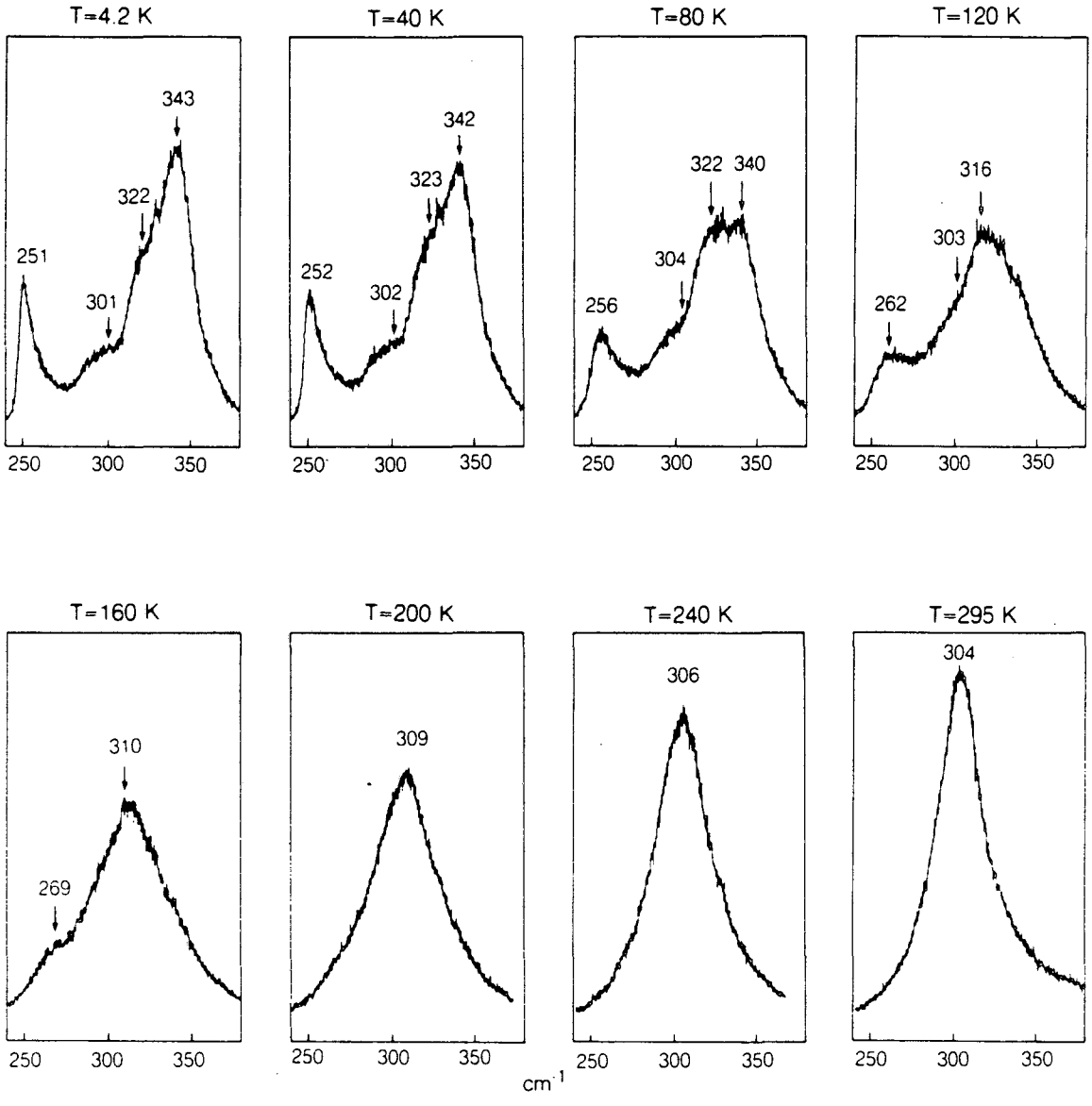

Figure 8.12: Temperature evolution of the XZ spectra of $Yb_{.75}Lu_{.25}PO_4$ in the 300 cm^{-1} region.

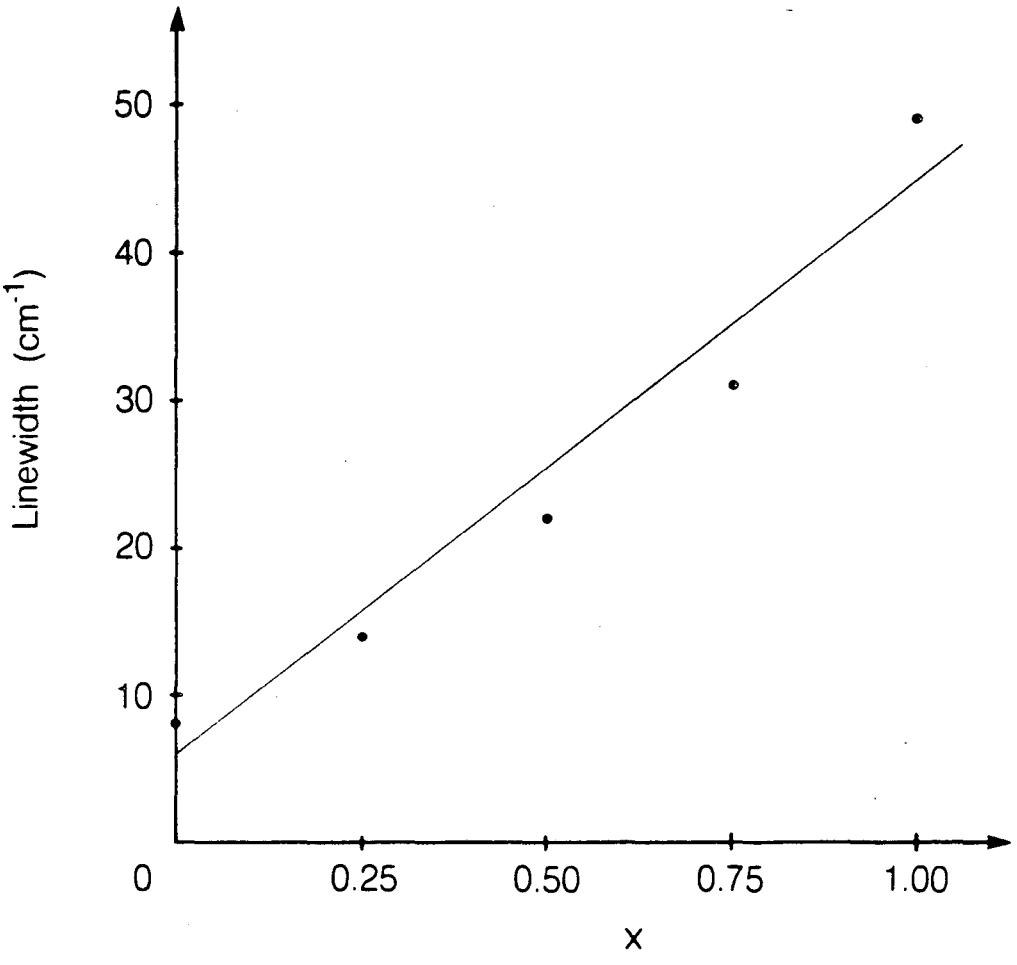

Figure 8.13: Linewidth of the 300 cm^{-1} peak at room temperature in XZ symmetry as a function of Yb^{3+} concentration in the $Yb_xLu_{1-x}PO_4$ crystals.

mind is to perform the Raman scattering with the crystal in a magnetic field. The coupled mode spectrum should then split according to the g values of the electronic states and their relative presence in the spectrum. It should also be very interesting to compare and contrast fluorescence and absorption spectra with the Raman spectra. The most important question, though, is why this electron-phonon coupling has occured with such strength in $YbPO_4$.

References

[1] K. Ahrens and G. Schaack, Phys. Rev. Lett. **42**, 1488 (1979).

[2] K. Ahrens, H. Gerlinger, H. Lichtblau, G. Schaack, G. Abstreiter, and S. Mroczkowski, J. Phys. C **13**, 4545 (1980).

[3] W. Dörfler, H.D. Hochheimer, and G. Schaack, Z. Phys. B **51**, 153 (1983).

[4] W. Dörfler and G. Schaack, Z. Phys. B **59**, 283 (1985).

[5] H. Gerlinger and G. Schaack, Phys. Rev. B **33**, 7438 (1986).

[6] P. Thalmeier and P. Fulde, Z. Phys. B **26**, 323 (1977).

[7] R.J. Elliott, R.T. Harley, W. Hayes, and S.R.P. Smith, Proc. R. Soc. Lond. **A. 328**, 217 (1972).

[8] E. Nakazawa and S. Shionoya, Phys. Rev. Lett. **25**, 1710 (1970).

[9] A.S. Barker and R. Loudon, Rev. Mod. Phys. **44**, 18 (1972).

[10] R.J. Elliott, private communication.

[11] D.L. Rousseau and S.P.S. Porto, Phys. Rev. Lett. **20**, 1354 (1968).

[12] J.F. Scott, Phys. Rev. Lett. **21**, 907 (1968).

[13] J.F. Scott, Phys. Rev. Lett. **24**, 1107 (1970).

[14] J.F. Scott, Ferro. **47**, 33 (1983).

[15] A.S. Barker and J.J. Hopfield, Phys. Rev. **135**, A 1732 (1964).

Appendix A

Crystal Field Fits and Energy Level Structure of Yb^{3+}, Tm^{3+}, Er^{3+}, and Ho^{3+}, in $LuPO_4$ and YPO_4

This appendix maps out the electronic energy level structure of the trivalent lanthanides of interest in this study, and provides the wavefunction information that is indispensable for a calculation of the electronic Raman transition intensities. The ions Yb^{3+}, Tm^{3+}, Er^{3+}, and Ho^{3+}, are treated, respectively, in sections A1 through A4. For each ion is provided:

- A complete list of the atomic and crystal field parameters obtained from a fit of the calculated to the energy levels.
- A list of the calculated and observed electronic energies and g values.
- A list of the wavefunctions of the states.

For the first three ions the host matrix is $LuPO_4$, for Ho^{3+} it is YPO_4. Except for Ho^{3+}, the results presented here have been reported previously in the literature. The published fits usually present the wavefunction content in percentages. This wipes out the sign of the coefficients of the expansion of the eigenfunctions in terms of the states $|4f^N, \alpha SLJJ_z\rangle$ and does not allow the calculation of quantities such as electronic Raman transition intensities. The tables presented here include the signs of these coefficients. Only the wavefunctions of the multiplets investigated by Raman scattering have been listed.

Appendix A1 Yb^{3+}

The crystal field fit and absorption spectrum of Yb^{3+} in $LuPO_4$ and YPO_4 was reported by P.C. Becker *et al*, J. Chem. Phys. **81**, 2872 (1984). We present here the results for Yb^{3+} in $LuPO_4$. Since as many parameters as there are observed transitions are varied, the rms energy deviation between calculated and observed energies is zero. The parameters are quite close to those for Tm^{3+} in $LuPO_4$, and the predicted Zeeman patterns are in excellent agreement with the experimental data.

Atomic and crystal field parameters (cm^{-1})

ζ	−2903.2
B_0^2	255.7
B_0^4	14.2
B_4^4	−608.0
B_0^6	−704.8
B_4^6	15.6

Energy levels and g values

	Energy (cm^{-1})			$g_{\parallel}$		$\lvert g_{\perp} \rvert$	
symmetry	calc.	obs.	incr.	calc.	obs.	calc.	obs.
Γ_6	0.0	0.0	0.0	-1.6	-1.3	3.2	3.2
Γ_7	99.0	99.0	0.0	1.1		3.5	
Γ_6	279.3			3.9		3.2	
Γ_7	288.6			5.8		1.1	
Γ_6	10244.7	10244.7	0.0	-0.4		1.8	
Γ_7	10271.8	10271.8	0.0	-0.9		2.6	
Γ_6	10475.5	10475.5	0.0	2.1		1.8	

Γ_6 Eigenfunctions

Energy (cm^{-1})		Eigenvector composition $^{2S+1}L(2J, 2J_z)$
calc.	obs.	
0.0	0.0	$-.893\ ^2F(7,-3) + 0.450\ ^2F(7,5)$
		$-.005\ ^2F(5,5) + 0.005\ ^2F(5,-3)$
279.3		$-.893\ ^2F(7,5) - .450\ ^2F(7,-3)$
		$+0.013\ ^2F(5,-3) - .004\ ^2F(5,5)$
10244.7	10244.7	$0.825\ ^2F(5,-3) - .565\ ^2F(5,5)$
		$+0.012\ ^2F(7,-3) + 0.008\ ^2F(7,5)$
10475.5	10475.5	$0.825\ ^2F(5,5) + 0.565\ ^2F(5,-3)$
		$+0.005\ ^2F(7,5)$

Γ_7 Eigenfunctions

Energy (cm^{-1})		Eigenvector composition $^{2S+1}L(2J, 2J_z)$
calc.	obs.	
99.0	99.0	$-.871\ ^2F(7,-1) + 0.491\ ^2F(7,7)$
		$-.016\ ^2F(5,-1)$
288.6		$0.871\ ^2F(7,7) + 0.491\ ^2F(7,-1)$
		$-.002\ ^2F(5,-1)$
10271.8	10271.8	$0.999\ ^2F(5,-1) - .013\ ^2F(7,-1)$
		$0.009\ ^2F(7,7)$

Appendix A2 Tm^{3+}

The crystal field fit and absorption spectrum of Tm^{3+} in $LuPO_4$ and YPO_4 was reported by P.C. Becker *et al*, J. Chem. Phys. **81**, 2872 (1984). We present here the results for Tm^{3+} in $LuPO_4$. The rms energy deviation between calculated and observed energies is 10 cm^{-1}.

Atomic and crystal field parameters (cm^{-1})

ζ	2628.90
F^2	101250.00
F^4	70753.65
F^6	50051.16
B_0^2	202.86
B_0^4	116.56
B_4^4	−672.95
B_0^6	−704.81
B_4^6	15.65
α	17.52
β	−635
γ	2200.00
M^0	4.93
M^2	2.72
M^4	1.37
P^2	729.60
P^4	547.00
P^6	364.00

Energy levels and g values

	Energy(cm^{-1})			$g_{\|\|}$	
symmetry	calc.	obs.	incr.	calc.	obs.
Γ_1	0.0	0.0	0.0		
Γ_5	21.9	25.2	−3.3	−4.6	−3.3
Γ_3	89.9	80.1	9.8		
Γ_5	131.8	124.8	7.0	−6.7	−7.7
Γ_2	182.6				
Γ_1	248.2				
Γ_4	254.4				
Γ_5	281.2			4.3	
Γ_3	303.0				
Γ_4	321.4				
Γ_3	5587.0				
Γ_5	5682.1	5674.0	8.1	1.5	
Γ_1	5700.2				
Γ_2	5735.3				
Γ_4	5769.3	5763.0	6.3		
Γ_5	5844.4	5842.0	2.4	3.0	
Γ_1	5856.7				
Γ_2	8222.6	8227.0	−4.4		
Γ_5	8257.7	8262.0	−4.3		
Γ_4	8277.8	8279.0	−1.2		
Γ_1	8321.9	8326.0	−4.1		
Γ_2	8384.7	8381.0	3.7		
Γ_5	8396.4	8395.0	1.4		
Γ_3	8425.2				
Γ_5	8444.6	8441.0	3.6		

	Energy(cm^{-1})			$g_{\|}$	
symmetry	calc.	obs.	incr.	calc.	obs.
Γ_1	12537.0	12530.8	6.2		
Γ_5	12544.1	12535.2	9.0	3.7	3.7
Γ_5	12672.6	12657.2	15.4	−0.1	
Γ_3	12676.8				
Γ_2	12704.7				
Γ_1	12723.3				
Γ_4	12782.6	12778.2	4.4		
Γ_5	14404.6	14402.3	2.2	4.3	5.4
Γ_5	14429.8	14435.3	−5.5	0.0	
Γ_4	14438.4	14454.2	−15.8		
Γ_3	14452.2				
Γ_2	14497.3				
Γ_4	14976.7	14964.0	12.7		
Γ_5	15080.5	15087.8	−7.2	−1.5	
Γ_1	15080.5				
Γ_3	15083.8				
Γ_3	20991.9	20983.0	8.9		
Γ_5	21133.6			0.9	
Γ_1	21178.9				
Γ_2	21257.5				
Γ_4	21267.5	21278.3	−10.8		
Γ_5	21381.7	21394.1	−12.4	3.0	
Γ_1	21389.5				
Γ_3	27755.7	27749.7	5.9		
Γ_4	27793.6	27785.0	8.6		
Γ_5	27818.8	27838.9	−20.1	−2.3	
Γ_1	27837.6				

	Energy(cm^{-1})			$g_{\|}$	
symmetry	calc.	obs.	incr.	calc.	obs.
Γ_4	34576.2	34579.0	−2.8		
Γ_5	34595.4	34595.0	0.4	0.9	
Γ_1	34613.4				
Γ_2	34834.3				
Γ_3	34834.6				
Γ_5	34846.4	34842.0	4.4	0.2	
Γ_4	34911.9				
Γ_3	34940.2				
Γ_1	34951.7				
Γ_5	34974.0			−7.1	
Γ_1	35224.9	35238.0	−13.1		
Γ_2	36216.9				
Γ_5	36276.5	36266.0	10.5	−3.0	
Γ_4	37862.0				
Γ_5	38049.4	38045.0	4.4	−2.6	
Γ_1	38049.5				
Γ_3	38091.4				
Γ_1	73579.9				

Γ_1 and Γ_2 Eigenfunctions

Energy(cm^{-1})		Eigenvector composition $^{2S+1}L(J,J_z)$
calc.	obs.	
0.0	0.0	$0.845\,^3H(6,0) + 0.371\,^3H(6,4)$
		$+0.371\,^3H(6,4)$
182.6		$-.704\,^3H(6,4) + 0.704\,^3H(6,-4)$
248.2		$0.598\,^3H(6,-4) + 0.598\,^3H(6,4)$
		$-.526\,^3H(6,0)$
5700.2		$-.499\,^3F(4,4) - .499\,^3F(4,-4)$
		$-.365\,^3F(4,0) - .337\,^1G(4,4)$
		$-.337\,^1G(4,-4) - .248\,^1G(4,0)$
		$0.175\,^3H(4,4) + 0.175\,^3H(4,-4)$
		$0.130\,^3H(4,0)$
5735.3		$-.564\,^3F(4,-4) + 0.5643F(4,4)$
		$-.378\,^1G(4,-4) + 0.378\,^1G(4,4)$
		$+0.195\,^3H(4,-4) - .1951\,^3H(4,4)$
5856.7		$0.712\,^3F(4,0) + 0.471\,^1G(4,0)$
		$-.261\,^3F(4,4) - .261\,^3F(4,-4)$
		$-.241\,^3H(4,0) - .172\,^1G(4,4)$
		$-.172\,^1G(4,-4)$

Γ_3 and Γ_4 Eigenfunctions

Energy(cm^{-1})		Eigenvector composition $^{2S+1}L(J,J_z)$
calc.	obs.	
89.9	80.1	$0.695\,^3H(6,-2) + 0.695\,^3H(6,2)$
		$0.113\,^3H(6,-6) + 0.113\,^3H(6,6)$
254.4		$-.565\,^3H(6,2) + 0.565\,^3H(6,-2)$
		$0.420\,^3H(6,-6) - .420\,^3H(6,6)$
303.0		$-.695\,^3H(6,-6) - .695\,^3H(6,6)$
		$+0.113\,^3H(6,-2)0.113\,^3H(6,2)$
321.4		$0.565\,^3H(6,6) - .565\,^3H(6,-6)$
		$-.420\,^3H(6,2) + 0.420\,^3H(6,-2)$
5587.0		$-.556\,^3F(4,2) - .556\,^3F(4,-2)$
		$-.386\,^1G(4,2) - .386\,^1G(4,-2)$
		$+0.204\,^3H(4,2) + 0.204\,^3H(4,-2)$
5769.3	5763.0	$-.562\,^3F(4,-2) + 0.562\,^3F(4,2)$
		$-.380\,^1G(4,-2) + 0.380\,^1G(4,2)$
		$+0.197\,^3H(4,-2) - .197\,^3H(4,2)$

Γ_5 Eigenfunctions

Energy(cm^{-1})		Eigenvector composition $^{2S+1}L(J,J_z)$
calc.	obs.	
21.9	25.2	$0.7396\,^3H(6,-1) + 0.587\,^3H(6,-5)$
		$+0.317\,^3H(6,3)$
131.8	124.8	$0.790\,^3H(6,-5) - .457\,^3H(6,-1)$
		$-.397\,^3H(6,3)$
281.2		$-.856\,^3H(6,3) + 0.486\,^3H(6,-1)$
		$-.149\,^3H(6,-5)$
5682.1	5674.0	$-.601\,^3F(4,-1) - .517\,^3F(4,3)$
		$-.410\,^1G(4,-1) - .349\,^1G(4,3)$
		$+0.215\,^3H(4,-1) + 0.182\,^3H(4,3)$
5844.4	5842.0	$-.611\,^3F(4,3) + 0.519\,^3F(4,-1)$
		$-.402\,^1G(4,3) + 0.346\,^1G(4,-1)$
		$0.205\,^3H(4,3) - .178\,^3H(4,-1)$

Appendix A3 Er^{3+}

The crystal field fit and absorption spectrum of Er^{3+} in was reported by Hayhurst *et al* (J. Chem. Phys. **74**, 5449 (1981)). We present here the results for Er^{3+} in $LuPO_4$. The rms energy deviation between calculated and observed energies is 13 cm^{-1}.

Atomic and crystal field parameters (cm^{-1})

ζ	2366
F^2	97015
F^4	69141
F^6	48232
B_0^2	146
B_0^4	68
B_4^4	−760
B_0^6	−643
B_4^6	−89
α	15.9
β	−632.0
γ	2017.0
M^0	4.5
M^2	2.5
M^4	1.7
P^2	667.0
P^4	500.3
P^6	333.5
T^2	157.5
T^3	48.0
T^4	18.0
T^6	−342.0
T^7	214.0
T^8	449.0

Energy levels and g values

	Energy(cm^{-1})			$g_{\parallel}$		$g_{\perp}$	
symmetry	calc.	obs.	incr.	calc.	obs.	calc.	obs.
Γ_7	−0.8	0.0	6.8	6.4	4.9	5.0	
Γ_6	34.8	36.1	−1.3	3.3		7.9	
Γ_7	48.8	52.9	−4.1	−7.1		4.0	
Γ_7	99.7	97.6	2.1	16.0		0.7	
Γ_6	132.4			−5.8		5.9	
Γ_6	229.4			−7.2		0.5	
Γ_7	245.9			−1.3		9.3	
Γ_6	286.0			14.4		1.5	
Γ_6	6548.0	6534.7	13.3	2.7		6.9	
Γ_7	6555.7	6544.2	11.5	4.0		5.0	
Γ_7	6608.3	6601.6	6.7	−5.3		4.4	
Γ_6	6619.4	6614.8	4.6	8.6		2.8	
Γ_6	6646.5	6641.1	5.4	2.2		1.9	
Γ_7	6687.2	6682.1	5.1	−2.0		7.1	
Γ_6	6697.3	6694.8	2.5	−9.0		2.1	
Γ_6	10198.4	10206.0	−7.6	1.3		5.4	
Γ_7	10211.0	10220.7	−9.7	3.6		3.4	
Γ_6	10239.9	10243.8	−3.9	−5.8		2.2	
Γ_7	10245.6	10252.3	−6.7	−1.5		1.4	
Γ_6	10256.8	10256.2	0.6	−4.4		3.2	
Γ_7	10271.7	10273.7	−2.0	−4.9		3.8	
Γ_6	12362.5	12371.6	−9.1	2.6	3.1	3.5	3.1
Γ_7	12428.9	12441.9	−13.0	−7.0	−8.2	1.1	3.3
Γ_6	12432.1	12432.2	−0.1	−0.9	1.6	3.5	3.2
Γ_7	12508.1	12531.2	−23.1	1.5		0.8	

	Energy(cm^{-1})			$g_{\parallel}$		$g_{\perp}$	
symmetry	calc.	obs.	incr.	calc.	obs.	calc.	obs.
Γ_7	12577.9	12586.4	−8.5	2.7		2.6	
Γ_7	15260.5	15235.4	25.1	4.1		3.0	
Γ_6	15290.0	15270.9	19.1	1.2	1.9	5.2	
Γ_7	15301.5	15277.1	24.4	−7.4		2.1	
Γ_7	15335.6	15319.6	16.0	−0.1	0.4	4.8	
Γ_6	15378.0	15363.2	14.8	1.0		5.2	
Γ_6	18367.2	18363.9	3.3	−5.2	−5.3	0.0	0.2
Γ_7	18395.8	18404.3	−8.5	−1.7	−2.0	3.4	3.4
Γ_6	19102.1	19077.8	24.3	2.3	3.1	6.2	6.0
Γ_7	19135.0			5.0		2.8	
Γ_6	19164.5	19139.9	24.6	−11.0	−10.0	0.6	0.5
Γ_7	19189.7	19178.3	11.4	−3.1	6.3	0.8	0.3
Γ_6	19192.8	19197.9	−5.1	−1.4	0.1	5.6	5.8
Γ_7	19222.9			−5.3		4.7	
Γ_6	20493.0	20482.6	10.4	−2.7	−2.9	2.5	2.0
Γ_7	20503.7			8.4		0.0	
Γ_6	20560.0	20553.8	6.2	5.1		2.5	
Γ_7	20565.3	20560.7	4.6	−1.0		4.8	
Γ_6	22148.9	22154.0	−5.1	3.5		1.5	
Γ_7	22175.7	22182.4	−6.7	−1.1		3.1	
Γ_6	22177.1	22192.1	−15.0	−1.4		1.9	
Γ_6	22521.8			−2.2		0.4	
Γ_7	22537.4	22541.3	−3.9	−0.8		1.4	
Γ_6	24487.3	24491.9	−4.6	3.3	5.0	4.2	2.0
Γ_7	24539.5	24538.7	0.8	−8.5		1.2	
Γ_6	24547.4	24529.5	17.9	−1.1		4.2	
Γ_7	24601.2	24619.8	−18.6	2.4		0.8	

	Energy(cm^{-1})			$g_{\parallel}$		$g_{\perp}$	
symmetry	calc.	obs.	incr.	calc.	obs.	calc.	obs.
symmetry	calc.	obs.	incr.	calc.	obs.	calc.	obs.
Γ_7	24665.5	24652.7	12.8	2.8		3.3	
Γ_6	26294.7	26294.1	0.6	0.9	1.0	6.4	5.8
Γ_7	26317.9	26316.8	1.1	2.8		5.1	5.3
Γ_6	26357.2	26342.9	14.3	−11.5	−10.6	0.0	
Γ_7	26393.2	26396.3	−3.1	−4.1	−6.3	4.1	
Γ_6	26439.8	26458.9	−19.1	−0.1		6.4	
Γ_7	26459.0	26477.7	−18.7	−2.1		6.1	
Γ_7	27343.5	27346.0	−2.5	4.2		2.7	
Γ_6	27349.7	27357.3	−7.6	1.6	4.1	5.2	
Γ_7	27357.7			−5.7		1.6	
Γ_6	27382.7	27401.6	−18.9	0.7	3.3	5.0	
Γ_7	27385.6	27397.8	−12.2	−2.0		4.3	

Γ_6

Energy(cm^{-1})		Eigenvector composition $^{2S+1}L(2J, 2J_z)$
calc.	obs.	
34.8	36.1	$.826\,^4I(15,5) + 0.476\,^4I(15,-3)$
		$.184\,^4I(15,-11) + 0.163\,^4I(15,13)$
		$-.144\,^2K(15,5)$
132.4		$-0.675\,^4I(15,-11) + -0.547\,^4I(15,-3)$
		$+0.438\,^4I(15,5) + 0.146\,^4I(15,13)$
		$+0.118\,^2K(15,-11)$
229.4		$-.6884\,^4I(15,-11) + 0.651\,^4I(15,-3)$
		$-.196\,^4I(15,13) + -0.183\,^4I(15,5)$
		$.120\,^2K(15,-11) + -0.114\,^2K(15,-3)$
286.0		$0.939\,^4I(15,13) - 0.250\,^4I(15,5)$
		$-.165\,^2K(15,13) + 0.138\,^4I(15,-3)$

Γ_7

Energy(cm^{-1})		Eigenvector composition $^{2S+1}L(2J, 2J_z)$
calc.	obs.	
0.0	0.0	$-0.845\,^4I(15,7) - 0.306\,^4I(15,-1)$
		$-0.292\,^4I(15,15) - .279\,^4I(15,-1)$
		$+0.147\,^2K(15,7)$
48.8	52.9	$-.887\,^4I(15,-9) + 0.291\,^4I(15,7)$
		$+0.227\,^4I(15,15) - .213\,^4I(15,-1)$
		$+0.155\,^2K(15,-9)$
99.7	97.6	$0.911\,^4I(15,15) - .330\,^4I(15,7)$
		$-0.159\,^2K(15,15) + 0.148\,^4I(15,-9)$
245.9		$-0.907\,^4I(15,-1) + 0.287\,^4I(15,-9)$
		$0.251\,^4I(15,7) + 0.159\,^2K(15,-1)$

Appendix A4 Ho^{3+}

The crystal field fit and absorption spectrum of Ho^{3+} is for Ho^{3+} in YPO_4. It is the result of unpublished work by N. Edelstein. The rms energy deviation between calculated and observed energies is 12 cm^{-1}. For the crystal field fit reported here, the zero of the energy level structure was calculated to be at 2.7 cm^{-1}. To reference the energy level values to a zero energy ground state, it is necessary to subtract 2.7 cm^{-1} from the calculated energy values reported here. The calculated values listed in other parts of this thesis (chapter 4, appendix B) are referenced to a ground state of energy zero.

Atomic and crystal field parameters (cm^{-1})

ζ	2134
F^2	93668
F^4	66113
F^6	49372
B_0^2	352
B_0^4	67
B_4^4	−673
B_0^6	−757
B_4^6	−3.7
α	18.9
β	−611.0
γ	2013.0
M^0	3.0
M^2	1.7
M^4	1.1
P^2	528.0
P^4	396.0
P^6	264.0
T^2	248.6
T^3	37.0
T^4	98.0
T^6	−316.0
T^7	440.0
T^8	372.0

Energy levels and g values

	Energy(cm^{-1})			$g_{\|\|}$	
symmetry	calc.	obs.	incr.	calc.	obs.
Γ_5	2.7	0.0	2.7	−17.3	−16.7
Γ_1	71.1	71.7	−0.7		
Γ_4	74.4	66.6	7.8		
Γ_3	86.5	80.9	5.7		
Γ_5	90.5	89.2	1.3	2.6	1.6
Γ_4	153.2	160.4	−7.3		
Γ_2	198.1	188.1	10.0		
Γ_1	198.8				
Γ_5	227.3			9.6	
Γ_3	247.9	250.2	−2.3		
Γ_5	279.3	279.3	0.0	−4.9	
Γ_2	279.7				
Γ_1	302.3				
Γ_3	5147.0	5153.2	−6.2		
Γ_4	5152.4	5158.6	−6.2		
Γ_5	5159.5			1.2	
Γ_2	5163.2				
Γ_5	5166.7			−11.0	
Γ_3	5194.3				
Γ_5	5202.5			2.3	
Γ_1	5212.9				
Γ_2	5255.3				
Γ_5	5256.1	5264.5	−8.4	−1.8	
Γ_4	5256.2				
Γ_4	8647.1				

	Energy(cm^{-1})			$g_{\parallel}$	
symmetry	calc.	obs.	incr.	calc.	obs.
Γ_3	8648.6				
Γ_1	8670.2				
Γ_5	8670.8	8670.7	0.1	−3.3	
Γ_4	8679.5				
Γ_2	8687.2				
Γ_5	8700.8	8708.4	−7.6	7.8	
Γ_3	8732.7				
Γ_5	8748.8	8746.5	2.3	2.2	
Γ_1	8757.4				
Γ_5	11213.8			8.4	
Γ_5	11231.6			−3.5	
Γ_3	11238.8				
Γ_2	11248.6				
Γ_1	11261.0				
Γ_4	11282.5				
Γ_5	11290.4			0.8	
Γ_2	11309.9				
Γ_1	13240.0				
Γ_5	13242.5			−3.2	
Γ_2	13291.5				
Γ_1	13325.7				
Γ_4	13360.4				
Γ_5	13370.9			0.2	
Γ_3	13461.1				
Γ_3	15445.2	15432.1	13.1		
Γ_5	15452.4	15452.3	0.1	−1.2	
Γ_2	15463.6	15463.7	−0.1		

	Energy(cm^{-1})			$g_{\|}$	
symmetry	calc.	obs.	incr.	calc.	obs.
symmetry	calc.	obs.	incr.	calc.	obs.
Γ_5	15532.7	15532.8	−0.1	6.2	
Γ_1	15538.3	15536.3	2.1		
Γ_4	15548.3	15539.0	9.3		
Γ_5	15562.3	15557.0	5.3	3.1	
Γ_2	15575.6	15567.3	8.4		
Γ_3	18426.4	18437.3	−10.9		
Γ_1	18430.8	18443.8	−13.0		
Γ_5	18433.6	18446.3	−12.7	3.3	
Γ_4	18446.7	18461.9	−15.3		
Γ_1	18523.0	18518.9	4.1		
Γ_5	18547.2	18545.9	1.4	−2.8	
Γ_5	18575.2	18571.5	3.7	−2.2	
Γ_3	18596.7	18593.3	3.3		
Γ_2	18618.7	18619.7	−1.0		
Γ_4	18623.5	18620.1	3.4		
Γ_1	18624.7	18625.0	−0.3		
Γ_5	20588.3	20584.0	4.3	0.7	
Γ_4	20600.7	20601.8	−1.2		
Γ_2	20650.2	20644.3	5.9		
Γ_5	20673.8	20688.7	5.1	−5.6	
Γ_3	20685.9	20675.6	10.4		
Γ_3	21059.6	21049.4	10.2		
Γ_1	21080.5	21078.0	2.5		
Γ_5	21083.7	21083.4	0.3	2.3	

Γ_1 and Γ_2 Eigenfunctions

Energy(cm^{-1})		Eigenvector composition $^{2S+1}L(J, J_z)$
calc.	obs.	
71.1	71.7	$-0.917\,{}^5I(8,0) + 0.218\,{}^5I(8,-4)$
		$+0.218\,{}^5I(8,4) + 0.208\,{}^3K2(8,0)$
198.1	188.1	$0.703\,{}^5I(8,-8) - 0.649\,{}^5I(8,8)$
		$-0.160\,{}^3K2(8,-8) + 0.148\,{}^3K2(8,8)$
198.8		$0.706\,{}^5I(8,8) + 0.652\,{}^5I(8,-8)$
		$-0.161\,{}^3K2(8,8) - 0.145\,{}^3K2(8,-8)$
279.3		$0.676\,{}^5I(8,-4) - 0.676\,{}^5I(8,4)$
		$-0.155\,{}^3K2(8,-4) + 0.155\,{}^3K2(8,4)$
302.3		$0.645\,{}^5I(8,4) + 0.645\,{}^5I(8,-4)$
		$0.303\,{}^5I(8,0) - 0.148\,{}^3K2(8,4)$
		$-0.148\,{}^3K2(8,-4)$

Γ_3 and Γ_4 Eigenfunctions

Energy(cm^{-1})		Eigenvector composition $^{2S+1}L(J,J_z)$
calc.	obs.	
74.4	66.6	$-0.593\,{}^5I(8,6) + 0.592\,{}^5I(8,-6)$
		$0.342\,{}^5I(8,2) - 0.342\,{}^5I(8,-2)$
		$0.134\,{}^3K2(8,6) - 0.134\,{}^3K2(8,-6)$
86.5	80.9	$0.668\,{}^5I(8,-6) + 0.668\,{}^5I(8,6)$
		$-0.152\,{}^3K2(8,-6) - 0.151\,{}^3K2(8,6)$
		$-0.148\,{}^5I(8,-2) - 0.148\,{}^5I(8,2)$
153.2	160.4	$-0.592\,{}^5I(8,2) + 0.592\,{}^5I(8,-2)$
		$-0.342\,{}^5I(8,6) + 0.342\,{}^5I(8,-6)$
		$0.135\,{}^3K2(8,2) - 0.135\,{}^3K2(8,-2)$
247.9	250.2	$0.667\,{}^5I(8,-2) + 0.667\,{}^5I(8,2)$
		$-0.153\,{}^3K2(8,-2) - 0.153\,{}^3K2(8,2)$
		$0.148\,{}^5I(8,-6) + 0.148\,{}^5I(8,6)$

Γ_5 Eigenfunctions

Energy(cm^{-1})		Eigenvector composition $^{2S+1}L(J, J_z)$
calc.	obs.	
2.7	0.0	$0.962\,^5I(8,-7) - 0.217\,^3K2(8,-7)$
		$+0.114\,^3K1(8,-7)$
90.5	89.2	$-0.879\,^5I(8,1) + 0.295\,^5I(8,5)$
		$0.268\,^5I(8,-3) + 0.200\,^3K2(8,1)$
227.3		$-0.887\,^5I(8,5) + 0.329\,^5I(8,-3)$
		$0.203\,^3K2(8,5) - 0.195\,^5I(8,1)$
279.3	279.3	$-0.863\,^5I(8,-3) - 0.352\,^5I(8,1)$
		$-0.246\,^5I(8,5) + 0.198\,^3K2(8,-3)$

Appendix B

Spherical and Cartesian Electronic Raman Scattering Tensors for Tm^{3+}, Er^{3+}, Ho^{3+}, and Yb^{3+}.

This appendix contains the spherical and cartesian Raman scattering tensors for the ions studied in this work. The wavefunctions used were those of Appendix A. The results presented here are particularly valuable for chapter 5.

The states are all listed by their energy, which, for convenience are the calculated values from the crystal field fits (in $LuPO_4$ for Tm^{3+}, Er^{3+}, and Yb^{3+}, and in YPO_4 for Ho^{3+}).

The Γ_5 states, used for the even electron systems Tm^{3+} and Ho^{3+}, are doubly degenerate, and the two components have been listed as (X) and (Y), this label being placed after the energy value. Appendix A lists the wavefunctions of the (X) components. The (Y) component wavefunction is obtained by making the replacement $J_z \rightarrow -J_z$ in the basis states that appear in the expansion of the (X) wavefunction. To obtain the total Raman scattering matrix for a transition involving a Γ_5 state, the (X) and (Y) component matrices are added incoherently. This has been done in the matrices reported here.

In the odd electron systems Yb^{3+} and Er^{3+} all the levels are doubly degenerate Kramers doublets. The wavefunctions of Appendix A list the wavefunctions of only one member of the doublet. The other member of the doublet has the wavefunction:

$$\Psi(\mathrm{K}) = \sum_{JJ_z} a^*_{JJ_z}(-1)^{J-J_z}|J - J_z\rangle$$

where the first component has the wavefunction:

$$\Psi = \sum_{JJ_z} a_{JJ_z} |J J_z\rangle$$

(see Hufner, Optical Spectra of Transparent Rare Earth Compounds, Academic Press, New York, 1978, p. 78). In what follows, the Kramers conjugate states of those listed in appendix A are labeled by the expression (K) following the energy value. The Cartesian scattering tensor for a doublet to doublet transition in the odd electron systems is the incoherent sum of the four possible transitions between the two Kramers doublets.

The Cartesian scattering tensors are listed in the crystallographic X,Y,Z frame.

Appendix B1 Tm^{3+}

Spherical Electronic Raman Scattering Tensors $^3H_6 \longrightarrow {}^3H_6$

$0.0 \longrightarrow 22\ cm^{-1}$ (X)

$\alpha^1_{-1} = .366F_1$

$\alpha^2_{-1} = .040F_2$

$0.0 \longrightarrow 22\ cm^{-1}$ (Y)

$\alpha^1_1 = -.366F_1$

$\alpha^2_1 = .040F_2$

$0.0 \longrightarrow 90\ cm^{-1}$

$\alpha^2_2 = -.151F_2$

$\alpha^2_{-2} = -.151F_2$

$0.0 \longrightarrow 132\ cm^{-1}$ (X)

$\alpha^1_{-1} = -.125F_1$

$\alpha^2_{-1} = .070F_2$

$0.0 \longrightarrow 132\ cm^{-1}$ (Y)

$\alpha^1_1 = .125F_1$

$\alpha^2_1 = .070F_2$

$0.0 \longrightarrow 182.6\ cm^{-1}$

$\alpha^1_0 = -.188F_1$

$\alpha^2_0 = 0$

$0.0 \longrightarrow 248.2\ cm^{-1}$

$\alpha^1_0 = 0$

$\alpha^2_0 = -.079F_2$

$0.0 \longrightarrow 254.4\ cm^{-1}$

$\alpha^2_2 = .069F_2$

$\alpha^2_{-2} = -.069F_2$

$0.0 \longrightarrow 281\ \mathrm{cm}^{-1}$ (X)

$\alpha^1_{-1} = .042F_1$

$\alpha^2_{-1} = .057F_2$

$0.0 \longrightarrow 281\ \mathrm{cm}^{-1}$ (Y)

$\alpha^1_1 = -.042F_1$

$\alpha^2_1 = .057F_2$

$0.0 \longrightarrow 303.0\ \mathrm{cm}^{-1}$

$\alpha^2_{-2} = -.006F_2$

$\alpha^2_2 = -.006F_2$

$0.0 \longrightarrow 321.4\ \mathrm{cm}^{-1}$

$\alpha^2_{-2} = -.028F_2$

$\alpha^2_2 = .028F_2$

Cartesian Electronic Raman Scattering Tensors $^3H_6 \longrightarrow {}^3H_6$

$0.0\ \text{cm}^{-1} \longrightarrow 22\ \text{cm}^{-1}$

$|\alpha_{XZ}|^2 = |\alpha_{YZ}|^2 = (-.183F_1 + .020F_2)^2$

$|\alpha_{ZX}|^2 = |\alpha_{ZY}|^2 = (.183F_1 + .020F_2)^2$

$0.0\ \text{cm}^{-1} \longrightarrow 90\ \text{cm}^{-1}$

$|\alpha_{XY}|^2 = |\alpha_{YX}|^2 = (-.151F_2)^2$

$0.0\ \text{cm}^{-1} \longrightarrow 132\ \text{cm}^{-1}$

$|\alpha_{XZ}|^2 = |\alpha_{YZ}|^2 = (.063F_1 + .035F_2)^2$

$|\alpha_{ZX}|^2 = |\alpha_{ZY}|^2 = (-.063F_1 + .035F_2)^2$

$0.0\ \text{cm}^{-1} \longrightarrow 183\ \text{cm}^{-1}$

$|\alpha_{XY}|^2 = |\alpha_{YX}|^2 = (.133F_1)^2$

$0.0\ \text{cm}^{-1} \longrightarrow 248\ \text{cm}^{-1}$

$|\alpha_{XX}|^2 = |\alpha_{YY}|^2 = (.032F_2)^2$

$|\alpha_{ZZ}|^2 = (-.064F_2)^2$

$0.0\ \text{cm}^{-1} \longrightarrow 254\ \text{cm}^{-1}$

$|\alpha_{XX}|^2 = |\alpha_{YY}|^2 = (.069F_2)^2$

$0.0\ \text{cm}^{-1} \longrightarrow 281\ \text{cm}^{-1}$

$|\alpha_{XZ}|^2 = |\alpha_{YZ}|^2 = (-.021F_1 + .029F_2)^2$

$|\alpha_{ZX}|^2 = |\alpha_{ZY}|^2 = (.021F_1 + .029F_2)^2$

$0.0\ \text{cm}^{-1} \longrightarrow 303\ \text{cm}^{-1}$

$|\alpha_{XY}|^2 = |\alpha_{YX}|^2 = (-.006F_2)^2$

$0.0\ \text{cm}^{-1} \longrightarrow 321\ \text{cm}^{-1}$

$|\alpha_{XX}|^2 = |\alpha_{YY}|^2 = (.028F_2)^2$

Spherical Electronic Raman Scattering Tensors $^3H_6 \longrightarrow {}^3F_4$

$0.0 \longrightarrow 5587\ \text{cm}^{-1}$

$\alpha^2_{-2} = .055F_2$

$\alpha^2_2 = .055F_2$

$0.0 \longrightarrow 5682\ \text{cm}^{-1}$ (X)

$\alpha^2_{-1} = -.097F_2$

$0.0 \longrightarrow 5682\ \text{cm}^{-1}$ (Y)

$\alpha^2_1 = -.097F_2$

$0.0 \longrightarrow 5700\ \text{cm}^{-1}$

$\alpha^2_0 = .081F_2$

$0.0 \longrightarrow 5735\ \text{cm}^{-1}$

all tensor elements are zero

$0.0 \longrightarrow 5769\ \text{cm}^{-1}$

$\alpha^2_{-2} = -.014F_2$

$\alpha^2_2 = .014F_2$

$0.0 \longrightarrow 5844\ \text{cm}^{-1}$ (X)

$\alpha^2_{-1} = .015F_2$

$0.0 \longrightarrow 5844\ \text{cm}^{-1}$ (Y)

$\alpha^2_1 = .015F_2$

$0.0 \longrightarrow 5857\ \text{cm}^{-1}$

$\alpha^2_0 = -.088F_2$

Cartesian Electronic Raman Scattering Tensors $^3H_6 \longrightarrow {}^3F_4$

$0.0\ \text{cm}^{-1} \longrightarrow 5587\ \text{cm}^{-1}$

$|\alpha_{XY}|^2 = |\alpha_{YX}|^2 = (.055F_2)^2$

$0.0\ \text{cm}^{-1} \longrightarrow 5682\ \text{cm}^{-1}$

$|\alpha_{XZ}|^2 = |\alpha_{YZ}|^2 = 2(-.049F_2)^2$

$|\alpha_{ZX}|^2 = |\alpha_{ZY}|^2 = 2(-.049F_2)^2$

$0.0\ \text{cm}^{-1} \longrightarrow 5700\ \text{cm}^{-1}$

$|\alpha_{XX}|^2 = |\alpha_{YY}|^2 = (-.033F_2)^2$

$|\alpha_{ZZ}|^2 = (.066F_2)^2$

$0.0\ \text{cm}^{-1} \longrightarrow 5769\ \text{cm}^{-1}$

$|\alpha_{XX}|^2 = (.014F_2)^2$

$|\alpha_{YY}|^2 = (-.014F_2)^2$

$0.0\ \text{cm}^{-1} \longrightarrow 5844\ \text{cm}^{-1}$

$|\alpha_{XZ}|^2 = |\alpha_{YZ}|^2 = 2(.007F_2)^2$

$|\alpha_{ZX}|^2 = |\alpha_{ZY}|^2 = 2(.007F_2)^2$

$0.0\ \text{cm}^{-1} \longrightarrow 5856\ \text{cm}^{-1}$

$|\alpha_{XX}|^2 = |\alpha_{YY}|^2 = (.036F_2)^2$

$|\alpha_{ZZ}|^2 = (-.072F_2)^2$

Appendix B2 Er^{3+}

Spherical Electronic Raman Scattering Tensors $^4I_{15/2} \longrightarrow {}^4I_{15/2}$

$0 \longrightarrow 36\ cm^{-1}$ $\quad$ $0(K) \longrightarrow 36\ cm^{-1}$

$\alpha^2_{-1} = .032F_2$ $\quad$ $\alpha^2_{-2} = .031F_2$

$\alpha^1_{-1} = -.419F_1$ $\quad$ $\alpha^2_2 = .047F_2$

$0 \longrightarrow 36(K)\ cm^{-1}$ $\quad$ $0(K) \longrightarrow 36(K)\ cm^{-1}$

$\alpha^2_{-2} = -.047F_2$ $\quad$ $\alpha^2_1 = -.032F_2$

$\alpha^2_2 = -.031F_2$ $\quad$ $\alpha^1_1 = -.419F_2$

$0 \longrightarrow 50\ cm^{-1}$ $\quad$ $0(K) \longrightarrow 50\ cm^{-1}$

$\alpha^2_0 = .005F_2$ $\quad$ $\alpha^2_{-1} = .052F_2$

$\alpha^1_0 = -.217F_1$ $\quad$ $\alpha^1_{-1} = .316F_1$

$0 \longrightarrow 50(K)\ cm^{-1}$ $\quad$ $0(K) \longrightarrow 50(K)\ cm^{-1}$

$\alpha^2_1 = .052F_2$ $\quad$ $\alpha^2_0 = .005F_2$

$\alpha^1_1 = -.316F_1$ $\quad$ $\alpha^1_0 = .217F_1$

$0 \longrightarrow 101\ cm^{-1}$ $\quad$ $0(K) \longrightarrow 101\ cm^{-1}$

$\alpha^2_0 = .034F_2$ $\quad$ $\alpha^2_{-1} = -.014F_2$

$\alpha^1_0 = -.075F_1$ $\quad$ $\alpha^1_{-1} = .003F_1$

$0 \longrightarrow 101(K)\ cm^{-1}$ $\quad$ $0(K) \longrightarrow 101(K)\ cm^{-1}$

$\alpha^2_1 = -.014F_2$ $\quad$ $\alpha^2_0 = .034F_2$

$\alpha^1_1 = -.003F_1$ $\quad$ $\alpha^1_0 = .075F_1$

$0 \longrightarrow 133\ cm^{-1}$ $\quad$ $0(K) \longrightarrow 133\ cm^{-1}$

$\alpha^2_{-1} = .037F_2$ $\quad$ $\alpha^2_{-2} = -.033F_2$

$\alpha^1_{-1} = -.025F_1$ $\quad$ $\alpha^2_2 = -.024F_2$

$0 \longrightarrow 133(\mathrm{K})\ \mathrm{cm}^{-1}$ $\quad$ $0(\mathrm{K}) \longrightarrow 133(\mathrm{K})\ \mathrm{cm}^{-1}$

$\alpha^2_{-2} = .024F_2$ $\quad$ $\alpha^2_1 = -.037F_2$

$\alpha^2_2 = .033F_2$ $\quad$ $\alpha^1_1 = -.025F_1$

$0 \longrightarrow 230\ \mathrm{cm}^{-1}$ $\quad$ $0(\mathrm{K}) \longrightarrow 230\ \mathrm{cm}^{-1}$

$\alpha^2_{-1} = -.001F_2$ $\quad$ $\alpha^2_{-2} = -.017F_2$

$\alpha^1_{-1} = .061F_1$ $\quad$ $\alpha^2_2 = .025F_2$

$0 \longrightarrow 230(\mathrm{K})\ \mathrm{cm}^{-1}$ $\quad$ $0(\mathrm{K}) \longrightarrow 230(\mathrm{K})\ \mathrm{cm}^{-1}$

$\alpha^2_{-2} = -.025F_2$ $\quad$ $\alpha^2_1 = .001F_2$

$\alpha^2_2 = .017F_2$ $\quad$ $\alpha^1_1 = .061F_2$

$0 \longrightarrow 247\ \mathrm{cm}^{-1}$ $\quad$ $0(\mathrm{K}) \longrightarrow 247\ \mathrm{cm}^{-1}$

$\alpha^2_0 = .011F_2$ $\quad$ $\alpha^2_{-1} = -.011F_2$

$\alpha^1_0 = -.044F_1$ $\quad$ $\alpha^1_{-1} = .003F_1$

$0 \longrightarrow 247(\mathrm{K})\ \mathrm{cm}^{-1}$ $\quad$ $0(\mathrm{K}) \longrightarrow 247(\mathrm{K})\ \mathrm{cm}^{-1}$

$\alpha^2_1 = -.011F_2$ $\quad$ $\alpha^2_0 = .011F_2$

$\alpha^1_1 = -.003F_1$ $\quad$ $\alpha^1_0 = .044F_1$

$0 \longrightarrow 287\ \mathrm{cm}^{-1}$ $\quad$ $0(\mathrm{K}) \longrightarrow 287\ \mathrm{cm}^{-1}$

$\alpha^2_{-1} = .006F_2$ $\quad$ $\alpha^2_{-2} = -.001F_2$

$\alpha^1_{-1} = .011F_1$ $\quad$ $\alpha^2_2 = .012F_2$

$0 \longrightarrow 287(\mathrm{K})\ \mathrm{cm}^{-1}$ $\quad$ $0(\mathrm{K}) \longrightarrow 287(\mathrm{K})\ \mathrm{cm}^{-1}$

$\alpha^2_{-2} = -.012F_2$ $\quad$ $\alpha^2_1 = -.006F_2$

$\alpha^2_2 = .001F_2$ $\quad$ $\alpha^1_1 = .011F_1$

Cartesian Electronic Raman Scattering Tensors $^4I_{15/2} \longrightarrow {}^4I_{15/2}$

$0.0\ \text{cm}^{-1} \longrightarrow 36\ \text{cm}^{-1}$

$|\alpha_{XX}|^2 = |\alpha_{YY}|^2 = (.008F_2)^2$

$|\alpha_{XY}|^2 = |\alpha_{YX}|^2 = (.039F_2)^2$

$|\alpha_{XZ}|^2 = |\alpha_{YZ}|^2 = (.209F_1 + .016F_2)^2$

$|\alpha_{ZX}|^2 = |\alpha_{ZY}|^2 = (-.209F_1 + .016F_2)^2$

$0.0\ \text{cm}^{-1} \longrightarrow 50\ \text{cm}^{-1}$

$|\alpha_{XX}|^2 = |\alpha_{YY}|^2 = (.002F_2)^2$

$|\alpha_{XY}|^2 = |\alpha_{YX}|^2 = (.153F_1)^2$

$|\alpha_{XZ}|^2 = |\alpha_{YZ}|^2 = (.158F_1 - .026F_2)^2$

$|\alpha_{ZX}|^2 = |\alpha_{ZY}|^2 = (-.158F_1 - .026F_2)^2$

$|\alpha_{ZZ}|^2 = (.004F_2)^2$

$0.0\ \text{cm}^{-1} \longrightarrow 101\ \text{cm}^{-1}$

$|\alpha_{XX}|^2 = |\alpha_{YY}|^2 = (.014F_2)^2$

$|\alpha_{XY}|^2 = |\alpha_{YX}|^2 = (.053F_1)^2$

$|\alpha_{XZ}|^2 = |\alpha_{YZ}|^2 = (.002F_1 + .007F_2)^2$

$|\alpha_{ZX}|^2 = |\alpha_{ZY}|^2 = (-.002F_1 + .007F_2)^2$

$|\alpha_{ZZ}|^2 = (.028F_2)^2$

$0.0\ \text{cm}^{-1} \longrightarrow 133\ \text{cm}^{-1}$

$|\alpha_{XX}|^2 = |\alpha_{YY}|^2 = (.004F_2)^2$

$|\alpha_{XY}|^2 = |\alpha_{YX}|^2 = (.029F_1)^2$

$|\alpha_{XZ}|^2 = |\alpha_{YZ}|^2 = (.013F_1 + .019F_2)^2$

$|\alpha_{ZX}|^2 = |\alpha_{ZY}|^2 = (-.013F_1 + .019F_2)^2$

$0.0\ \text{cm}^{-1} \longrightarrow 230\ \text{cm}^{-1}$

$|\alpha_{XX}|^2 = |\alpha_{YY}|^2 = (.021F_2)^2$

$|\alpha_{XY}|^2 = |\alpha_{YX}|^2 = (.004F_2)^2$

$|\alpha_{XZ}|^2 = |\alpha_{YZ}|^2 = (.031F_1 + .001F_2)^2$

$|\alpha_{ZX}|^2 = |\alpha_{ZY}|^2 = (-.031F_1 + .001F_2)^2$

$0.0\ \text{cm}^{-1} \longrightarrow 247\ \text{cm}^{-1}$

$|\alpha_{XX}|^2 = |\alpha_{YY}|^2 = (.004F_2)^2$

$|\alpha_{XY}|^2 = |\alpha_{YX}|^2 = (.031F_1)^2$

$|\alpha_{XZ}|^2 = |\alpha_{YZ}|^2 = (.002F_1 + .005F_2)^2$

$|\alpha_{ZX}|^2 = |\alpha_{ZY}|^2 = (-.002F_1 + .005F_2)^2$

$|\alpha_{ZZ}|^2 = (.009F_2)^2$

$0.0\ \text{cm}^{-1} \longrightarrow 287\ \text{cm}^{-1}$

$|\alpha_{XX}|^2 = |\alpha_{YY}|^2 = (.007F_2)^2$

$|\alpha_{XY}|^2 = |\alpha_{YX}|^2 = (.005F_2)^2$

$|\alpha_{XZ}|^2 = |\alpha_{YZ}|^2 = (.005F_1 + .003F_2)^2$

$|\alpha_{ZX}|^2 = |\alpha_{ZY}|^2 = (-.005F_1 + .003F_2)^2$

Appendix B3 Ho^{3+}

Spherical Electronic Raman Scattering Tensors $^5I_8 \longrightarrow {}^5I_8$

0.0 (X) $\longrightarrow$ 68 cm^{-1} (X)	0.0 (X) $\longrightarrow$ 68 cm^{-1} (Y)
all tensor elements are zero	all tensor elements are zero
0.0 (X) $\longrightarrow$ 72 cm^{-1}	0.0 (Y) $\longrightarrow$ 72 cm^{-1}
$\alpha^1_1 = -.169F_1$	$\alpha^1_{-1} = -.191F_1$
$\alpha^2_1 = .041F_2$	$\alpha^2_{-1} = -.037F_2$
0.0 (X) $\longrightarrow$ 84 cm^{-1}	0.0 (Y) $\longrightarrow$ 84 cm^{-1}
$\alpha^1_1 = -.188F_1$	$\alpha^1_{-1} = .218F_1$
$\alpha^2_1 = .047F_2$	$\alpha^2_{-1} = .043F_2$
0.0 (X) $\longrightarrow$ 88 (X) cm^{-1}	0.0 (Y) $\longrightarrow$ 88 (X) cm^{-1}
all tensor elements are zero	$\alpha^2_{-2} = .010F_2$
0.0 (X) $\longrightarrow$ 88 (Y) cm^{-1}	0.0 (Y) $\longrightarrow$ 88 (Y) cm^{-1}
$\alpha^2_2 = .010F_2$	all tensor elements are zero
0.0 (X) $\longrightarrow$ 150 cm^{-1}	0.0 (Y) $\longrightarrow$ 150 cm^{-1}
$\alpha^1_1 = -.103F_1$	$\alpha^1_{-1} = -.103F_1$
$\alpha^2_1 = .024F_2$	$\alpha^2_{-1} = -.024F_2$
0.0 (X) $\longrightarrow$ 195 cm^{-1}	0.0 (Y) $\longrightarrow$ 195 cm^{-1}
$\alpha^1_{-1} = .146F_1$	$\alpha^1_1 = .154F_1$
$\alpha^2_{-1} = -.041F_2$	$\alpha^2_1 = .034F_2$
0.0 (X) $\longrightarrow$ 196 cm^{-1}	0.0 (Y) $\longrightarrow$ 196 cm^{-1}
$\alpha^1_{-1} = .132F_1$	$\alpha^1_1 = -.168F_1$
$\alpha^2_{-1} = -.038F_2$	$\alpha^2_1 = -.037F_2$

0.0 (X) $\longrightarrow$ 225 (X) cm^{-1}	0.0 (Y) $\longrightarrow$ 225 (X) cm^{-1}
all tensor elements are zero	$\alpha^2_{-2} = -.030F_2$
0.0 (X) $\longrightarrow$ 225 (Y) cm^{-1}	0.0 (Y) $\longrightarrow$ 225 (Y) cm^{-1}
$\alpha^2_2 = -.030F_2$	all tensor elements are zero
0.0 (X) $\longrightarrow$ 245 cm^{-1}	0.0 (Y) $\longrightarrow$ 245 cm^{-1}
$\alpha^1_1 = -.046F_1$	$\alpha^1_{-1} = .046F_1$
$\alpha^2_1 = .010F_2$	$\alpha^2_{-1} = .010F_2$
0.0 (X) $\longrightarrow$ 276 (X) cm^{-1}	0.0 (Y) $\longrightarrow$ 276 (X) cm^{-1}
all tensor elements are zero	$\alpha^2_{-2} = -.008F_2$
0.0 (X) $\longrightarrow$ 276 (Y) cm^{-1}	0.0 (Y) $\longrightarrow$ 276 (Y) cm^{-1}
$\alpha^2_2 = -.008F_2$	all tensor elements are zero
0.0 (X) $\longrightarrow$ 277 cm^{-1}	0.0 (Y) $\longrightarrow$ 277 cm^{-1}
$\alpha^1_{-1} = .023F_1$	$\alpha^1_1 = .023F_1$
$\alpha^2_{-1} = -.006F_2$	$\alpha^2_1 = .006F_2$
0.0 (X) $\longrightarrow$ 300 cm^{-1}	0.0 (Y) $\longrightarrow$ 300 cm^{-1}
all tensor elements are zero	all tensor elements are zero

Cartesian Electronic Raman Scattering Tensors $^3H_6 \longrightarrow {}^3H_6$

$0.0\ \mathrm{cm}^{-1} \longrightarrow 68\ \mathrm{cm}^{-1}$

scattering matrix is zero

$0.0\ \mathrm{cm}^{-1} \longrightarrow 72\ \mathrm{cm}^{-1}$

$|\alpha_{XZ}|^2 = |\alpha_{YZ}|^2 = (.084F_1 - .021F_2)^2 + (.095F_1 - .019F_2)^2$

$|\alpha_{ZX}|^2 = |\alpha_{ZY}|^2 = (-.084F_1 - .021F_2)^2 + (-.095F_1 - .019F_2)^2$

$0.0\ \mathrm{cm}_C^{-1} \longrightarrow 84\ \mathrm{cm}^{-1}$

$|\alpha_{XZ}|^2 = |\alpha_{YZ}|^2 = (.094F_1 - .023F_2)^2 + (-.109F_1 + .022F_2)^2$

$|\alpha_{ZX}|^2 = |\alpha_{ZY}|^2 = (-.094F_1 - .023F_2)^2 + (.109F_1 + .022F_2)^2$

$0.0\ \mathrm{cm}^{-1} \longrightarrow 88\ \mathrm{cm}^{-1}$

$|\alpha_{XX}|^2 = |\alpha_{YX}|^2 = |\alpha_{XY}|^2 = |\alpha_{YY}|^2 = 2(-.005F_2)^2$

$0.0\ \mathrm{cm}^{-1} \longrightarrow 150\ \mathrm{cm}^{-1}$

$|\alpha_{XZ}|^2 = |\alpha_{YZ}|^2 = 2(.052F_1 - .012F_2)^2$

$|\alpha_{ZX}|^2 = |\alpha_{ZY}|^2 = 2(-.052F_1 - .012F_2)^2$

$0.0\ \mathrm{cm}_C^{-1} \longrightarrow 195\ \mathrm{cm}^{-1}$

$|\alpha_{XZ}|^2 = |\alpha_{YZ}|^2 = (-.073F_1 - .021F_2)^2 + (-.077F_1 - .017F_2)^2$

$|\alpha_{ZX}|^2 = |\alpha_{ZY}|^2 = (.073F_1 - .021F_2)^2 + (.077F_1 - .017F_2)^2$

$0.0\ \mathrm{cm}_C^{-1} \longrightarrow 196\ \mathrm{cm}^{-1}$

$|\alpha_{XZ}|^2 = |\alpha_{YZ}|^2 = (-.066F_1 - .019F_2)^2 + (.084F_1 + .019F_2)^2$

$|\alpha_{ZX}|^2 = |\alpha_{ZY}|^2 = (.066F_1 - .019F_2)^2 + (-.084F_1 + .019F_2)^2$

$0.0\ \mathrm{cm}^{-1} \longrightarrow 225\ \mathrm{cm}^{-1}$

$|\alpha_{XX}|^2 = |\alpha_{YX}|^2 = |\alpha_{XY}|^2 = |\alpha_{YY}|^2 = 2(-.015F_2)^2$

$0.0\ \mathrm{cm}^{-1} \longrightarrow 245\ \mathrm{cm}^{-1}$

$|\alpha_{XZ}|^2 = |\alpha_{YZ}|^2 = 2(.023F_1 - .005F_2)^2$

$|\alpha_{ZX}|^2 = |\alpha_{ZY}|^2 = 2(-.023F_1 - .005F_2)^2$

$0.0\ \mathrm{cm}^{-1} \longrightarrow 276\ \mathrm{cm}^{-1}$

$|\alpha_{XX}|^2 = |\alpha_{YX}|^2 = |\alpha_{XY}|^2 = |\alpha_{YY}|^2 = 2(-.004F_2)^2$

$0.0\ \text{cm}^{-1} \longrightarrow 277\ \text{cm}^{-1}$

$|\alpha_{XZ}|^2 = |\alpha_{YZ}|^2 = 2(-.012F_1 - .003F_2)^2$

$|\alpha_{ZX}|^2 = |\alpha_{ZY}|^2 = 2(.012F_1 - .003F_2)^2$

$0.0\ \text{cm}^{-1} \longrightarrow 300\ \text{cm}^{-1}$

scattering metrix is zero

Appendix B4 Yb^{3+}

Spherical Electronic Raman Scattering Tensors $^4I_{15/2} \longrightarrow {}^4I_{15/2}$

$0 \longrightarrow 99\ \mathrm{cm}^{-1}$

$\alpha_1^2 = -.035F_2$

$\alpha_1^1 = -.238F_1$

$0(\mathrm{K}) \longrightarrow 99\ \mathrm{cm}^{-1}$

$\alpha_2^2 = -.132F_2$

$\alpha_{-2}^2 = .171F_2$

$0 \longrightarrow 99(\mathrm{K})\ \mathrm{cm}^{-1}$

$\alpha_2^2 = -.171F_2$

$\alpha_{-2}^2 = .132F_2$

$0(\mathrm{K}) \longrightarrow 99(\mathrm{K})\ \mathrm{cm}^{-1}$

$\alpha_{-1}^2 = .035F_2$

$\alpha_{-1}^1 = -.238F_1$

$0 \longrightarrow 279\ \mathrm{cm}^{-1}$

$\alpha_0^2 = .055F_2$

$\alpha_0^1 = -.150F_1$

$0(\mathrm{K}) \longrightarrow 279\ \mathrm{cm}^{-1}$

$\alpha_1^2 = -.197F_2$

$\alpha_1^1 = .136F_1$

$0 \longrightarrow 279(\mathrm{K})\ \mathrm{cm}^{-1}$

$\alpha_{-1}^2 = -.197F_2$

$\alpha_1^1 = -.136F_1$

$0(\mathrm{K}) \longrightarrow 279(\mathrm{K})\ \mathrm{cm}^{-1}$

$\alpha_0^2 = .055F_2$

$\alpha_0^1 = .150F_1$

$0 \longrightarrow 288\ \mathrm{cm}^{-1}$

$\alpha_1^2 = .137F_2$

$\alpha_1^1 = .044F_1$

$0(\mathrm{K}) \longrightarrow 288\ \mathrm{cm}^{-1}$

$\alpha_2^2 = -.059F_2$

$\alpha_{-2}^2 = -.097F_2$

$0 \longrightarrow 288(\mathrm{K})\ \mathrm{cm}^{-1}$

$\alpha_2^2 = .097F_2$

$\alpha_{-2}^2 = .059F_2$

$0(\mathrm{K}) \longrightarrow 288(\mathrm{K})\ \mathrm{cm}^{-1}$

$\alpha_{-1}^2 = -.137F_2$

$\alpha_{-1}^1 = .044F_1$

Cartesian Electronic Raman Scattering Tensors $^2F_{7/2} \longrightarrow {}^2F_{7/2}$

$0.0\ \text{cm}^{-1} \longrightarrow 99\ \text{cm}^{-1}$

$|\alpha_{XX}|^2 = |\alpha_{YY}|^2 = (.152F_2)^2$

$|\alpha_{XY}|^2 = |\alpha_{YX}|^2 = (.020F_2)^2$

$|\alpha_{XZ}|^2 = |\alpha_{YZ}|^2 = (.119F_1 + .018F_2)^2$

$|\alpha_{ZX}|^2 = |\alpha_{ZY}|^2 = (-.119F_1 + .018F_2)^2$

$0.0\ \text{cm}^{-1} \longrightarrow 279\ \text{cm}^{-1}$

$|\alpha_{XX}|^2 = |\alpha_{YY}|^2 = (.022F_2)^2$

$|\alpha_{XY}|^2 = |\alpha_{YX}|^2 = (.106F_1)^2$

$|\alpha_{XZ}|^2 = |\alpha_{YZ}|^2 = (-.068F_1 + .098F_2)^2$

$|\alpha_{ZX}|^2 = |\alpha_{ZY}|^2 = (.068F_1 + .098F_2)^2$

$|\alpha_{ZZ}|^2 = (.045F_2)^2$

$0.0\ \text{cm}^{-1} \longrightarrow 288\ \text{cm}^{-1}$

$|\alpha_{XX}|^2 = |\alpha_{YY}|^2 = (.019F_2)^2$

$|\alpha_{XY}|^2 = |\alpha_{YX}|^2 = (.078F_2)^2$

$|\alpha_{XZ}|^2 = |\alpha_{YZ}|^2 = (.022F_1 + .068F_2)^2$

$|\alpha_{ZX}|^2 = |\alpha_{ZY}|^2 = (-.022F_1 + .068F_2)^2$

LAWRENCE BERKELEY LABORATORY
TECHNICAL INFORMATION DEPARTMENT
UNIVERSITY OF CALIFORNIA
BERKELEY, CALIFORNIA 94720